AC Microgrids Analysis, Optimization and Planning for Resilience Enhancement

Thèse

Youthanalack Vilaisarn

Doctorat en génie électrique
Philosophiæ doctor (Ph. D.)

Québec, Canada

AC Microgrids Analysis, Optimization and Planning for Resilience Enhancement

Thèse

Youthanalack Vilaisarn

Sous la direction de :

Jérôme Cros, directeur de recherche
Morad Abdelaziz, codirecteur de recherche

Résumé

Face à des événements météorologiques violents, un système de distribution électrique peut souffrir de la perte ou de la défaillance d'un ou de plusieurs de ses composants. Ce phénomène est connu sous le nom de contingence de système. Néanmoins, en tirant parti des systèmes de protection, de l'électronique de puissance et de la pénétration des ressources énergétiques décentralisées dans le réseau électrique, un système de distribution électrique a la possibilité d'être reconfiguré en micro-réseaux. Cela permet de résister contre de telles éventualités en gardant au minimum la possibilité d'une interruption de l'alimentation. Poussé par des facteurs techniques, économiques et environnementaux, ainsi que par le déploiement rapide d'un grand nombre de ressources de production décentralisées, le micro-réseau est récemment devenu un concept important dans un système de distribution actif et rapidement reconfigurable.

Les micro-réseaux ont la capacité de fonctionner à la fois en mode connecté au réseau et en mode isolé. En raison de cet avantage, le micro-réseau est devenu un élément clé du futur réseau intelligent. Bien que le concept de micro-réseau puisse apporter différents avantages aux services de distribution et aux clients, à savoir une amélioration de l'économie, de l'environnement et de la résilience, il offre toujours un défi au niveau de la planification et la gestion opérationnelle. Les défis de la planification des micro-réseaux proviennent de : 1) la nature intermittente et incertaine des ressources décentralisées et des charges des systèmes distribués, ainsi que l'incertitude relative aux contingences auxquelles le réseau de distribution est confronté, 2) la charge de calcul que la prise en compte des incertitudes du micro-réseau implique, et 3) le grand nombre de compromis entre les différents objectifs d'optimisation possibles du micro-réseau qui doivent être pris en compte dans la phase de planification. Motivée par ces défis, cette recherche propose le développement de nouvelles méthodologies d'analyse et de planification qui peuvent assurer l'efficacité du processus de création du micro-réseau en tenant compte des caractéristiques particulières et de la philosophie opérationnelle du micro-réseau.

Dans un premier temps, les modèles d'étude d'écoulement de puissance linéaires et non linéaires sont développés en prenant compte des caractéristiques réelles d'un micro-réseau insulaire équilibré et déséquilibré, c'est-à-dire l'absence de bus infini, la présence d'une fréquence du système variable et de certains générateurs fonctionnant en mode de contrôle « statisme ». Tout d'abord, nous présentons un algorithme non linéaire basé sur la méthode des mailles et la matrice Z_{bus} pour un micro-réseau opéré en mode « droop ». Cet algorithme sans inversion est particulièrement adapté aux grandes dimensions des systèmes de distribution pratiques comprenant des milliers de nœuds électriques,

lorsqu'ils fonctionnent comme des micro-réseaux insulaires. Deuxièmement, un modèle linéaire pour étudier l'écoulement de puissance (LPF) basé sur la méthode des nœuds est proposé. Étant basé sur la méthode des nœuds, le modèle proposé est utilisable dans différents problèmes d'optimisation de micro-réseaux. Des études de cas numériques sont développées et utilisées pour démontrer la précision des modèles proposés et garantir leur application réussie pour modéliser avec précision l'écoulement d'énergie dans un micro-réseau. Cela permet son application dans un processus d'optimisation présenté à l'étape suivante de cette recherche.

Dans la deuxième étape, cette recherche propose un modèle d'écoulement de puissance optimal (OPF) pour le fonctionnement optimal des micro-réseaux à courant alternatif, équilibrés et déséquilibrés, avec un contrôle hiérarchique (c'est-à-dire, un contrôle primaire et secondaire). Le modèle proposé a d'abord été formulé comme un modèle non linéaire en nombres entiers (MINLP), puis il a été linéarisé et converti en un modèle linéaire en nombres entiers (MILP) en utilisant le modèle LPF développé dans la première étape de cette recherche. La philosophie de fonctionnement du micro-réseau, en mode connecté au réseau et en mode îloté, a été prise en compte. De plus, plusieurs types de générateurs distribués, y compris ceux qui sont disptachables et non disptachables, ainsi que des ressources de stockage d'énergie, ont été pris en compte dans le modèle MILP proposé. Plusieurs études de cas numériques ont été menées pour valider et prouver l'efficacité et la précision du modèle MILP développé. Les résultats de ces études de cas ont démontré la précision et la supériorité de calcul du modèle MILP proposé.

Enfin, un cadre de planification pour les micro-réseaux dans les réseaux de distribution actifs est proposé. Ce cadre de planification vise à améliorer la résilience des systèmes de distribution d'électricité face à des événements de faible probabilité, à fort impact. Dans le cadre proposé, le problème de planification a été présenté comme un problème d'optimisation stochastique à deux niveaux. Tout d'abord, le niveau externe traite du placement optimal des éléments de planification du système de distribution (c.-à-d. les ressources répartissables ou non répartissables, les unités de stockage d'énergie et les interrupteurs d'isolement). Ce problème a été formulé en utilisant une formulation d'optimisation multi-objectifs et ensuite l'algorithme métaheuristique bien connu NSGA-II est adopté pour la recherche d'une solution optimale. Cette approche permet de déterminer les solutions qui impliquent le meilleur compromis entre plusieurs objectifs éventuellement conflictuels du problème de planification, à savoir le coût, la résilience et l'impact environnemental. Deuxièmement, le niveau interne du cadre de planification traite du problème d'optimisation relatif au fonctionnement optimal des micro-réseaux qui peuvent être créés par les éléments de planification du système de distribution alloués dans le niveau externe. Le problème du fonctionnement optimal

du micro-réseau est présenté comme un problème d'étude de l'écoulement de puissance optimal linéaire (LOPF). À cette fin, le modèle MILP développé dans la deuxième étape est adopté. Néanmoins, il est nécessaire de prendre en compte différents scénarios stochastiques dans le niveau interne pour tenir compte des différentes incertitudes du système. Il faut aussi considérer la nature métaheuristique du niveau externe ce qui demande la résolution du modèle LOPF pour chacun des scénarios stochastiques et aussi pour chaque individu de la population. La prise en compte de ces facteurs présente un défi au niveau du calcul. Par conséquent, une nouvelle méthodologie utilisant un modèle de réseau de neurones (DNN) est proposée. Cette méthode permet de dériver rapidement l'information requise des solutions LOPF pour les scénarios stochastiques considérés. Enfin, l'efficacité du cadre proposé est validée par des résultats de simulation numérique.

Abstract

Facing severe weather events, a distribution system may suffer from the loss or failure of one or more of its components, known as N-K contingencies. Nevertheless, taking advantage of the system's isolate switches and the penetration of the distributed energy resources in the electrical grid, a distribution system has the possibility to be clustered into microgrids in order to withstand such contingencies with minimal power interruption. Driven by technical, economic and environmental factors, as well as by the rapid deployment of a large number of distributed generation resources, the microgrid has recently become an important concept in the active distribution system.

Microgrids have the ability to operate in both grid-connected and islanded modes. The benefits that the microgrid concept can bring to the operation of the distribution grids make the microgrid a key component of the future smart grid. While, the microgrid concept can bring different benefits to both distribution utilities and customers i.e., economic, environmental and resilience enhancement; the planning and operational management of microgrids still present several challenges for the decision maker and the distribution network operator. The challenges with the planning of microgrids arise from: 1) the intermittent and uncertain nature of the distributed energy resources and loads as well as the uncertainty pertaining to the contingencies facing the distribution network, 2) the computational burden that considering the microgrid's uncertainties entails, and 3) the large number of trade-offs between the different possible microgrid optimization objectives that need to be considered in the planning stage. Motivated by these challenges, this research proposes the development of new analysis and planning methodologies that can ensure the efficacy of the microgrid creation process considering the microgrids special features and operational philosophy.

Initially, nonlinear and linear power flow models are developed to cope with the real characteristics of balanced and unbalanced islanded microgrid i.e. the absence of the slack bus, the system frequency being a variable and some DGs operating in droop-control mode. First, a non-linear branch-based $\mathbf{Z_{bus}}$ algorithm for the droop-controlled islanded microgrid is introduced. This algorithm is inversion free and is particularly suited for the large dimensions of practical distribution systems comprising up to thousands of electrical node, i.e., when operated as islanded microgrids. Secondly, a node-based linear power flow (LPF) model for droop-controlled islanded microgrids is proposed. The node-based nature of the proposed LPF model, allows this model to be integrated in different microgrid optimization models. Numerical case studies are developed and are used to demonstrate the accuracy of the proposed power flow models and guarantee its successful application to accurately model the microgrid power flow in the optimization application in the next stage of this research.

In the second stage, this research proposes an optimal power flow (OPF) model for the optimal operation of balanced and unbalanced AC microgrids with hierarchical control (i.e., primary droop and secondary control). The proposed model has been first formulated as a mixed integer nonlinear programing (MINLP) model, then it was linearized and converted into a mixed integer linear programing (MILP) model by adapting the LPF model developed in the first stage of this research. The operating philosophy of the microgrid, in both grid-connected and islanded modes of operation, was considered. Additionally, several types of distributed generators, including dispatchable and non-dispatchable, as well as energy storage resources, were considered in the proposed MILP model. Several numerical case studies were conducted to validate, and prove the effectiveness and the accuracy of the developed MILP model. The results from the developed case studies demonstrated the accuracy and the computational superiority of the proposed MILP model.

Finally, a planning framework for microgrids in active distribution networks is proposed. The proposed planning framework is aimed at enhancing the resilience of power distribution systems facing high impact low probability events. In the proposed framework, the planning problem has been casted as a stochastic bi-level optimization problem. First, the outer level deals with the optimal placement of the distribution system planning elements (i.e., dispatchable/non-dispatchable resources, energy storage units and isolating switches). This problem has been formulated using a multi-objective optimization formulation and the well know metaheuristic Non-dominated Sorting Genetic Algorithm (NSGA-II) algorithm is adopted for its solution. This approach allows for determining the solutions that entail the best trade-off between the possibly conflicting multi-objectives of the planning problem, namely, cost, resilience and environmental impact. Second, the inner level of the planning framework handles the optimization problem pertaining to the optimal operation of the microgrids that can be created by the distribution system planning elements allocated in the outer level. The problem of the microgrid's optimal operation is casted as a Linear Optimal Power Flow (LOPF) problem. To this end, the proposed MILP model developed in the second stage is adopted. Despite using a LOPF model, considering different stochastic scenarios in the inner level, to account for the different system uncertainties, along with the metaheuristic nature of the outer level make solving the LOPF model for each of the stochastic scenarios for each individual in the metaheuristic optimization's population, using a numerical optimization solver computationally challenging. Motivated by this challenge, a novel methodology using a deep neural network (DNN) model is proposed for deriving the information required from the LOPF solutions for the stochastic scenarios under consideration. The effectiveness of the proposed framework is finally validated by numerical simulation results.

Table of Contents

List of Figures

Introduction:

Chapter 1:

Chapter 2:

Chapter 3:

Chapter 4:

Chapter 5:

Appendix C:

Appendix D:

List of Tables

Appendix D:

Appendix F:

Appendix G:

Nomenclature

The notation for this thesis has been listed as following. In the order to quick reference, the parameters, variables, and some of notation type has been stated for each chapter.

Abbreviations

ISW^{sub}	Isolate Switch at the upstream substation
AC/DC	Alternative/Direct Current system
ADS	Active Distribution System
AMG	Autonomous or Islanded Microgrid
BFS	Backward-Forward-Sweep
BRB	Bayesian Regularization Backpropagation
CCS	Compressed Column Storage
DDG	Dispatchable Distributed Generation
DER	Distributed Energy Resource
DFS	Depth First Search algorithm
DG	Distributed Generation
DMS	Demand Side Management
DNN	Deep Neural Network
DOE	U.S. Department of Energy
$droop/2^{nd}$	Primary droop mode with a supervisory secondary control layer
DSO	Distributed System Operator
ESS	Energy Storage System unit
GC	Grid-Connected operation
GS	Gauss Seidel
HILP	High Impact Low Probability
IMG	Islanded Microgrid
IS	Islanded operation
ISW	Isolate Switch
$LOPF^{AC,DL}$	Deep Learning AC-LOPF
LPF	Linear Power Flow
MBF	Modified Backward Forward power flow method
MG(s)	Microgrid(s)
MILP	Mixed Integer Linear Programming
MINLP	Mixed Integer Nonlinear Programming
NaS	Technology Sodium Sulfur
N-K	Level of contingencies
non-LPF	Nonlinear Power Flow
NR	Newton Raphson
NREL	National Renewable Energy Laboratory

NSGA-II	Non-dominated Sorting Genetic Algorithm II
NTR	Newton Trust Region power flow method
NYISO	New York Independent System Operator
O&M	Operation and Maintenance
OPF/LOPF	Non-Linear/Linear Optimum Power Flow
PCC	Point of Common Coupling
PHEVs	Plug-In Hybrid Electric Vehicles
PQ bus	Active and reactive power controllable bus
PQ mode	Active and Reactive power control mode
PV	Photovoltaic energy
PV bus	Active power and voltage controllable bus
SOC	State of Charge of the ESS
SPF	System Performance
SRF-PLL	Synchronous Reference Frame Phase Locked-Loop
T&D	Transmission and Distribution
TR	Transformer
WT	Wind Turbine energy

Sets and Numbers

n_{br}	Number of the branches in the test system
n_{bus}	Number of buses in the test system
n_{ddg}	Number of DDGs in the planning problem
n_{DG}	Number of DG units
n_{ess}	Number of ESSs in the planning problem
n_{feat}	Number of features in a vector of sample
n_{hl}	Number of hidden layers for DNN model
n_{isw}	Number of ISWs in the planning problem
n_{MG}	Number of the microgrids
n_{path}	Number of the paths search
n_{pv}	Number of PVs in the planning problem
n_{pw}	Number of pieces for piecewise linearization
N_s'	Number of normal scenarios
N_s''	Number of severe scenarios
n_{sam}	Number of samples for training DNN model
N_T	Planning horizon time e.g., 24h
n_{wt}	Number of WTs in the planning problem
$\mathbb{R}$	Continuous variable or real number
$\mathbb{Z}$	Integer variable or binary number
Ω_x	Set of buses type x, where x can be {BUS, LIN, PCC, DDG, WDG, PV or ESS}
Ω_{DDG}^{can}	Set of candidate buses for DDGs
Ω_{ESS}^{can}	Set of candidate buses for ESSs
Ω_{ISW}^{can}	Set of candidate branches for SSWs

Ω_{PV}^{can}	Set of candidate buses for PV units
Ω_{WT}^{can}	Set of candidate buses for WT units
Ω_{LIN}^{fail}	Set of failure branches in the test system
Ω_{TG}^{node}	Set of targets node(s)
Ω_s'	Set of generated scenarios for normal situation
Ω_s''	Set of generated scenarios for severe situation considering network SPF progression phase I and II (i.e., $t^e \rightarrow t^r$)
$\Omega_s^{'',orig}$	Original set before reduction of generated scenarios for severe situation considering network SPF progression phase I and II (i.e., $t^e \rightarrow t^r$)
Ω_s^{pre}	Set of generated pre-scenarios for severe situation considering only network SPF progression phase I (i.e., $t^e \rightarrow t^d$)
Ω_{SAM}	Set of DNN training samples
Ω_{se}	Set of seasonal periods i.e. {fall, winter, spring, summer}
Ω_T	Set of segments or hours in the planning horizon e.g. $\Omega_T = \{1,2,3,\dots,24\}$
$\mathfrak{D}$	Set of droop buses
$\mathcal{F}$	Set of electrical phases i.e. A, B and C

List of Symbols Used in Chapter 1

f	System frequency
f^*	Frequency reference for primary control of the droop unit
f^{max}/f^{min}	Maximum/Minimum frequency violation
$f^{OPF}(\mathbf{x})$	Objective function for OPF problem dependent on set of variables **x**
$F^{plan}(\mathbf{x})$	Objective function of the planning problem dependent on set of variables **x**
$\mathbf{g}^{\mathbf{OPF}}(\mathbf{x})$	Set of equality constraints dependent on set of variables **x**
$\mathbf{G}^{\mathbf{plan}}(.)$	Set equality and inequality constraint for the planning problem
$\mathbf{h}^{\mathbf{OPF}}(\mathbf{x})$	Set of inequality constraints dependent on set of variables **x**
$\mathbf{H}^{\mathbf{plan}}(.)$	Set inequality and inequality constraint for the planning problem
$\bar{\boldsymbol{I}}$	Vector containing current injection in complex form for the buses in the balanced IMG
m^p	Active droop gain of the droop unit
n^q	Reactive droop gain of the droop unit
OF_m	m^{th} objective function for the case multi-objective problem
$P^{G,max}$	Maximum allowable for active power generated by DDG unit
P^G	Active power generated by the droop unit
P_i	Active power injected to bus i
P_i^L	Active power demand located at bus i
$Q^{G,max}$	Maximum allowable for reactive power generated by DDG unit
Q^G	Reactive power generated by the droop unit
Q_i	Reactive power injected to bus i
Q_i^L	Reactive power demand located at bus i
$\bar{S}_i$	Complex form appearance power injected to bus i

$\mathbf{u}^{\mathbf{OPF}}$	Set control variables
$\bar{\boldsymbol{V}}$	Vector containing voltage in complex form for the buses in the balanced IMG
$\lvert\bar{V}\rvert$	Magnitude of voltage
V^*	Voltage reference for primary control of droop unit
V^{max}/V^{min}	Maximum/Minimum voltage violation
$\mathbf{x}^{\mathbf{OPF}}$	Set of dependent variables
$\mathbf{x}^{\mathbf{plan}}$	Set decision variables for the planning problem
$\bar{\mathbf{Y}}^{\mathbf{bus}}$	Admittance matrix in rectangular form for the balanced IMG
$\bar{\mathbf{Z}}^{\mathbf{bus}}$	Impedance matrix in rectangular form for the balanced IMG
δ	Phase angle of voltage
ω	Angular frequency

List of Symbols Used in Chapter 2

Parameters:

$P_{i,\Psi}^{L}$	Active power demand phase Ψ located at bus i
$P_{i}^{L,3\Phi}$	Three phase active power demand located at bus i
P_{i}^{L}	Active power demand located at bus i
$Q_{i,\Psi}^{L}$	Reactive power demand phase Ψ located at bus i
$Q_{i}^{L,3\Phi}$	Three phase reactive power demand located at bus i
Q_{i}^{L}	Reactive power demand located at bus i
V_{i}^{*}	Voltage reference for primary control of the i^{th} DDG
f_{i}^{*}	Frequency reference for primary control of the i^{th} DDG
m_{i}^{p}	Active droop gain of the i^{th} DDG unit
n_{i}^{q}	Reactive droop gain of the i^{th} DDG unit

Variables and elements exclusive used for chapter 2:

Δf	Frequency deviation of the IMG from the nominal frequency
$\overline{\boldsymbol{dV}}$	Vector containing voltage deviation for the buses in the balanced IMG
$\overline{dV_i}$	Voltage deviation calculated for bus i
f	Islanded Microgrid's frequency
f^0	System frequency of nominal operating point
$f^{3\Phi}$	Islanded Microgrid's frequency considering 3 phase power flow
$\bar{\boldsymbol{I}}$	Vector containing current injection in complex form for the buses in the balanced IMG
$\bar{\boldsymbol{I}}^{\boldsymbol{br,abc}}$	Vector containing complex form of branch current phase A, B and C for the unbalanced IMG
$\bar{\boldsymbol{I}}^{\boldsymbol{abc}}$	Vector containing complex form of current injected to phase A, B and C for the buses in the unbalanced IMG
$\bar{\boldsymbol{I}}^{\boldsymbol{br}}$	Vector containing complex form of branch current in the unbalanced IMG
$\bar{I}_{1,\Psi}^{br}$	Sum of branch current phase Ψ that adjacent to bus 1
$\bar{I}_{i,\Psi}$	Current injected to phase Ψ of bus i

$\bar{I}_{i,\Psi}^{br}$	Current flowing on phase Ψ of branch i
$\bar{I}_{1}^{br}$	Sum of branch current that adjacent to bus 1
$\bar{I}_{i}$	Current injected to bus i
$\bar{I}_{i}^{br}$	Current of branch i
it^{M}	Iteration counter of the middle loop of Z_{bus} algorithm
$\mathbf{K/K^{T}}$	Incidence matrix and it transpose of the unbalanced IMG
$\mathbf{K^{3\Phi}}/(\mathbf{K^{3\Phi}})^{T}$	Three phase incidence matrix and it transpose of the unbalanced IMG
K^{pf}/K^{qf}	Active and reactive power frequency dependencies factors
$P_{i,\Psi}$	Active power injected phase Ψ to bus i
$P_{i,\Psi}^{G,init}$	Initial active power generated phase Ψ by i^{th} DG unit
$P_{j,\Psi}^{L,spec}$	Specified nominal active power demand
$P_{i}^{a,b,c}$	Active power injected specific to phase A, B or C of bus i
$P_{i}^{br,3\Phi}$	Three-phase active power flowing on branch i
$P_{i}^{G,(a,b,c)}$	Active power generated phase A, B or C by the i^{th} DG unit
$P_{i}^{G,3\Phi}$	Three phase active power generated by the i^{th} DG unit
P_{i}^{G}	Active power generated by the i^{th} DG unit
Q_{i}^{G}	Reactive power generated by the i^{th} DG unit
$Q_{i,\Psi}^{G,init}$	Initial reactive power generated phase Ψ by i^{th} DG unit
$Q_{j,\Psi}^{L,spec}$	Specified nominal reactive power demand
$Q_{i}^{a,b,c}$	Reactive power injected specific to phase A, B or C of bus i
$Q_{i}^{br,3\Phi}$	Three-phase reactive power flowing on branch i
$Q_{i}^{G,(a,b,c)}$	Reactive power generated phase A, B or C by the i^{th} DG unit
$Q_{i}^{G,3\Phi}$	Three phase reactive power generated by the i^{th} DG unit
$Q_{i}^{L,3\Phi}$	Three phase reactive power demand located at bus i
$\mathbf{R^{bus}}$	Real part of $\bar{\mathbf{Z}}^{\mathbf{bus}}$
$\bar{\boldsymbol{S}}$	Vector containing power injection in complex form for the buses in the balanced IMG
$\bar{\boldsymbol{S}}^{\boldsymbol{abc}}$	Vector containing complex form of power injected to phase A, B and C for the buses in the unbalanced IMG
$\boldsymbol{V}$	Vector containing voltage magnitude in for the buses in the balanced IMG
$\bar{\boldsymbol{V}}$	Vector containing voltage in complex form for the buses in the balanced IMG
$\bar{\boldsymbol{V}}^{\boldsymbol{abc}}$	Vector containing the voltages in complex form for the buses in the unbalanced IMG
$\bar{V}_{1,\Psi}$	Voltage in complex form for phase Ψ of bus 1
$\bar{V}_{i,\Psi}$	Voltage in complex form for phase Ψ of bus i
$\bar{\boldsymbol{V}}_{\mathbf{1}}^{\boldsymbol{abc}}$	Vector containing voltage in complex form for phase A, B and C of bus 1
$\bar{V}_{i}$	Voltage in complex form of bus i
$\bar{V}_{i}^{a,b,c}$	Voltage in complex form specific to phase A, B and C of bus i

$\boldsymbol{V}^{it}$	Vector of iteration it, containing voltage magnitude for the buses in the balanced IMG
V_1	Voltage magnitude of bus 1
V_1^{it}	Voltage magnitude of bus 1 for iteration it
V_i	Voltage magnitude of the bus i
$\mathbf{X}^{\mathbf{br},3\Phi}$	Reactance matrix for the branches in the unbalanced IMG
$\mathbf{X}^{\mathbf{bus},(\mathbf{0})}$	Reactance matrix for the buses in the balanced IMG based on initial data import
$\mathbf{X}^{\mathbf{bus},3\Phi}$	Reactance matrix for the buses in the unbalanced IMG
$\mathbf{X}^{\mathbf{bus}}$	Reactance matrix for the buses in the balanced IMG
$Y_{ij}^{\Psi\beta}$	Admittance between node i and j considering phase Ψ to β
$\bar{\mathbf{Z}}^{\mathbf{br},3\Phi}$	Primitive impedance matrix in rectangular form of the unbalanced IMG
$\bar{\mathbf{Z}}^{\mathbf{bus},3\Phi}$	Three-phase bus impedance matrix in rectangular form for unbalanced IMG
$\bar{\mathbf{Z}}^{\mathbf{bus}}$	Impedance matrix in rectangular form for the balanced IMG
$\bar{Z}_{ij}^{br,\Psi\beta}$	Impedance between node i and j considering phase Ψ to β
α/β	Active and reactive power exponents
$\boldsymbol{\delta}$	Vector containing voltage magnitude angle in for the buses in the balanced IMG
$\boldsymbol{\delta}^{\boldsymbol{abc}}$	Vector containing the voltage magnitude angles for the buses in the unbalanced IMG
δ_i	Voltage magnitude angle of the bus i
$\delta_i^{a,b,c}$	Voltage magnitude angle specific to phase A, B or C of bus i
$\theta_{ij}^{\Psi\beta}$	Admittance angle between node i and j considering phase Ψ to β
λ	Step size exclusive used for the middle of Z_{bus} algorithm

List of Symbols Used in Chapter 3

Parameters:

$P_{i,\Psi}^{L}$	Active power demand phase Ψ located at bus i
$Q_{i,\Psi}^{L}$	Reactive power demand phase Ψ located at bus i
V_i^*	Voltage reference for primary control of the i^{th} DDG
f_i^*	Frequency reference for primary control of the i^{th} DDG
m_i^p	Active droop gain of the i^{th} DDG unit
n_i^q	Reactive droop gain of the i^{th} DDG unit

Variables:

$B_{ij}^{\Psi\beta}$	Element of the susceptance matrix denote the connection of bus i phase Ψ to bus j phase β
$f^{3\Phi}$	Islanded Microgrid's frequency considering 3 phase power flow
$G_{ij}^{\Psi\beta}$	Element of the conductance matrix denote the connection of bus i phase Ψ to bus j phase β
$P_{i,\Psi}$	Active power injected phase Ψ to bus i
$P_{i,\Psi}^{G}$	Active power generated by the i^{th} DG unit

$P_i^{G,3\Phi}$	Three phase active power generated by the i^{th} DG unit
$Q_{i,\Psi}$	Reactive power injected phase Ψ to bus i
$Q_i^{G,3\Phi}$	Three phase reactive power generated by the i^{th} DG unit
$\bar{V}_{i,\Psi}$	Voltage magnitude in complex form of phase Ψ of the bus i
$\bar{V}_i^{a,b,c}$	Voltage magnitude in complex form specific to phase A, B or C of the bus i
$\delta_{i,\Psi}$	Voltage magnitude angle of phase Ψ of the bus i
$\delta_i^{a,b,c}$	Voltage magnitude angle of specific to phase A, B or C of the bus i

List of Symbols Used in Chapter 4

Parameters and vector/matrix:

Δt	Step time (i.e., 1 segment = 1 hour)
APL_t	Annual peak load factor according to seasonal pattern
$B_{ij}^{\Psi\beta}$	Element of the susceptance matrix denote the connection of bus i phase Ψ to bus j phase β
b_t^m	Binary input parameter indicates the operation mode of the MG at time t
b_i^{ESSm}	Binary input parameter indicates the operation mode of the i^{th} ESS
CR_i^{DDG}	Consumption rate of the natural gas of DDG_i [scf/kWh]
$E_i^{ESS,max}$	Maximum allowable stored energy of the ESS unit i
$E_i^{ESS,min}$	Minimum allowable stored energy of the ESS unit i
$G_{ij}^{\Psi\beta}$	Element of the conductance matrix denote the connection of bus i phase Ψ to bus j phase β
$I_k^{br,max}$	Maximum ampacity of the branch k
ki^{ω}	Integral gain for frequency restoration for DDG or for ESS with primary droop control mode with a supervisory secondary control layer
m_i^p	Active droop gain of the i^{th} DDG unit or the i^{th} ESS with primary droop control mode with a supervisory secondary control layer
n_i^q	Reactive droop gain of the i^{th} DDG unit or the i^{th} ESS with primary droop control mode with a supervisory secondary control layer
N_i^{curt}	Limit on the number of load shedding switchings for each load at bus i
$P_{i,t}^{L,3\Phi}$	Three phase active power demand located at bus i, time t
$P_{i,t}^{PV,3\Phi}$	Three phase active power generated by i^{th} PV units at time i
$P_{i,t}^{WT,3\Phi}$	Three phase active power generated by i^{th} wind units at time i
$P_{i,\Psi}^{L,peak}$	Annual peak active demand of bus i
$P_{i,\Psi,t}^{L}$	Active power demand phase Ψ located at bus i, time t
$P_i^{DDG,max}$	Maximum allowable for active power generated by i^{th} DDG unit
$P_i^{DDG,min}$	Minimum allowable for active power generated by i^{th} DDG unit
PC^{VI}	Penalty coefficient of voltage violation [$/kV]
$PF_i^{DDG,1st/4th}$	Minimum operating power factor allowable of the 1st/4th quadrant of the DDG unit i

$PF_i^{TR,1st/4th}$	Minimum operating power factor allowable of the 1st/4th quadrant of the transformer i
PF_i^{PV}	Power factor set of the PV unit i
PF_i^{WT}	Power factor set of the wind unit
$Q_{i,t}^{WT,3\Phi}$	Three phase reactive power generated by i^{th} wind units at time i
$Q_{i,\Psi}^{L,peak}$	Annual peak reactive demand of bus i
$Q_{i,\Psi,t}^{L}$	Reactive power demand phase Ψ located at bus i, time t
$Q_i^{DDG,max}$	Maximum allowable for reactive power generated by i^{th} DDG unit
$Q_i^{DDG,min}$	Minimum allowable for reactive power generated by i^{th} DDG unit
$Q_i^{ESS,max}$	Maximum allowable for reactive power of ith ESS unit
$Q_i^{ESS,min}$	Minimum allowable for reactive power of ith ESS unit
R^C	Certain radiation point, typically set to 0.15 kW/m^2
R^{STD}	Solar radiation in standard test conditions, typically specified as 1000 W/m^2
r_t^m	Solar irradiance in kW/m^2
$S_i^{DDG,max}$	Capacity rating of the DDG unit i
$S_i^{PV,max}$	Capacity rate of the PV unit located at bus i
$S_i^{TR,max}$	Capacity rate of the transformer located at the substation
$S_i^{WT,max}$	Capacity rate of the wind DG located at bus i
SOC_i^0	Initial state of charge of the ESS unit i
T_i^{curt}	Maximum hours of load curtailment of bus i
v^{ci},v^{co},v^{ra}	Cut-in, cut-out, and the rated speed of the wind DG, respectively
V^{max}	Maximum voltage violation
V^{min}	Minimum voltage violation
V_i^{**}	Voltage reference for secondary control of the i^{th} DDG or the i^{th} ESS with primary droop control mode with a supervisory secondary control layer
V_i^{*}	Voltage reference for primary control of the i^{th} DDG or the i^{th} ESS with primary droop control mode with a supervisory secondary control layer
V_{spec}^{GC}	Nominal specified voltage during grid-connected mode
v_t^m	Wind speed in m/s
η_i^{ESS}	Efficiency of the energy storage
σ^{curt}	Cost of load curtailment [$/kWh]
σ^{fuel}	Natural gas price [$/Thousands of cubic feet]
σ_t^{PCC}	Market energy price at time t [$/kWh]
ω^*	Nominal angular frequency of the system

Sets of Variables:

$\boldsymbol{X}^{MINLP,3\Phi}$	Vector containing the decision variables for the MINLP problem formulation
$\boldsymbol{X}^{MILP,3\Phi}$	Vector containing the decision variables for the MILP problem formulation

Continuous variables:

$E_{i,t}^{ESS}$	Energy SOC of the ESS unit i at time t

$P_{i,t}^{DDG,3\Phi}$	Three phase active power generated by the i^{th} DDG unit at time t
$P_{i,t}^{PCC,3\Phi}$	Three phase active power imported from the main grid across the i^{th} PCC of the MG at time t
$P_{i,t}^{ch,3\Phi}$	Active power charge by i^{th} ESS unit at time t
$P_{i,t}^{dch,3\Phi}$	Active power discharge by i^{th} ESS unit at time t
$P_{i,\Psi,t}$	Active power injected phase Ψ to bus i at time t
$P_{i,\Psi,t}^{DDG}$	Active power phase Ψ generated by the i^{th} DDG unit at time t
$P_{i,\Psi,t}^{PCC}$	Active power phase Ψ imported from the main grid across the i^{th} PCC of the MG at time t
$P_{i,\Psi,t}^{dch}$	Active power phase Ψ discharged by i^{th} ESS unit at time t
$P_{k,\Psi,t}^{br}$	Active power phase Ψ flowing across the transmission branch k at time t
$Q_{i,t}^{ESS,3\Phi}$	Three reactive power generate/receive of the i^{th} ESS unit, at time t
$Q_{i,\Psi,t}$	Re-active power injected phase Ψ to bus i at time t
$Q_{i,\Psi,t}^{DDG}$	Reactive power phase Ψ generated by the i^{th} DDG unit at time t
$Q_{i,\Psi,t}^{ESS}$	Reactive power phase Ψ generated by i^{th} ESS unit at time t
$Q_{i,\Psi,t}^{PCC}$	Three phase reactive power imported from the main grid across the i^{th} PCC of the MG at time t
$Q_{k,\Psi,t}^{br}$	Reactive power phase Ψ flowing across the transmission branch k at time t
$u_{i,\Psi,t}^{v,int}$	Integrator output of secondary voltage restoration considering phase Ψ of i^{th} DDG unit or the i^{th} ESS operating with secondary control at time t
$V_{i,\Psi,t}$	Voltage magnitude phase Ψ , of the bus i at time t
$\delta_{i,\Psi,t}$	Voltage magnitude angle of phase Ψ, bus i at time t
$\delta_{\Psi,t}^{MG}$	Phase angle of the bus where the frequency control act

Binary variables:

$b_{i,t}^{curt}$	Binary variable representing load curtailment (1: load shaded and 0: load fed)
$b_{i,t}^{ESS}$	Binary variable indicates the status of ESS i.e. 1: discharge and 0: charge
$z_{i,t}^{curt}$	Binary variable representing a linearization of absolute term $\left\|b_{i,t}^{curt} - b_{i,t-1}^{curt}\right\|$

Function and Metric:

C_t^{CURT}	Cost of energy curtailment during islanding mode at time t
C_t^{DDG}	Cost of natural gas consumption by the DDG units at time t
C_t^{PCC}	Cost of energy imported from the substation across the PCC of the microgrid at time t
C_t^{VI}	Cost of voltage deviation at time t
$C_t^{VI,Lin}$	Linearized version of C_t^{VI}

List of Symbols Used in Chapter 5

Parameters and vector/matrix:

Δt	Step time (i.e., 1 segment = 1 hour)
$\mathbf{A}^{\mathbf{MG}}$	Adjacency matrix for generating $\mathbf{MG}_t^{\mathbf{set}}$
$APL_{t,s,se}$	Annual peak load pattern in percentage at time t for s^{th} scenario of season se
$\mathbf{AV}$	Line or branch availability binary matrix
$\mathbf{AV}_{s,se}^{\mathbf{I-II}}$	Reduction version of $\mathbf{AV}_{s,se}^{\mathbf{I-II,orig}}$
$\mathbf{AV}_{s,se}^{\mathbf{I-II,orig}}$	Matrix constraining the binary element represents an availability of the branches for s^{th} scenario of season se, considering full network SPF progression i.e., phase I and II (i.e., $t^e \rightarrow t^r$)
$\mathbf{AV}_{s,se}^{\mathrm{I}}$	Matrix constraining the binary element represents an availability of the branches for s^{th} scenario of season se, considering only network SPF progression phase I (i.e., $t^e \rightarrow t^d$)
$B_{ij,t,s,se}$	Element of the time-coupled susceptance matrix denote the connection of bus i to bus j at time t for s^{th} scenario of season se
$\mathbf{B}_{s,se}$	3D matrix containing the time coupled susceptance matrices for s^{th} scenario of season se
$b_{t,s,se}^{m}$	Binary input parameter indicates the operation mode of the microgrid at time t for s^{th} scenario of season se
$\mathbf{b}_i$	Vector of biases for i^{th} hidden layer of DNN architecture
B_{ij}	Element of the susceptance matrix denote the connection of bus i to bus j
$\boldsymbol{b_t^m}$	Vector containing binary elements $b_{i,t,s,se}^{m}$ indicates the operation mode for each bus at time t
$\boldsymbol{BFa}_t$	Binary vector represents the bus(es) affected/non-affected by fault(s) at time t
br_i^{fail}	Branch location corresponding to failure branch i
$\boldsymbol{bus^{on}}$	Bus online or bus non affected by fault(s)
$\boldsymbol{bus}_t^{ne}$	Vector containing binary elements $bus_{i,t,s,se}^{ne}$ that indicates bus energize/non-energize at time t for s^{th} scenario of season se
$cdf^{nor}(.)$	Normal Cumulative Distribution Function
$DDG_{n,sp}^{site}$	Location of n^{th} DDG of sample sp
$\boldsymbol{DDG}_{sp}^{site}$	Vector containing the location of the DDGs for sample sp
$\boldsymbol{DDG}_{sp}^{size}$	Vector containing the size of DDGs for sample sp
$\boldsymbol{DDG}_t^{down}$	Vector containing binary elements $DDG_{n,t}^{down}$ that indicate the n^{th} DDG deactivation at time t
$DIJK(.)$	Shortest path between two points by Dijkstra algorithm
DoD^{max}	Maximum Depth of Discharge allowable for ESS
$E_i^{ESS,size}$	Energy rating of ESS at candidate bus i
$\boldsymbol{ESS}_{sp}^{site}$	Vector containing the location of the ESSs for sample sp
$\boldsymbol{ESS}_t^{down}$	Vector containing the status of the ESSs (i.e., $ESS_{i,t,s,se}^{down}$) at time t
$f^{dnn'}$	Activation function for the output layer
$f_i^{dnn}(.)$	Activation function for the i^{th} hidden layer
$\boldsymbol{f}_t^{\boldsymbol{bus}}$	Vector containing $f_{n,t}^{bus}$ that indicate the location of the controllable bus at time t for a n^{th} DDG

$\mathbf{FA}^{\mathbf{br}}$	Binary matrix represents branches affected by different location of faults
$\mathbf{FA}^{\mathbf{bus}}$	Binary matrix represents buses affected by different location of faults
$fb(br_i^{fail})$	From bus of the failure overhead line of branch i
$\boldsymbol{fb, tb}$	Set of from bus and to bus for the test case tropology
$\boldsymbol{floc}_t$	Vector containing the i^{th} fault at location i.e., $floc_{i,t}$ at time t
$\mathbf{G}^{\mathbf{bus}}$	Undirected graph representation by set of vertices (nodes) $\boldsymbol{ND^{bus}}$ and set of edge (branch) $\boldsymbol{ED^{br}}$
$G_{ij,t,s,se}$	Element of the time-coupled conductance matrix denote the connection of bus i to bus j at time t for s^{th} scenario of season se
$\mathbf{G}_{s,se}$	3D matrix containing the time coupled conductance matrices for s^{th} scenario of season se
G_{ij}	Element of the conductance matrix denote the connection of bus i to bus j
$\boldsymbol{h^{ddg}}$	Vector containing h_m^{ddg} that indicate the presents of DDG for m^{th} MG
h_1^{high}/h_2^{high}	Pre-determined range for determining φ^{br} for the case corresponding to higher wind $v_{t,s,se}^{gust} > v_{cri}^{high}$
h_1^{low}/h_2^{low}	Pre-determined range for determining φ^{br} for the case corresponding to $v_{cri}^{low} \leq v_{t,s,se}^{gust} \leq v_{cri}^{high}$
$I_k^{br,max}$	Maximum ampacity of the branch k
$\mathbf{IN}^{\mathbf{dnn}}$	Matrix containing vector of feature $\boldsymbol{IN_{sp}^{dnn}}$ for training DNN model, $sp \in \Omega_{SAM}$
$\boldsymbol{ISW}^{open}$	Vector containing the location of mth ISW (i.e., ISW_m^{open}) in open state
$\boldsymbol{ISW}^{site}$	Vector containing the location of ISWs
k^{gust}	Constant factor for calculating wind-gust
$k^{i\omega}$	Integral gain for frequency restoration for DDG with $\mathrm{droop}/2^{\mathrm{nd}}$
$K_{s,se}/K_{s,se}^{HI}$	Level of contingencies
K_{CO2}^{DDG}	Carbon emission factor in kg/kWh according to energy generated by DDGs
K_{CO2}^{GRID}	Carbon emission factor kg/kWh according to energy imported from the main grid
$L_{i,t,s,se}^{DDG}$	Set of piecewise linearization for DDG quadratic constraint
$L_{i,t,s,se}^{ES}$	Set of piecewise linearization for ESS quadratic constraint
$L_{i,t,s,se}^{PCC}$	Set of piecewise linearization for PCC quadratic constraint
$L_{k,t,s,se}^{br}$	Set of piecewise linearization for line ampacity quadratic constraint
$\boldsymbol{LFa}_t$	Binary vector represents the line(s) affected/non-affected by fault(s) at time t
$\mathbf{M}^{\mathbf{adj}}$	Adjacency matrix
m_i^p	Active droop gain of the i^{th} DDG unit with primary $\mathrm{droop}/2^{\mathrm{nd}}$
M_{ij}^{adj}	Binary element of $\mathbf{M}^{\mathbf{adj}}$ represents the connection between two adjacent nodes ij
$\boldsymbol{MG_m^{DFS}}$	Vector of m^{th} microgrid obtained by DFS of m^{th} $root^{MG}$
$\mathbf{MG}^{\mathbf{set0}}$	Initial set of microgrid formation
$\boldsymbol{MG_{m,t}^{set}}$	Set of buses in m^{th} MG formed at time t
$\mathbf{MG}_t^{\mathbf{set}}$	Matrix containing the set of possible microgrids formation due to fault at time t

MSE	Mean sum of squares of the DNN errors
MSW	Mean sum of squares of the DNN weights
$MTTR^{nw}$	Specified mean time to repair under normal weather condition
N_i^{pole}	Number of the poles according to span length of branch i
n_i^q	Reactive droop gain of the i^{th} DDG unit with primary $\mathrm{droop}/2^{\mathrm{nd}}$
N_s^{pre}	Number of generated scenarios in Ω_s^{pre}
$net^n(.)$	Trained DNN model for target n
$P^{DDG,max}$	Planning upper bound for DDGs allocation
$P^{ESS,max}$	Planning upper bound for ESSs allocation
$P^{PV,max}$	Planning upper bound for PVs allocation
$P^{WT,max}$	Planning upper bound for WTs allocation
$\boldsymbol{p}_{i,sp}^{dnn}$	Vector of neuron pre-activation obtained by i^{th} hidden layer according to sample sp
$P_{i,t,s,se}$	Active power injected to bus i at time t for s^{th} scenario of season se
$P_{i,t,s,se}^{L}$	Active power load for bus i at time t for s^{th} scenario of season se
$P_{i,t,s,se}^{PV}$	Active power generated by i^{th} PV unit at time t for s^{th} scenario of season se
$P_{i,t,s,se}^{WT}$	Active power generated by i^{th} WT unit at time t for s^{th} scenario of season s
$P_{t,s,se}^{GRID+}$	Active power imported from the main grid at time t for s^{th} scenario of season se. Its corresponding to $P_{i=1,t,s,se}^{PCC} > 0$
$P_i^{DDG,size}$	Active power rating of DDG at candidate bus i
$P_i^{ESS,size}$	Active power rating of ESS at candidate bus i
$P_{i,t,s,se}^{L,peak}$	Original active peal load from data sheet, bus i at time t for s^{th} scenario of season se
$P_i^{PV,size}$	Active power rating of PV at candidate bus i
$P_i^{WT,size}$	Active power rating of WT at candidate bus i
$P_i^{bus,max}$	Maximum installation power allowable for DERs at candidate bus i
P_{step}^{DDG}	Step size for DDG allocation
P_{step}^{ESS}	Step size for ESS allocation
P_{step}^{PV}	Step size for PV allocation
P_{step}^{WT}	Step size for WT allocation
$\mathbf{PATH}^{\mathbf{br}}$	Matrix containing the vector $\boldsymbol{path}_i^{\boldsymbol{br}}$ with $\forall i \in \Omega_{TG}^{node}$
$\mathbf{PATH}^{\mathbf{bus}}$	Matrix containing the vector $\boldsymbol{path}_i^{\boldsymbol{bus}}$ with $\forall i \in \Omega_{TG}^{node}$
$\boldsymbol{path}_i^{\boldsymbol{br}}$	Vectors containing the branches in i^{th} road
$\boldsymbol{path}_i^{\boldsymbol{bus}}$	Vectors containing the buses in i^{th} road
PC^{VI}	Penalty coefficient of voltage violation in \$/kV
$PF_i^{DDG,1st}$	Minimum operating power factor allowable of the 1st quadrant of the DDG unit i
$PF_i^{DDG,4th}$	Minimum operating power factor allowable of the 4th quadrant of the DDG unit i

$PF_i^{TR,1st}$	Minimum operating power factor allowable of the 1st quadrant of the transformer i
$PF_i^{TR,4th}$	Minimum operating power factor allowable of the 4th quadrant of the transformer i
$\boldsymbol{PV}_{sp}^{site}$	Vector containing the location of the PVs for sample sp
$\boldsymbol{PV}_{t}^{down}$	Vector containing the status of the PVs (i.e., $PV_{i,t,se}^{down}$) at time t
$Q_{i,t,s,se}$	Reactive power injected to bus i at time t for s^{th} scenario of season se
$Q_{i,t,s,se}^{L}$	Reactive power load for bus i at time t for s^{th} scenario of season se
$Q_{i,t,s,se}^{L,peak}$	Original reactive peal load from data sheet, bus i at time t for s^{th} scenario of season se
R_i^C	Certain solar radiation point of the ith PV unit, typically set to 0.15 kW/m^2
R_i^{STD}	Solar radiation in standard test conditions of the i^{th} PV un, typically specified as 1000 W/m^2
$\boldsymbol{r}_{ele,sp}^{dnn}$	Vector containing uniform random number between [0,1] for planning element ele for sample sp
$r_{i,t,s}$	Uniform random number for generating $a_{i,t,s,se}^{br}$
$\boldsymbol{r}_{s,se}^{\boldsymbol{m}}$	Vector constraining $r_{t,s,se}^{m}$ for s^{th} scenario of season se
$r_{i,t,s,se}^{m}$	Measured solar radiation of the i^{th} PV unit at time t for s^{th} scenario of season se (kW/m^2)
r_i^{ES}	Ratio between the rated capacity and rated power for the ESS
$\boldsymbol{root}^{\boldsymbol{MG}}$	Vector containing root of each microgrids
$round(.)$	Round deployment, "1" for input ≥ 0.5 and "0" otherwise
S_{base}	Setting power base value
$S_i^{DDG,max}$	Capacity rating of the DDG unit i
$S_i^{TR,max}$	Capacity rate of the transformer
SOC_i^0	Initial state of charge of the ESS unit
SPF_0/SPF	Expected actual system performance
st_n^{isw}	Status of ISW n
$t^{r'}$	Time t corresponding to first failure branch revered
t^d	Time t corresponding to the end of event
t^e	Time t corresponding to the beginning of impact or severe event
T^{event}	Time segment period of the event Phase I
t^r	Time t corresponding to the full system recovery
$t_{i,s,se}^{br,fail}$	Time corresponding to the moment when branch i fail for s^{th} scenario of season se
$t_{i,s,se}^{br,rep}$	Time t when branch recovered or repaired for s^{th} scenario of season se
$t_{s,se}^{d}$	Time t^d for s^{th} scenario of season se
$t_{s,se}^{e}$	Time t^e for s^{th} scenario of season se
$\boldsymbol{TG}^{bus}$	Vector containing the set of target node TG_i^{bus} with $\forall i \in \Omega_{TG}^{node}$
TL	Project lifetime, typical set by 10 years
TTR	Time to repair

$TTR_{i,s,se}^{br,fail}$	Time to repair of the failure branch i for s^{th} scenario of season se
$\boldsymbol{TTR}_{s,se}^{\boldsymbol{br,fail}}$	Vector TTR containing $TTR_{i,s,se}^{br,fail}$
V^{max}, V_{min}	Maximum/Minimum voltage violation of the bus
$v_i^{ci}, v_i^{co}, v_i^{ra}$	Cut-in, cut-out, and the rated speed of the i[th] wind DG, respectively
$\boldsymbol{v}_{s,se}^{\boldsymbol{m}}$	Vector constraining $v_{t,s,se}^{m}$ for s^{th} scenario of season se
$v_{i,t,s,se}^{m}$	Measured wind speed of the i^{th} wind DG at time t for s^{th} scenario of season se
V_{base}	Setting voltage magnitude base value
$v_{cri}^{low}/v_{cri}^{high}$	Specified low and higher bound for critical wind
V_{GC}^{spec}	Nominal specified voltage during grid-connected mode
V_i^{**}	Voltage reference for secondary control of the DDG at candidate bus i operated with $\mathrm{droop}/2^{\mathrm{nd}}$
V_i^{*}	Voltage reference for primary control of the i^{th} DDG at candidate bus i operated with $\mathrm{droop}/2^{\mathrm{nd}}$
$\boldsymbol{v}_{se}^{gust}$	Vector containing 3-Second wind gust in proportional to $\boldsymbol{v}_{se}^{worst}$
$\mathbf{v}_{se}^{\mathbf{m}}$	Matrix constraining $\boldsymbol{v}_{s,se}^{\boldsymbol{m}}$ for season se
$\boldsymbol{v}_{se}^{worst}$	Vector of wind scenario contains the word wind speed in m/s
$\mathbf{W}_i$	Matrix of weight for i^{th} hidden layer of DNN architecture
w_i^{load}	Weighing coefficient of loads
$\boldsymbol{WT}_{sp}^{site}$	Vector containing the location of the WTs for sample sp
$\boldsymbol{WT}_{t}^{down}$	Vector containing the status of the WTs (i.e., $WT_{i,t,s,se}^{down}$) at time t
$\mathbf{Y}_{s,se}^{\mathbf{bus}}$	3D matrix containing the time couple admittance matrix $\mathbf{Y}_{t,s,se}^{\mathbf{bus}}$ at time t for s^{th} scenario of season se
$Z_{i,t,s,se}$	Time coupled impedance of branch i at time t for s^{th} scenario of season se
Z_i^0	Initial impedance value for branch i
$\boldsymbol{a}_{0,sp}^{\boldsymbol{dnn}}$	Vector input sample sp for DNN architecture
$\boldsymbol{a}_{i,sp}^{\boldsymbol{dnn}}$	Vector of neuron activation obtained by i^{th} hidden layer according to sample sp
$a_{i,t,s,se}^{br,new}$	Updated number for $a_{i,t,s,se}^{br}$ at time $t = t_{i,s,se}^{br,rep}$
$a_{i,t,s,se}^{br}$	Binary element represents the availability of branch i at time t of season se
$a_{sp}^{dnn'}$	Neuron activation obtained by the output- layer according to sample sp
η^{DDG}	Power efficiency of the DDG
η_i^{ESS}	Efficiency of the energy storage
$\mu^{cond}, \sigma^{cond}$	Mean and Standard deviation of the normal distribution for conductor's fragility curve
$\mu^{pole}, \sigma^{pole}$	Mean and Standard deviation of the normal distribution for pole's fragility curve
$\pi^{br,nvul}$	Vulnerability threshold for distribution branch
$\pi_{i,t,se}^{br}$	Failure probability of the branch i at time t of season se, considering $\pi_{i,t,se}^{poles}$ and $\pi_{i,t,se}^{cond}$
$\pi_{i,t,se}^{cond}$	Failure probability for a conductor of branch i at time t of season se

$\pi_{i,t,se}^{Pole}$ Failure probability for single pole of branch i at time t of season se

$\pi_{i,t,se}^{poles}$ Failure probability considering all poles of branch i at time t of season se

$\boldsymbol{\pi}_{s,se}^{wiso}$ Vector of probability for both wind and solar scenario for s^{th} scenario of season se obtained by forward reduction technic

$\boldsymbol{\pi}_{se}$ Matrix in 3D format containing the failure probability $\pi_{i,t,se}^{br}$ for season se

σ^{curt} Cost of load curtailment in \$/kWh

σ^{fuel} Fuel cost for DDG in \$/kWh

$\sigma_{O\&M}^{DDG}$ Cost \$/kWh for O&M the DDG

$\sigma_{O\&M}^{ESS}$ Cost \$/kWh/year for O&M the ESS

$\sigma_{O\&M}^{ISW}$ Cost \$/kWh/year for O&M the ISW

$\sigma_{O\&M}^{PV}$ Cost \$/kWh/year for O&M the PV

$\sigma_{O\&M}^{WT}$ Cost \$/kWh/year for O&M the WT

$\sigma_{t,s,se}^{PCC}$ Market energy price in #/kWh corresponding to time t for s^{th} scenario of season se

σ_{INS}^{ESS} Installation cost \$/kWh of ESS at candidate bus i

$\sigma_{INV}^{ESS,E}$ Investment cost \$/kWh for energy density rating for ESS

$\sigma_{INV}^{ESS,P}$ Investment cost \$/kW for power rating for ESS

σ_{INV}^{DDG} Investment cost for DDG in \$/kW

σ_{INV}^{PV} Investment cost for PV in \$/kW

σ_{INV}^{SSW} Investment cost in \$ per allocated ISW

σ_{INV}^{WT} Investment cost for WT in \$/kW

Sets of Variables:

$\boldsymbol{X^{MILP}}$ Vector containing the decision variables for the MILP problem formulation

$\boldsymbol{X^{OLEV}}$ Vector containing the decision variables for the outer level problem

Continuous variables:

$E_{i,t,s,se}^{ESS}$ Energy SOC of the ESS unit i at time t for s^{th} scenario of season se

$P_{k,t,s,se}^{br}$ Active power flowing across the transmission branch k at time t for s^{th} scenario of season se

$P_{i,t,s,se}^{ch}$ Active power charge by i^{th} ESS unit at time t for s^{th} scenario of season se

$P_{i,t,s,se}^{dch}$ Active power discharge by i^{th} ESS unit at time t for s^{th} scenario of season se

$P_{i,t,s,se}^{DDG}$ Active power generated by DDG i at time t for s^{th} scenario of season se

$P_{i,t,s,se}^{PCC}$ Active power imported from the main grid across the i^{th} PCC of the MG at time t for s^{th} scenario of season se

$P_{i,t,s,se}^{PV,use}$ PV's adjusting power output and used at time t for s^{th} scenario of season se

$P_{i,t,s,se}^{WT,use}$ WT's adjusting power output used at time t for s^{th} scenario of season se

$Q_{k,t,s,se}^{br}$ Reactive power flowing across the transmission branch k at time t for s^{th} scenario of season se

$Q_{i,t,s,se}^{DDG}$ Reactive power generated by the i^{th} DDG unit at time t for s^{th} scenario of season se

$Q_{i,t,s,se}^{ESS}$	Reactive power generate/receive of the i^{th} ESS unit, at time t for s^{th} scenario of season se
$Q_{i,t,s,se}^{PCC}$	Reactive power imported from the main grid across the i^{th} PCC of the MG at time t for s^{th} scenario of season se
$u_{i,t,s,se}^{v}$	Integrator output of secondary voltage restoration of i^{th} DDG unit operating with $\mathrm{droop}/2^{\mathrm{nd}}$ at time t for s^{th} scenario of season se
$V_{i,t,s,se}$	Voltage magnitude of the bus i at time t for s^{th} scenario of season se
$\delta_{i,t,s,se}$	Voltage magnitude angle of bus i at time t for s^{th} scenario of season se
$\delta_{f_{i,t}^{bus},t,s,se}^{MG}$	Phase angle of the frequency controllable bus $f_{i,t}^{bus}$ at time t for s^{th} scenario of season se
$\delta_{t,s,se}^{MG}$	Phase angle of the bus where the frequency control act at time t for s^{th} scenario of season se

Binary variables:

$b_{i,t,s,se}^{curt}$	Binary variable for load curtailment (1: load shaded and 0: load fed) for bus i at time t for s^{th} scenario of season se
$b_{i}^{DDG,size}$	Integer variable for DDG allocation at candidate bus i
$b_{i,t,s,se}^{ESS}$	Binary variable indicates the status of i^{th} ESS at time t for s^{th} scenario of season se, i.e. 1: discharge and 0: charge
$b_{i}^{ESP,size}$	Integer variable for ESS allocation at candidate bus i
b_{i}^{ISW}	Binary decision variable for ISW allocation at candidate branch i
$b_{i}^{PV,size}$	Integer variable for PV allocation at candidate bus i
$b_{i}^{WT,size}$	Integer variable for WT allocation at candidate bus i

Function and Metric:

$AEMIS^{DDG}$	Annual CO_2 emission in kg/kWh/year according to DDGs generation
$AEMIS^{DDG,dl}$	$AEMIS^{DDG}$ based on DNN model
$AEMIS^{GRID}$	Annual CO_2 emission in kg/kWh/year according to power imported from main grid
$AEMIS^{GRID,dl}$	$AEMIS^{GRID}$ based on DNN model
$AEMIS^{OLEV}$	Total CO_2 emission, use as an objective function for the outer level problem
$AEMIS^{OLEV,dl}$	$AEMIS^{OLEV}$ based on DNN model
$AOMC^{DDG}$	Annual O&M cost for DDGs in \$/kWh/year
$AOMC^{DDG,dl}$	$AOMC^{DDG}$ based on DNN model
$AOMC^{ESS}$	Annual O&M cost for ESSs in \$/kWh/year
$AOMC^{ISW}$	Annual O&M cost for ISWs in \$/year
$AOMC^{PV}$	Annual O&M cost for PVs in \$/kWh/year
$AOMC^{WT}$	Annual O&M cost for WTs in \$/kWh/year
$C^{DDG,dl}$	C^{DDG} based on DNN model
$C_{t,s,se}^{CURT}$	Cost of energy curtailment during IS mode at time t for s^{th} scenario of season se
C^{DDG}	Total cost in \$ for DDGs considering TL

$C_{t,s,se}^{DDG}$	Cost of natural gas consumption by the DDG units at time t for s^{th} scenario of season se
C^{ESS}	Total cost in \$ for ESSs considering TL
C^{ISW}	Total cost in \$ for ISWs considering TL
$C_{t,s,se}^{PCC}$	Cost of energy imported from the substation across the PCC of the microgrid at time t for s^{th} scenario of season se
C^{PV}	Total cost in \$ for PVs considering TL
$C_{t,s,se}^{VI}$	Cost of voltage violation at time t for s^{th} scenario of season se
$C_{t,s,se}^{VI,MGs}$	Cost of voltage violation considering MGs at time t for s^{th} scenario of season se
C^{WT}	Total cost in \$ for WTs considering TL
$CPC^{ESS,P}$	Total capital cost for ESSs in \$/kWh
CPC^{DDG}	Total capital cost for DDGs in \$/kWh
CPC^{ISW}	Total capital cost for ISWs in \$
$EMIS_{s,se}^{DDG}$	Daily CO_2 emission in kg/kWh according to DDGs generation
$EMIS_{s,se}^{GRID}$	Daily CO_2 emission in kg/kWh according to power imported from main grid
$INSC^{ESS}$	Installation cost in \$ for ESSs
$OF_{s,se}^{MILP}$	Normalized objective function for MILP problem at time t for s^{th} scenario of season se
$OF_{s,se}^{MILP,MGs}$	Normalized objective function for MILP problem considering microgrid formations at time t for s^{th} scenario of season se
$OMC_{s,se}^{DDG}$	Pre-representation O&M cost for DDGs in kWh/day for s^{th} scenario of season se
$RESI$	Basic resilience index
$RESI^{OLEV}$	Resilience index considering SPF progression phase I and II, use as an objective function for the outer level problem.
$RESI^{OLEV,dl}$	$RESI^{OLEV}$ based on DNN model
TC^{OLEV}	Total cost in \$, use as an objective function of the outer level
$TC^{OLEV,dl}$	TC^{OLEV} based on DNN model
$TG_{sp,n}$	Target n for training DDN model corresponding to LOPF solution of sample sp

This Thesis is dedicated to my beloved parents and brother for their endless encouragement, support and love

Remerciements

Ma plus profonde gratitude va à mes superviseurs, Professeur Jérôme Cros et Professeur Morad Abdelaziz qui m'ont encadré tout au long de cette thèse. Je tiens à remercier pour leur gentillesse, leurs conseils et leur soutien, leur disponibilité permanente et pour les nombreux encouragements qu'ils m'ont prodigués. Un grand merci à eux pour m'avoir accepté et donné l'opportunité de découvrir et d'apprendre beaucoup de choses merveilleuses en tant que leur étudiant doctorat.

Je tiens à remercier les membres de l'équipe du Programme Canadien de Bourse de la Francophonie ou PCBF pour leur accueil chaleureux depuis mon arrivée au Canada. Mes séjours ont été bien remplis par les merveilleuses aventures, les expériences et c'est grâce à leur collaboration et leur soutien tout au long de mon séjour. Cette thèse n'aurait pas pu être réalisée sans leur soutien financier.

Rien de plus que ma plus profonde gratitude et un grand merci à mes parents et à mon frère pour leur compréhension, leur patience, leur soutien et leurs encouragements interminables tout au long de mes études de doctorat.

Je tiens à exprimer ma reconnaissance à toutes les personnes et organisations qui m'ont offert un soutien constant pendant toutes mes années d'études de doctorat.

A cet effet, je tiens à remercier les membres du jury d'avoir accepté d'assister à la soutenance de cette thèse.

Enfin, aucun acte n'est plus noble qu'une démonstration de gratitude. Mes remerciements les plus profonds vont au LEEPCI, Département de génie électrique et de génie informatique; Faculté des sciences et de génie; et spécialement à l'Université Laval pour m'avoir ouvert la porte et m'avoir permis d'améliorer mes connaissances et mes compétences en tant qu'étudiant doctorat de l'Université Laval à Québec, Canada.

Youthanalack Vilaisarn,
Quebec, Canada

Foreword

The thesis consists of 5 chapters in addition to an introduction and a conclusion. First, the introduction has been originally written by the author of this thesis Youthanalack Vilaisarn and is presented at the beginning of the thesis. Then chapter 1 introduces the background information pertaining to this thesis, while additionally including the state of the art and literature review pertaining to the work presented in this thesis. The literature review in chapter 1 has been extracted from the submitted, accepted or published version of the articles presented by chapters 2 to 5. Finally, the conclusion has been originally written by the author for concluding the work and presenting the future perspective. A general description for chapter 1 through 5 is presented as follows:

The Introduction introduces general information about active distribution systems and the advantage of the microgrids application in power distribution. Then, the research motivations are provided as well as the summary of research objectives and the thesis outline.

Chapter 1 introduces the necessary background for the thesis's research including the microgrids planning and the microgrid operation and control aspects. Additionally, this chapter includes the literature survey pertaining to the topics addressed in this thesis; namely: 1) the islanded microgrid power flow problem, 2) the optimal power flow of the microgrid system, and 3) the general microgrids planning and the specific topic related to the resilience oriented microgrids planning.

Chapter 2 presents the proposed branch based $\mathbf{Z_{bus}}$ power flow algorithm for the balanced and unbalanced droop controlled islanded microgrids. This method solves the non-linear power flow problem without linearization and is accurate enough for validating the linear power flow to be developed in chapter 3. This part has been published with original contribution in the Elsevier Journal (IJEPES). The major details and results in this chapter has been summited and published as the following papers:

- ***Paper:*** [1] Y. Vilaisarn and M. Abdelaziz, "An inversion-free sparse Z power flow algorithm for large-scale droop controlled islanded microgrids," Int. J. Electr. Power Energy Syst., vol. 121, no. August 2019, p. 106048, Oct. 2020.

- ***Status:*** published with « doi.org/10.1016/j.ijepes.2020.106048 »

- ***Author:*** Youthanalack Vilaisarn; ***contribution:*** proposed the islanded microgrid $\mathbf{Z_{bus}}$ power flow algorithm, implemented the model, performed the simulation, developed the case studies and prepared this paper.

- ***Co-author:*** Morad Abdelaziz; ***contributions:*** supervised the development of the proposed model and its implementation, revised the code implementation, provided important insights on the simulations and the interpretation of the results. Aided in the preparation of the manuscript.

Chapter 3 presents a linear power flow model for balanced and unbalanced droop islanded microgrids. This work shows higher computational efficiency by developing a linearized power flow model. The model is node based and is later integrated into the optimal operation model that will be developed in chapter 4. This original contribution has been presented in the conference CIRED Berlin 2020 and published in IET Library as the following paper:

- ***Paper:*** [2] Y. Vilaisarn, M. Abdelaziz, and J. Cros, "Linear Three-Phase Power Flow Model for Autonomous Microgrid Systems," CIRED - Open Access Proc. J., vol. 2020, no. 1, pp. 50–53, 2021.

- ***Status:*** published with « doi:10.1049/oap-cired.2021.0019 »

- ***Author:*** Youthanalack Vilaisarn; ***contributions:*** proposed the linear power flow model, implemented the model, performed the simulation, developed the case studies and prepared this paper.

- ***Co-author:*** Morad Abdelaziz; ***contributions:*** supervised the development of the proposed model and its implementation, revised the code implementation, provided important insights on the simulations and the interpretation of the results. Aided in the preparation of the manuscript.

- ***Co-author:*** Jérôme Cros; ***contributions:*** supervised the development of the proposed model and its implementation, revised the code implementation, provided important insights on the simulations and the interpretation of the results. Aided in the preparation of the manuscript.

Chapter 4 provided a time coupled MILP formulation for determining the optimal operation of balanced and unbalanced AC microgrids. The formulation considers the microgrids operation with hierarchical control during both GC and IS mode. The energy storage and renewable resource (i.e.,

WT and PV) have been accounted for. A major result of this chapter is submitted and published in IJEPES of Elsevier as the following paper:

- ***Paper:*** [3] Y. Vilaisarn, M. Moradzadeh, M. Abdelaziz, and J. Cros, "An MILP formulation for the optimum operation of AC microgrids with hierarchical control," *Int. J. Electr. Power Energy Syst.*, vol. 137, no. September 2021, p. 107674, May 2022.

- ***Status:*** published with « doi.org/10.1016/j.ijepes.2021.107674 »

- ***Author:*** Youthanalack Vilaisarn; ***contributions:*** proposed the optimal linear power flow model, implemented the model, performed the simulation, developed the case studies and prepared this paper.

- ***Co-author:*** Majid Moradzadeh; ***contributions:*** Reviewed the paper, polished the paper in terms of structure and mathematics, proposed several case studies.

- ***Co-author:*** Morad Abdelaziz; ***contributions:*** supervised the development of the proposed model and its implementation, revised the code implementation, provided important insights on the simulations and the interpretation of the results. Aided in the preparation of the manuscript.

- ***Co-author:*** Jérôme Cros; ***contributions:*** supervised the development of the proposed model and it implementation, revised the code implementation, provided important insights on the simulations and the interpretation of the results. Aided in the preparation of the manuscript.

Chapter 5 presents the resilience oriented microgrid planning framework. The planning problem is based on a two-level optimization with 1) the outer level been formulated as a multi-objective optimization problem to allocate the distribution system planning elements, and 2) the inner level dealing with the stochastic optimization operation solution using time coupled MILP model delivered from chapter 4. This chapter has been submitted on IEEE Access and with the details as follows:

- ***Paper:*** A Deep Learning based Multi-Objective Optimization for the Planning of Resilience Oriented Microgrids in Active Distribution System". *Accepted for publication in IEEE Access, July 2022.*

- ***Status:*** Accepted for publication in IEEE Access by 30-July-2022

- ***Author:*** Youthanalack Vilaisarn; ***contributions:*** proposed the planning framework, implemented the planning framework, performed the simulation, developed the case studies and prepared this paper.

- ***Co-author:*** Yuri R. Rodrigues; ***contributions:*** Reviewed the paper, polished the paper in terms of structure and mathematics, proposed several case studies.

- ***Co-author:*** Morad Abdelaziz; ***contributions:*** supervised the development of the proposed model and its implementation, revised the code implementation, provided important insights on the simulations and the interpretation of the results. Aided in the preparation of the manuscript.

- ***Co-author:*** Jérôme Cros; ***contributions:*** supervised the development of the proposed model and its implementation, revised the code implementation, provided important insights on the simulations and the interpretation of the results. Aided in the preparation of the manuscript.

The Conclusion concludes the research in this thesis and summarizes the contributions. Afterwards, future perspectives are provided for future work.

Thesis Original Contribution

The general contribution of this thesis can be summarized as follows:

- A branch-based inversion free Z_{bus} power flow algorithm for droop islanded microgrid is proposed. The proposed algorithm does not require bus renumbering, nor does it require a DG to be allocated at the reference bus. Moreover, the proposed method is particularly well suited for sparse implementation and delivers an enhanced computational efficiency in the power flow solution, making it particularly useful for large scale microgrid systems comprising up to thousands of buses.

- Proposed a node based LPF model that accounts for the droop-controlled autonomous microgrid philosophy of operation as well as considering both balanced and unbalanced network characteristics.

- Proposed a time coupled MINLP and MILP OPF models for the optimum operation problem of balanced and unbalanced microgrid with hierarchical control structure. The proposed models consider the microgrid philosophy of operation during GC and IS. Moreover, the energy storage system and the renewable energy resources i.e., WTs and PVs have been accounted for.

- Proposed a general framework using meta-heuristic multi-objective optimization for planning resilience oriented microgrid(s) in active distribution systems considering economic, resilience and environmental points of views. The proposed framework employs novel deep learning models to speed up the determination of the economic, resilience and environmental metrics pertaining to the MG(s).

Introduction

0.1 Thesis motivation

Power distribution systems are currently undergoing a major transition towards reduced carbon emissions and increased sustainable development. The key drivers for this transition are the need to control electricity costs, mitigate global climate change, improve power system reliability and resilience, replace aging infrastructure, and provide reliable electricity to new developing communities [4]. One enabling solution to this transition is making good use of distributed generation (DG) units, especially those based on solar and wind energies, different kind of energy storage systems (EESs) and active load control strategies [5]. Based on this transition, power distribution networks have been changing towards higher penetration of renewable energy recourses along with increased application of energy storage technologies and are as such transforming from their traditionally passive structure into an active distribution system (ADS). This transition towards the ADS structure brings benefits to both utilities and customers, as well as respond to the key driving techno-economic issues.

The ADS paradigm enhances the distribution system operators' (DSOs) ability to operate and manage the distribution of electricity by offering new possibilities and flexibility [6]. In this context, microgrids (MGs) have been put forward as an attractive new concept. The microgrid is proposed as the building block of future active distribution systems. The microgrid is an electrical region within the active distribution system with the capability to operate in the grid connected where it is connected to the upstream network; or in the islanded mode of operation where it is operated in isolation from the upstream network. Here, clustering active distribution system into microgrids can offer significant benefits for both the utility and the customers [7]. Here, they are some examples of such benefits:

- *Support the grid performance*: the utmost value of microgrids for DSOs is to support the grid performance by: a) improving the reliability of power supply by enabling self-healing at the local region; b) improving the resiliency which refers to the capability of the power system to withstand a low probability high-impact event such as an extreme weather events, natural disasters, cyber-attack…etc. c) Improving the power quality for the customers' by providing services such as voltage support.

- *Reduction of carbon emissions*: microgrids can enable wider penetration of renewable DG units in the distribution system, leading accordingly to a significant reduction in the overall system carbon footprint.

- *Enhanced economics*: the proximity of local generation/load of the microgrid can bring back the investment benefit in term of reduced losses and the transmission and distribution (T&D) payment as well as reduce the energy purchasing from the main.

- *Enable Increased Demand Response*: microgrids can facilitate the implementation of demand side management (DMS) or demand respond. The DMS programs encourage the consumers to modify the pattern of electricity usage to reduce their consumption payment instead of planning more generation.

While the deployment of microgrids is rapidly growing, its widespread adoption is still facing many challenges in aspects such as planning and the availability of steady state analysis tools/simulators to accurately account for the microgrid operational characteristics. Additionally, many distribution utilities worldwide are increasingly suffering from power outages due to rare but intense impact events known as High-Impact Low Probability (HILP) events. While microgrids can help in alleviating the impacts of these HILP events, there is still a need for a general framework for planning microgrids targeted at alleviating such contingency events. One of the utmost challenges to address in this regard is the need to incorporate an accurate microgrid model in such planning methodology. Moreover, the uncertainty due to the presence of renewable energy resources, loads and the contingencies introduce complexity in the planning problem and consequently affect the efficacy of the planning solution. Regarding the described motivation and problematic, the challenges can be summarized as follows:

- There is a lack of a framework for planning resilience oriented microgrids that consider the microgrid optimal operation under the hierarchical control structure. Additionally, such planning framework need to also account for the effect of the uncertainties arising from the stochastic nature of the contingencies and those of the renewable resources.

- The microgrids are typically operated and controlled via a hierarchical control structure. Yet, this control structure has not been accounted for in the optimal operation models existing in the literature. The lack of this consideration can lead to infeasible and/or inaccurate solutions. Moreover, the optimal operation model should be computationally efficient, allow for time coupling and be able to capture the operation constraints for different kind of resources (i.e.,

DDG, WT, PV and storage). These considerations are needed to allow for the application of the optimal operation model in different stochastic planning and real time applications.

- There is a need for a computationally efficient power flow model of the droop-controlled islanded microgrids. While, the power flow models of droop-controlled islanded microgrids have been heavily studied in the recent literature, still all of the previous work in this area focused on the nonlinear power flow equations which can be computationally demanding to solve. As such, there is still a need for a fast and accurate linearized power flow model of droop-controlled islanded microgrid that accounts for the islanded microgrid operation and control philosophy. A computationally efficient linearized droop-controlled islanded microgrid model is crucial for many stochastic planning and real time optimal operation problems.

- The typical power distribution system that are to be operated in islanded microgrid mode can comprise up to thousands of buses. Yet, the islanded microgrid power flow analysis algorithms found in the literature are not suited for such large-scale systems. This challenge put forward a need for an accurate islanded microgrid power flow algorithm suited for large scale systems comprising thousands of buses. The needed algorithm should not only account for the operation and control philosophy of the droop controlled islanded microgrid but should also be computationally efficient and accurate.

0.2 Research Objective

The ultimate objective of this research is to propose a general flamework for the planning of resilience oriented microgrids in active distribution systems. To this end, this research also concentrated on the development and deployment of the necessary power flow and optimal power flow models needed to accurately account for the operation of the microgrid system within the planning framework. The specific objective of this research can as such be summarized as follows:

- *Objective 1:* Developing a power flow algorithm suitable for large scale balanced and unbalanced droop controlled islanded microgrids.

- *Objective 2:* Developing a node based linear power flow model for balanced and unbalanced microgrid systems operated in droop controlled islanded mode.

- *Objective 3:* Developing a mixed integer linear programming model for the optimum operation of the AC microgrids with hierarchical control.

- *Objective 4:* Proposing a general framework for resilience oriented microgrids planning in active distribution networks.

This objective has been interlinked and can be shown in figure as follows:

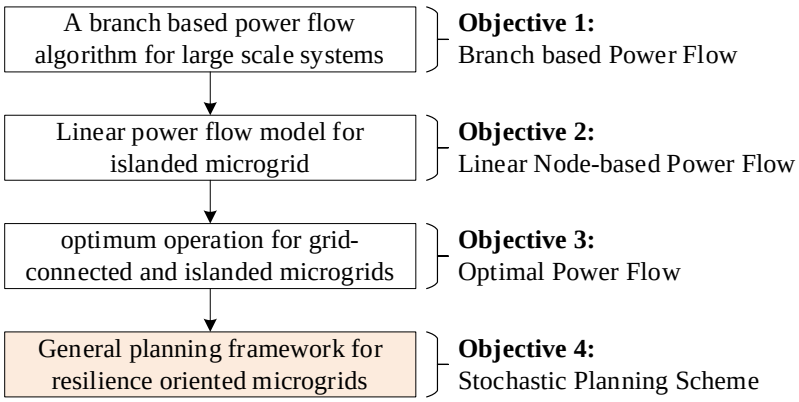

FIGURE 0. 1: Basic outline of the research objectives

0.3 Thesis Outline

First, **Chapter 1** presents the necessary background and the state of the art for the research study. Additionally, this chapter introduce the specific literature survey on the microgrids steady state analysis and planning application.

Chapter 2 introduces the inversion free Z_{bus} algorithm for the droop islanded microgrid power flow. This algorithm is based on branch-based method and has been initially developed for balanced systems and was then extended to unbalanced system while still considering the special characteristics and philosophy of operation of droop controlled microgrids. The proposed algorithm has been tested, validated and was shown to be superior in terms of computational efficiency. Moreover, the proposed algorithm has been tested with the large-scale IMG and was shown to be able to handle the practical systems comprising up to a thousand of buses.

Chapter 3 derivers the LPF model for droop controlled islanded microgrid. This model is later integrated in the optimal operation application presented **Chapter 4**. The developed model accurately accounts for the philosophy of the microgrid operation in droop control in either balanced or unbalanced conditions. The accuracy and the effectiveness of the proposed LPF model has been tested

across several balanced and unbalanced test system, and the results were validated by comparison with other methods proposed in the literature and with those of the proposed Z_{bus} method introduced in **Chapter 2**.

Chapter 4 starts by providing the time coupled MINLP model for the optimum operation of the microgrid with hierarchical control. Subsequently, the LPF model from **Chapter 3** is adopted to account for the microgrid operational characteristics as linear constraints. Then, linearization is performed for 1) the absolute value operation in the objective function, and the 2) quadratic constraints. By using these linearization and the LPF model, the developed MILP OPF model provides the basis for accounting for the microgrid optimal operation as needed in the microgrids planning framework introduced in **Chapter 5.**

Chapter 5 introduces the ultimate goal of the research by providing the general framework for resilience oriented microgrids planning for distribution system. The proposed framework delivers the optimal allocation of the resources (i.e., DDGs, WTs, PVs and ESSs) and the ISWs, that simultaneously improve the distribution system resiliency against N-K contingencies as well as account for the economic and environment impacts viewpoints. The optimal resources and ISWs allocation are based on the multi-objective optimization problem, that incorporates the stochastic time coupled optimal operation model developed in **Chapter 4**. Then, a deep learning approach is adopted for dealing with the computation burden arising from the stochastic consideration and the need for many optimum operation simulations.

Finally, the last chapter presents the general conclusion including the thesis summary, contribution and the specific direction for the future work.

Chapter 1 Research Background and State of Art

1.1 Introduction

In this chapter, the research background and state of the art are presented. First, the differences between the conventional distribution system (the so-called passive distribution system) and the active distribution system are presented. Then, we introduce the microgrids and their basic operation and control characteristics. Subsequently, the background related to the research objectives, namely; microgrids power flow, microgrids optimal operation (optimal power flow) and the microgrid planning aspect are presented. Finally, the remainder of this chapter is dedicated to the literature survey including 1) the survey of microgrids power flow algorithms 2) the survey of microgrids optimal operation algorithms and 3) the survey on power system resilience enhancement related to microgrids. Finally, a discussion of the literature survey is introduced leading the way to the proposed research works.

1.2 Passive and Active Distribution System in the Power System

Conventional or passive distribution system (PDS) are being changed into active distribution systems (ADS) due to the inclusion of DERs in the distribution level. The difference between PDS and ADS can be defined by the direction of the power flowing in the distribution network [8]. In PDS, the power flow is unidirectional where the power is flowing from main bus (substation) to the consumers (loads). While, in the ADS bidirectional power flow is dominant, where local generators located at given load points can feed other load points in the system. ADSs have local systems in place to control different DERs (including the distributed generators (DGs) and energy storages) and loads, where using these systems DSOs are able to manage/configurate the energy flow using flexible and effective network topologies [6]. Generally, in active distribution systems, DGs include dispatchable and non-dispatchable units. The former is a firm generator (e.g., natural gas micro-turbine and biomass generator) that can be dispatched to deliver a constant amount of power. On the other hand, non-dispatchable are stochastic generation units including wind turbines and photovoltaics. The power production of these resources is stochastic and they cannot be dispatched along the planning horizon, as their production is dependent on the stochastic wind speed and solar irradiance. The basic definition and framework of ADS have been well acknowledged by different academic organizations, such as CIRED [9] and IEEE [10]. Figure 1. 1 show the different structure of both systems.

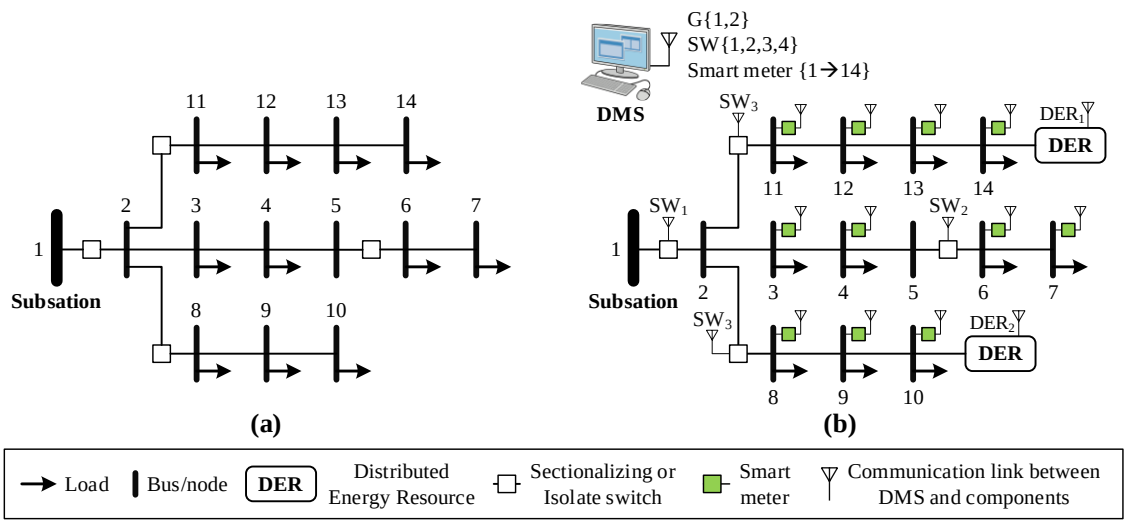

FIGURE 1. 1: Different features of typical PDS(a) and ADS(b)

A shown Figure 1. 1(a), a typical PDS consists of single or multiple feeders and several sectionalizing switches. While Figure 1. 1(b) the ADS additionally the DERs. These devices are controlled via the distribution management system (DMS) with the supervisory control. Traditionally, section switches in PDS are always manually operated, whereas the operation in the ADS makes use of advanced automation technologies.

1.2.1 Microgrids

The microgrid have been identified as a key component of the Smart-Grid. The microgrid is deployed for improving the reliability and quality, increasing system energy efficiency, and providing the possibility of grid-independency to individual local users. In [11] the DOE has given the definition of the microgrid as: "*a group of interconnected loads and distributed energy resources within clearly defined electrical boundaries that acts as a single controllable entity with respect to the grid. A microgrid can connect and disconnect from the grid to enable it to operate in both grid-connected or island- mode."* The concept of the microgrid comprises micro sources which are typically smaller generation units (<100 kW) and connected to the bus via the power electronic interface. Usually, the microgrid(s) are located at the distribution level where the locally supplied demands (loads) are fed at a low voltage (480 Volt or less) [12]. This kind of microgrid has the possibility of being connected or disconnected from the main grid via the main isolation switch. This allows the microgrid to be operated in the autonomous islanded mode, while balancing the generation and load within its boundary. On the other hand, there are also the microgrids that are located in remote areas and that have to interconnection to the main electrical grid. Microgrids typically employ a hybrid of renewable

energy, storage and dispatchable DGs in order to supply their customers without interruption. Traditionally, the typical microgrid comprises the an interconnection between DERs (generation and storage) and the different types of loads; and are controlled via a microgrid control center with smart integrated devices [13]. Figure 1. 2 present a general scheme of a basic microgrid.

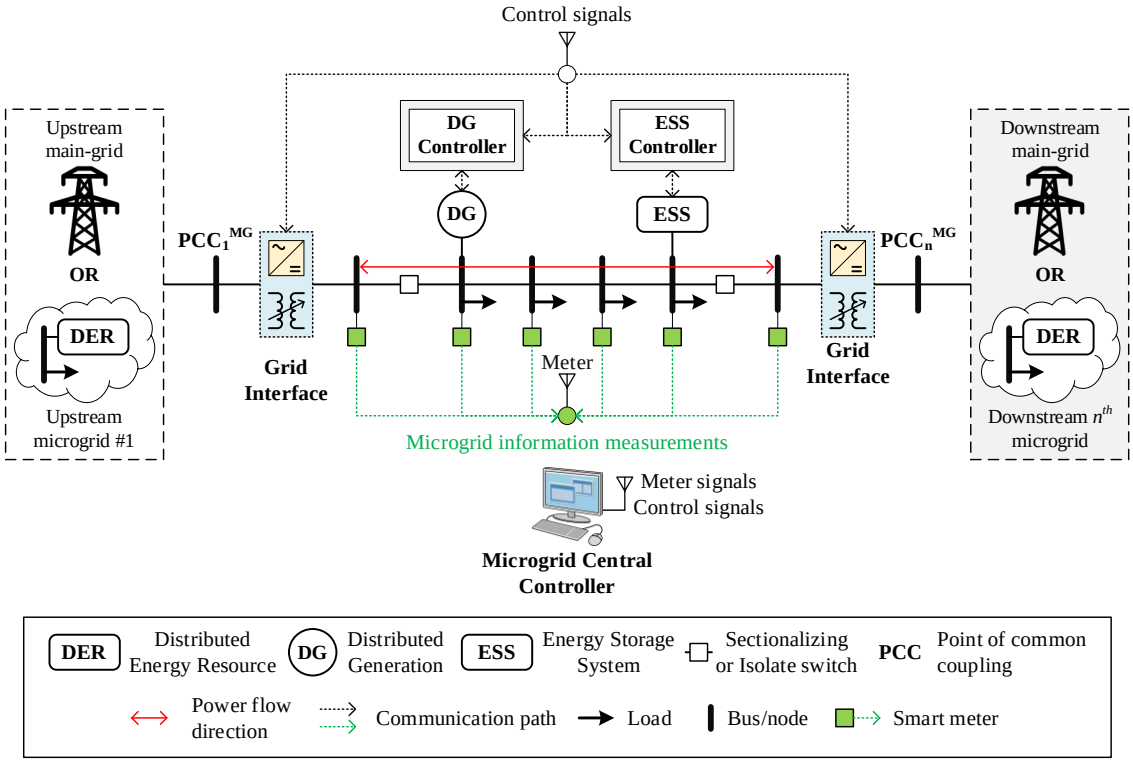

FIGURE 1. 2: General scheme of the basic microgrid

First of all, it is easy to identify the electrical boundaries of the microgrids as the point of common coupling (PCC_1^{MG} to PCC_n^{MG} this case). These points are interconnected with the external grid (another microgrids or main-grid). It is possible to have different level of voltage between the microgrid and the external grid. In this case the interface element in required and must be installed to permit the interconnection between them. The control in microgrid can be centralized or decentralized [14] and permits the operation as a single controllable entity. Thus, smart meters and smarts communications infrastructure are typically required. Finally, the microgrid is permitted to operate in the islanded mode by the switch at PCC. Depending on the technology of the microgrid infrastructure and the devices installed, the microgrid can be operated in AC, DC of mixed. But in this research, we focus on the planning of the microgrid in the AC active distribution system only.

1.2.2 Basic Droop Controlled Microgrid and the Implementation

As mentioned, the microgrid can be operated in grid-connected or islanded mode based on the grid specific situation and the decisions of DSOs. In the grid-connected mode, the deficit in power between the microgrid demand and generation can be supplied by the main grid. Similarly, excess power generated in the microgrid can be traded with the main grid and used to provide ancillary services [14]. Thus, the frequency is pre-specified, the voltage regulation are maintained at different microgrid buses and given that the small size of the DG units compared to the power grid, the DG units within the microgrids are controlled as PV or PQ buses [15]. However, in the islanded mode the DG units are basically operated in droop mode to maintain balance of the generation and demand simultaneously while controlling the voltage magnitude and frequency within the permissible ranges. In this case, there is no slack bus which able to act as the reference in the network. On the other hand, the microgrid can be operated with primary droop and the supervisory of secondary control (droop/2nd). This kind of control structure guaranties that the microgrid is operated with the nominal frequency and voltage as well as allows the microgrid be ready to re-synchronize to the main grid when this is needed [16].

In the droop mode of operation, the power is shared with respect to the droop-characteristic. Here, Figure 1. 3 present the steady-state, fundamental frequency model of the DG units operating in droop mode [15]. In this model, the energy source, the power electronic converter and the output filter are modeled as an ideal voltage source whose frequency and the voltage magnitude are controlled thought the droop characteristics. This model is sufficient for the steady state analysis of droop controlled islanded microgrid systems. Figure 1. 4 show the droop characteristic curves implemented by the DG controller. In these figures, Figure 1. 4(a) illustrates the relation of the frequency and the active power generated by the DG units; namely f/P curve. While, the Figure 1. 4(b) represents the reactive power and voltage magnitude relations namely V/Q curve.

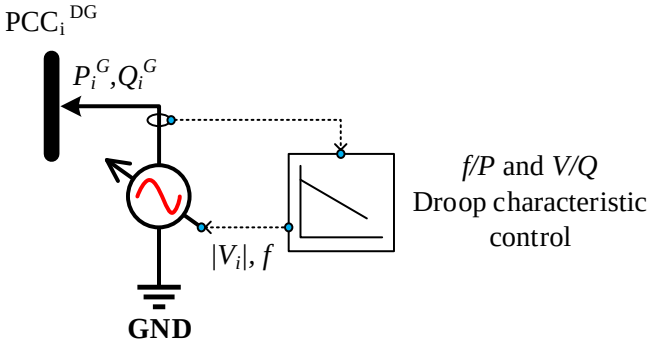

FIGURE 1. 3: Steady state, fundamental model of a DG unit operating in the droop mode

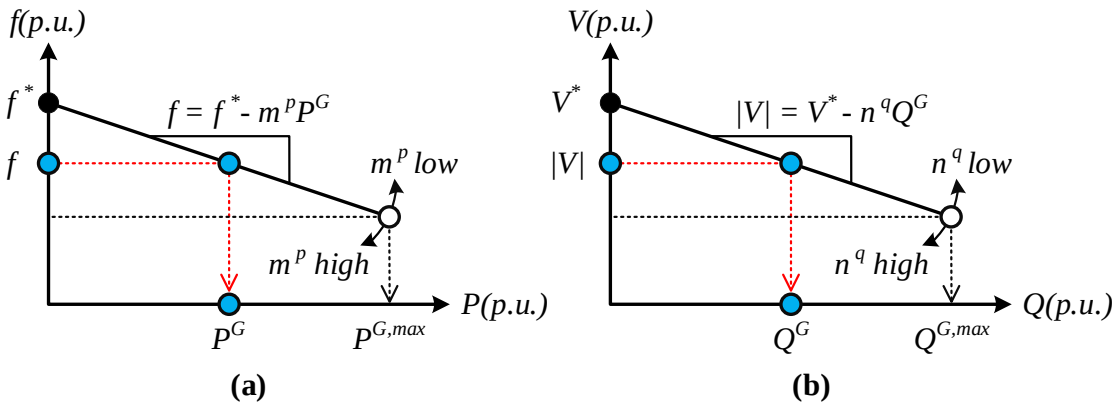

FIGURE 1. 4: Static Droop characteristics, f/P (a) and V/Q (b)

Eq. (1.1) and Eq. (1.2) give droop characteristics implemented by the droop controller.

$$f = f^* - m^p P^G \tag{1.1}$$

$$|\bar{V}| = V^* - n^q Q^G \tag{1.2}$$

In these equations above, f and V are the output frequency and voltage of the DG unit. While, f^* and V^* represented the frequency and voltage set point at no load. Given the per unit representation of the power system, in f is interchanged with ω in the literature. P^G and Q^G are the active and reactive power generated by the DG unit. Finally, m^p and n^q expressed the static active and reactive droop gain.

One way to calculate the static droop gains is to use the range of permissible frequency and voltage deviation over the maximum capacity of generation of the DG units. Eq. (1.3) and (1.4) illustrate the formulation for the droop gains calculation using this method:

$$m^P = \left(f^{max} - f^{min}\right)/P^{G,max} \tag{1.3}$$

$$n^q = \left(V^{max} - V^{min}\right)/Q^{G,max} \tag{1.4}$$

where, f^{max} and f^{min} represent per unit max and min allowable range of frequency in system. While, V^{max} and V^{min} are the per unit max and min permissible range for voltage. $P^{G,max}$ and $Q^{G,max}$ denoted the max and min capability of active and reactive power generated by DG units. Supposed, i is the number of the droop-controlled DG unit in the microgrid; in case having a DG unit with different rating; To achieve proper sharing of the load among these DG units, the static droop gains should be calculated using the equations below [15], [17]:

$$m_1^p P_1^{G,max} = m_2^p P_2^{G,max} = \cdots = m_i^p P_i^{G,max} \quad (1.5)$$

$$n_1^q Q_1^{G,max} = n_2^q Q_2^{G,max} = \cdots = n_i^q Q_i^{G,max} \quad (1.6)$$

The DG units in the microgrid are sharing active and the reactive power via droop control. Here, the active power is shared through the global frequency of the system while the reactive power depends on the output voltage of each DG unit. The Figure 1. 5 illustrates the droop sharing of the two DG units in the microgrids.

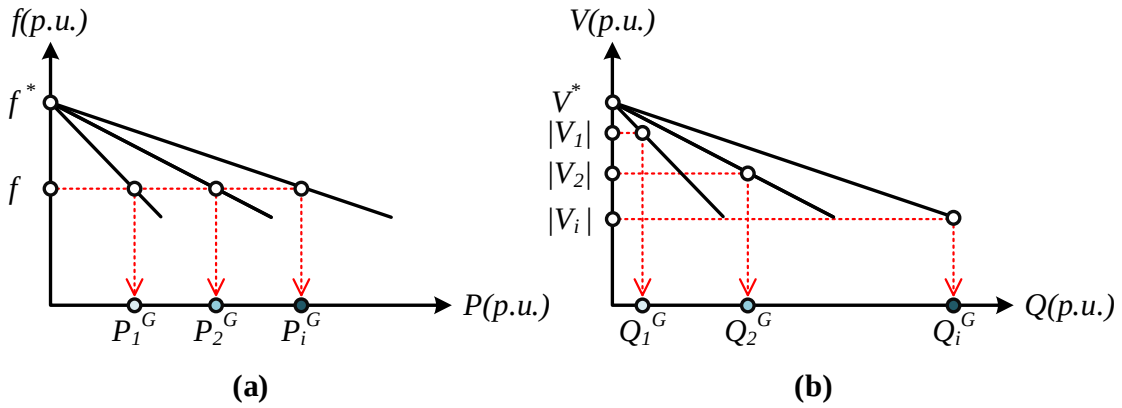

FIGURE 1. 5: Droop sharing of two DG units in the microgrid

1.3 Conventional Power Flow and Introduction to Microgrid Power Flow

The power flow problem is the computation of the voltage magnitude and phase angle at each bus in the power system at steady-state conditions. Based on these two variables, the real and reactive power injected at each bus can be computed [18], [19]. Traditionally, given that the bus impedance matrix $\bar{\mathbf{Z}}^{\mathbf{bus}}$ or the bus admittance matrix $\bar{\mathbf{Y}}^{\mathbf{bus}}$ are known, starting from equation (1.7) or (1.8) the power flow problem can be solved:

$$\bar{\boldsymbol{I}} = \bar{\mathbf{Y}}^{\mathbf{bus}}\, \bar{\boldsymbol{V}} \quad (1.7)$$

or by the inverse from,

$$\bar{\boldsymbol{V}} = \left(\bar{\mathbf{Y}}^{\mathbf{bus}}\right)^{-\mathbf{1}} \bar{\boldsymbol{I}} = \bar{\mathbf{Z}}^{\mathbf{bus}}\, \bar{\boldsymbol{I}} \quad (1.8)$$

In the power flow analysis, each bus is associated with 4 quantities [20], namely the magnitude of voltage ($|\bar{V}|$), phase angle of voltage (δ), active power (P) and reactive power (Q). For each bus, two of these quantities are specified and the other two are required to be calculated through the power flow solution. Figure 1. 6 represent the bus in the power system with their variables.

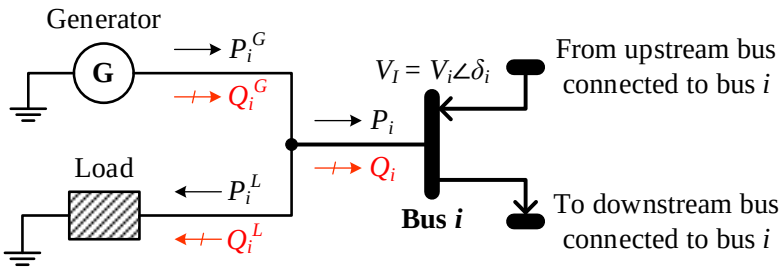

FIGURE 1. 6: Bus representation and its variables

As shown in the Figure 1. 6, they are four basic quantities associated in each bus k including the bus voltage magnitude V_i, bus phase angle δ_i, real and reactive power injected to the bus P_i and Q_i. While the real and reactive power injected to the bus can be combined and obtained by:

$$\bar{S}_i = P_i + jQ_i = \left(P_i^G - P_i^L\right) + j(Q_i^G - Q_i^L) \qquad ,\forall i \in \Omega_{BUS} \tag{1.9}$$

where, P_i^G and Q_i^G are the real and reactive generated power flowing into the bus i; P_i^L and Q_i^L are the real and reactive load power flowing out from the bus i.

Conventionally, in the distribution system or microgrid operated in grid connected the buses are classified depending on the two specified quantities as shown as Table 1. 1. Buses are divided into three categories as shown in Table 1. 1.

TABLE 1. 1: Summary of bus classification and variables

Type of the bus	Variables or quantities specified and un-specified of the bus			
	P	Q	V	δ
Slack bus	Unknown	Unknown	Known	Known
Generator bus or PV bus	Known	Unknown	Known	Unknown
Load bus or PQ bus	Known	Known	Unknown	Unknown

A PQ bus the Active (P) and Reactive (Q) power demand at the bus are specified. While, for a generator bus or known as PV bus P and V are specified. The magnitude of the voltage is kept constant by adjust the field current (excitation system). Reactive power link to the quantity of adjust the field current and possible to control the active power P due to governor system. Finally, slack bus or infinity bus represent the infinity network in the power system which has a special generator bus served as reference bus for the system. The slack can supply whatever power needed to make the flow in system balanced due to any load change. Therefore, the slack bus can be assumed to have a fixed voltage magnitude and its Phase angle is taken as a reference.

Accordingly, in the order to determine the un-specified variables, an iterative technique such newton Raphson (NR)[20], backward-forward-sweep (BFS)[21], gauss seidel (GS) or Levenberg-Marquardt [22], are deployed to determine the correct answer. This iterative technique is traditionally repeated until the unknown quantities (an updating of the voltage at each bus per iteration for example) of the system get closer to the correct answer. When those quantities no longer change from one iteration to the next, the solution has converged to the correct answer.

On the other hand, in islanded mode, there is no slack bus in the system which can serve as reference bus for the power flow calculation. Moreover, the active and reactive power generated from the DG units are un-specified and might be governed by their droop characteristic [15], up to secondary control [23]. Additionally, the frequency is not pre-specified i.e. 50/60 Hz and need to be determined. According to this issues, the islanded power tools have been developed in the literature.

1.4 Optimum Operation

In the electrical power system, the optimum operation is a steady state analysis problem/tool associated with higher level of system operation and control (e.g., DSO level). This tool is used for identifying the optimal dispatch of generation resources, load and other controllable devices according to some predetermined technical and economic considerations. The optimal operation problem has been addressed based on the AC or DC optimal power (OPF) formulation [24]. Generally, the OPF problem can be formulated as the nonlinear and non-convex problem including the objective function to be optimized and a set equality/inequality constraint which should be satisfied to ensure the correct system operation. The OPF delivers the optimal operation state for the system without violating system and equipment operation constraints [25]. The basic OPF problem can be formulated as follows:

$$\max or \min f^{OPF}\left(\mathbf{x}^{\mathbf{OPF}}, \mathbf{u}^{\mathbf{OPF}}\right) \tag{1.10}$$

subject to:

$$\mathbf{g}^{\mathbf{OPF}}\left(\mathbf{x}^{\mathbf{OPF}}, \mathbf{u}^{\mathbf{OPF}}\right) = 0 \tag{1.11}$$

$$\mathbf{h}^{\mathbf{OPF}}\left(\mathbf{x}^{\mathbf{OPF}}, \mathbf{u}^{\mathbf{OPF}}\right) \leq or \geq 0 \tag{1.12}$$

First, $f^{OPF}\left(\mathbf{x}^{\mathbf{OPF}}, \mathbf{u}^{\mathbf{OPF}}\right)$ in (1.10) is the objective function determined by the dependent variables $\mathbf{x}^{\mathbf{OPF}}$ and control variables $\mathbf{u}^{\mathbf{OPF}}$. Then, equation (1.11) is compact vectorial format represents the

equality constraints related to $\mathbf{x}^{\mathbf{OPF}}$ and $\mathbf{u}^{\mathbf{OPF}}$, while (1.12) is denoted for the inequality constraints. In the power system, the objective function $f^{OPF}(.)$ can consider both economic and technical criteria which is dependent on the specific application domain. Typically, $f^{OPF}(.)$ include the minimization of generation cost, system losses, voltage deviation, etc. Then, the constraints represent the characteristics of the system and their operation limit [26]. Typically, the equality constraints include the power flow equations. The equality constraints also include particular models representing the operation of specific devices and systems in the grid under consideration e.g., storage and microgrid. On the other hand, the inequality constraint guaranties that the control variables $\mathbf{u}^{\mathbf{OPF}}$ obtained are within some prespecified ranges e.g., generation and storage capacity. Additionally, the inequality constraints limit the dependent variables $\mathbf{x}^{\mathbf{OPF}}$ (e.g., voltage magnitude and system frequency) and allow the system to be operated within the permissible and tolerable ranges.

The variables include the set $\mathbf{x}^{\mathbf{OPF}}$ and $\mathbf{u}^{\mathbf{OPF}}$ which are dependent on the specific application. Generally, $\mathbf{x}^{\mathbf{OPF}}$ represented the solution state of the system e.g., frequency, voltage magnitude and phase angle, while $\mathbf{u}^{\mathbf{OPF}}$ represent the optimum control variables of the optimization problem which make the problem maximize or minimize its objective function. Typically, $\mathbf{u}^{\mathbf{OPF}}$ can comprise variables of continuous nature (e.g., optimal generator power dispatch and the set point of generator voltage controller), binary nature (e.g., generator unit commitment and load shedding decision), the integer or a combination of all of them. The combination of different variables can lead the OPF problem become nonlinear. In the optimum operation problem, one of the most important non-linearity terms is the power equations. Moreover, the introduction of integer/binary variables renders the problem Mixed Integer Non-Linear Programming (MINLP) problem. In this case, due to the non-linearity or non-convex, the solution delivered by this OPF problem can be representative of local optimal solutions. The OPF problem can be linearized, realizing better computational efficiency and reaching the global optimal solution. The transformation from non-linear OPF problem to linear OPF problem can be archived by the linearization of the non-linear term/equations of original non-linear OPF problem [24][26]. Nonetheless, applying linearization to the problem can lead to loss of accuracy. For this case, the validation process is required in the order to verify that any deviations are within an acceptable tolerance.

1.5 Active Power Distribution System and Microgrid Planning

The planning of the distribution system is the problem intended to answer questions pertaining to how to strategically meet the increase in load demand and to expand the electrical services driven by different technical, economic, reliability, and environment aspects. Basically, the distribution system

planning today can be classified into the conversion planning and microgrid planning [8]. The first type of planning focuses on the transformation from the PDS into the ADS by the integration of DERs and storages in the power distribution network. In this case, the optimum allocation of the DER units and distributed storage systems serves as a crucial solution to satisfy the increase in load demand. If the DERs are integrated optimally, many benefits can be obtained such as reduced power losses, improved voltage profile, enhanced reliability, enhanced economic and so on [6]. On the other hand, microgrid planning is concentrated on the design of self-sufficient regions within the distribution network. This can be achieved by deploying optimal microgrid(s) construction and can serve difference perspectives e.g., self-sufficient, reliable and both [27] [28].

Generally, the ADS and MG planning can be categorized into the 1) investment planning, 2) operational planning and 3) combination of both strategies. Additionally, the key features of the planning problem can be categorized based on different perspectives such as the allocation problem (e.g., DGs and storage placement), the operation problem and the uncertainty consideration problem. An important aspect of the planning task is the planning objective. The planning objective represent the goal of the planning which satisfy the stake holders involved (network operator and customers) such as minimizing the costs, minimizing losses, improving reliability, minimizing carbon footprint, etc. The objective of the planning can be a single objective, where in this case only one perspective is considered. Or, it can be multi-objective where different objectives are combined together and tradeoff between them are determined. To date, the planning problem formulated include the numerous decision variables, more comprehensive objectives, complex constraints and with higher level of uncertainties [6]. Here, the basic mathematical model of the planning is shown as:

$$\begin{aligned} &\max \, or \, \min F^{plan}\left(\mathbf{x}^{\mathbf{plan}}\right) = [OF_m] \\ &\text{subject to } \begin{cases} \mathbf{G}^{\mathbf{plan}}\left(\mathbf{x}^{\mathbf{plan}}\right) = 0 \\ \mathbf{H}^{\mathbf{plan}}\left(\mathbf{x}^{\mathbf{plan}}\right) \leq or \geq 0 \end{cases} \end{aligned} \tag{1.13}$$

Where, $F^{plan}(.)$ denote the objective function representing the goal or the target of the optimization problem. $F^{plan}(.)$ can be a single objective or multi-objective and comprised OF_1 to OF_m. Traditionally, the objective function can be the investment in the planning elements, operation and maintenance costs or indices of reliability. Still, these are dependent on the perspective of planner. Then, $\mathbf{G}^{\mathbf{plan}}(.)$ and $\mathbf{H}^{\mathbf{plan}}(.)$ are equality and inequality constraints, respectively, of the optimization problem. Finally, $\mathbf{x}^{\mathbf{plan}}$ are the decision variables for the planning problem e.g., the location, size and type of the DERs.

Nowadays, a major aspect of planning ADS or microgrids include the allocation of the intermittent resource such as PV and wind. This mandates that the planning problem consider the uncertainty and renders the planning problem more complex and harder to solve. Moreover, the increasing number of faults arising due to natural disasters push forward the microgrids as a solution to increase reliability and resilience. The microgrid concept has attracted the planners due to their ability to operate in grid connected mode or islanded from the main grid. The microgrid planning can also coordinate the basic conversion of PDS to ADS with the microgrid planning across using a multi-level optimization framework that considers both investment and operation in the same framework [29]. Generally, the outer level is made for the investment decisions pertaining to the planning elements. On the other hand, the inner level deals with the microgrids operation strategy to hedge the difference stochastic (e.g., renewable energy and contingencies) while respecting to the microgrids operation and control's behavior. This allows the planning problem able to capture the conversion from PDS to ADS as well as considers the microgrid operation and control while considering the stochastic nature of resources and possible faults in the system.

1.6 Literature Survey

1.6.1 Islanded Microgrids Power Flow

As discussed, the microgrid can be operated independently (i.e., islanded mode) or as a part of their upstream network (i.e., grid connected mode). In the grid connected mode the microgrid operated similar as an ADS, wherein the balance between the generation/demand were supported by their upstream network and the DGs are controlled in a power-controlled mode. In this case, the traditional power flow analysis is applicable. Nonetheless, in islanded mode the microgrid operated in the absence of the infinite bus to impose the system frequency and system voltage magnitude. Accordingly, the power flow analysis of islanded microgrids (IMG) exhibits several distinct features compared to the traditional distribution system power flow problem; namely: (1) the absence of a slack bus, (2) system frequency is one of the power flow variables, and (3) DG units are controlled as droop units. These features have recently been recognized in the literature (e.g., [15], [30]). On the other hand, practical distribution systems hosting IMGs can comprise thousands of electrical nodes and there is nothing that preclude the possibility of creating an IMG comprising thousands of buses in such systems. In these scenarios, despite comprising thousands of buses, the IMG cannot be treated as a traditional distribution system due to the lack of an infinite bus in the system and requires an IMG power flow algorithm.

Yet, existing IMG power flow algorithms in the literature are still not suited for the analysis of practical large-scale IMG systems comprising thousands of buses. For instance, in [15] a node-based IMG power flow analysis tool based on the Newton Trust Region (NTR) approach was proposed. However, this algorithm is unsuitable for the sparse implementation required for a large-scale IMG because this algorithm depends on matrix inversion processes which are generally complex to perform for sparse matrices, due to the problem of fill-in and the large number of arithmetic operations required ($O(N^3)$). The use of the famous Newton-Raphson (NR), and some of its variants, was also investigated for solving the power flow problem for droop-controlled IMG systems in [31]–[34]. Nonetheless, given their dependence on NR these algorithms, these algorithms are similar to [15] in their dependence on matrix inversion processes. In [35] a branch-based algorithm was proposed to solve the IMG power flow problem. Still, the algorithm in [35] depends on the incidence matrix and its inversion, whose representation in sparse format will create the same problems associated with sparse matrices inversion. Additionally, the algorithm in [35] requires that a DG unit be located at the upstream bus (i.e., at the main grid bus) and that the voltage at the point of common coupling (PCC) of this DG unit be used as a global variable to determine the reactive power generation of the other DG units in the IMG. This leads to inaccurate representation of the V/Q droop characteristics of the other DG units in the power flow analysis. To address the latter problem, the work in [30] proposed the choice of the respective DG units PCC bus voltages as variables in order to determine reactive power generation of the DG units accurately. However, the algorithm proposed in [30] still requires that a DG unit be present at the upstream bus. A solution to handle this requirement in the cases where no DG unit is not present at the upstream bus would be the renumbering of the IMG buses. However, the renumbering of large-scale radial systems is generally cumbersome and error-prone. In [36], a branch-based power flow algorithm for IMG that does not require the presence of a DG unit at the upstream bus was proposed. However, this algorithm depends on handling system elements/branches one by one and finding the shortest path between each node and the reflection point which is problematic to do for large-scale systems, especially when the system data is stored in sparse format. The work in [37] proposed a nested backward/forward sweep power flow algorithm for droop-controlled IMG systems. Nonetheless, similar to [35], this algorithm depends on the incidence matrix and its inversion. The algorithm in [38] proposed using conventional power flow algorithms iteratively until the power flowing from the main grid is forced to zero. However, this algorithm is dependent on running the power flow multiple times which is computationally expensive especially for large-scale systems. Moreover, this algorithm also requires a binary search for the voltage at the main grid bus, which add to the computational cost of the algorithm.

On the other hand, the consideration of unbalance in the power flow problem of traditional distribution networks has received much attention over the years. For instance, the work in [20] proposed a direct approach for balanced and unbalanced load flow. In [39] and [40], an implicit Z_{bus} method incorporating a three phase power distribution model was used for an unbalanced load flow application. Despite being suited for unbalanced distribution systems connected to the upstream network, these works (e.g., [39]–[41]) do not consider the islanded operation of droop-controlled IMGs and its implications on the power flow problem. Recently, the work in [42] and [43] proposed unbalanced power flow methods for IMGs. Nevertheless, the methods proposed in [42] and [43] mandate that DG units be located at the selected refence buses which creates similar problems to those faced with [35]. In [44], the authors proposed an iterative branch-based method to compute the power flow solution for balanced and unbalanced IMG systems. However, the algorithm in [44] depends on the formation of the bus admittance matrix and its inversion to renew the network voltage in each iteration, which is unsuitable for the sparse implementation required for a large-scale IMG due to the problems of fill-ins and the large number of arithmetic operations required.

According to this review of literature, the existing power flow tools can be computationally expensive. This issue renders the existing work not suitable for solving the power flow for a large-scale IMG. Typically, the existing node-based methods, like Newton-based methods, need matrix inversion processes which are generally complex to perform using the sparse matrices needed for large scale IMG representation. On the other hand, while some branch-based IMG power flow are proposed in the literature, most of them still require the incidence matrix and its inversion which will create the same problem associated with the sparse matrices. Moreover, most of the existing branch-based methods required a droop-controlled DG unit be located at the upstream bus which is require bus renumbering to make them applicable to the general case. An alternative solution to deal with the computation problem is using Linear Power Flow (LPF). Typically, the LPF models can provide fast power flow solutions and enable a wide range of operational control and stochastic planning algorithms that would otherwise be computationally infeasible [45]. Realizing the importance of such models, different work in the literature have proposed balanced and unbalanced LPF models for the distribution network (e.g., [46] and [47]). Yet, existing LPF models do not account for the droop-controlled IMG special features in terms of the lack of a slack bus, the variability of autonomous microgrid frequency and the operation of DG units in droop control mode. According to these challenges, new power flow models/algorithms are required.

1.6.2 Microgrid Optimal Power Flow

In order to optimize and control the operation of the microgrid, the hierarchical control structure has been widely adopted in the literature [48]. This structure employs several control layers, wherein each of these layers has its own functionality and response time. A higher-level layer is typically employed for economic purposes and manages the DG units and ESSs commitment and dispatching decisions as well as the load curtailment decisions. Lower-level and intermediary-level layers are on the other hand deployed for controlling the DG units power production and for maintaining the microgrid's voltage and frequency within bounds [49]. Still, the operation of the microgrid and its hierarchical control structure are conceptually different in both grid-connected and islanding modes of operation. In the grid-connected mode, the voltage and the frequency of the microgrid are imposed by the upstream grid at the point of common coupling (PCC) and any mismatch between the microgrid's local generation and demand is supplied by the upstream grid. As such, in the grid-connected mode of operation, the DG units are controlled to inject constant amounts of power prespecified by the high-level layer of the hierarchical control structure [26]. On the other hand, in the islanding mode of operation, the DG units cannot be controlled to supply some prespecified constant amount of power and need to follow the load variations in order to ensure a stable system operation [14][50]. To this end, in the islanding mode, primary droop control is deployed as the lower-level control layer in order to control the DG units to follow the load variations. Secondary control is deployed as the intermediary-level control layer responsible for compensating the steady-state errors in the system voltage and frequency derived by the primary control. The secondary control hence ensures that the microgrid's voltage and frequency are maintained within bounds and that the microgrid is ready for re-synchronization with the main grid when moving back from the islanding mode to the grid-connected mode. Finally, tertiary control is adopted as the higher-level control layer used for ensuring the economic viability of the microgrid operation by optimizing the microgrid's commitment and dispatch decisions.

The optimization of the operation of the microgrid resources and loads, performed by the higher-level control layer of the microgrid's hierarchal control structure, is based on an AC optimum power flow (ACOPF) problem. In this context, the considered ACOPF problem seeks to optimize the microgrid's operation subject to the system's operational constraints. Several research works have recently attempted to accurately formulate and solve the ACOPF problem for microgrid systems. For instance, a bi-level model has been proposed in [51] to optimally schedule the microgrid operation. However, this model was restricted to the grid connected mode and the ability of the system to operate in islanded mode was not considered. The mathematical formulation proposed in [52] has considered

the islanded mode of the microgrid. Yet, the primary and secondary control layers were not considered, which can lead to infeasible solutions. In [53], an ACOPF for inverter based microgrids operating in the islanded mode has been proposed. In this work, the primary droop control has been considered and the microgrid operation was optimized for minimizing the distribution losses. Additionally, an MINLP model for the optimal operation of unbalanced islanded droop based microgrid has also been proposed in [26]. This formulation was also linearized and transferred into a MILP model that can be solved with linear commercial solvers. While the work in [53], [26] has overcome earlier drawbacks pertaining to the consideration of the primary droop control layer, still these models were restricted to the islanded mode of operation and did not consider the secondary control layer. Recently, a generalized model has been introduced in [54] to consider both the grid-connected and islanded modes of operation of an unbalanced microgrid. However, the secondary control layer has not been considered in this work. On the other hand, as the secondary control layer change the DG units operating points and their active and reactive power injections, overlooking the secondary control in the microgrid ACOPF problem formulation can lead to infeasible and suboptimal operating points [16]. As mentioned, the existing works fall short in accounting the operation and control of the microgrid with primary and supervisory with secondary control. In this sense, a new ACOPF model for optimal operation the microgrid is required.

1.6.3 Power System Resilience Enhancement

The increasing recurrence of extreme weather events is demanding significant changes to the distribution networks operation and design. Extreme weather events can cause power outages in what would otherwise be a reliable distribution system. In fact, many distribution utilities worldwide are increasingly suffering from power outages due to high-impact-low-probability (HILP) events. For instance, in the ten years period from 2003 to 2013 more than 70 million customers in the United States were affected by HILP events [55]. In order to address this issue, major efforts toward distribution system resilience enhancement have been introduced recently. In this context, resilience generally refers to the ability of the system to anticipate and withstand extreme HILP events, allowing for a rapid recovery from possible interruptions due to the event [56]. To date, power distribution utilities are in the lookout for practical solutions to increase their distribution systems' resiliency, allowing for continuous supply for critical loads, e.g., hospitals and data center, during HILP events [57]. To this end, resilience enhancement solutions have been recently put forward in the literature. Generally, these solutions can be categorized into 1) planning and infrastructure-oriented strategies, and 2) operational strategies. The first kind of solutions mainly focuses on preventive actions to protect the power distribution system against contingencies that may arise due to HILP events, e.g.,

DER allocation [58], optimal sizing [59] and hardening [60]. On the other hand, operational strategies seek to improve the load restoration ability in case of a HILP event, e.g., pro-active operation [61], network configuration [62] and MGs formation [63].

The concept of microgrids planning for resilience enhancement was recently introduced in the literature. The majority of the work in this area opted for a multi-stage optimization problem for delivering the optimal resilience enhancement solutions. Generally, the outer level is dedicated to the investment decisions pertaining to the planning elements. On the other hand, the inner level deals with the microgrids operation strategy to hedge the contingencies as well as to consider the microgrids operation and control behavior. In [64], the authors proposed a two-stage model for planning microgrids considering both economics and resilience enhancement. In this work, the determination of the optimal site/size of the DERs and the backup distribution lines were considered. The problem was formulated as a master/sub-problem and solved iteratively. The master problem focused on deploying DERs and distribution lines while the sub problem identified the extreme events scenarios allowing for up to N-3 contingencies. The solution delivered by this method improved the ability of the microgrids to restore the power supply to loads during contingencies using either DERs or backup distribution lines. Still, this work lacked in terms of accounting for the AC optimal power flow representing the microgrid operation with hierarchical control. In [29] a stochastic planning model was proposed for enhancing the distribution systems resilience using a microgrid formation strategy. The proposed method was formulated as a multiple stage optimization model. The upper stage dealt with the optimal line hardening and DG allocation while the lower stage dealt with the optimum operation strategies (i.e., network reconfiguration, microgrids formation and demand side management). This work considered the uncertainty of loads as well as the uncertainty of the damage in the feeders caused by the weather events. Still, this work only considered dispatchable DG units. Renewable energy resources and energy storage units were not considered. Additionally, the microgrid hierarchical control structure was not considered in modeling the microgrid operation. The work in [59] focused on developing a planning model for the optimal sizing of isolated networked MGs considering the trade-off between economics and resilience enhancement. In this work, the problem was formulated as a three level, wherein the first level focused on the optimal sizing of the DERs and energy storage considering the normal operation (without contingencies). The second level coordinated with third level allowed for considering both normal operation and emergency operation of isolated networked MGs. For each of level, the AC optimal power flow has been used for delivering the minimum of the generation cost, load shedding or both according to the operation condition (i.e., normal and emergency). A time coupled AC optimal power flow has been simulated for 4

representative days to allow for the uncertain characteristics of the seasonal load profile. Still, renewable energy resources were not considered in this work. Moreover, the location of the DERs and storage were pre-predetermined a priori to the solution. Authors in [65] proposed the optimal sizing of mobile energy storage system in networked MGs. This work considered renewable energy resources (i.e., PV), wherein different scenarios were adopted for considering the uncertain characteristic of the PV generation as well as the load. Still, the microgrid hierarchical control structure was not considered in modeling the microgrid operation. Moreover, this problem was limited to the optimal sizing and placement of mobile energy storage, while the location and size of PV and DGs were pre-predetermined a priori.

In regards to the existing resilience-oriented microgrids planning methodologies, one of the main concerns is the computational burden. Attempting to manage their computational burden, existing work endeavored to minimize the problem size by omitting renewable energy resources, pre-specifying the location of some resources, neglecting the microgrid hierarchical control structure, and/or considering a limited number of stochastic scenarios. While these techniques can reduce the problem size, they on the other hand render the planning problem incomplete and only applicable to particular planning instances. As a possible solution to this problem, the concept of deep learning can provide an attractive solution for handling computationally demanding problems, i.e., its ability to significantly increase the computation performance of large-scale analysis/optimization problems make their solution more attainable in comparison to traditional methods. For instance, the concept of deep learning has been applied for in the development of power flow and optimal power flow tools, respectively, [66] and [67]. In these works, the deep learning technique was used for enhancing the performance and computation efficiency of the power flow/optimal power flow solution approach. Still, the concept of AC microgrids considering hierarchical control solutions has not been introduced in this work and making its application not appropriate for microgrid planning problems. On the other hand, the work in [68], proposes the use of deep learning for the restoration problem of critical loads after experiencing a major outage. In this work, the deep Q-learning method is applied for speeding up the solution approach, making the problem solvable for small distribution system up to large-scale network. However, there is no consideration of the microgrid concept and its planning in this work. Next, a new planning problem based on deep learning for a resilient transmission system is introduced in [69]. In this work, a deep learning technique is adopted to forecast the load growth while improving the forecasting task compared to an existing method. Still, the concept of microgrids is also not introduced in this work. Recently, in [70], the concept of microgrid has been introduced while coordinating several renewable resources and Plug-In Hybrid Electric Vehicles (PHEVs). In this

work, the deep learning technique is adopted to forecast the renewable output seeking to mitigate the uncertainty caused by the renewable energy elements in the microgrid. While the deep learning technique is adopted in this work, this work only discusses the operation stage and presents a simplified problem by omitting the hierarchical control philosophy of the microgrid in its problem formulation. Considering these challenges, a new framework for planning resilience oriented microgrid(s) is need and developed in this thesis.

1.6.4 Discussion of the Literature Survey

According to the literature survey, steady state analysis, optimal operation and planning frameworks that emphasize the microgrid concept have been heavily studied in the literature. Nonetheless, the critical review of literature presented in this chapter shows that there are still several key challenges that need to be addressed. First, the literature survey shows that the existing power flow tools are mainly suited for small microgrid systems and cannot scale to large scale microgrid systems comprising thousands of buses. This problem limits the existing power flow tools and make them not suitable for many stochastic planning and real time operational problems. Thus, new power flow models/algorithms are required. Furthermore, existing work in the area of ACOPF for the microgrid systems fall short in accounting the operation and control of the microgrid with hierarchical control (i.e., primary droop and secondary control). This can in turn lead to infeasible and sub-optimal solutions. Thus, a new ACOPF model for optimal operation of the microgrid considering the hierarchical control is required. Finally, the survey of literature in this chapter addressed the ultimate challenges facing the resilience oriented microgrid planning and show that there is a need to consider the operation of microgrids in the planning problem. Moreover, the survey shows that there is a need of new methodology to deal the computation problem in the planning.

Chapter 2 Power Flow Algorithm for Islanded MGs

Y. Vilaisarn and M. Abdelaziz, "An inversion-free sparse Z power flow algorithm for large-scale droop controlled islanded microgrid". Published in International Journal of Electrical Power Energy Systems, October 2020.

Résumé

L'une des principales caractéristiques des systèmes de micro-réseaux est leur capacité à fonctionner de manière isolée du réseau principal. L'étude d'écoulement de puissance (EP) des micro-réseaux isolé présente plusieurs caractéristiques distinctes par rapport à celui des méthodes traditionnelles, comme : (1) l'absence le bus infini, (2) la fréquence est une variable à déterminer, et (3) les générateurs sont contrôlés par le mode « statisme ». Plusieurs études dans la littérature ont traité ces particularités. Cependant, les algorithmes existants qui servent à l'étude d'EP d'un micro-réseau isolé ne sont pas adaptés à l'analyse un micro-réseau isolé à grande échelle qui se compose des milliers de nœuds électriques. D'autre part, dans les systèmes de distribution pratiques, les micro-réseaux isolés créés dans ces systèmes peuvent comprendre des milliers nœuds électriques. Ainsi, la mise en œuvre du concept de micro-réseau dans les systèmes de distribution réels nécessite des outils l'étude d'EP adaptés à l'analyse des micro-réseaux isolés à grande échelle. Pour cette raison, ce travail propose un algorithme basé sur une matrice Z_{bus} pour faire une étude d'écoulement de puissance d'un micro-réseau isolé. Cet algorithme proposé est particulièrement adapté à une mise en œuvre une matrice éparse ou creuse. Ceci permet de faire l'étude d'EP d'un micro-réseau qui se compose des milliers de nœuds électriques. La précision et l'efficacité de l'algorithme proposé sont validées par plusieurs études de cas portant sur des systèmes équilibrés et déséquilibrés.

Abstract

A main feature of microgrid systems is their ability to operate in isolation from the main grid, i.e., islanded microgrid (IMG) operation. The power flow (PF) problem of IMGs has been shown to exhibit several distinct features compared to that of traditional distribution systems; namely: (1) having no slack bus, (2) frequency being a PF variable, and (3) generators controlled as droop units. Several studies in the literature have focused on and addressed these particularities. Still, existing IMG PF algorithms are not suitable for the analysis of large- scale IMG systems comprising thousands of buses. On the other hand, practical distribution systems and the IMGs created within such systems may in many cases comprise thousands of electric nodes. As such, the implementation of the microgrid concept in real distribution systems requires PF tools suitable for the analysis of large-scale

IMGs. This chapter proposes a Z_{bus} PF algorithm for droop-controlled IMG that is particularly suited for sparse implementation. The proposed algorithm is inversion-free, does not require bus renumbering and is independent of third party sparse linear algebra libraries. The accuracy and effectiveness of the proposed algorithm is validated through several case studies considering balanced and unbalanced test systems.

2.1 Introduction

In this chapter we propose a Z_{bus} power flow algorithm for droop-controlled IMGs of larger dimensions. The proposed algorithm is inversion free and is particularly well-suited for sparse implementation. The remainder of this chapter is organized as follows; First, Section 2.2 introduce the proposed algorithm for balanced droop-controlled IMG. Subsequently, Section 2.3 discuss the extension of the proposed algorithm to allow for the consideration of unbalanced IMGs as well as to capture load voltage and frequency dependencies. The validation of the proposed algorithm is discussed in Section 2.4, where balanced and unbalanced case studies are used to illustrate the effectiveness of the algorithm. Finally, Section 2.5 summarize and conclude the chapter.

2.2 Proposed Algorithm

In droop-controlled IMGs, droop regulation is deployed to control the DG units output and achieve an equilibrium between the demand and generation in the IMG. Accordingly, irrespective of the generator type (i.e., whether machine based or inverter based) and its control, the DG units are represented by their droop characteristics in the power flow problem [1]. In the droop mode, the frequency and the voltage at the DG unit PCC depend on the DG units' droop characteristic [15]. With the vector "$\mathfrak{D}$" denoting the set of droop buses, the droop characteristic equations, f/P and V/Q, of the DG units in the IMG can be given as follows:

$$f = f_i^* - m_i^p P_i^G \qquad ,\forall i \in \mathfrak{D} \tag{2.1}$$

$$V_i = V_i^* - n_i^q Q_i^G \qquad ,\forall i \in \mathfrak{D} \tag{2.2}$$

where f is the IMG's frequency, f_i^* and V_i^* denote the no-load nominal frequency and voltage magnitude set points of droop bus i, respectively. V_i is the voltage magnitude at the PCC of the DG unit connected to bus i. The active and reactive static droop gains are denoted by m_i^p and n_i^q respectively. P_i^G and Q_i^G are the active and reactive power generated by the DG unit at bus i, respectively. In the order to enhance the rate of convergence, the initial values for the active and

reactive power generation are initialized by distributing the total demand (neglecting line losses) among the DG units in proportion to their droop gains.

In this work the Compressed Column Storage (CCS) format is used to store all matrices. Figure 2. 1 shows a flowchart of the proposed algorithm.

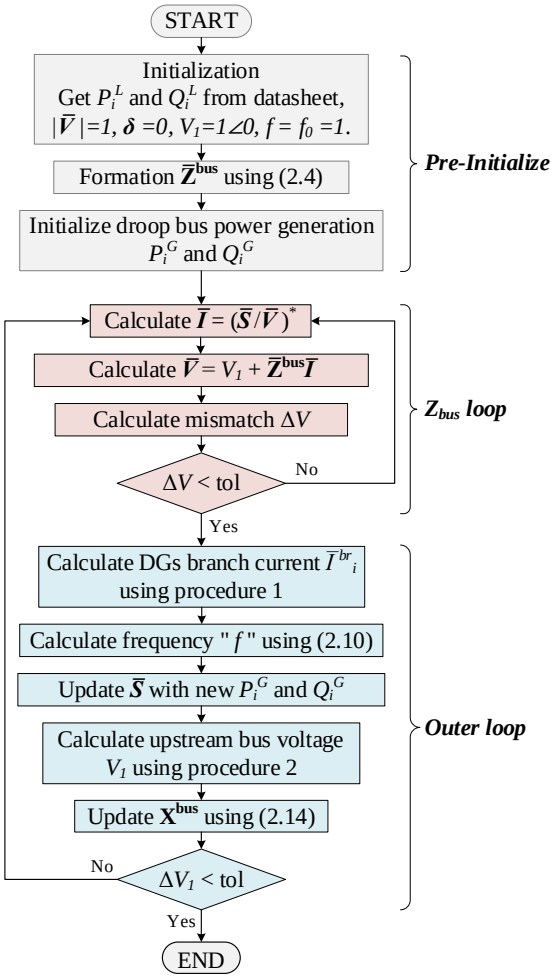

FIGURE 2. 1: Flowchart of the proposed algorithm

First, the sparse Z_{bus} matrix is calculated and stored in rectangular form to enable updating the imaginary part (which is frequency dependent) each iteration:

$$\bar{\mathbf{Z}}^{\mathbf{bus}} = \mathbf{K}^{\mathbf{T}}\bar{\mathbf{Z}}^{\mathbf{br}}\mathbf{K} \tag{2.3}$$

$$\bar{\mathbf{Z}}^{\mathbf{bus}} = \mathbf{R}^{\mathbf{bus}} + j\mathbf{X}^{\mathbf{bus}} \tag{2.4}$$

where $\mathbf{K}$ and $\bar{\mathbf{Z}}^{\mathbf{br}}$ are the incidence matrix and the primitive impedance matrix, respectively [71]. $\mathbf{R}^{\mathbf{bus}}$ and $\mathbf{X}^{\mathbf{bus}}$ are a real and imaginary part of $\bar{\mathbf{Z}}^{\mathbf{bus}}$. The proposed algorithm then uses two nested loops.

In the inner loop, an implicit Z_{bus} method is implemented. The Z_{bus} method run the power flow every iteration (it) in order to update the bus voltage vector $\bar{\boldsymbol{V}}$ and the voltage deviation vector $\overline{\boldsymbol{dV}} = \bar{\mathbf{Z}}^{\mathbf{bus}}\bar{\boldsymbol{I}}$. By using the superposition, the voltage is updated until the mismatch $\Delta V = max\left(\left|\boldsymbol{V}^{it} - \boldsymbol{V}^{it-1}\right|\right)$ is less than a given tolerance. The formulations are given directly in Figure 2. 1.

In the outer loop, the frequency and reference bus voltage are updated. In this work, similar to [35] and [30], the upstream bus #1 is chosen as the system reference. However, unlike [35] and [30], in this work a DG unit may or may not be located at bus #1. Here it is worth noting that in [35] and [30], f and V_1 were updated using the branch power of the branch adjacent to the upstream bus (denoted in this work by $\bar{I}_1^{br}$). However, when no DG is located at the upstream bus, V_1 and f cannot be updated this way. Accordingly, in this work procedures 1 and 2 are used to update f and V_1, as shown in Figure 2. 1, based on the DGs branch currents.

Procedure 1: Calculate the branch current element $\bar{I}_i^{br}$ of $\bar{\boldsymbol{I}}^{\boldsymbol{br}}$

Step 1: Calculate the complex branch current vector based on the injected current and the incidence matrix

$$\bar{\boldsymbol{I}}^{\boldsymbol{br}} = \mathbf{K}\bar{\boldsymbol{I}} \tag{2.5}$$

Step 2: Calculate the sum of branch current adjacent to bus 1

$$\bar{I}_1^{br} = \sum_{i \in Adjacent\ to\ bus\ 1} \bar{I}_i^{br} \tag{2.6}$$

Step 3: Based on (2.5) and with I_i being i^{th} element of $\boldsymbol{I}$, update I_i^{br}

$$\bar{I}_i^{br} = \bar{I}_1^{br} - (-\bar{I}_1^{br} - \bar{I}_i) \qquad ,i = \mathfrak{D}(1) \tag{2.7}$$

$$\bar{I}_{(i+1)}^{br} = -\bar{I}_{(i+1)}^{br} \qquad ,\forall i \in \mathfrak{D} \tag{2.8}$$

From the new $\bar{I}_i^{br}$, the frequency can be directly calculated by (2.9) and (2.10). Denote by $\bar{V}_i$ the i^{th} element of vector $\bar{\boldsymbol{V}}$ from the inner loop and the frequency expression becomes:

$$f_i^x = f_i^* - m_i^p[P_i^L + real\left(\bar{V}_i\left(\bar{I}_i^{br}\right)^*\right)] \ ,\forall i \in \mathfrak{D} \tag{2.9}$$

$$f = [\sum_{i=DG} f_i^x]/n_{DG} \qquad ,\forall i \in \mathfrak{D} \tag{2.10}$$

where f_i^x is the pre-updated frequency considering a droop bus i. The pre-updated frequency f_i^x in (2.9) is calculated based on the equilibrium condition for active power in each droop bus node (i.e., $P_i^G = P_i^L + real\left(\bar{V}_i\left(\bar{I}_i^{br}\right)^*\right)$ used in equation (2.1). As such, f_i^x in (2.9) depend on "$P_i^L + real\left(\bar{V}_i\left(I_i^{br}\right)^*\right)$" which represent the summation of the active power demand and the active branch power flowing out from the i^{th} bus where the DG is located. The new frequency is computed, from (2.10), and is then used to update P_i^G using (2.1). Afterward, Q_i^G can be updated directly using (2.2) with the updated voltage $\boldsymbol{V}$ from the inner loop. Then, the procedure 2 is used to determine V_1 as follows:

Procedure 2: Calculate reference bus voltage V_1

Step 1: Calculate the magnitude of the new DGs voltage from DGs branch current obtained by (7) and (8)

$$\|V_i^x\| = V_i^* - n_i^q \left[Q_i^L + imag\left(\bar{V}_i\left(\bar{I}_i^{br}\right)^*\right)\right] \qquad ,\forall i \in \mathfrak{D} \tag{2.11}$$

Step 2: Update $\bar{V}_i$ of vector $\bar{\boldsymbol{V}}$ from the inner loop with new $\|V_i^x\|$ and δ_i from the inner loop

$$\bar{V}_i = \|V_i^x\|\sin(\delta_i) + j\|V_i^x\|\cos(\delta_i) \qquad ,\forall i \in \mathfrak{D} \tag{2.12}$$

Step 3: Update the element of $\bar{\boldsymbol{I}}$ with new $\bar{V}_i$, P_i^G and Q_i^G. And then recalculate new $\overline{\boldsymbol{dV}}$.

Step 4: V_1 can be calculated using the number of droop buses and the two vectors $\bar{\boldsymbol{V}}$ and $\overline{\boldsymbol{dV}}$.

$$V_1 = [\sum ||\bar{V}_i - \overline{dV}_i||]/n_{DG} \qquad ,\forall i \in \mathfrak{D} \tag{2.13}$$

Similar to (2.9), in equation (2.11) the voltage magnitude is updated through the reactive power generation equilibrium and respecting (2.2). To note here that the use of the variables and matrix with the superscript "x" is limited to the scope of procedure 2 only and does not affect processes outside procedure 2. Also, the bar over the variables, vectors and matrices represents the complex representation. According to the calculated frequency, the $\bar{\mathbf{Z}}^{\mathbf{bus}}$ impedance is then updated. As

intended from the beginning, only $\mathbf{X^{bus}}$ will be updated and this alleviate the need to rebuild $\bar{\mathbf{Z}}^{\mathbf{bus}}$. The update expression is given as follow:

$$\mathbf{X^{bus}} = \mathbf{X^{bus,(0)}} \frac{f}{f^0} \tag{2.14}$$

Where f^0 denote the system frequency of nominal operating point, and in this work f^0 set to one. The algorithm ends when the mismatch $\Delta V_1 = |V_1^{it} - V_1^{it-1}|$ of the outer loop is less than a prespecified tolerance.

2.3 Extended to Unbalanced Systems

The proposed algorithm can be extended to allow for the consideration of three-phase unbalanced systems. Figure 2. 2 shows a flowchart describing the implementation of the proposed algorithm in three-phase unbalanced systems.

In the initialization stage the three-phase bus impedance matrix $\bar{\mathbf{Z}}^{\mathbf{bus,3\Phi}}$ is formulated in rectangular form to enable updating the imaginary part as the iterations progress. The formulation of $\bar{\mathbf{Z}}^{\mathbf{bus,3\Phi}}$ for unbalanced systems can be given as follows:

$$\bar{\mathbf{Z}}^{\mathbf{bus,3\Phi}} = (\mathbf{K^{3\Phi}})^{\mathrm{T}} \bar{\mathbf{Z}}^{\mathbf{br,3\Phi}} \mathbf{K^{3\Phi}} \tag{2.15}$$

where $\mathbf{K^{3\Phi}}$ and $\bar{\mathbf{Z}}^{\mathbf{br,3\Phi}}$ are the incidence matrix and primitive impedance matrix of the unbalanced IMG, respectively. More details about formulating $\bar{\mathbf{Z}}^{\mathbf{bus,3\Phi}}$ can be found in [39]. To note here, that $\bar{\mathbf{Z}}^{\mathbf{bus,3\Phi}}$, $\mathbf{K^{3\Phi}}$ and $\bar{\mathbf{Z}}^{\mathbf{br,3\Phi}}$ are stored in CCS format similar to their corresponding matrices in the balanced case. The initial values for the active and reactive power generation are initialized by distributing the total demand (neglecting line losses) among the DG units in proportion to the DG units respective droop gains considering the respective phase loading, where the three phases are denoted by the superscripts *a*, *b* and *c* and the detailed procedures for initializing the DGs generation will be provided later in this section. The initialization of the reference bus voltage is realized by using procedure 4, which will also be explained later in this section. The proposed algorithm then uses three nested loops. The inner and outer loops are similar to the ones used in the balanced case, where in the inner loop an implicit Z_{bus} method is implemented and in the outer loop the frequency and reference bus voltage are updated. The middle loop is dedicated to calculating the power distribution among the three phases. Procedure 3 describes how the DGs' three-phase branch power are calculated.

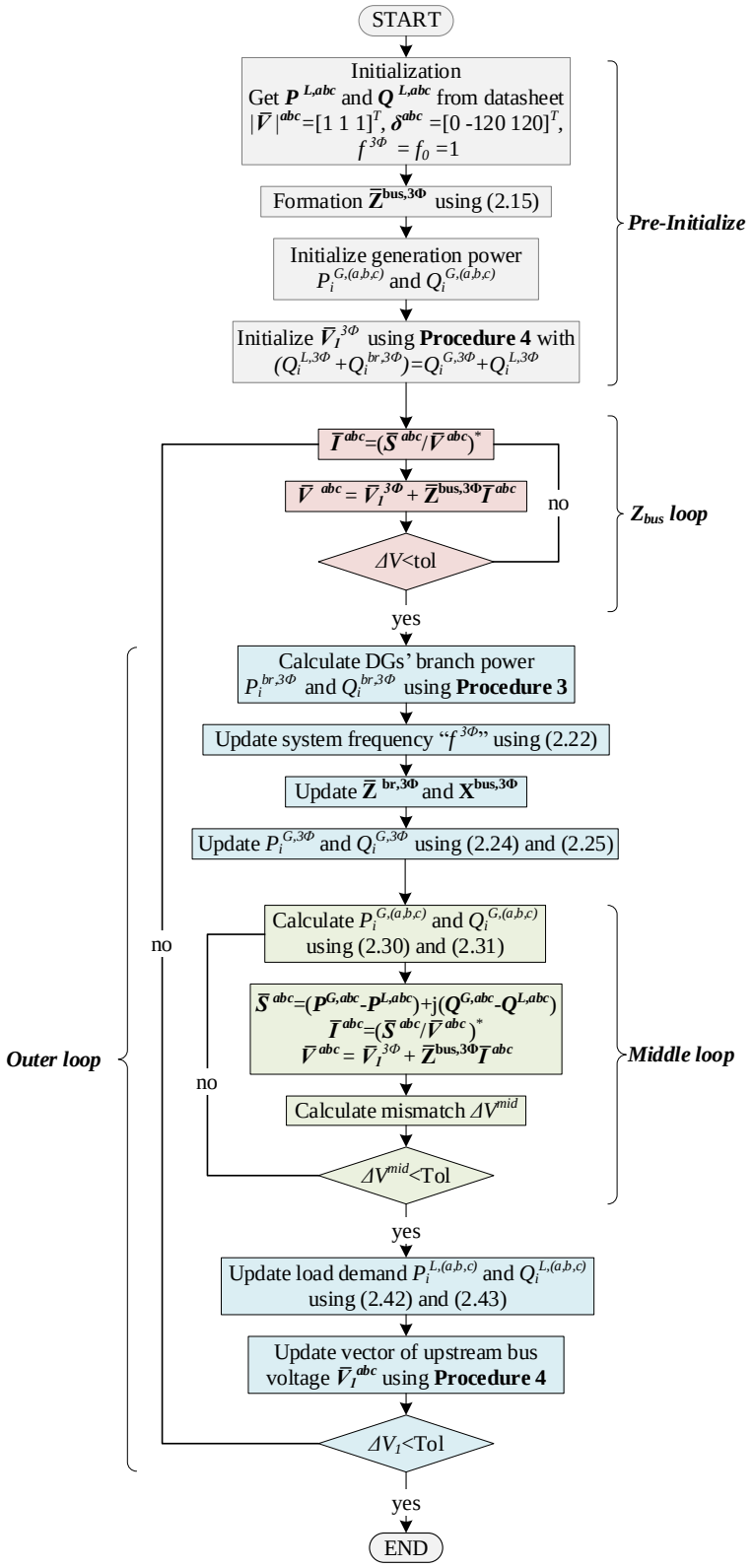

FIGURE 2. 2: Flowchart of the proposed algorithm for unbalanced system

Procedure 3: Calculate the three-phase active and reactive branch power $P_i^{br,3\Phi}$ and $Q_i^{br,3\Phi}$

Step 1: Calculate branch current vector of three phase unbalanced system

$$\bar{\boldsymbol{I}}^{\boldsymbol{br,abc}} = \mathbf{K}^{\mathbf{3\Phi}}\bar{\boldsymbol{I}}^{\boldsymbol{abc}} \tag{2.16}$$

Step 2: Calculate sum of branch current adjacent to bus 1 of each phase

$$\bar{I}_{1,\Psi}^{br} = \sum_{i \in Adjacent\ to\ bus\ 1} \bar{I}_{i,\Psi}^{br} \qquad ,\forall \Psi \in \mathcal{F} \tag{2.17}$$

Step 3: similar to procedure 1, update I_i^{br} but in this case for phase A, B and C

$$\bar{I}_{i,\Psi}^{br} = \bar{I}_{1,\Psi}^{br} - (-\bar{I}_{1,\Psi}^{br} - \bar{I}_{i,\Psi}) \qquad ,i = \mathfrak{D}(1), \forall \Psi \in \mathcal{F} \tag{2.18}$$

$$\bar{I}_{(i+1),\Psi}^{br} = -\bar{I}_{(i+1),\Psi}^{br} \qquad ,\forall i \in \mathfrak{D}, \forall \Psi \in \mathcal{F} \tag{2.19}$$

Step 5: Calculate active and reactive branch power generated by (18) and (19)

$$P_i^{br,3\Phi} = \sum_{\Psi=a,b,c}\left[real\left(\bar{V}_{i,\Psi}\left(\bar{I}_{i,\Psi}^{br}\right)^*\right)\right] \qquad ,\forall i \in \mathfrak{D} \tag{2.20}$$

$$Q_i^{br,3\Phi} = \sum_{\Psi=a,b,c}\left[imag\left(\bar{V}_{i,\Psi}\left(\bar{I}_{i,\Psi}^{br}\right)^*\right)\right] \qquad ,\forall i \in \mathfrak{D} \tag{2.21}$$

The $P_i^{br,3\Phi}$ obtained by (2.20) is used to updated $f^{3\Phi}$. Respecting to the f/P droop characteristic and the number of the droop bus in IMG, the updated system frequency expression becomes:

$$f^{3\Phi} = \left[f_i^* - m_{pi}\left(P_i^{br,3\Phi} + P_i^{L,3\Phi}\right)\right]/n_{DG} \ ,\forall i \in \mathfrak{D} \tag{2.22}$$

where $P_i^{L,3\Phi}$ denote the active three phase power of the load demand installed at bus i; and expressed by:

$$P_i^{L,3\Phi} = \sum_{\Psi=a,b,c} P_{i,\Psi}^{L} \qquad ,\forall i \in \mathfrak{D} \tag{2.23}$$

Then, according to (1) the new updated frequency $f^{3\Phi}$ is used to update the new active droop three-phase power generation $P_i^{G,3\Phi}$, as well as the reactances $\mathbf{X}^{\mathbf{bus},\mathbf{3\Phi}}$ and $\mathbf{X}^{\mathbf{br},\mathbf{3\Phi}}$. Then, the new reactive droop three-phase power generation $Q_i^{G,3\Phi}$ is updated using the selected voltage phase B of $\bar{\boldsymbol{V}}^{\boldsymbol{abc}}$ from the inner loop. Thus, respecting to (2.1) and (2.2) the generation power $P_i^{G,3\Phi}$ and $Q_i^{G,3\Phi}$ expression becomes:

$$P_i^{G,3\Phi} = (f^* - f^{3\Phi})/m_i^p \qquad ,\forall i \in \mathfrak{D} \tag{2.24}$$

$$Q_i^{G,3\Phi} = (V_i^* - |\bar{V}_i^b|)/n_i^q \qquad ,\forall i \in \mathfrak{D} \tag{2.25}$$

Comparing to the balanced case, the droop generation power from (2.1) and (2.2) cannot be used directly, due to the requirement of $P_i^{G,(a,b,c)}$ and $Q_i^{G,(a,b,c)}$. In fact, there is a need for a methodology to split the three phases power generation from (2.24) and (2.25) into the respective phases generation. In this work, the DGs are assumed to have negative sequence compensators that mitigate the voltage unbalances at the PCC [72] (i.e., the DGs produce balanced voltages despite the system unbalance). Similar, assumption has been also made in previous three-phase IMG power flow studies (e.g., [15], [44]). Moreover, the summation of the three-phase power generation should respect the droop relations. These characteristics can be expressed as following:

$$|\bar{V}_i^a| = |\bar{V}_i^b| = |\bar{V}_i^c| \qquad ,\forall i \in \mathfrak{D} \tag{2.26}$$

$$\delta_i^a = \delta_i^b + \left(\frac{2\pi}{3}\right) = \delta_i^c - \left(\frac{2\pi}{3}\right) \quad ,\forall i \in \mathfrak{D} \tag{2.27}$$

$$P_i^{G,3\Phi} = P_i^{G,a} + P_i^{G,b} + P_i^{G,c} \qquad ,\forall i \in \mathfrak{D} \tag{2.28}$$

$$Q_i^{G,3\Phi} = Q_i^{G,a} + Q_i^{G,b} + Q_i^{G,c} \qquad ,\forall i \in \mathfrak{D} \tag{2.29}$$

Equations (2.26) to (2.29) were previously formulated as mismatch equations in [15] and solved among the system power flow problem using a newton trust region method. However, there is no direct way for these equations to be implemented in the branch based unbalanced power flow that we are adopting in this work. Thus, as can see in Figure 2. 2 the middle loop is used. This loop allows for the determination of $P_i^{G,(a,b,c)}$ and $P_i^{G,(a,b,c)}$ respecting to (2.26) to (2.29) and thus capturing the DG's behavior in unbalanced three-phase conditions. The expressions for determining each phase generation power in the middle loop can be given as:

$$\begin{bmatrix} P_i^{G,b} \\ P_i^{G,c} \\ Q_i^{G,b} \\ Q_i^{G,c} \end{bmatrix}^{it^M} = \begin{bmatrix} P_i^{b} \\ P_i^{c} \\ Q_i^{b} \\ Q_i^{c} \end{bmatrix}^{it^M-1} - \lambda . \begin{bmatrix} \frac{\partial P_i^b}{\partial \delta_i^b} & 0 & \frac{\partial P_i^b}{\partial V_i^b} & 0 \\ 0 & \frac{\partial P_i^c}{\partial \delta_i^c} & 0 & \frac{\partial P_i^c}{\partial V_i^c} \\ \frac{\partial Q_i^b}{\partial \delta_i^b} & 0 & \frac{\partial Q_i^b}{\partial V_i^b} & 0 \\ 0 & \frac{\partial Q_i^c}{\partial \delta_i^c} & 0 & \frac{\partial Q_i^c}{\partial V_i^c} \end{bmatrix}^{it^M-1} \begin{bmatrix} \delta_i^a - \delta_i^b - \left(\frac{2\pi}{3}\right) \\ \delta_i^a - \delta_i^c + \left(\frac{2\pi}{3}\right) \\ |\bar{V}_i^a| - |\bar{V}_i^b| \\ |\bar{V}_i^a| - |\bar{V}_i^c| \end{bmatrix}^{it^M-1}$$

$$,\forall i \in \mathfrak{D} \tag{2.30}$$

$$\begin{bmatrix} P_i^{G,a} \\ Q_i^{G,a} \end{bmatrix}^{it_M} = \begin{bmatrix} P_i^{G,3\Phi} \\ Q_i^{G,3\Phi} \end{bmatrix}^{it_M-1} - \begin{bmatrix} P_i^{G,b} + P_i^{G,c} \\ Q_i^{G,b} + Q_i^{G,c} \end{bmatrix}^{it_M} \quad ,\forall i \in \mathfrak{D} \qquad (2.31)$$

Where it^M is the iteration counter of the middle loop, λ denote the step size and selected small enough to maintain the convergence of the middle loop (set as 0.01 in this work). Here it is worth highlighting that equations (2.30) and (2.31) were previously proposed in [44] for splitting the power among the three phases and are adopted here for the same purpose. Details about the formulation of the elements of the matrix in (2.30) are provided in Appendix A of this work. The generation power in (2.30) and (2.31) are updated through the iterations of the middle loop's until the mismatch Δ^{mid} is less than a given tolerance, where Δ^{mid} is formulated as:

$$\Delta^{mid} = \max\left(\left|\sum_{\Psi=a,b,c} \bar{V}_{i,\Psi}\right|\right) \quad ,\forall i \in \mathfrak{D} \qquad (2.32)$$

Afterward, procedure 4 is used to update $\bar{\boldsymbol{V}}_{\mathbf{1}}^{\mathbf{3\Phi}}$:

Procedure 4: Calculate reference bus complex voltage $\bar{\boldsymbol{V}}_{\mathbf{1}}^{3\Phi}$ for the proposed unbalanced power flow

---

Step 1: Update the magnitude of DGs voltage magnitude using the branch reactive power obtained by procedure 3

$$\|V_i^x\|^a = V_i^* - n_{qi}\left[Q_i^{L,3\Phi} + Q_i^{br,3\Phi}\right] \quad ,\forall i \in \mathfrak{D} \qquad (2.33)$$

Step 2: Update $\bar{V}_i^{a,b,c}$ of $\bar{\boldsymbol{V}}^{\boldsymbol{abc}}$ from the inner loop with new $\|V_i^x\|^{a,b,c}$ obtained by (33) and δ_i^a from the inner loop

$$\begin{bmatrix} \bar{V}_i^a \\ \bar{V}_i^b \\ \bar{V}_i^c \end{bmatrix} = \begin{bmatrix} \|V_i^x\|^a cos\,(\delta_i^a) + j\|V_i^x\|^a sin\,(\delta_i^a) \\ \|V_i^x\|^a cos\,(\delta_i^a - \left(\frac{2\pi}{3}\right)) + j\|V_i^x\|^a sin\,(\delta_i^a - \left(\frac{2\pi}{3}\right)) \\ \|V_i^x\|^a cos\,(\delta_i^a + \left(\frac{2\pi}{3}\right)) + j\|V_i^x\|^a sin\,(\delta_i^a + \left(\frac{2\pi}{3}\right)) \end{bmatrix} \quad ,\forall i \in \mathfrak{D} \qquad (2.34)$$

Step 3: Update the element of $\bar{\boldsymbol{I}}^{\boldsymbol{abc}}$ with new $\bar{V}_i^{a,b,c}$ as well as $P_i^{G,(a,b,c)}$ and $Q_i^{G,(a,b,c)}$ obtained by the middle loop; And calculated $\overline{\boldsymbol{dV}}^{\boldsymbol{x,abc}}$ expressed by:

$$\overline{\boldsymbol{dV}}^{\boldsymbol{x,abc}} = \bar{\mathbf{Z}}^{\mathbf{bus,3\Phi}}\bar{\boldsymbol{I}}^{\boldsymbol{abc}} \qquad (2.35)$$

Step 4: $\bar{V}_1^{a,b,c}$ and $\delta_1^{a,b,c}$ can be calculated based on the number of droop bus of the vector $\overline{\boldsymbol{V}}^{\boldsymbol{abc}}$ and $\overline{\boldsymbol{dV}}^{\boldsymbol{x,abc}}$.

$$\bar{V}_{1,\Psi} = \left[\sum(\bar{V}_{i,\Psi} - \overline{dV}_{i,\Psi}^{x})\right]/n_{DG} \qquad ,\forall i \in \mathfrak{D}, \forall \Psi \in \mathcal{F} \tag{2.36}$$

$$\delta_{1,\Psi} = angle\left(\bar{V}_{1,\Psi}\right) - angle(\bar{V}_1^a) \qquad ,\forall \Psi \in \mathcal{F} \tag{2.37}$$

Step 5: store (36) and (37) in the vector $\overline{\boldsymbol{V}}_{\boldsymbol{1}}^{\boldsymbol{abc}}$ and convert to $\overline{\boldsymbol{V}}_{\boldsymbol{1}}^{3\Phi}$.

$$\overline{\boldsymbol{V}}_{\boldsymbol{1}}^{\boldsymbol{abc}} = \left[|\bar{V}_1^a|\angle\delta_1^a; \left|\bar{V}_1^b\right|\angle\delta_1^b; |\bar{V}_1^c|\angle\delta_1^c\right] \tag{2.38}$$

$$\overline{\boldsymbol{V}}_{\boldsymbol{1}}^{3\Phi} = \left[\overline{\boldsymbol{V}}_{\boldsymbol{1}}^{\boldsymbol{abc}}\ \overline{\boldsymbol{V}}_{\boldsymbol{1}}^{\boldsymbol{abc}} \ldots \overline{\boldsymbol{V}}_{\boldsymbol{1}}^{\boldsymbol{abc}}\right]^T_{(1\times 3.n_{br})} \tag{2.39}$$

To note here that the use of the variables and matrix with the superscript "x" is limited to the scope of procedure 4 only and does not affect processes outside procedure 4 (i.e., does not affect $\overline{\boldsymbol{V}}$ and $\overline{\boldsymbol{dV}}$ of the inner loop and middle loops). Similar to the proposed balanced algorithm, the algorithm ends when the mismatch ΔV_1 goes below a prespecified tolerance. As mentioned earlier, procedure 4 is also used to initialize $\overline{\boldsymbol{V}}_{\boldsymbol{1}}^{3\Phi}$ at the pre-initialize stage. However for step 1 and step 2 in procedure 4, $P_i^{G,(a,b,c)}$, $Q_i^{G,(a,b,c)}$ and $Q_i^{br,3\Phi}$ need to be specified. Thus, $P_i^{G,(a,b,c)}$ and $Q_i^{G,(a,b,c)}$ are initialized by distributing the total demand (neglecting line losses) in the proportion to the droop gains. Equations (2.40) and (2.41) express the initialization power of each phase power generation:

$$P_{i,\Psi}^{G,init} = \left(\frac{\left[\sum\frac{1}{m_i^p}\right]^{-1}}{m_i^p}\right)\sum_{j=1}^{n_{bus}} P_{j,\Psi}^{L,spec} \qquad ,\forall i \in \mathfrak{D}, \forall \Psi \in \mathcal{F} \tag{2.40}$$

$$Q_{i,\Psi}^{G,init} = \left(\frac{\left[\sum\frac{1}{n_i^q}\right]^{-1}}{n_i^q}\right)\sum_{j=1}^{n_{bus}} Q_{j,\Psi}^{L,spec} \qquad ,\forall i \in \mathfrak{D}, \forall \Psi \in \mathcal{F} \tag{2.41}$$

As can be seen in Figure 2. 2, the power term of (2.33) are replaced by $Q_{i,\Psi}^{L,init}$ and (2.41) in the pre-initialize stage.

2.4 Algorithm Validation and Numerical Results

In this section, balanced and unbalanced radial distribution test systems have been chosen to evaluate the effectiveness of the proposed algorithm compared to other algorithms available in the literature. All case studies were performed in MATLAB environment on a PC equipped with 3.40GHz Intel Core i7 processor with 8GB of RAM.

2.4.1 Balanced Microgrids

For the validation of the proposed algorithm in balanced conditions, the balanced 33-bus and the 10476-bus distribution test systems were used. Test systems description, feeder parameters and nominal loads are available online at [73]. The DGs locations, droop coefficients and nominal no-load settings for the 33-bus and the 10476-bus distribution test systems are summarized in Table G. 1 of Appendix G.

For the balanced case, the validation methodology is divided into two steps. First, the well-known 33-bus system used in [15] and [30] is used to validate the accuracy of the proposed algorithm, by comparing its results with those obtained using the NTR algorithm of [15] and the modified backward/forward sweep (MBF) algorithm of [30]. Figure 2. 3 gives the voltage profile obtained using the three algorithms.

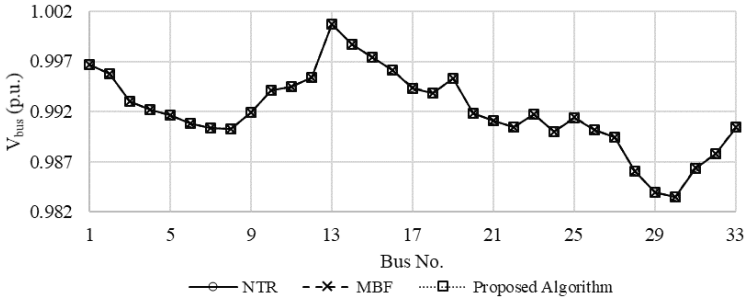

FIGURE 2. 3: Voltage profile for 33-bus IMG system as calculated by NTR [15], MBF [30] **and the proposed algorithm (f = 0.9198 p.u.)**

As can be seen in Figure 2. 3, the results from the three algorithms are almost identical. The maximum difference in V/δ between the results of the proposed algorithm and the results of NTR algorithm of [15] was found to be $7.34 \times 10^{-7}/2.14 \times 10^{-5}$. Similarly, comparing the results of the proposed algorithm with those obtained by the MBF algorithm of [30], the maximum difference in V/δ was found to be $3.92 \times 10^{-5}/5.61 \times 10^{-4}$.

In terms of computational performance, the number of inner/outer loops iteration required by the proposed algorithm is 70/23 compared to 327/93 when using the MBF algorithm of [30]. Figure 2. 4 shows the inner/outer loop errors along the required iterations for the proposed algorithm and for the MBF algorithm of [30]. Figure 2. 5 shows a close up of the iterations error data of the proposed algorithm presented in Figure 2. 1.

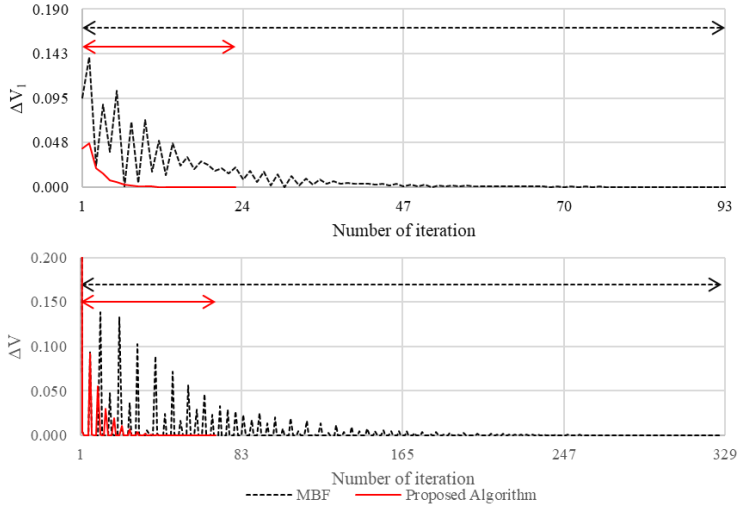

FIGURE 2. 4: Comparison between the convergence characteristics of proposed algorithm and the MBF algorithm of [30] **in terms of inner and outer loops error for the 33-bus IMG system**

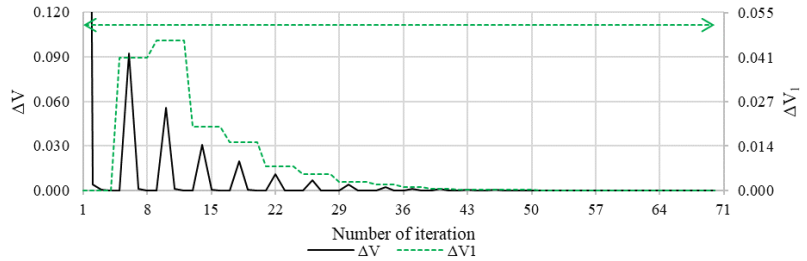

FIGURE 2. 5: Evolution of inner and outer loops error of the proposed algorithm for the 33-bus IMG system

On the other hand, the NTR algorithm of [15] converges in only 4 iterations. Despite that, the NTR algorithm of [15] is computationally more expensive than both the MBF algorithm of [30] and the proposed algorithm, with an average runtime (computed over 10 runs) of 367.3 ms compared to 69.3 ms and 47.9 ms for the MBF algorithm of [30] and the proposed algorithm, respectively.

In the second step of the algorithm validation under balanced conditions, the proposed algorithm is implemented to solve the PF problem for a large-scale IMG comprising 10476-bus [71]. As anticipated, the NTR algorithm of [15] and the MBF algorithm of [30] were not able to solve the PF problem for this large-scale IMG and they both did not converge. For the proposed algorithm, the number of required iterations was 47/19 of inner/outer loops and 14753.6 ms of average runtime (computed over 10 runs). The bus voltage of the 10476-bus system is illustrated in Figure 2. 6.

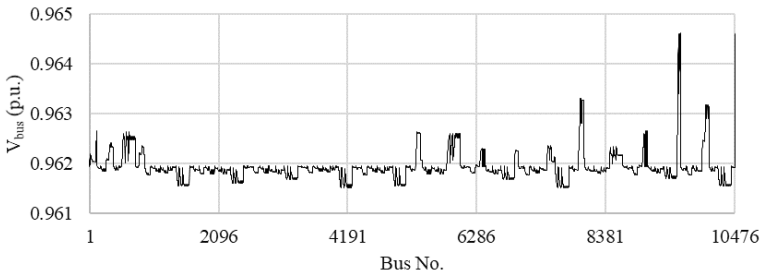

FIGURE 2. 6: Voltage profile of 10476-bus IMG system (f = 0.9952 p.u.)

2.4.2 Unbalanced Microgrids

To show the effectiveness of the proposed algorithm under unbalanced conditions, the unbalanced 25-bus test system is used. Details about the test system feeder parameters and nominal loads can be found in [74]. Similar to [15], in this work the system loads have been modified to make the system heavily unbalanced (by decreasing phase A by 20% and increasing Phase C load by 20%). The DGs locations, droop coefficients and nominal no-load settings for the DG units the unbalanced 25-bus test system is found in Table G. 1 of Appendix G. The tolerances were set at 10^{-6} and 10^{-4} for outer/inner loop and middle loop, respectively.

First, we validate the accuracy of the proposed algorithm by comparing its results with those obtained using the NTR algorithm of [15]. Here it is worth noting that the modified backward/forward sweep (MBF) algorithm of [30] does not consider unbalanced cases and as such was not used in this comparison. Figure 2. 7 shows the bus voltage profile obtained by the proposed algorithm and that obtained by using the NTR algorithm of [15].

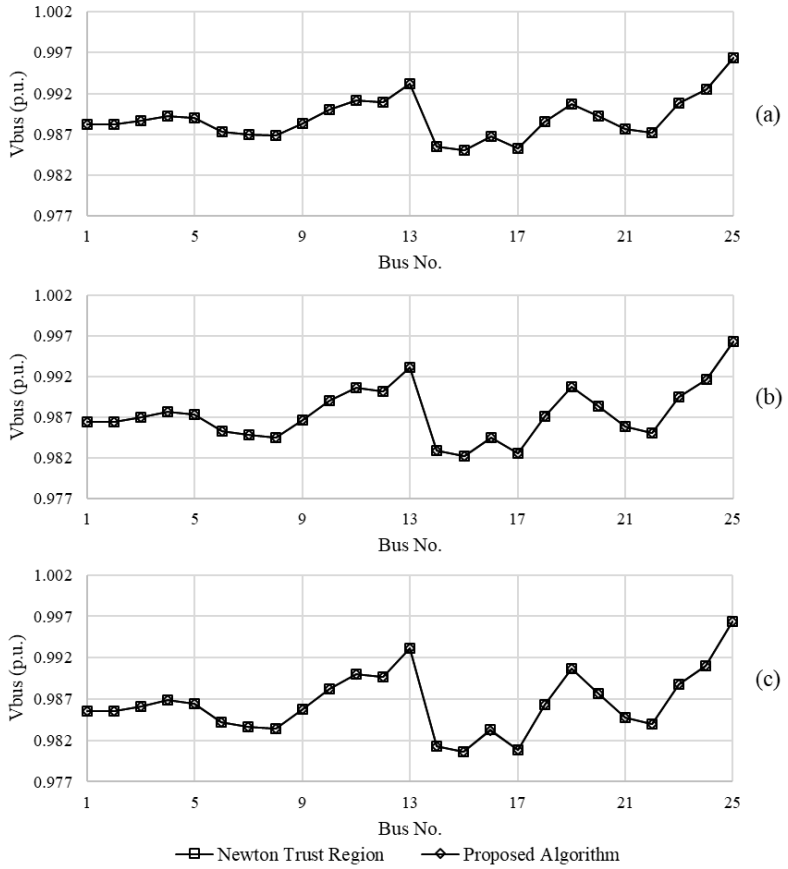

FIGURE 2. 7: Voltage profile for 25-bus unbalanced IMG as calculated by NTR [15] and by the proposed algorithm (f = 0.9978 p.u.): (a) Phase A, (b) Phase B and (c) Phase C

As can be seen in Figure 2. 7 the results obtained from the proposed algorithm are almost identical to those obtained using the NTR algorithm of [15]. The maximum difference in V/δ between the results of the proposed algorithm and the results of NTR algorithm of [15] was found to be $1.21 \times 10^{-5}/4.22 \times 10^{-3}$.

In terms of computational performance, the number of inner/middle/outer loops iteration required by the proposed algorithm is 114/571/49. However, the number of iteration is 5 when using the NTR algorithm of [15]. Despite that, the NTR algorithm of [15] is computationally more expensive than the proposed algorithm, with an average runtime (computed over 10 runs) of 3590.08 ms compared to 686.09 ms for the proposed algorithm, i.e., the proposed algorithm is around six time faster than the NTR [15] for the 25-bus unbalanced IMG. Figure 2. 8 shows the evolution of the error against time of case 1 for the 25-bus unbalanced IMG. As can be seen, the middle loop takes the majority of computation time compared to the inner and outer loops.

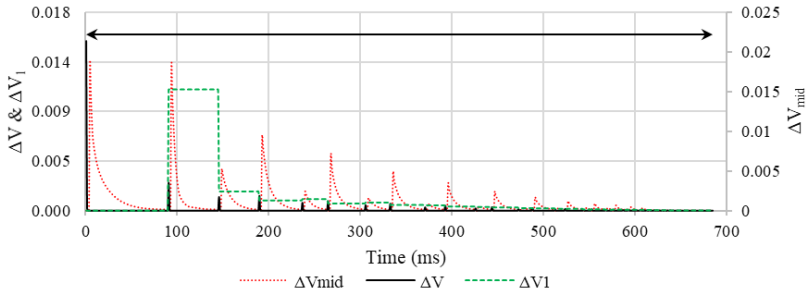

FIGURE 2. 8: Evolution of inner, middle and outer loops error of the proposed algorithm for the base case 25-bus system

2.4.3 Microgrids with voltage and frequency dependent loads

In order to illustrate the effectiveness of proposed algorithm in capturing the load dependency on voltage and frequency, voltage and frequency dependent load models were adopted in the proposed power algorithm as expressed by [15]:

$$P_{i,\Psi}^{L} = P_{i,\Psi}^{L,spec}\left|\bar{V}_{i,\Psi}\right|^{\alpha}(1 + K^{pf}(\Delta f)) \qquad ,\forall i \in \Omega_{BUS}, \forall \Psi \in \mathcal{F} \tag{2.42}$$

$$Q_{i,\Psi}^{L} = Q_{i,\Psi}^{L,spec}\left|\bar{V}_{i,\Psi}\right|^{\beta}(1 + K^{qf}(\Delta f)) \qquad ,\forall i \in \Omega_{BUS}, \forall \Psi \in \mathcal{F} \tag{2.43}$$

where $P_{i,\Psi}^{L,spec}$ and $Q_{i,\Psi}^{L,spec}$ are the specified nominal active and reactive power demand; Δf denote the frequency deviation of the IMG from the nominal frequency; α and β are the active and reactive power exponents which are used to represent constant power, constant current, constant impedance loads [15]; and K^{pf} and K^{qf} are the active and reactive power frequency dependencies factors. Three cases studies were considered; case 1 represents the base case where all the loads are considered as constant power loads and independent to changes in voltage and frequency (i.e., similar to the case studies presented in subsections 4A and 4B). Cases 2A and 2B consider the system loads as constant current and constant impedance loads, respectively; and both are dependent to the change of frequency with K^{pf} and K^{qf} set as 1 and -1 respectively. Table 2. 1 summarizes the accuracy validation, by comparing the maximum error in voltage magnitude, phase angle, active and reactive power with respect to the results obtained by MBF and NTR, respectively. These results demonstrate the effectiveness of the proposed balanced and unbalanced system under various load models.

TABLE 2. 1: Proposed algorithm maximum errors compared to MBF [30] **and NTR [15] for the 33-bus balanced and 25-bus unbalanced IMG under different load characteristics**

Test system	Case	max|V| (p.u.)	max|δ| (deg.)	max|P| (p.u.)	max|Q| (p.u.)
		MBF and Proposed algorithm			
33-bus system	1	3.92×10^{-05}	5.61×10^{-04}	1.10×10^{-07}	1.34×10^{-04}
	2A	1.65×10^{-06}	4.63×10^{-06}	1.26×10^{-05}	1.49×10^{-05}
	2B	1.88×10^{-05}	1.88×10^{-04}	1.89×10^{-04}	3.00×10^{-04}
		NTR and Proposed algorithm			
33-bus system	1	7.34×10^{-07}	2.14×10^{-05}	1.72×10^{-04}	1.40×10^{-04}
	2A	9.54×10^{-07}	2.05×10^{-05}	1.09×10^{-06}	1.02×10^{-05}
	2B	2.76×10^{-06}	2.43×10^{-05}	5.81×10^{-06}	3.73×10^{-05}
25-bus system	1	1.21×10^{-05}	4.22×10^{-03}	1.75×10^{-04}	2.03×10^{-04}
	2A	3.73×10^{-05}	4.78×10^{-03}	2.96×10^{-04}	6.32×10^{-05}
	2B	5.66×10^{-05}	6.37×10^{-03}	4.19×10^{-04}	6.83×10^{-05}

In terms of computational performance, Table 2. 2 and Table 2. 3, respectively, summarize the average runtime (computed over 10 runs) and the number of iterations required for all methods (i.e. MBF [30], NTR [15] and the proposed algorithm) for cases 1, 2A and 2B.

TABLE 2. 2: Average runtime (s) of proposed algorithm, MBF [30] **and NTR [15] under different load characteristics**

Test system	Case	MBF (ms)	NTR (ms)	Proposed algorithm (ms)
33-bus system	1	69.3	367.3	47.9
	2A	72.8	379.8	48.1
	2B	75.7	393.3	48.8
10476-bus system	1	-	-	14753.6
	2A			14969.3
	2B			15145.4
25-bus system	1	-	3590.1	686.1
	2A		3578.3	755.4
	2B		3553.1	797.2

Similar to the results of case 1 (discussed in subsection 2.4.1), the MBF and NTR could not handle the 10476-bus system in cases 2A and 2B, and both algorithms did not converge for this system. For the 33-bus balanced and the 25-bus unbalanced IMG, even though the NTR only takes 4 and 5 iterations, respectively, it is found to be around 8 and 6 six time slower than the proposed algorithm. For the proposed algorithm, in cases 2A and 2B the load frequency and voltage dependencies require active and reactive power demand calculation to compute the reference voltage in the outer loop as

well as the current injection in the inner loop and as such the proposed algorithm require slightly more time compared to case 1 wherein the load is constant.

TABLE 2. 3: Number of iterations of proposed algorithm, MBF [30] **and NTR [15] under different load characteristics**

Test system	Case	MBF	NTR	Proposed algorithm
		inner/outer	iteration	inner/outer
33-bus system	1	327/93	4	70/23
	2A	218/73	4	71/23
	2B	306/98	4	76/24
10476-bus system	1	-	-	47/19
	2A			48/20
	2B			57/24
			iteration	inner/middle/outer
25-bus system	1	-	5	114/571/49
	2A		5	117/617/49
	2B		5	121/673/49

2.5 Conclusion

This chapter proposed a Z_{bus} PF algorithm for IMGs. The proposed algorithm is inversion-free and does not require bus renumbering. This algorithm overcomes the problems that existing IMG PF algorithms face when handling a practical large-scale IMG system comprising thousands of buses. The accuracy and effectiveness of the proposed algorithm has been validated through several case studies on a 33-bus and 10476-bus balanced test systems. The algorithm is also extended for the unbalanced IMG cases. The unbalanced 25 bus system was used and solved considering three cases for the load model i.e. constant power, constant current and constant impedance. The proposed algorithm shows superior in terms of simulation time and applicability to practical large-scale IMG cases.

Chapter 3 Linear Power Flow Model for MG system

Y. Vilaisarn, M. Abdelaziz, and J. Cros, "Linear Three-Phase Power Flow Model for Autonomous Microgrid Systems". Published in CIRED – Open Access Proceedings Journal, April 2021.

Résumé

Dans ce travail, nous proposons un modèle linéaire triphasé pour l'étude d'écoulement de puissance des micro-réseaux autonomes fonctionnement en mode « statisme ». Ce modèle linéaire adopte un ensemble d'équations algébriques linéaires et peut, avec de petites erreurs par rapport au modèle non linéaire, tenir compte de l'absence d'un bus infini, de la variabilité de la fréquence des micro-réseaux autonomes et du fonctionnement des unités DG en mode « statisme ». Le modèle linéaire proposé peut donc fournir une solution rapide et précise. Ces qualités sont très utile pour l'étude d'un problème de planification qui demande une analyse stochastique et aussi les applications temps réel liée aux fonctionnements des micro-réseaux autonomes. En plus, ce modèle linéaire est très avantageux pour faire l'analyse linéaire ou convexe des problèmes d'opération optimale et des problèmes probabilistes. La précision et l'efficacité du modèle linéaire proposé sont validées par différentes études de cas portant sur des systèmes de test équilibrés et déséquilibrés.

Abstract

In this work, we propose a linear three-phase power flow model for droop-controlled autonomous microgrids. The proposed linear power flow model adopts a set of linear algebraic equations and can, with small errors compared to the detailed nonlinear model, account for the lack of a slack bus, the variability of autonomous microgrid frequency and the operation of DG units in droop control mode. The proposed linear model can as such provide a fast and accurate power flow solution and has great potential in the stochastic planning and online operational applications of autonomous microgrids, as well as in linear or convex optimal power flow and probabilistic load flow analysis. The accuracy and effectiveness of the proposed linear power flow model is validated though different case studies considering balanced and unbalanced test systems.

3.1 Introduction

The planning and operation of microgrids require an accurate power flow analysis of the network in both grid-connected and autonomous/islanded modes of operation. On the other hand, conventional power flow model are not suitable for the analysis of autonomous microgrids (AMGs) for three main

reasons: (i) the absence of a slack bus in AMGs, (ii) the variability of the system frequency in the AMGs operation mode, where the frequency is one of the power flow variables to be calculated, and (iii) the operation of the DG units forming the AMG in droop mode, which cannot be modelled in conventional distribution power flow models [75], [76].

In this chapter, a linear power flow model for autonomous microgrid or IMG is proposed. Linear power flow (LPF) models can provide fast power flow solutions and enable a wide range of operational control and stochastic planning algorithms that would otherwise be computationally infeasible [45]. Moreover, the nature of LPF model is a node-based which can be used in system optimization problems as a power equation (i.e., planning and optimal operation). The non-linear power flow (non-LPF) equations for unbalanced droop-controlled AMG are first presented. Then, the linearization operator is adopted in the order to turn the non-LPF model to an accurate LPF model. To this end, the accuracy and the effectiveness of the proposed LPF model are validated thought the solution delivered by the existing method i.e., Newton Trust Region (NTR) [15], Modified Backward Forward (MBF) [30] and the proposed sparse $\mathbf{Z_{bus}}$ in chapter 2.

The remainder of this chapter is organized as follows: Section 3.2 introduces the formulation of the linear model and the methodology for solving them. The validation of the proposed algorithm is discussed in Section 3.3, where balanced and unbalanced case studies were deployed to illustrate the effectiveness of the proposed LPF model. Finally, in Section 3.4 we summarize and conclude the chapter.

3.2 Formulation and Linear Power Flow

In droop-controlled AMGs, the frequency and voltage at a DG unit's point of common coupling (PCC) are controlled to follow the droop characteristic equations, f/P and V/Q, given as follows:

$$P_i^{G,3\Phi} = (f_i^* - f^{3\Phi})/m_i^p \qquad ,\forall i \in \mathfrak{D} \tag{3.1}$$

$$Q_i^{G,3\Phi} = (V_i^* - |\bar{V}_i^a|)/n_i^q \qquad ,\forall i \in \mathfrak{D} \tag{3.2}$$

where $P_i^{G,3\Phi}$ and $Q_i^{G,3\Phi}$ are the active and reactive three-phase generation power delivered by the DG unit at the bus i, respectively, $f^{3\Phi}$ is the AMG's frequency, f_i^* and V_i^* denote the no-load nominal frequency and voltage set point of droop bus i, respectively. The active and reactive static droop gains are denoted by m_i^p and n_i^q. Then, $\bar{V}_i$ denote the voltage at the PCC of the DG unit connected to bus i.

As can be seen, $Q_i^{G,3\Phi}$ are respected to the droop by referring to $\bar{V}_i^a$ at the PCC of the DG unit connected to bus i [15].

The non-linear power flow equation in unbalanced droop-controlled AMG can be given as [15], [77]:

$$P_{i,\Psi} = \left(P_{i,\Psi}^G - P_{i,\Psi}^L\right) = \left|\bar{V}_{i,\Psi}\right| \sum_{j=1}^{n_{bus}} \sum_{\beta \in \mathcal{F}} \left|\bar{V}_{j,\beta}\right| \begin{pmatrix} G_{ij}^{\Psi\beta} \cos\left(\delta_{i,\Psi} - \delta_{j,\beta}\right) \\ +B_{ij}^{\Psi\beta} \sin\left(\delta_{i,\Psi} - \delta_{j,\beta}\right) \end{pmatrix} \quad ,\forall i \in \Omega_{BUS}, \forall \Psi \in \mathcal{F} \qquad (3.3)$$

$$Q_{i,\Psi} = \left(Q_{i,\Psi}^G - Q_{i,\Psi}^L\right) = \left|\bar{V}_{i,\Psi}\right| \sum_{j=1}^{n_{bus}} \sum_{\beta \in \mathcal{F}} \left|\bar{V}_{j,\beta}\right| \begin{pmatrix} -B_{ij}^{\Psi\beta} \cos\left(\delta_{i,\Psi} - \delta_{j,\beta}\right) \\ +G_{ij}^{\Psi\beta} \sin\left(\delta_{i,\Psi} - \delta_{j,\beta}\right) \end{pmatrix} \quad ,\forall i \in \Omega_{BUS}, \forall \Psi \in \mathcal{F} \qquad (3.4)$$

where Ψ and β denote phase indices, n_{bus} is the number of buses in the AMG, $P_{i,\Psi}^L$ and $Q_{i,\Psi}^L$ are the active and reactive load demand of phase Ψ located at bus i, respectively, $G_{ij}^{\Psi\beta}$ and $B_{ij}^{\Psi\beta}$ denote the self/mutual conduction and susceptance connecting bus i to j, respectively. $\bar{V}$ and δ are the complex voltage magnitude and its phase angle, respectively. Considering constant power loads, the only non-linearity in (3.3) and (3.4) came from the production of voltage magnitude and trigonometric i.e. sines and cosines. In order to linearize these equations, the following linear approximation are adopted:

Approximation 1: deal with the non-linearity obtained by the effect of trigonometric sines, cosines and the deviation between the phase angle i.e. $\left(\delta_{i,\Psi} - \delta_{j,\beta}\right)$ as follows [46]:

$$\cos\left(\delta_{i,\Psi} - \delta_{j,\beta}\right) \approx \begin{cases} 1 \quad , \text{ if } \Psi = \beta \\ -\frac{1}{2} - \frac{\sqrt{3}}{2}\left(\delta_{i,\Psi} - \delta_{j,\Psi}\right), \text{ if } \beta \text{ lag } to\ \Psi \\ -\frac{1}{2} + \frac{\sqrt{3}}{2}\left(\delta_{i,\Psi} - \delta_{j,\Psi}\right), \text{ if } \beta \text{ lead } to\ \Psi \end{cases} \qquad (3.5)$$

$$sin\left(\delta_{i,\Psi} - \delta_{j,\beta}\right) \approx \begin{cases} \left(\delta_{i,\Psi} - \delta_{j,\Psi}\right) \quad , \text{ if } \Psi = \beta \\ -\frac{1}{2}\left(\delta_{i,\Psi} - \delta_{j,\Psi}\right) + \frac{\sqrt{3}}{2}, \text{ if } \beta \text{ lag } to\ \Psi \\ -\frac{1}{2}\left(\delta_{i,\Psi} - \delta_{j,\Psi}\right) - \frac{\sqrt{3}}{2}, \text{ if } \beta \text{ lead } to\ \Psi \end{cases} \qquad (3.6)$$

Approximation 2: deal with the second order of the voltage as well as the relation between the phase angle deviation and the susceptance term as follows [46]:

$$\left|\bar{V}_{i,\Psi}\right|\left|\bar{V}_{j,\beta}\right| H_{ij}^{\Psi\beta} \cos\left(\delta_{i,\Psi} - \delta_{j,\beta}\right) \approx \left|\bar{V}_{j,\beta}\right| H_{ij}^{\Psi\beta} \cos\left(\delta_{i,\Psi} - \delta_{j,\beta}\right) \qquad (3.7)$$

$$\left|\bar{V}_{i,\Psi}\right|\left|\bar{V}_{j,\beta}\right|H_{ij}^{\Psi\beta}\sin\left(\delta_{i,\Psi}-\delta_{j,\beta}\right)\approx H_{ij}^{\Psi\beta}\sin\left(\delta_{i,\Psi}-\delta_{j,\beta}\right) \tag{3.8}$$

$$\sum_{j=1}^{n_{bus}}H_{ij}^{\Psi\beta}\left(\delta_{i,\Psi}-\delta_{j,\Psi}\right)\approx H_{ij}^{\Psi\beta}\delta_{j,\Psi} \tag{3.9}$$

Where H can be replaced by G or B depending on (3.3) and (3.4); Cosines in (3.5) and sines (3.6) were eliminated by approximation 1. In this work, the frequency was assumed close to the nominal value and its effect on the lines impedances was neglected. By applying approximations 1 and 2 to eqs. (3.3) and (3.4), the linearized droop three-phase power flow model for droop-controlled AMG can be given as:

$$P_i^{G,\Psi}-P_i^{L,\Psi}=\sum_{j=1}^{n_{bus}}\begin{bmatrix}\begin{pmatrix}\boldsymbol{G}_{ij}^{\Psi,a:c}\circ\boldsymbol{R}_1^{\Psi,a:c}.\boldsymbol{V}_j^{a:c}\\+\boldsymbol{G}_{ij}^{\Psi,a:c}.\boldsymbol{R}_2^{\Psi,a:c}\boldsymbol{\delta}_j^{a}\end{pmatrix}\\+\begin{pmatrix}-\boldsymbol{B}_{ij}^{\Psi,a:c}\circ\boldsymbol{R}_1^{\Psi,a:c}.\boldsymbol{\delta}_j^{a:c}\\+\boldsymbol{B}_{ij}^{\Psi,a:c}.\boldsymbol{R}_2^{\Psi,a:c}\end{pmatrix}\end{bmatrix} \tag{3.8}$$

$$Q_i^{G,\Psi}-Q_i^{L,\Psi}=\sum_{j=1}^{n_{bus}}\begin{bmatrix}-\begin{pmatrix}\boldsymbol{B}_{ij}^{\Psi,a:c}\circ\boldsymbol{R}_1^{\Psi,a:c}.\boldsymbol{V}_j^{a:c}\\+\boldsymbol{B}_{ij}^{\Psi,a:c}.\boldsymbol{R}_2^{\Psi,a:c}\boldsymbol{\delta}_j^{a}\end{pmatrix}\\+\begin{pmatrix}-\boldsymbol{G}_{ij}^{\Psi,a:c}\circ\boldsymbol{R}_1^{\Psi,a:c}.\boldsymbol{\delta}_j^{a:c}\\+\boldsymbol{G}_{ij}^{\Psi,a:c}.\boldsymbol{R}_2^{\Psi,a:c}\end{pmatrix}\end{bmatrix} \tag{3.9}$$

$\boldsymbol{V}_j^{a:c}=[V_j^a\ V_j^b\ V_j^c]$ and $\boldsymbol{\delta}_j^{a:c}=[\delta_j^a\ \delta_j^b\ \delta_j^c]$. In this work, "$\circ$" and "." represent the Hadamard and scalar multiplication respectively. $\boldsymbol{R}_1^{\Psi,a:c}$ and $\boldsymbol{R}_2^{\Psi,a:c}$ are the row vector of rotation based on cosine and sines of the phase deviation. The matrices contained these vectors are:

$$\mathbf{R}_1^{a:c,a:c}=\begin{bmatrix}1&-0.5&-0.5\\-0.5&1&-0.5\\-0.5&-0.5&1\end{bmatrix} \tag{3.10}$$

$$\mathbf{R}_2^{a:c,a:c}=\begin{bmatrix}0&0.866&-0.866\\-0.866&0&0.866\\0.866&-0.866&0\end{bmatrix} \tag{3.11}$$

Similar to [15], in this work the voltage angle of phase A at bus #1 is taken as the reference and set by $\delta_1^a=0$, which allows for the consideration of the system frequency as one of the power flow variables while maintaining the number of equations equal to the number of variables. The DG units are also assumed to have negative sequence compensators that mitigate the voltage unbalances at the PCC (i.e., the DGs produce balanced voltages despite the system unbalance) [15]. Moreover, the

summation of the three-phase power generation should respect the droop relations. These characteristics can be expressed as following:

$$|\bar{V}_i^a| = |\bar{V}_i^b| = |\bar{V}_i^c| \tag{3.12}$$

$$\delta_i^a = \delta_i^b + \frac{2\pi}{3} = \delta_i^c - \frac{2\pi}{3} \tag{3.13}$$

$$P_i^{G,a} = P_i^{G,3\Phi} - P_i^{G,b} - P_i^{G,c} \tag{3.14}$$

$$Q_i^{G,a} = Q_i^{G,3\Phi} - Q_i^{G,b} - Q_i^{G,c} \tag{3.15}$$

3.3 Validation of the Algorithm

In the order to evaluate the effectiveness of the proposed LPF model, balanced an unbalanced radial distribution have been used and the results of the developed model were compared with the results of the nonlinear models in [15] and [30], denoted NTR and MBF, respectively.

Here it is worth noting that the MBF algorithm of [30] does not consider unbalanced cases. All case studies were performed in MATLAB environment on a PC equipped with 2.50GHz Intel Core i7 processor with 8GB of RAM. In this work, the well-known 33-bus system [15], [31] and the large scale 10476-bus [73] were used for the simulation under balanced criteria; while in the case of unbalanced system 25-bus [15] system has been chosen. Similar to [15], in this work the system loads of 25-bus have been modified to make the system heavily unbalanced (by decreasing phase A by 20% and increasing Phase C load by 20%). The tolerances were set at 10^{-6} for NTR and similar value to MBF.

The DG units' configuration and location are given in Table G. 1 of Appendix G. First, to illustrate the computation performance, Table 3. 1 summarize the average runtime (computed over 10 runs) and the number of iterations of required for NTR [15] and MBF [30].

TABLE 3. 1: Average runtime (ms) and number of iterations of proposed linear model, MBF [30] and NTR [15]

Test system	MBF		NTR		Proposed LPF
	(ms)	(inner/outer)	(ms)	(iter.)	(ms)
33-bus	112.6	327/93	516.2	5	8.2
10497-bus	un-convergence		un-convergence		102052.2
25-bus	unsupportable		3414.1	5	30.9

It is worth noting that the proposed LPF is solved by matrix inversion and as such does not require any iterations to solve the power flow, which explained its superior computational performance compared to NTR and MBF under both balanced or unbalanced conditions. In the case of the large-scale AMG, both MBF [30] and NTR [15] could not handle the system dimensions and end up with the un-convergence of the simulation.

In the order to evaluate the accuracy of the proposed LPF, Table 3. 2 summarize the accuracy validation, by comparing the error indices i.e. maximum error in voltage magnitude, phase angle, power generation and total losses with respect to the result derived by MBF [30] and NTR [15].

TABLE 3. 2: Proposed LPF error indices compared to MBF [30] **and NTR [15] for 33-bus balanced and 25-bus unbalanced AMG.**

Error indices		**33-bus** Balanced system		**25-bus** Unbalanced system
		MBF & LPF	NTR & LPF	NTR & LPF
$\|V\|^{max}$	(p.u.)	7.84×10^{-4}	8.25×10^{-4}	3.48×10^{-3}
$\|\delta\|^{max}$	(deg.)	2.98×10^{-2}	3.02×10^{-2}	1.32×10^{-1}
$\|P^G\|^{max}$	(p.u.)	1.86×10^{-2}	1.85×10^{-2}	4.04×10^{-3}
$\|Q^G\|^{max}$	(p.u.)	1.27×10^{-2}	1.34×10^{-2}	3.48×10^{-3}
$P^{loss,total}$	(p.u.)	9.72×10^{-4}	9.77×10^{-4}	9.08×10^{-4}
$Q^{loss,total}$	(p.u.)	1.49×10^{-3}	1.48×10^{-3}	1.02×10^{-4}

Then, Figure 3. 1 and Figure 3. 2 illustrate the comparison of voltage profile between proposed LPF and the other algorithms (i.e. MBF [30] and NTR [15]) under balanced and unbalanced, respectively.

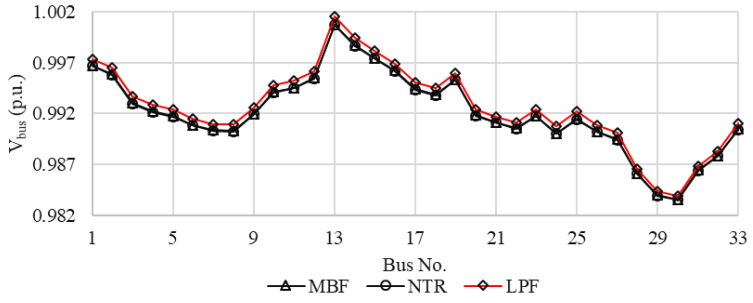

FIGURE 3. 1: Voltage profile for 33-bus AMG system as calculated by MBF [30]**, NTR [15] and the proposed LPF ($f^{MBF} \approx f^{NTR}$ = 0.9198 and f^{LPF}= 0.9208)**

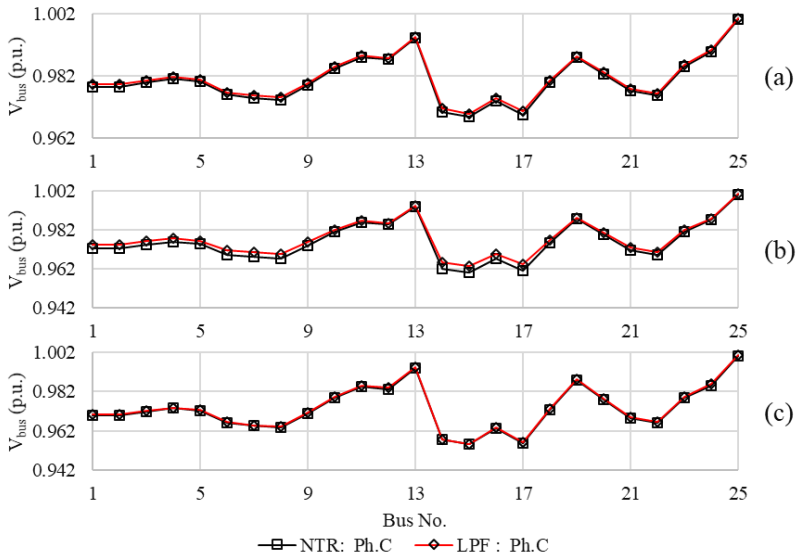

FIGURE 3. 2: Voltage profile for unbalanced 25-bus unbalanced IMG as calculated by NTR [15] and by the proposed LPF ($f^{NTR,3\Phi}$= 0.9978 and $f^{LPF,3\Phi}$ = 0.9981): (a) Phase A, (b) Phase B and (c) Phase C

Despite its computational superiority, and as can be expected, there is some deviation between the results obtained by the proposed LPF model and those obtained by MBF [30] and NTR [15] due to the linearization approximations applied. Nevertheless, the deviations were limited under the range of 10^{-3}~10^{-4}.

Figure 3. 3 shows the voltage profile of the 10476-bus droop-controlled AMG. This result demonstrates the capability of the proposed LPF to handle the large-scale droop-controlled AMG system comprising up to a thousand bus, where NTR [15] and MBF [30] fail to converge under these conditions.

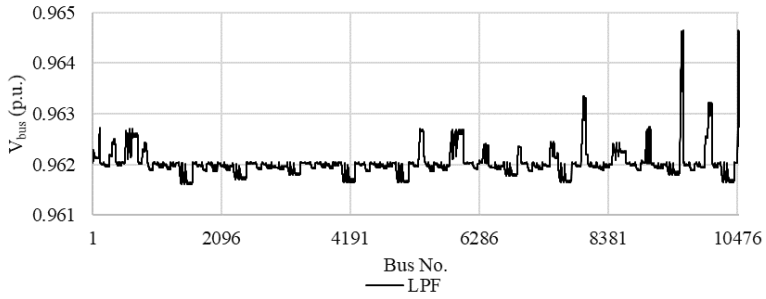

FIGURE 3. 3: Voltage profile of 10476-bus AMG system (f= 0.9952)

Finally, in the order to validate the results for the case 10476-bus delivered by the proposed LPF, the proposed Z_{bus} method in chapter 2 is used. In this case, the maximum difference in voltage between both method is found at 1.42×10^{-4} p.u., while in term of the phase angle the maximum difference is 1.95×10^{-3} degree.

3.4 Conclusion

A new LPF model for droop-controlled AMG was proposed in this work. The proposed model respects the droop-controlled AMG system special philosophy of operation and allow for the consideration of the unbalanced conditions typically present in practical distribution systems. The accuracy and effectiveness of the proposed algorithm has been validated through several balanced and unbalanced case studies applied on the 33-bus, 10476-bus and 25-bus test systems and comparing its results to those of two state-of-the art algorithms in [15] and [30]. The results demonstrated the computational superiority of proposed LPF model and its ability to provide fast power flow solutions. The deviation between the proposed LPF model solutions and those obtained by the nonlinear models of the literature were found to be under the range of $10^{-3} \sim 10^{-4}$. The proposed LPF is also able to handle a large-scale network that existing nonlinear model cannot solve. The proposed linear model can be effective in enabling linear optimization applications for droop-controlled AMGs.

Chapter 4 MILP Model for MG's Optimum Operation

Y. Vilaisarn, M. Moradzadeh, and M. Abdelaziz, "An MILP formulation for the optimum operation of AC microgrids with hierarchical control". *Published in International Journal of Electrical Power Energy Systems, September 2021.*

Résumé

Un modèle linéaire qui sert à déterminer le fonctionnement a l'état optimal du micro-réseau est une clé de solution important pour des nombreuses applications en temps réel et stochastiques. Néanmoins, nombreux existant modèles ne prennent pas en compte les détails du contrôle hiérarchique nécessite pour opérer le micro-réseau. Cet omet peut conduire à des solutions infaisables et sous-optimales. Dans ce travail, un nouveau modèle de programmation linéaire en nombres entiers (i.e., MILP) pour déterminer le fonctionnement à l'état optimal des micro-réseaux triphasés avec contrôle hiérarchique est proposé. Tout d'abord, le modèle non linéaire est dérivé pour tenir compte de la philosophie de fonctionnement du micro-réseau à l'état connecté et l'état isolé du réseau principal. Ensuite, une approche de linéarisation est adoptée à ce modèle non linéaire afin de le transformer à un modèle linéaire MILP. L'efficacité du modèle linéaire proposé est validée par plusieurs études de cas portant sur des systèmes de test équilibrés et déséquilibrés. De plus, une évaluation détaillée des erreurs est menée pour justifier le modèle proposé.

Abstract

An accurate linear model for the optimal operation of the microgrid is a key enabling solution for many real time and stochastic applications. Nonetheless, many of the existing microgrid's optimal power flow models fall short in considering the details of the microgrid hierarchical control, which can lead to infeasible and suboptimal solutions. In this work, a new mixed integer linear programing (MILP) model for the optimal operation of three phase microgrids with hierarchical control is proposed. First, the nonlinear formulation is derived to account for the microgrid philosophy of operation in both grid connected and islanding modes of operation. Subsequently, a linearization approach is adopted to the derived nonlinear model to transform it into the required MILP formulation. The effectiveness of the proposed model is validated through several case studies considering balanced and unbalanced test systems. Additionally, a detailed error assessment is conducted to justify the proposed model.

4.1 Introduction

A microgrid can be disconnected from the main grid and operated in the islanding mode due to intentional (scheduled) or unintentional events (unscheduled). In this islanding mode of operation, the microgrid's local generation and energy storage resources are controlled to supply its demand. On the other hand, a microgrid can also be operated in the grid connected mode to provide ancillary services to the main grid in its upstream. To optimally control the operation of the microgrid, the hierarchical control structure is adopted. As explained in the literature in chapter 1, the hierarchical control structure comprises multiple layers. Typically, the lower-level and intermediate level are employed for controlling the DG units and for maintaining the microgrid's frequency and voltage within the permissible range. On the other hand, higher-level deal with the economic and technical objectives, wherein the optimization of the operation of the microgrid resources and loads is based on the required AC optimal power flow (ACOPF) problem which is discussed in this chapter.

In chapter 1, it was shown that there is a need to account for the operation and control of the microgrid with primary and supervisory secondary control in the ACOPF model in order to deliver accurate and feasible solutions. In this sense, seeking to overcome the mentioned limitations of the existing literature, in this chapter we seek to develop an ACOPF formulation for AC microgrids with hierarchical control to simultaneously consider: 1) both grid-connected and islanded modes of operation; 2) balanced and unbalanced operation of microgrids; 3) the primary and secondary control layers of the DG units in the islanded mode; 4) general models of dispatchable resources, non-dispatchable resources and the energy storage; 5) the time coupling constraints of the resources and storage located in the microgrid. To this end, first we develop a new MINLP formulation for the optimal operation of AC microgrids with hierarchical control. Subsequently, the proposed MINLP formulation is linearized and a MILP formulation is extracted, which can be solved by commercial optimization solvers.

The remainder of this chapter is organized as follows: First, the proposed MINLP formulation to model the optimal operation of the unbalanced AC microgrid is presented in Section 4.2. Subsequently, proposed MINLP model is linearized and the proposed MILP model is introduced in Section 4.3. The numerical simulation results are given in Section 4.4. Finally, Section 4.5 concludes the chapter.

4.2 MINLP Problem Formulation

In this section, the problem for the optimal operation of a three phase microgrid is formulated as an MINLP problem. The proposed formulation accounts for both islanded and grid connected modes of operation, wherein the operation mode is defined by the status of the island isolating switch (ISW) located at the microgrid's PCC as shown in Figure 4. 1. b_t^m denotes the status of ISW along the planning horizon Ω_T; if $b_t^m = 0$, the microgrid operates in grid-connected mode, and if $b_t^m = 1$, the microgrid operates in islanding mode. This allows the problem to consider the objective function and constraints pertaining to the microgrid's operation mode. In this work, the load and the generation are modelled using the method described in Appendix B [78]. The objective function and the related constraints for the MINLP model are mathematically formulated in the following subsections.

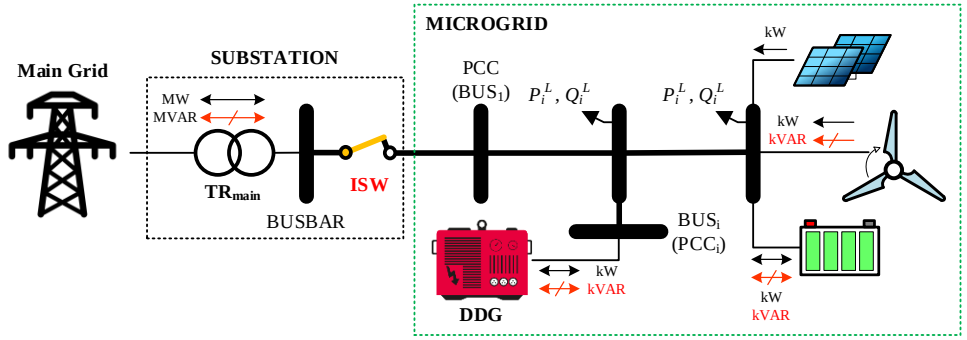

FIGURE 4. 1: Basic scheme of the microgrid

4.2.1 Objective function

The objective function given by (4.1) is comprised of four terms aiming to minimize the total operation cost over the planning horizon Ω_T. The first term in (4.1) represents the cost of power exchange between the microgrid and the main grid as determined by (4.2). The second term, given by (4.3), refers to the fuel cost consumed by the DDG units [79]. These two terms are restricted for the grid connected mode of the microgrid. The third term represents the cost of load curtailment during islanding mode of the microgrid, given by (4.4) [26]. The last term characterizes the voltage violation index used for improving the voltage quality of the microgrid during both operation modes by (4.5).

$$\min_{\boldsymbol{X}^{MINLP,3\Phi}} \sum_{t\in\Omega_T}[(C_t^{PCC} + C_t^{DDG})(1 - b_t^m) + C_t^{CURT} b_t^m + C_t^{VI}] \tag{4.1}$$

$$C_t^{PCC} = S_{base}\left(\sigma_t^{PCC} \sum_{i\in\Omega_{PCC}} P_{i,t}^{PCC,3\Phi}\right)\Delta t \qquad ,\forall t \in \Omega_T \tag{4.2}$$

$$C_t^{DDG} = S_{base}\left(\sum_{i\in\Omega_{DDG}} CR_i^{DDG} P_{i,t}^{DDD,3\Phi} \sigma^{fuel}\right)\Delta t \qquad ,\forall t \in \Omega_T \qquad (4.3)$$

$$C_t^{CURT} = S_{base}\left(\sigma^{curt} \sum_{i\in\Omega_{BUS}} b_{i,t}^{curt} w_i^{load} P_{i,t}^{L,3\Phi}\right)\Delta t \qquad ,\forall t \in \Omega_T \qquad (4.4)$$

$$C_t^{VI} = V_{base}\left(PC^{VI}\left[\sum_{i\in\Omega_{BUS}}\sum_{\Psi\in\mathcal{F}}\left(\left|\begin{matrix}(1-b_t^m)V_{spec}^{GC} + b_t^m V^{**} \\ -V_{i,\Psi,t}\end{matrix}\right|\right)\right]\right)\Delta t \qquad ,\forall t \in \Omega_T \qquad (4.5)$$

4.2.2 Constraints

The inequality (4.6) is adopted to have the voltage magnitude of different buses restricted to voltage magnitude constraints. Eq. (4.7) ensures the quality of power supply by limiting the load curtailment duration. Then, inequality (4.8) is used to limit the number of load shedding switching cycles for each load at bus i. Finally, the inequality (4.9) ensures $b_{i,t}^{curt}$ activate only for islanded mode.

$$V^{min} \le V_{i,\Psi,t} \le V^{max} \qquad ,\forall i \in \Omega_{BUS}, \forall \Psi \in \mathcal{F}, \forall t \in \Omega_T \qquad (4.6)$$

$$\sum_{t\in\Omega_T} b_{i,t}^{curt} \le T_i^{curt} \qquad ,\forall i \in \Omega_{BUS} \qquad (4.7)$$

$$\sum_{t\in\Omega_T} \left|b_{i,t}^{curt} - b_{i,t-1}^{curt}\right| \le 2N_i^{curt} \qquad ,\forall i \in \Omega_{BUS} \qquad (4.8)$$

$$0 \le b_{i,t}^{curt} \le b_t^m \qquad ,\forall i,k \in \Omega_{BUS}, \forall t \in \Omega_T \qquad (4.9)$$

In the following subsections, the constraints corresponding to the modeling of the microgrid, and the components located inside and outside the microgrid (i.e., DDG, ESS, and substation) are described.

4.2.2.1 Power flow constraints

The three-phase power flow model is used to model the microgrid given by (4.10) to (4.13). The model takes into account the mutual inductance and interphase capacitance among the different phase [46].

$$P_{i,\Psi,t} = V_{i,\Psi,t}\sum_{j\in\Omega_{BUS}}\sum_{\beta\in\mathcal{F}} V_{i,\Psi,t}\left(\begin{matrix} G_{ij}^{\Psi\beta}\cos\begin{pmatrix}\delta_{i,\Psi,t} \\ -\delta_{i,\beta,t}\end{pmatrix} \\ +B_{ij}^{\Psi\beta}\sin\begin{pmatrix}\delta_{i,\Psi,t} \\ -\delta_{i,\beta,t}\end{pmatrix}\end{matrix}\right) = \left(\begin{matrix} P_{i,\Psi,t}^{PCC} + P_{i,\Psi,t}^{DDG} \\ +\left(\begin{matrix}P_{i,t}^{WT,3\Phi} + P_{i,t}^{PV,3\Phi} \\ +P_{i,t}^{dch,3\Phi} \\ -\eta_{ESS_i} P_{i,t}^{ch,3\Phi}\end{matrix}\right)\Big/3 \\ -P_{i,\Psi,t}^{L}(1-b_t^{curt})\end{matrix}\right)$$
$$,\forall i \in \Omega_{BUS}, \forall \Psi \in \mathcal{F}, \forall t \in \Omega_T \qquad (4.10)$$

$$Q_{i,\Psi,t} = V_{i,\Psi,t} \sum_{j\in\Omega_{BUS}} \sum_{\beta\in\mathcal{F}} V_{i,\Psi,t} \begin{pmatrix} -B_{ij}^{\Psi\beta} \cos\begin{pmatrix} \delta_{i,\Psi,t} \\ -\delta_{i,\beta,t} \end{pmatrix} \\ +G_{ij}^{\Psi\beta} \sin\begin{pmatrix} \delta_{i,\Psi,t} \\ -\delta_{i,\beta,t} \end{pmatrix} \end{pmatrix} = \begin{pmatrix} +Q_{i,\Psi,t}^{PCC} + Q_{i,\Psi,t}^{DDG} \\ +\left(Q_{i,t}^{WT,3\Phi} + Q_{i,t}^{ESS,3\Phi}\right)/3 \\ -Q_{i,\Psi,t}^{L}(1 - b_t^{curt}) \end{pmatrix}$$

$$,\forall i \in \Omega_{BUS}, \forall \Psi \in \mathcal{F}, \forall t \in \Omega_T \qquad (4.11)$$

$$P_{k,\Psi,t}^{br} = V_{i(k),\Psi,t} \sum_{\beta\in\mathcal{F}} \left(V_{i(k),\beta,t} - V_{j(k),\beta,t}\right) \begin{pmatrix} g_{i(k)j(k)}^{\Psi\beta} \cos\left(\delta_{i(k),\Psi,t} - \delta_{j(k),\Psi,t}\right) \\ +b_{i(k)j(k)}^{\Psi\beta} \sin\left(\delta_{i(k),\Psi,t} - \delta_{j(k),\Psi,t}\right) \end{pmatrix}$$

$$,\forall k \in \Omega_{LIN}, \forall \Psi \in \mathcal{F}, \forall t \in \Omega_T \qquad (4.12)$$

$$Q_{k,\Psi,t}^{br} = V_{i(k),\Psi,t} \sum_{\beta\in\mathcal{F}} \left(V_{i(k),\beta,t} - V_{j(k),\beta,t}\right) \begin{pmatrix} g_{i(k)j(k)}^{\Psi\beta} \sin\left(\delta_{i(k),\Psi,t} - \delta_{j(k),\Psi,t}\right) \\ -b_{i(k)j(k)}^{\Psi\beta} \cos\left(\delta_{i(k),\Psi,t} - \delta_{j(k),\Psi,t}\right) \end{pmatrix}$$

$$,\forall k \in \Omega_{LIN}, \forall \Psi \in \mathcal{F}, \forall t \in \Omega_T \qquad (4.13)$$

$$\sqrt{\left(P_{k,\Psi,t}^{br}\right)^2 + \left(Q_{k,\Psi,t}^{br}\right)^2} \leq I_k^{br,max} V_{i(k),\Psi,t} \qquad ,\forall k \in \Omega_{LIN}, \forall \Psi \in \mathcal{F}, \forall t \in \Omega_T \qquad (4.14)$$

The constraints (4.10) and (4.11) defines the power injected to the i^{th} bus of the microgrid which are the well-known node-based three phase power flow equations. Then, (4.12) and (4.13) define respectively the active and reactive power flowing along the branch k in the microgrid [15]. It is worth noting that, $i(k)$ and $j(k)$ denote bus i located at the upstream of branch k and bus j for the downstream of the branch k, respectively. Eq. (4.14) is the quadratic constraints representing the limitation over the transmission line ampacity.

4.2.2.2 DDG operation constraints

The DDG units are typically interfaced with power electric converters and passive output filters [15]. In this study, the hierarchical control structure is employed to control the operation of DDG units. Figure 4. 2(a) illustrates the basic scheme of the DDG unit with hierarchical control. The control structure involves multi-layers i.e., internal voltage/current control, primary droop control, and secondary control layers. The synchronous reference frame phase-locked loop (SRF-PLL) is used to measure the frequency of the microgrid [16]. More detail about the DDG's control structure and their functionality can be found in [49], [80].

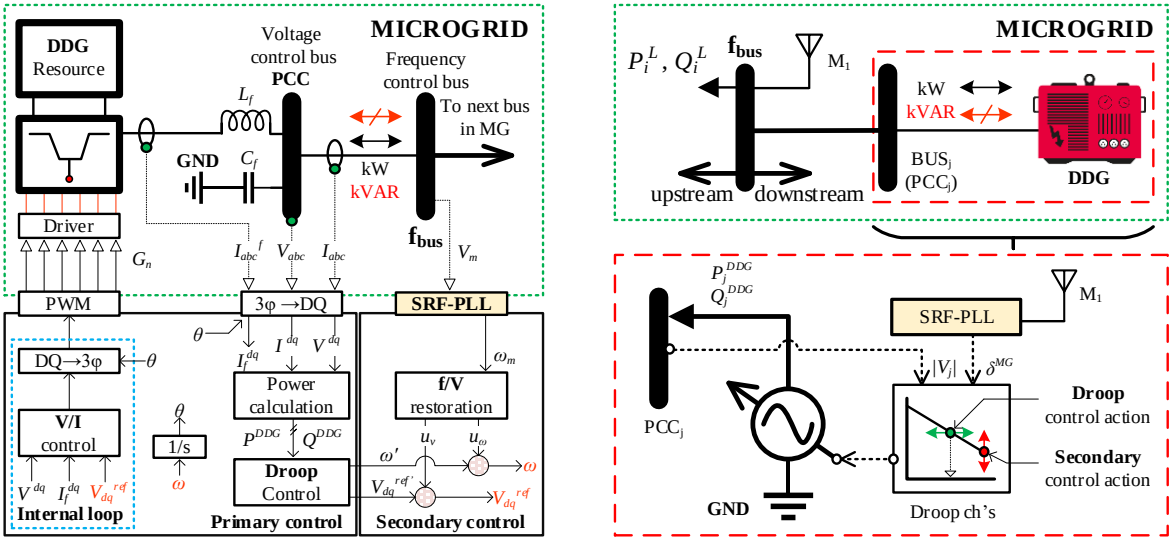

FIGURE 4. 2: (a) Basic scheme of the microgrid (b) Steady-state model of DDG unit's operation with primary and secondary control under IS mode

In this work, the steady state model is adopted for dealing with the operation constraints of the DDG units [15], [16]. Figure 4. 2(b) shows the steady state model for the DDG units operated with the primary droop and secondary controls. This model is sufficient for determining the electrical variables of the PCC bus where the DDG unit is connected, while respecting to the DDG unit's internal circuit and the control structure.

As can be seen in the Figure 4. 2(b), the operation of the DDG unit, their internal circuits and its control structure can be modeled as a voltage source where the frequency and the voltage are controlled via the droop control and restored through the secondary control. Following this definition, the DGG considering the primary droop and secondary control in the steady state can be modeled as expressed by (4.15) and (4.16):

$$\omega = \omega^* - m^p P^{DDG} + u_\omega \tag{4.15}$$

$$V = V^* - n^q Q^{DDG} + u_v \tag{4.16}$$

Where, the output signals u_ω and u_v are delivered through a proportional-integral (PI) controller of the secondary layer and dependent to the measured frequency ω^m and voltage V^m as expressed by:

$$u_\omega = k^{p\omega}(\omega^* - \omega^m) + k^{i\omega}\int(\omega^* - \omega^m)dt \tag{4.17}$$

$$u_v = k^{pv}(V^{**} - V^m) + k^{iv}\int(V^{**} - V^m)dt \tag{4.18}$$

As the proposed problem is formulated to model the steady state condition, the proportional term for (4.17) and (4.18) can be eliminated (in steady state: $\omega^* - \omega^m = 0$ and $V^{**} - V^m = 0$) [16]. Nonetheless, the same approach could not be applied to the integrator part of the (4.17) and (4.18). Let $u^{\omega,int}$ denotes the integrator part of (4.17) and $u^{v,int}$ for (4.18), as such $u_\omega = u^{\omega,int}$ and $u_v = u^{v,int}$. As explained in [16], $u^{\omega,int}$ can be determined using $u^{\omega,int} = -k^{i\omega}(\delta^{MG} - \pi/2)$ under steady state condition. On the other hand, in the steady state condition the voltage of the voltage-controlled bus V^m is fixed by $V^{**} = V^m$ and there is no need to consider V^m to be a variable in the proposed problem. This allows us to consider $u^{v,int}$ to be a variable to be determined in the proposed optimization problem. As such, the primary droop and secondary control are considered with the DDG model in the proposed model. Let f_{bus} denotes the i^{th} bus where the secondary frequency control acts. The DDG unit considering three phase microgrid can be modeled by (4.19) to (4.23):

$$P_{i,\Psi,t}^{DDG} = \begin{cases} \left[-ki^{\omega}\left(\delta_{\Psi,t}^{MG} - \pi/2\right)/m_i^p\right]b_t^m + (1 - b_t^m)P_{i,t}^{DDG,3\Phi}/3, & \Psi = a \\ \left[-ki^{\omega}\left(\delta_{\Psi,t}^{MG} + \pi/6\right)/m_i^p\right]b_t^m + (1 - b_t^m)P_{i,t}^{DDG,3\Phi}/3, & \Psi = b \\ \left[-ki^{\omega}\left(\delta_{\Psi,t}^{MG} - 7\pi/6\right)/m_i^p\right]b_t^m + (1 - b_t^m)P_{i,t}^{DDG,3\Phi}/3, & \Psi = c \end{cases}$$
$$,\forall i \in \Omega_{DDG}, \forall t \in \Omega_T \tag{4.19}$$

$$Q_{i,\Psi,t}^{DDG} = \left[\left(V_i^* - V_{i,\Psi,t} + u_{i,\Psi,t}^{v,int}\right)/n_i^q\right]b_t^m + (1 - b_t^m)Q_{i,t}^{DDG,3\Phi}/3$$
$$,\forall i \in \Omega_{DDG}, \forall \Psi \in \mathcal{F}, \forall t \in \Omega_T \tag{4.20}$$

$$P_{i,t}^{DDG\_3\Phi} = \sum_{\Psi\in\mathcal{F}} P_{i,\Psi,t}^{DDG} \qquad ,\forall i \in \Omega_{DDG}, \forall t \in \Omega_T \tag{4.21}$$

$$Q_{i,t}^{DDG\_3\Phi} = \sum_{\Psi\in\mathcal{F}} Q_{i,\Psi,t}^{DDG} \qquad ,\forall i \in \Omega_{DDG}, \forall t \in \Omega_T \tag{4.22}$$

$$V_{i,\Psi,t}b_t^m = V_i^{**}b_t^m \qquad ,\forall i \in \Omega_{DDG}, \forall \Psi \in \mathcal{F}, \forall t \in \Omega_T, \tag{4.23}$$

The constraint (4.19) and (4.20) defines the active and reactive power generated by the DDG units. The first terms of the constraints refer to the secondary control mode of DDGs in the islanding operation mode, while their second terms represent the PQ mode for the grid connected operation mode. The binary input parameter b_t^m is used to activate the terms of (4.19) and (4.20) according to the microgrid operation mode. In this work, the active and reactive droop gains of the DDG units are determined using the capacity-based method and expressed by (4.24) and (4.25). By using this definition, the load in the system can be shared in proportion to the capacity of the DDG units [26],[54].

$$m_i^p = \Delta\omega / P_i^{DDG,max} \qquad ,\forall i \in \Omega_{DDG} \tag{4.24}$$

$$n_i^q = \Delta V / 2\mathrm{Q}_i^{DDG,max} \qquad ,\forall i \in \Omega_{DDG} \tag{4.25}$$

Then, the constraints (4.21) and (4.22) defines the three-phase active and reactive power flowing to the bus where the DDG is connected. The constraints (4.23) define the voltage magnitude restored by the secondary control of the DDGs.

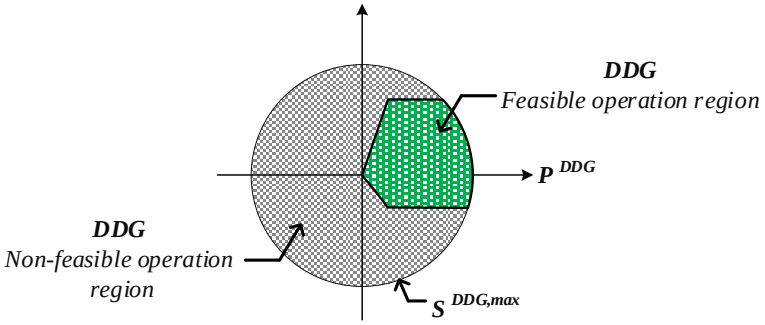

FIGURE 4. 3: Feasible operation region of the DDG units in IS and GC mode

With the interfaced power electronic converter, the DDG units is allowed to control the reactive power by producing to or receiving from the microgrid [80], [81]. Figure 4. 3 shows the feasible operating region of the DDG units and the following constraints defines this region accurately.

$$P_i^{DDG,min} \le P_{i,t}^{DDG,3\Phi} \le P_i^{DDG,max} \qquad ,\forall i \in \Omega_{DDG}, \forall t \in \Omega_T \tag{4.26}$$

$$Q_i^{DDG,min} \le Q_{i,t}^{DDG,3\Phi} \le Q_i^{DDG,max} \qquad ,\forall i \in \Omega_{DDG}, \forall t \in \Omega_T \tag{4.27}$$

$$-P_{i,t}^{DDG,3\Phi}\, tg\left(\cos^{-1} PF_i^{DDG,4th}\right) \le Q_{i,t}^{DDG,3\Phi} \le P_{i,t}^{DDG,3\Phi}\, tg\left(\cos^{-1} PF_i^{DDG,1st}\right) \qquad ,\forall i \in \Omega_{DDG}, \forall t \in \Omega_T \tag{4.28}$$

$$\sqrt{\left(P_{i,t}^{DDG,3\Phi}\right)^2 + \left(Q_{i,t}^{DDG,3\Phi}\right)^2} \le S_i^{DDG,max} \qquad ,\forall i \in \Omega_{DDG}, \forall t \in \Omega_T \tag{4.29}$$

where (4.26) and (4.27) limit the active and reactive power while the constraint (4.28) guarantees the operation of the DDG unit respecting to the minimum power factor set. Finally, (4.29) outlines the boundary of the feasible region for limiting the active and reactive power with respect to the rating of the DDG. More details regarding the derivation for the operation feasible region can be found in the Appendix D.

4.2.2.3 Energy storage operational constraints

In this study, a general model is employed for the ESSs that is not limited to any particular energy storage technology. The ESSs are interfaced with power conversion systems (PCSs) to control the ESSs active and reactive powers in accordance with the connected network requirements [82]. Accordingly, the ESS can be utilized to provide ancillary services such as voltage support, frequency regulation, grid stabilization, etc. In this work, the ESSs are supposed to operate at four-quadrant areas. To this end, the ESS active and reactive powers are limited via the quadratic function as illustrated in Figure 4. 4.

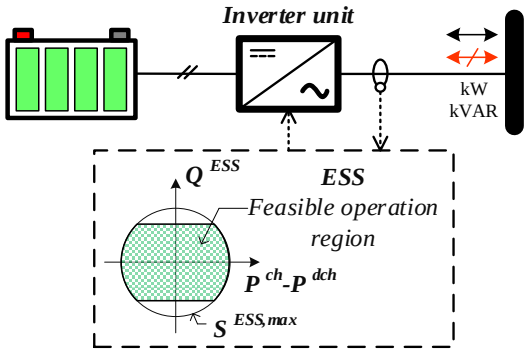

FIGURE 4. 4: Principle of the ESS units

Considering three phase microgrid, the ESS, therefore, can be model using [82]-[83].

$$0 \le P_{i,t}^{dch,3\Phi} \le P_i^{ESS,max} b_{i,t}^{ESS} \qquad ,\forall i \in \Omega_{EES}, \forall t \in \Omega_T \quad (4.30)$$

$$0 \le P_{i,t}^{ch,3\Phi} \le P_i^{ESS,max} \left(1 - b_{i,t}^{ESS}\right) \qquad ,\forall i \in \Omega_{EES}, \forall t \in \Omega_T \quad (4.31)$$

$$P_i^{ESS,min} \le Q_{i,t}^{ESS,3\Phi} \le Q_i^{ESS,max} \qquad ,\forall i \in \Omega_{ESS}, \forall t \in \Omega_T \quad (4.32)$$

$$\sqrt{\left(P_{i,t}^{dch,3\Phi} - P_{i,t}^{ch,3\Phi}\right)^2 + \left(Q_{i,t}^{ESS,3\Phi}\right)^2} \le S_i^{ESS,max} \qquad ,\forall i \in \Omega_{ESS}, \forall t \in \Omega_T \quad (4.33)$$

$$E_{i,t}^{ESS} = \begin{cases} SOC_i^0 E_i^{ESS,max} + \left(\eta_i^{ESS} P_{i,t}^{ch,3\Phi} - P_{i,t}^{dch,3\Phi}\right)\Delta t \,, t = 1 \\ E_{i,t-1}^{ESS} + \left(\eta_i^{ESS} P_{i,t}^{ch,3\Phi} - P_{i,t}^{dch,3\Phi}\right)\Delta t \qquad , t \ge 2 \end{cases} \qquad ,\forall i \in \Omega_{EES}, \forall t \in \Omega_T \quad (4.34)$$

$$E_i^{ESS,min} \le E_{i,t}^{ESS} \le E_i^{ESS,max} \qquad ,\forall i \in \Omega_{EES}, \forall t \in \Omega_T \quad (4.35)$$

$$E_{i,t}^{ESS} \ge SOC_i^0 E_i^{ESS,max} \qquad ,\forall i \in \Omega_{EES}, t = N_T \quad (4.36)$$

The ESS charging and discharging powers are restricted by their rated power using (4.30) and (4.31). The output apparent power of the energy storage, connected through an inverter, is restricted by the maximum apparent power supplied/consumed of the inverter, denoted as $S_i^{ESS,max}$ (4.33). The ESS stored energy in each time segment, $E_{i,t}^{ESS}$, is updated based on its charging/discharging energy flows and the efficiency of the ESS (4.34). The efficiency η^{ESS} the round trip efficiency of the energy storage systems [84]-[85]. Although the stored energy level of the ESS is not affected by the consumed/supplied reactive power of the connected inverter, the amount of active power is dependent on it due to the line current limitations (4.33)-(4.34). The energy stored in the ESS is limited to its rated capacity and minimum stored energy (4.35). The ESSs are assumed to be initially charged up to $SOC_i^0 E_i^{ESS,max}$ and it must remain equal to or greater than the same amount of energy at the end of the planning horizon (4.36). In this work, the ESS units are assumed to be operated in power-controlled mode (PQ mode) formulated by (4.30) and (4.36) similar to the works in [26],[54],[82]. Nevertheless, as the ESS units are interfaced with power electronics inverters, the ESSs units are capable of operating in droop mode and accordingly with the secondary control. A case study is provided in subsection 4.4.5 to investigate the ESS operation with primary droop and secondary control layer.

4.2.2.4 Power exchange constraints

The constraints represent the power exchange between the microgrid, and the main grid can be given by (4.37) to (4.42). The constraints (4.37) and (4.38) defines the active and reactive three phase power at the PCC of microgrid. Then, the power imported from the main grid were enforced their limit by the rating of the transformer located in the substation and given by the quadratic equation (4.39). The constraint (4.40) limits the operation of the transformer above the minimum power factor allowable. Moreover, (4.41) and (4.42) specified the voltage magnitude and their phase angle at the PCC which imposed by the main grid during grid connected mode.

$$P_{i,t}^{PCC,3\Phi}(1-b_t^m) = (1-b_t^m)\sum_{\Psi\in\mathcal{F}} P_{i,\Psi,t}^{PCC} \qquad ,\forall i \in \Omega_{PCC}, \forall t \in \Omega_T \qquad (4.37)$$

$$Q_{i,t}^{PCC,3\Phi}(1-b_t^m) = (1-b_t^m)\sum_{\Psi\in\mathcal{F}} Q_{i,\Psi,t}^{PCC} \qquad ,\forall i \in \Omega_{PCC}, \forall t \in \Omega_T \qquad (4.38)$$

$$\sqrt{\left(P_{i,t}^{PCC,3\Phi}\right)^2 + \left(Q_{i,t}^{PCC,3\Phi}\right)^2} \le S_i^{TR,max} \qquad ,\forall i \in \Omega_{PCC}, \forall t \in \Omega_T \qquad (4.39)$$

$$-P_{i,t}^{PCC,3\Phi}\, tg\left(\cos^{-1} PF_i^{TR,4th}\right) \le Q_{i,t}^{PCC,3\Phi} \le P_{i,t}^{PCC,3\Phi}\, tg\left(\cos^{-1} PF_i^{TR,1st}\right) \qquad ,\forall i \in \Omega_{PCC}, \forall t \in N_T \qquad (4.40)$$

$$V_{i,\Psi,t}(1-b_t^m) = V_{spec}^{GC}(1-b_t^m) \qquad ,\forall i \in \Omega_{PCC}, \forall \Psi \in \mathcal{F}, \forall t \in \Omega_T \qquad (4.41)$$

$$\delta_{i,\Psi,t}^{PCC}(1-b_t^m) = \begin{cases} 0(1-b_t^m), & \Psi = a \\ -2\pi/3(1-b_t^m), & \Psi = b \\ +2\pi/3(1-b_t^m), & \Psi = c \end{cases} \qquad ,\forall i \in \Omega_{PCC}, \forall t \in \Omega_T \qquad (4.42)$$

4.3 Linearize Formulation

Solving the proposed MINLP model is computationally expensive due to the nonlinear terms found in (4.1) to (4.37). In this section, the nonlinear terms are linearized, and the proposed MILP model is derived.

4.3.1 Linearization Approach

4.3.1.1 Linearization of Absolute Value Operator

Eqs. (4.5) and (4.8) include absolute value operators which make the model non-linear. In order to linearize (4.5), the two following assumptions are made:

1) During the grid connected mode of the microgrid, the DDG units are operated in PQ mode and no DDG operates in PV mode in the system similar to the work in [52], [54]. Thus, there is no other type of resources can specify the voltage rather than V_{spec}^{GC} imposed by the upstream network. In this case, the voltage magnitude for all the buses located at downstream of the bus which interlinked with the upstream power grid (i.e., bus #1) are lower than V_{spec}^{GC}.

2) During the islanded mode of the microgrid, the DDG units are operated with secondary control layer. Then, a voltage restoration reference V^{**} is identically set for all DDG units allocated in the test system. In this case, the voltage of the system attempt to follow V^{**}.

As there is no bus in the microgrid that its voltage magnitude could overcome V_{spec}^{GC} or V^{**}, the absolute of voltage deviation can be omitted. Hence, the linearized voltage deviation index (4.5) can be modified as:

$$C_t^{VI,Lin} = V_{base}\left(PC^{VI}\left[\sum_{i\in\Omega_{BUS}}\sum_{\Psi\in\mathcal{F}}\left(\begin{matrix}(1-b_t^m)V_{GC}^{spec} + b_t^m V^{**} \\ -V_{i,\Psi,t}\end{matrix}\right)\right]\right)\Delta t \quad ,\forall t \in \Omega_T \qquad (4.43)$$

Nevertheless, if the aforementioned assumptions made to linearize (4.5) are not applicable, the method introduced in the Appendix E can be applied.

The same linearization method described in Appendix E can be adopted to linearize the absolute value operator employed in (4.8). In this case, a new binary variable z_i^{curt} is introduced for representing the term $\left|b_{i,t}^{curt} - b_{i,t-1}^{curt}\right|$. Then, the inequality constraints employed for linearizing (4.8) can be expressed by:

$$\sum_{t\in\Omega_T} z_{i,t}^{curt} \leq 2N_i^{curt} \qquad ,\forall i \in \Omega_{BUS} \tag{4.44}$$

$$b_{i,t}^{curt} - b_{i,t-1}^{curt} \leq z_{i,t}^{curt} \qquad ,\forall i \in \Omega_{BUS}, \forall t \in \Omega_T \tag{4.45}$$

$$-b_{i,t}^{curt} + b_{i,t-1}^{curt} \leq z_{i,t}^{curt} \qquad ,\forall i \in \Omega_{BUS}, \forall t \in \Omega_T \tag{4.46}$$

The constraints (4.45) and (4.46) are adopted to force $z_{i,t}^{curt}$ to be "1" when there is a transition between load shedding and power supply for the load in the bus i. Otherwise, z_i^{curt} is forced to be zero using (4.44) to (4.46).

4.3.1.2 Linearization of power flow and line flow

In (4.10) and (4.11), with the production of voltage magnitude and trigonometric i.e., sines and cosines the non-linearity has been introduced in these equations. In this case, two linear approximation is employed for these equations:

Approximation #1: This approximation technique deals with the non-linearity introduced by the trigonometric sine and cosine functions and the deviation between the phase angle $\theta_{ij}^{\Psi\beta}$ as follows [46]:

$$\cos\left(\delta_{i,\Psi,t} - \delta_{j,\beta,t}\right) \approx \begin{cases} 1 \quad , \text{ if } \Psi = \beta \\ -1/2 - \sqrt{3}/2\left(\delta_{i,\Psi,t} - \delta_{j,\Psi,t}\right), \text{ if } \beta \text{ lag } to\ \Psi \\ -1/2 + \sqrt{3}/2\left(\delta_{i,\Psi,t} - \delta_{j,\Psi,t}\right), \text{ if } \beta \text{ lead } to\ \Psi \end{cases}$$
$$,\forall i,j \in \Omega_{BUS}, \forall \Psi,\beta \in \mathcal{F}, \forall t \in \Omega_T \tag{4.47}$$

$$\sin\left(\delta_{i,\Psi,t} - \delta_{j,\beta,t}\right) \approx \begin{cases} \delta_{i,\Psi,t} - \delta_{j,\Psi,t} \quad , \text{ if } \Psi = \beta \\ -1/2\left(\delta_{i,\Psi,t} - \delta_{j,\Psi,t}\right) + \sqrt{3}/2\,, \text{ if } \beta \text{ lag } to\ \Psi \\ -1/2\left(\delta_{i,\Psi,t} - \delta_{j,\Psi,t}\right) - \sqrt{3}/2\,, \text{ if } \beta \text{ lead } to\ \Psi \end{cases}$$
$$,\forall i,j \in \Omega_{BUS}, \forall \Psi,\beta \in \mathcal{F}, \forall t \in \Omega_T \tag{4.48}$$

Approximation 2: This approximation technique deals with the second order of the voltage as well as the relation between the phase angle deviation and the susceptance term as follows [46]:

$$V_{i,\Psi,t}V_{j,\beta,t}H_{ij}^{\Psi\beta}\cos\left(\delta_{i,\Psi,t}-\delta_{j,\beta,t}\right)\approx V_{j,\beta,t}H_{ij}^{\Psi\beta}\cos\left(\delta_{i,\Psi,t}-\delta_{j,\beta,t}\right)$$
$$,\forall i,j\in\Omega_{BUS},\forall\Psi,\beta\in\mathcal{F},\forall t\in\Omega_T \qquad (4.49)$$

$$V_{i,\Psi,t}V_{j,\beta,t}H_{ij}^{\Psi\beta}\sin\left(\delta_{i,\Psi,t}-\delta_{j,\beta,t}\right)\approx H_{ij}^{\Psi\beta}\sin\left(\delta_{i,\Psi,t}-\delta_{j,\beta,t}\right)$$
$$,\forall i,j\in\Omega_{BUS},\forall\Psi,\beta\in\mathcal{F},\forall t\in\Omega_T \qquad (4.50)$$

$$\sum_{j=1}^{n_{bus}}H_{ij}^{\Psi\beta}\left(\delta_{i,\Psi,t}-\delta_{j,\beta,t}\right)\approx H_{ij}^{\Psi\beta}\delta_j^{\Psi,t} \qquad ,\forall i,j\in\Omega_{BUS},\forall\Psi,\beta\in\mathcal{F},\forall t\in\Omega_T \qquad (4.51)$$

where, H can be replaced by G or B depending on (4.10) and (4.11); Cosine and sine functions within (4.49) and (4.50) have already been eliminated by Approximation #1. In this work, the frequency of the system is restored to the nominal value due to the DDGs' secondary control and its effect on the lines impedances can be neglected. By applying Approximations #1 and #2, the three-phase power flow model can be linearized as:

$$P_{i,\Psi,t}=\sum_{j=1}^{n_{bus}}\begin{pmatrix}\begin{pmatrix}\boldsymbol{G}_{ij}^{\Psi,a:c}\circ\boldsymbol{R}_1^{\Psi,a:c}.\boldsymbol{V}_j^{a:c\,t,s,se}\\+\boldsymbol{G}_{ij}^{\Psi,a:c}.\boldsymbol{R}_2^{\Psi,a:c}\boldsymbol{\delta}_j^{\Psi\,t,s,se}\end{pmatrix}\\+\begin{pmatrix}-\boldsymbol{B}_{ij}^{\Psi,a:c}\circ\boldsymbol{R}_1^{\Psi,a:c}.\boldsymbol{\delta}_j^{a:c\,t,s,se}\\+\boldsymbol{B}_{ij}^{\Psi,a:c}.\boldsymbol{R}_2^{\Psi,a:c}\end{pmatrix}\end{pmatrix}=\begin{pmatrix}P_{i,\Psi,t}^{PCC}+P_{i,\Psi,t}^{DDG}\\+\begin{pmatrix}P_{i,t}^{WT,3\Phi}+P_{i,t}^{PV,3\Phi}\\+P_{i,t}^{dch,3\Phi}-\eta_{ESS_i}P_{i,t}^{ch,3\Phi}\end{pmatrix}/3\\-P_{i,\Psi,t}^{L}(1-b_t^{curt})\end{pmatrix}$$
$$,\forall i\in\Omega_{BUS},\forall\Psi\in\mathcal{F},\forall t\in\Omega_T \qquad (4.52)$$

$$Q_{i,\Psi,t}=\sum_{j=1}^{n_{bus}}\begin{pmatrix}-\begin{pmatrix}\boldsymbol{B}_{ij}^{\Psi,a:c}\circ\boldsymbol{R}_1^{\Psi,a:c}.\boldsymbol{V}_j^{a:c\,t,s,se}\\+\boldsymbol{B}_{ij}^{\Psi,a:c}.\boldsymbol{R}_2^{\Psi,a:c}\boldsymbol{\delta}_j^{\Psi\,t,s,se}\end{pmatrix}\\+\begin{pmatrix}-\boldsymbol{G}_{ij}^{\Psi,a:c}\circ\boldsymbol{R}_1^{\Psi,a:c}.\boldsymbol{\delta}_j^{a:c\,t,s,se}\\+\boldsymbol{G}_{ij}^{\Psi,a:c}.\boldsymbol{R}_2^{\Psi,a:c}\end{pmatrix}\end{pmatrix}=\begin{pmatrix}+Q_{i,\Psi,t}^{PCC}+Q_{i,\Psi,t}^{DDG}\\+(Q_{i,t}^{WT,3\Phi}+Q_{i,t}^{ESS,3\Phi})/3\\-Q_{i,\Psi,t}^{L}(1-b_t^{curt})\end{pmatrix}$$
$$,\forall i\in\Omega_{BUS},\forall\Psi\in\mathcal{F},\forall t\in\Omega_T \qquad (4.53)$$

where, $\boldsymbol{V}_j^{a:c}=[V_j^a\ V_j^b\ V_j^c]$ and $\boldsymbol{\delta}_j^{a:c}=[\delta_j^a\ \delta_j^b\ \delta_j^c]$. In this work, "$\circ$" and "." respectively represent the Hadamard and scalar multiplications. $\boldsymbol{R}_1^{\Psi,a:c}$ and $\boldsymbol{R}_2^{\Psi,a:c}$ are the row vector of rotation based on cosine and sines of the phase deviation, respectively. These vectors are as follows:

$$\mathbf{R}_1^{a:c,a:c}=\begin{bmatrix}1 & -1/2 & -1/2\\-1/2 & 1 & -1/2\\-1/2 & -1/2 & 1\end{bmatrix} \qquad (4.54)$$

$$\mathbf{R}_2^{a:c,a:c} = \begin{bmatrix} 0 & \sqrt{3}/2 & -\sqrt{3}/2 \\ -\sqrt{3}/2 & 0 & \sqrt{3}/2 \\ \sqrt{3}/2 & -\sqrt{3}/2 & 0 \end{bmatrix} \tag{4.55}$$

The same approximation techniques are also applied to the nonlinear constraints (4.12)-(4.13) and they are linearized as follows:

$$P_{k,\Psi,t}^{br} = -\begin{pmatrix} \boldsymbol{G}_{ij}^{\Psi,a:c} \circ \boldsymbol{R}_1^{\Psi,a:c}.\boldsymbol{V}_i^{a:c^{t,s,se}} \\ +\boldsymbol{G}_{ij}^{\Psi,a:c}.\boldsymbol{R}_2^{\Psi,a:c}\boldsymbol{\delta}_i^{\Psi^{t,s,se}} \\ -\boldsymbol{B}_{ij}^{\Psi,a:c} \circ \boldsymbol{R}_1^{\Psi,a:c}.\boldsymbol{\delta}_i^{a:c^{t,s,se}} \end{pmatrix} + \begin{pmatrix} \boldsymbol{G}_{ij}^{\Psi,a:c} \circ \boldsymbol{R}_1^{\Psi,a:c}.\boldsymbol{V}_j^{a:c^{t,s,se}} \\ +\boldsymbol{G}_{ij}^{\Psi,a:c}.\boldsymbol{R}_2^{\Psi,a:c}\boldsymbol{\delta}_j^{\Psi^{t,s,se}} \\ -\boldsymbol{B}_{ij}^{\Psi,a:c} \circ \boldsymbol{R}_1^{\Psi,a:c}.\boldsymbol{\delta}_j^{a:c^{t,s,se}} \end{pmatrix}$$
$$,\forall k \in \Omega_{LIN}, \forall \Psi \in \mathcal{F}, \forall t \in \Omega_T \tag{4.56}$$

$$Q_{k,\Psi,t}^{br} = -\begin{pmatrix} -\boldsymbol{B}_{ij}^{\Psi,a:c} \circ \boldsymbol{R}_1^{\Psi,a:c}.\boldsymbol{V}_i^{a:c^{t,s,se}} \\ -\boldsymbol{B}_{ij}^{\Psi,a:c}.\boldsymbol{R}_2^{\Psi,a:c}\boldsymbol{\delta}_i^{\Psi^{t,s,se}} \\ -\boldsymbol{G}_{ij}^{\Psi,a:c} \circ \boldsymbol{R}_1^{\Psi,a:c}.\boldsymbol{\delta}_i^{a:c^{t,s,se}} \end{pmatrix} + \begin{pmatrix} -\boldsymbol{B}_{ij}^{\Psi,a:c} \circ \boldsymbol{R}_1^{\Psi,a:c}.\boldsymbol{V}_j^{a:c^{t,s,se}} \\ -\boldsymbol{B}_{ij}^{\Psi,a:c}.\boldsymbol{R}_2^{\Psi,a:c}\boldsymbol{\delta}_j^{\Psi^{t,s,se}} \\ -\boldsymbol{G}_{ij}^{\Psi,a:c} \circ \boldsymbol{R}_1^{\Psi,a:c}.\boldsymbol{\delta}_j^{a:c^{t,s,se}} \end{pmatrix}$$
$$,\forall k \in \Omega_{LIN}, \forall \Psi \in \mathcal{F}, \forall t \in \Omega_T \tag{4.57}$$

4.3.1.3 Linearization of quadratic function

The piecewise linearization technique is applied for the nonlinear quadratic constraints (4.14), (4.29), (4.33) and (4.39). Specifically in this work, multi-segment polygon region piecewise linearization technique is employed [86], [87], [88]. This technique focuses on forming multiple constraints representing the perimeters of circle for restricting the quadratic summation. Figure 4. 5 illustrates the polygon piecewise technique.

Let's $L_n^{\{1^{st},2^{\mathrm{nd}},3^{\mathrm{rd}},4^{\mathrm{th}}\}}$ and denote the nth piecewise constraints of the quadrants $\{1^{st}, 2^{\mathrm{nd}}, 3^{\mathrm{rd}}, 4^{\mathrm{th}}\}$. According to Figure 4. 5, each segment constraints $L_n^{\{1^{st},2^{\mathrm{nd}},3^{\mathrm{rd}},4^{\mathrm{th}}\}}$ can be formulated by:

$$L_n^{1st} = \{\alpha_n^{1^{st}} X + \beta_n^{1^{st}} Y - \gamma^{1^{st}} Z \leq 0 \qquad ,n = 1,2,\dots,n_{pw} \tag{4.58}$$

$$L_n^{2nd} = \{-\alpha_n^{1^{st}} X + \beta_n^{1^{st}} Y - \gamma^{1^{st}} Z \leq 0 \qquad ,n = 1,2,\dots,n_{pw} \tag{4.59}$$

$$L_n^{3rd} = \{-\alpha_n^{4^{th}} X - \beta_n^{4^{th}} Y - \gamma^{4^{th}} Z \leq 0 \qquad ,n = 1,2,\dots,n_{pw} \tag{4.60}$$

$$L_n^{4th} = \{\alpha_n^{4^{th}} X - \beta_n^{4^{th}} Y - \gamma^{4^{th}} Z \leq 0 \qquad ,n = 1,2,\dots,n_{pw} \tag{4.61}$$

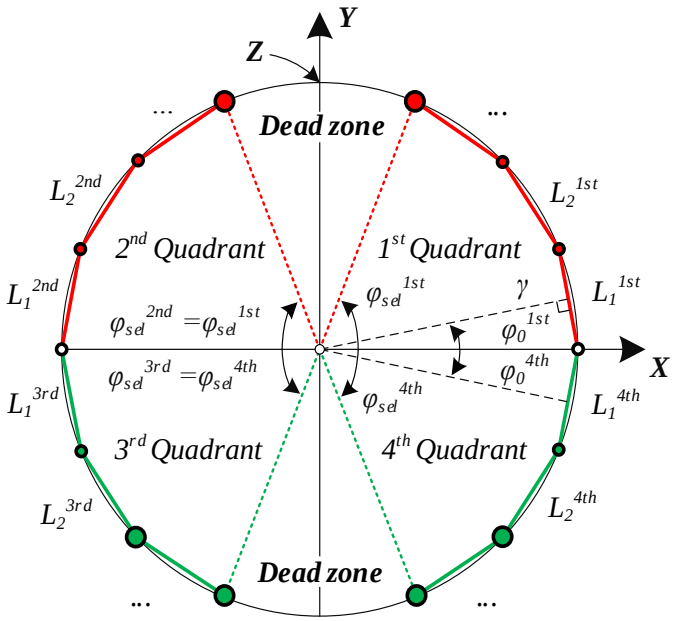

FIGURE 4. 5: Polygon piecewise linearization plan for the quadratic function approximation

where, n_{pw} is the number of piecewise constraints for each quadrant. The n_{pw} can be set high to improve the accuracy. Nonetheless, higher n_{pw} increases the number of constraints and the computation burden is accordingly increased. The piecewise constraint coefficients for each quadrant can be calculated as following:

$$\alpha_n^{1^{st},4^{th}} = \cos\left(\varphi_n^{1^{st},4^{th}} + \left(n^{1^{st},4^{th}} - 1\right)\varphi_{sel}^{1^{st},4^{th}} / n_{pw}^{1^{st},4^{th}}\right) \quad ,n = 1,2,\dots,n_{pw} \tag{4.62}$$

$$\beta_n^{1^{st},4^{th}} = \sin\left(\varphi_n^{1^{st},4^{th}} + \left(n^{1^{st},4^{th}} - 1\right)\varphi_{sel}^{1^{st},4^{th}} / n_{pw}^{1^{st},4^{th}}\right) \quad ,n = 1,2,\dots,n_{pw} \tag{4.63}$$

$$\gamma^{1^{st},4^{th}} = \cos\left(\varphi_{sel}^{1^{st},4^{th}} / 2n_{pw}^{1^{st},4^{th}}\right) \quad ,n = 1,2,\dots,n_{pw} \tag{4.64}$$

$$\varphi_0^{1^{st},4^{th}} = \varphi_{sel}^{1^{st},4^{th}} / 2n_{pw}^{1^{st},4^{th}} \quad ,n = 1,2,\dots,n_{pw} \tag{4.65}$$

By applying the piecewise constraints to the quadratic functions of Section 4.2 and respecting to the operation characteristic of the equipment, the formation of linear piecewise constraint associated with each equipment is summarized in Table 4. 1.

TABLE 4. 1: Summarize of piecewise linear constraint formation for each equipment

Equip.	Operating	Set of piecewise		Set belong	Eqs.
	(quadrant)	(name)	(elements selected)		#
DDG	1st/2nd	L_i^{DDG}	$\{L_n^{1st}, L_n^{4th}\}$		
ESS	full	L_i^{ESS}	$\{L_n^{1st}, L_n^{2nd}, L_n^{3rd}\ L_n^{4th}\}$		
TR	full	L_i^{PCC}	$\{L_n^{1st}, L_n^{2nd}, L_n^{3rd}\ L_n^{4th}\}$		
LINE	full	L_i^{br}	$\{L_n^{1st}, L_n^{2nd}, L_n^{3rd}\ L_n^{4th}\}$		
	X	**Y**	**Z**		
DDG	$P_{i,t}^{DDG,3\Phi}$	$Q_{i,t}^{DDG,3\Phi}$	$S_i^{DDG,max}$	$,\forall i \in \Omega_{DDG}$	(4.66)
ESS	$P_{i,t}^{dch,3\Phi} - P_{i,t}^{ch,3\Phi}$	$Q_{i,t}^{ESS,3\Phi}$	$S_i^{ESS,max}$	$,\forall i \in \Omega_{ESS}$	(4.67)
TR	$P_{i,t}^{PCC,3\Phi}$	$P_{i,t}^{PCC,3\Phi}$	$S_i^{TR,max}$	$,\forall i \in \Omega_{PCC}$	(4.68)
LINE	$P_{k,\Psi,t}^{br}$	$Q_{k,\Psi,t}^{br}$	$I_k^{br,max} V_{i(k),\Psi,t}$	$,\forall k \in \Omega_{LIN}, \forall i \in \Omega_{BUS}$	(4.69)
where, $n = 1,2,\dots,n_{pw}; \Psi \in \mathcal{F}, \forall t \in N_T$					

4.3.2 MILP Model

The proposed MILP model can be formulated by the set of linearized constraints and objective function as following:

$$\min_{\boldsymbol{X}^{MILP,3\Phi}} \sum_{t\in\Omega_{DDG}} \left[(C_t^{PCC} + C_t^{DDG})(1 - b_t^m) + C_t^{CURT} b_t^m + C_t^{VI,Lin}\right] \quad (4.70)$$

subject to:

- Voltage and load curtailment constraints: (4.6), (4.7), (4.44), (4.45), (4.46), (4.9).
- Power flow constraints: (4.52), (4.53), (4.56), (4.57), (4.69).
- DDG operation constrains: (4.19), (4.20), (4.21), (4.22), (4.23), (4.26), (4.27), (4.28), (4.66).
- ESS operational constraints: (4.30), (4.31), (4.32), (4.67), (4.34), (4.35), (4.36).
- Power exchange constraints: (4.37), (4.38), (4.68), (4.40), (4.41), (4.42).

The details of the decision variables of the proposed model are also summarized in Appendix F.

4.4 Numerical Results

In this section, the well-known balanced 33-bus and unbalanced 25-bus test system have been chosen for testing the proposed MINLP and MILP model. The characteristic of these test system can be found in [1]. The planning horizon is set to 24 hours representing a typical day. The daily market electricity price and the percentage of annual peak load are taken from NYISO [89] and [90]. The wind speed and solar irradiance data are given in Table G. 2 of Appendix G. The load curtailment cost and the penalty coefficient of the voltage violation are obtained from [91] and [92]. The characteristic of the DDG, WTs, PVs, ESS, transformer, and transmission line are summarized in the Table G. 4 and Table G. 5, respectively. The weighing coefficient of the load at i^{th} bus and its maximum curtailment duration are assumed to be proportional to their annual peak and are summarized in Table G. 3 of Appendix G. The parameters of the adopted piecewise linearization technique is set to $\varphi_{sel}^{1^{st}} = \varphi_{sel}^{4^{th}} = 90°$ and $n_{pw}^{1^{st}} = n_{pw}^{4^{th}} = 15$ pieces which is high enough to obtain an acceptable accuracy [88]. The maximum and minimum voltage of the buses is set to 1.05 and 0.95 per units, respectively.

To study the effectiveness of the proposed ACOPF model considering the microgrid operation in both grids connected (GC) and islanding (IS), three scenarios (SCEN 1, SCEN 2 and SCEN 3) are considered. First, in SCEN 1 the microgrid is assumed to operates in grid connected mode all along the considered time horizon. Then, SCEN 2 assume that the microgrid operates only in islanding mode. Finally, SCEN 3 assume that the microgrid is disconnected from the substation by opening the switch ISW (i.e., $b_t^m = 1$) between 8:00 and 14:00. In this work, the proposed MILP model and the reference MINLP model have been built in MATLAB environment and solved using "Intlingprog" and "Fmincon" solvers, respectively. All the simulation are implemented on a PC computer equipped with 3.40 GHz Quad-Core Intel(R) Core™ i7-6700 CPU with 32GB of RAM.

4.4.1 Optimum Operation of the Microgrid

The MG optimal operation obtained by solving the proposed MILP model for the three aforementioned scenarios (i.e., SCEN 1, SCEN 2 and SCEN 3) is presented. Figure 4. 6 shows the total three phase active power for the generation, storage and load for the planning horizon. Table 4. 2 shows a comparison between SCEN 1, SCEN 2 and SCEN 3 in terms of costs and voltage violation.

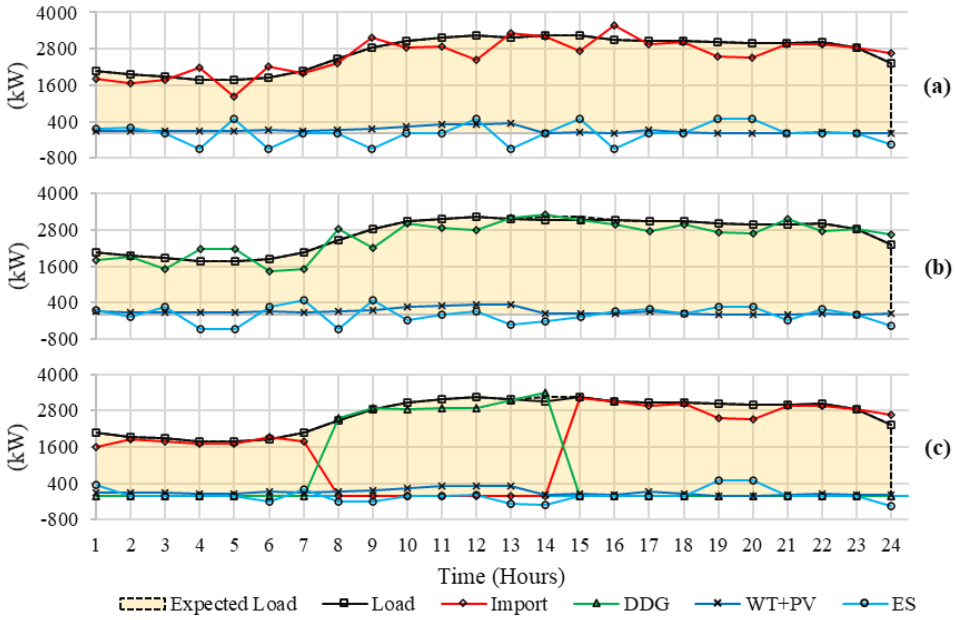

FIGURE 4. 6: Total active power profile for the 25-bus test system: (a) SCEN 1 (b) SCEN 2 (c) SCEN 3

TABLE 4. 2: Optimization results obtained by MILP for 33-bus and 25-bus in difference scenarios.

Optimization goals		33-bus (balanced)			25-bus (unbalanced)		
		SCEN 1	SCEN 2	SCEN 3	SCEN 1	SCEN 2	SCEN 3
Total C^{PCC}	($/24h)	1123.22	0.00	805.45	993.63	0.00	706.89
Total C^{DDG}	($/24h)	0.00	5109.92	1676.71	0.00	4802.60	1603.03
Total C^{CURT}	($/24h)	0.00	149.94	145.35	0.00	829.60	414.80
Total C^{VD}	($/24h)	401.80	94.95	301.81	158.24	56.99	124.32
Total cost	($/24h)	1525.03	5354.81	2929.32	1151.87	5689.20	2849.04
$\min\{V_{i,\Psi,t}\}$	(p.u.)	0.9716	1.0124	0.9719	0.9753	1.0131	0.9753
Avg. Runtime	(s)	4.85	58.78	34.34	23.89	63.57	68.04

Due to the availability of the main grid during SCEN 1, the demand can be fully supplied by the grid and the resources located in the test system. Thus, there is no load curtailment in this scenario compared to other two scenarios. On the other hand, 0.38% of energy demand and 0.19% of energy demand has to be respectively curtailed for the scenarios SCEN 2 and SCEN 3, not only for balancing the power in the system but also for satisfying the secondary control of the DDG units such as voltage restoration layer. The cost associated with the power exchange with the main grid is zero in SCEN 2 as the microgrid is isolated from the main grid during this scenario. The PV and WT renewable

resources account for 3.91% of the total generated energy for the three scenarios. In the grid connected mode, the DDG units are turned off due to the high cost of fuel consumption compared to the cost of energy imported from the main grid. Thus, no active power is generated by the DDG units and its reactive power is accordingly bounded to zero by (4.28). In other words, as it is not economical to generate active power by DDGs during grid connected operation mode, their reactive power generation will accordingly be bounded to zero by (4.28). Hence, no reactive power is generated. As the DDG units are generating no reactive power in this case, the cost of voltage deviation during the SCEN 1 is high. For the same reason, the cost of voltage deviation in the SCEN 2 and SCEN 3 is lower than that in SCEN 1. Nevertheless, the total operation cost during SCEN 1 is always lower than that in SCEN 2 and SCEN 3. That is why the IS mode is usually operated during emergencies and/or when the main grid is not available. In term of the minimum voltage, they are limited the minimum voltage magnitude constraints.

4.4.2 Accuracy Evaluation

For evaluating the accuracy, the results obtained by the proposed MILP model are compared to those obtained by the original MINLP model. For the sake of the comparison with the solutions obtained by the proposed MILP, the MINLP model is changed to a nonlinear problem (NLP) by setting all binary variables according to those obtained by solving the proposed MILP model [26]. The third scenario (SCEN 3) is used and the solution obtained via NLP and MILP as well as the relative error obtained by the solving the models are provided in Table 4. 3.

TABLE 4. 3: Comparison of results obtained by MILP to those obtained by NPL

Error indices		33-bus (balanced)			25-bus (unbalanced)		
		NLP	MILP	Error	NLP	MILP	Error
Total energy DDG	(MWh)	23.094	22.858	1.02%	20.721	20.548	0.84%
Total energy curtailment	(kWh)	44.1	44.1	0.00%	122	122	0%
Total energy losses	(MWh)	1.907	1.930	1.20%	1.632	1.676	2.68%
$\min\{V_{i,\Psi,t}\}$	(p.u.)	0.9703	0.972	0.17%	0.9790	0.9753	0.38%
$\min\{\delta_{i,\Psi,t}\}$	(deg.)	-0.50	-0.496	0.14%	-120.66	-120.87	0.17%
$\max\{\delta_{i,\Psi,t}\}$	(deg.)	90.418	90.446	0.03%	211.31	211.36	0.02%
$\max\{\lvert I^{br}_{i,\Psi,t}\rvert\}$	(kA)	0.322	0.321	0.27%	0.640	0.643	0.35%
Avg. Runtime	(min)	137.22	0.572		612.01	1.134	

Table 4. 3 shows that the relative errors in the calculation of the total energy produced by the DDG units are around 1%. In terms of power loss, the maximum absolute error in the lines active power losses by lines is lower than 3×10^{-3} per unit. Nonetheless, the error is accumulated when

calculating the total energy losses along the considered time horizon and lead to 1.20% and 2.68% for 33-bus and 25-bus test systems, respectively.

On the other hand, the relative error of the voltage magnitude, the voltage phase angle, and the current is lower than 0.5% which validates the accuracy of the proposed MILP model. Figure 4. 7 and Figure 4. 8 show the voltage profile at time $t = 7{:}00$ (the MG operate in GC mode) and $t = 8{:}00$ (the MG operate in IS mode) obtained by proposed MILP and NPL for the 33-bus and 25-bus test systems, respectively. As Table 4. 3 shows, the proposed MILP is computationally superior compared to NLP which is a crucial for real-time operation and stochastic planning applications.

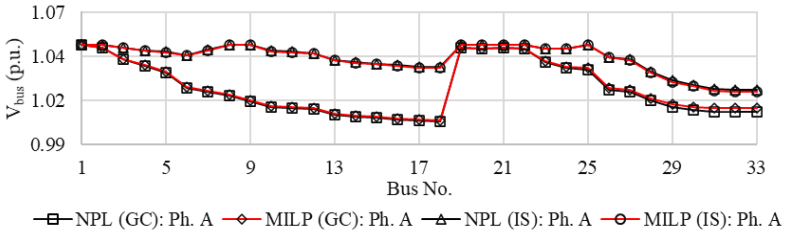

FIGURE 4. 7: Voltage profile at 7:00 (IS mode) and at 8:00 (GC mode) for the unbalanced 33-bus test case obtained by NPL and MILP

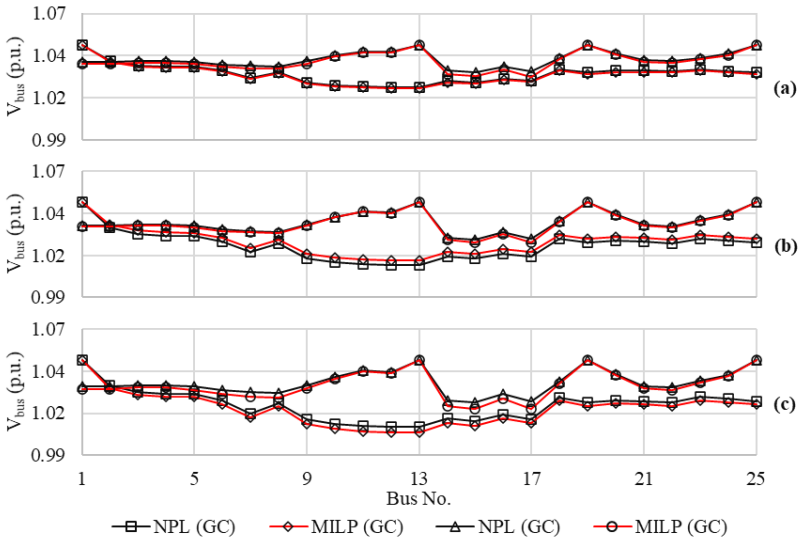

FIGURE 4. 8: Voltage profile at 7:00 (IS mode) and at 8:00 (GC mode) for the unbalanced 25-bus test case obtained by NPL and MILP: (a) Phase A, (b) Phase B, (c) Phase C

4.4.3 Primary Droop and Secondary Control Impact Evaluation

As discussed in the literature, the secondary control has been adopted for compensating the steady-state error derived by the primary droop control layer and to restore the microgrid's voltage and frequency [16]. In this subsection, the impact of considering the secondary control layer in the OPF formulation on the microgrid's operation is evaluated. To this end, the constraints (4.19)-(4.23) of the proposed MILP model representing the operation of DDGs with secondary control are modified and transformed into the well-known droop-based power generation model as expressed in (4.71)-(4.75) [54], i.e., only primary control. Then, the set of decision variables, included in Table F. 1 of Appendix F, are modified by eliminating a set of $u^{v}_{i,\Psi,t}$ and introducing the system frequency ω_t as variables to be solved [54].

$$P^{DDG,3\Phi}_{i,t} = [(\omega^* - \omega_t)/m^p_i]b^m_t + (1 - b^m_t)P^{DDG,3\Phi}_{i,t}/3 \qquad ,\forall i \in \Omega_{DDG}, \forall t \in \Omega_T \qquad (4.71)$$

$$Q^{DDG,3\Phi}_{i,t} = \left[\left(V^*_i - V^a_{i,t}\right)/n^q_i\right]b^m_t + (1 - b^m_t)Q^{DDG,3\Phi}_{i,t}/3 \qquad ,\forall i \in \Omega_{DDG}, ,\forall t \in \Omega_T \qquad (4.72)$$

$$P^{DDG,3\Phi}_{i,t} = \sum_{\Psi \in \mathcal{F}} P^{DDG}_{i,\Psi,t} \qquad ,\forall i \in \Omega_{DDG}, \forall t \in \Omega_T \qquad (4.73)$$

$$Q^{DDG,3\Phi}_{i,t} = \sum_{\Psi \in \mathcal{F}} Q^{DDG}_{i,\Psi,t} \qquad ,\forall i \in \Omega_{DDG}, \forall t \in \Omega_T \qquad (4.74)$$

$$V^a_{i,t}b^m_t = V^b_{i,t}b^m_t = V^c_{i,t}b^m_t \qquad ,\forall i \in \Omega_{DDG}, \forall t \in \Omega_T, \qquad (4.75)$$

Finally, both MILP OPF models, with and without the secondary control, are used to solve the 33-bus test system considering SCEN 2. The results are derived and the effect of primary droop and secondary controls are evaluated accordingly. For the ease of notation, we denote the proposed MILP model in which both primary and secondary control layer have been considered as MILP^{2nd}. Similarly, we denote the modified model with only droop primary control layer as $\text{MILP}^{\text{droop}}$.

First, with the application of secondary control layer the voltage magnitudes at the buses where the DDG units are connected are restored. Figure 4. 9 shows the voltage magnitude profile for bus #25 where a DDG is connected.

In SCEN 2, the microgrid is operated in IS mode along the planning horizon 24h. As can be seen in Figure 4. 9, with MILP^{2nd} the voltage restoration layer of secondary control is activated and the voltage magnitude at the bus #25 is restored to the secondary voltage control reference ($V^{**} =$

1.05 $p.u.$). Nonetheless, the result derived by the MILP^{droop}, show that the voltage magnitude at bus #25 follows the primary control voltage droop with a reference $V^* = 1.01\ p.u.$.

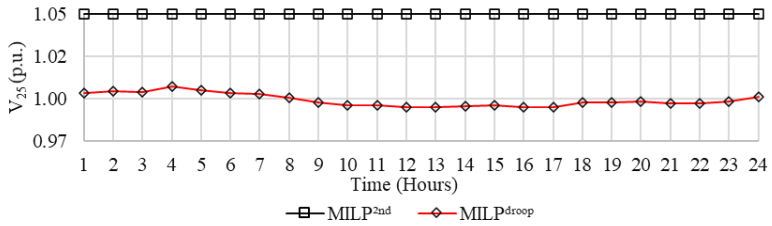

FIGURE 4. 9: Daily voltage magnitude profile of bus #25 obtained by the MILP^{2nd} and MILP^{droop} for the 33-bus test system SCEN 2

Additionally, Figure 4. 10 shows the voltage profile for all the system buses during the at 12:00 am in SCEN 2.

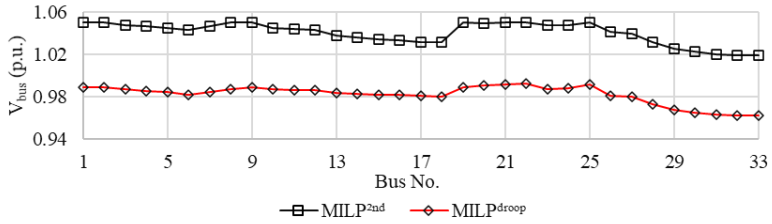

FIGURE 4. 10: Voltage magnitude profile with and without secondary control for the 33-bus test system for SCEN 2 at 12:00 am

As can be seen in Figure 4. 10, the voltage magnitude profile derived by the MILP^{2nd} follows V^{**} at the DDG units connection points, while the voltage profile obtained using the MILP^{droop} model is always maintained below V^* by following the primary droop control. Figure 4. 11 shows the power flowing in the branch #24 i.e., $|P_{24}|$. This branch is connected between bus #24 and #25. As can see, the power flows obtained by MILP^{droop} are different compared to those obtained by MILP^{2nd}.

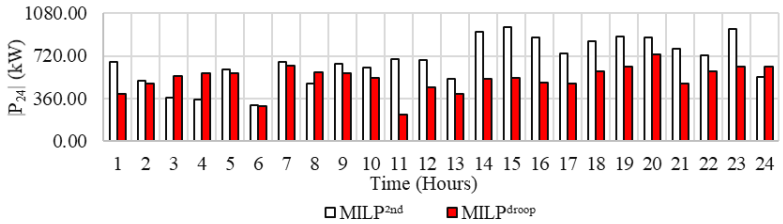

FIGURE 4. 11: Daily power flowing on branch #24 obtained by MILP^{2nd} and MILP^{droop} for the 33-bus test system for SCEN 2

The secondary control has also been used for maintaining the system frequency to its nominal value and make the microgrid ready for synchronization and reconnection to the main grid. The daily frequency of the microgrid system is shown in Figure 4. 12.

The system frequency derived by the proposed MILP^{2nd} model can be directly specified by $\omega_t = 1.00\ p.u.$ or e.g., $60\ Hz$ in this work. Nonetheless, in the MILP^{droop} model with only the primary droop control adoption, the system frequency is a variable to be found [54]. In this case, this frequency is dependent on the active droop characteristic $P - \omega$ and the normal angular frequency, set to $\omega^* = 1.00\ p.u.$ in this work.

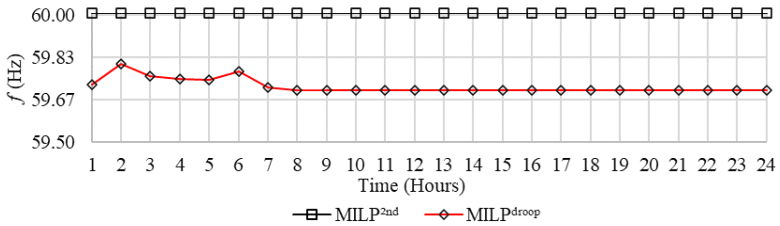

FIGURE 4. 12: Daily system frequency obtained by the MILP^{2nd} and MILP^{droop} for the 33-bus test system SCEN 2

Given that the results of the MILP^{2nd} closely match those of the detailed MINLP model as depicted in Table 4. 3, the results of the comparison between MILP^{2nd} OPF model and MILP^{droop} OPF model demonstrate that the MILP^{droop} OPF formulation is not sufficient for representing the actual behavior of the microgrid with hierarchal control i.e., when a secondary control layer is employed.

4.4.4 Evaluation of Load Shedding Switching State Cycle

In this section, in order to evaluate the impacts of constraints (4.44)-(4.46) employed to limit the number of load shedding cycles on the microgrid operation, we consider a case in which it is assumed that the DDGs #3 to #5 are disactivated. This will force a large portion of load to be shed in order to balance the generation and demand. Figure 4. 13 shows the total number of switching cycles for each load i within 24 hours for 33-bus test system in SCEN 2 with DDGs #3 to #5 disactivated.

As can be seen in Figure 4. 13, the maximum number of switching cycles for the case without considering (4.44)-(4.46) are 5.5 cycles. It this necessary to note that, 0.5 cycle represents a single switching state, e.g., on to off or vice versa. Two more cases where the number of cycles is limited by $N^{curt} = 1$ and $N^{curt} = 3$ are also provided. In these cases, the number of cycles has been limited to $N^{curt} = 1$ and $N^{curt} = 3$ cycles.

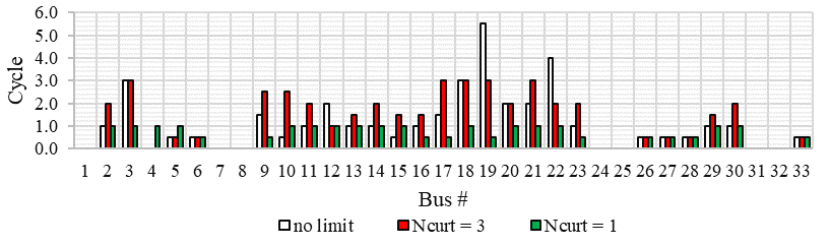

FIGURE 4. 13: Number of load shedding switching state cycle

The loads energy demand has been shed from the network by 26.95%, 27.27%, and 26.47% for the cases without (4.44)-(4.46), with $N^{curt} = 1$, and with $N^{curt} = 3$, respectively. The $b_{19,t}^{curt}$ for these cases is shown in Figure 4. 14. As can be seen, the load in bus #19 is more often switched between the shedding and supply states in the "no limit" case compared to other cases. This situation might not be satisfying for the consumers/operators as there is no control over the load shedding cycles. Nonetheless, with (4.44)-(4.46) applied, the number of cycles is limited.

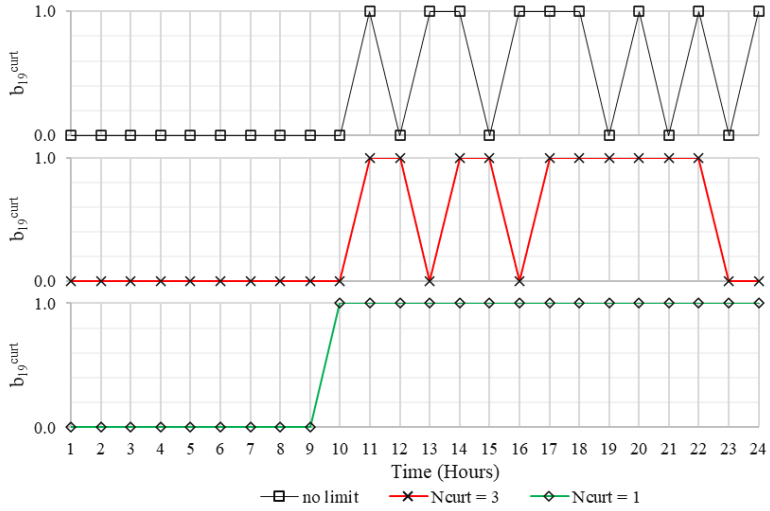

FIGURE 4. 14: Profile of load shedding at bus #19

4.4.5 Evaluation of ESS with primary droop and secondary control

4.4.5.1 Formulation for ESS with primary droop and secondary control

With the power electronics inverter interface, the ESS has the ability to be operated in droop control mode with a supervisory secondary control layer. In this mode, the ESS units participate with the dispatchable resources microgrid to maintain the system frequency and the voltage to the nominal value. The ESS operates in primary droop control mode with a supervisory secondary control layer when it discharges, while during charging mode they act like a load and are as such operated in the PQ mode. For considering the ESS operation in primary droop control mode with a supervisory

secondary control layer, a new set of constraints expressed by (4.76)-(4.80) are added to the constraints (4.30)-(4.36), representing the operation of the ESS in PQ mode:

$$P_{i,\Psi,t}^{dch} b_{i,t}^{ESS} b_t^m b_i^{ESSm} = \begin{cases} \left[-ki^{\omega}\left(\delta_{\Psi,t}^{MG} - \pi/2\right)/m_i^p\right] b_{i,t}^{ESS} b_t^m b_i^{ESSm}, & \Psi = a \\ \left[-ki^{\omega}\left(\delta_{\Psi,t}^{MG} + \pi/6\right)/m_i^p\right] b_{i,t}^{ESS} b_t^m b_i^{ESSm}, & \Psi = b \\ \left[-ki^{\omega}\left(\delta_{\Psi,t}^{MG} - 7\pi/6\right)/m_i^p\right] b_{i,t}^{ESS} b_t^m b_i^{ESSm}, & \Psi = c \end{cases}$$

$$,\forall i \in \Omega_{ESS}, \forall t \in \Omega_T \qquad (4.76)$$

$$Q_{i,\Psi,t}^{ESS} b_{i,t}^{ESS} b_t^m b_i^{ESSm} = \left[\left(V_i^* - V_{i,\Psi,t} + u_{i,\Psi,t}^{v,int}\right)/n_i^q\right] b_{i,t}^{ESS} b_t^m b_i^{ESSm}$$

$$,\forall i \in \Omega_{ESS}, \forall \Psi \in \mathcal{F}, \forall t \in \Omega_T \qquad (4.77)$$

$$P_{i,t}^{dch,3\Phi} b_{i,t}^{ESS} b_t^m b_i^{ESSm} = b_{i,t}^{ESS} b_t^m \, b_i^{ESSm} \sum_{\Psi \in \mathcal{F}} P_{i,\Psi,t}^{dch} \qquad ,\forall i \in \Omega_{ESS}, \forall t \in \Omega_T \qquad (4.78)$$

$$Q_{i,t}^{ESS,3\Phi} b_{i,t}^{ESS} b_t^m b_i^{ESSm} = \; b_{i,t}^{ESS} b_{i,t}^m b_i^{ESSm} \sum_{\Psi \in \mathcal{F}} Q_{i,\Psi,t}^{ESS} \qquad ,\forall i \in \Omega_{ESS}, \forall t \in \Omega_T \qquad (4.79)$$

$$V_{i,\Psi,t} b_{i,t}^{ESS} b_t^m b_i^{ESSm} = V_i^{**} b_{i,t}^{ESS} b_t^m b_i^{ESSm} \qquad ,\forall i \in \Omega_{ESS}, \forall \Psi \in \mathcal{F}, \forall t \in \Omega_T \qquad (4.80)$$

These set of constraints are derived from those implemented for the DDG units operating with secondary control. Nonetheless, $b_{i,t}^{ESS}$ introduced in (4.76)-(4.80) to ensure that the constraints are activated only when the ESS is in discharging state i.e., $b_{i,t}^{ESS} = 1$. Moreover, the binary input parameter b_t^m introduced in this set of constraints guaranties that the ESS operates in PQ mode during grid-connected operation mode. The binary input parameter b_i^{ESSm} represents the operation mode for the ESS and is set to "0" for PQ mode and "1" for droop control mode with a supervisory secondary control layer. The active and reactive droop gains of the ESS units are determined using the capacity-based method similar to those used for the DDG unit. As can be seen in (4.76)-(4.80), there are nonlinear terms in this set of constraints due to the multiplication between continuous variables and the binary variable $b_{i,t}^{ESS}$. In order to resolve this nonlinearity, the linearization approach for the multiplication between continuous and binary variables introduced in Appendix E is adopted. Finally, as $P_{i,\Psi,t}^{dch}$ and $Q_{i,\Psi,t}^{ESS}$ are introduced for each phase, the power flow constraints are needed to be modified from (4.10) and (4.11) to (4.81) and (4.82), while respecting to $b_{i,t}^{ESS}$, b_t^m and b_i^{ESSm} as follows:

$$P_{i,\Psi,t} = V_{i,\Psi,t} \sum_{j\in\Omega_{BUS}} \sum_{\beta\in\mathcal{F}} V_{i,\Psi,t} \begin{pmatrix} G_{ij}^{\Psi\beta} \cos\left(\delta_{i,\Psi,t} - \delta_{i,\beta,t}\right) \\ +B_{ij}^{\Psi\beta} \sin\left(\delta_{i,\Psi,t} - \delta_{i,\beta,t}\right) \end{pmatrix} =$$

$$\begin{pmatrix} P_{i,\Psi,t}^{PCC} + P_{i,\Psi,t}^{DDG} + P_{i,\Psi,t}^{dch} b_{i,t}^{ESS} b_t^m b_i^{ESSm} \\ + \begin{pmatrix} P_{i,t}^{WT,3\Phi} + P_{i,t}^{PV,3\Phi} \\ +P_{i,t}^{dch,3\Phi}\left(1 - b_{i,t}^{ESS} b_t^m b_i^{ESSm}\right) - \eta_{ESS_i} P_{i,t}^{ch,3\Phi} \end{pmatrix} /3 \\ -P_{i,\Psi,t}^{L}(1 - b_t^{curt}) \end{pmatrix}, \forall i \in \Omega_{BUS}, \forall \Psi \in \mathcal{F}, \forall t \in \Omega_T \quad (4.81)$$

$$Q_{i,\Psi,t} = V_{i,\Psi,t} \sum_{j\in\Omega_{BUS}} \sum_{\beta\in\mathcal{F}} V_{i,\Psi,t} \begin{pmatrix} -B_{ij}^{\Psi\beta} \cos\left(\delta_{i,\Psi,t} - \delta_{i,\beta,t}\right) \\ +G_{ij}^{\Psi\beta} \sin\left(\delta_{i,\Psi,t} - \delta_{i,\beta,t}\right) \end{pmatrix} =$$

$$\begin{pmatrix} +Q_{i,\Psi,t}^{PCC} + Q_{i,\Psi,t}^{DDG} + Q_{i,\Psi,t}^{ESS} b_{i,t}^{ESS} b_t^m b_i^{ESSm} \\ + \begin{pmatrix} Q_{i,t}^{WT,3\Phi} \\ +Q_{i,t}^{ESS,3\Phi}\left(1 - b_{i,t}^{ESS} b_t^m b_i^{ESSm}\right) \end{pmatrix} /3 \\ -Q_{i,\Psi,t}^{L}(1 - b_t^{curt}) \end{pmatrix}, \forall i \in \Omega_{BUS}, \forall \Psi \in \mathcal{F}, \forall t \in \Omega_T \quad (4.82)$$

4.4.5.2 Evaluation of ESS with primary droop and secondary control

In this subsection, the operation of the ESS in primary droop control mode with a supervisory secondary control layer is evaluated. A new ESS is added into microgrid with the capability to operate in both the power control mode or in primary droop control mode with a supervisory secondary control layer. As such, two new case studies, CASE^{P} and $\text{CASE}^{2\text{nd}}$, are introduced for the proposed MILP model. In CASE^{P}, the ESS is operated power control PQ mode while in $\text{CASE}^{2\text{nd}}$ it is operated in droop control mode with a supervisory secondary control layer. Both case studies are used to solve the 33-bus test system considering SCEN2. The ESS is allocated to bus #13 of the test system with the following characteristic: $S_i^{ESS,max} = 1.2$ MVA, $E_i^{ESS,max} = 4.5$ MWh, $E_i^{ESS,min} = 0.9$ MWh, and $\eta_i^{ESS} = 95\%$.

Figure 4. 15 shows the charging/discharge state of the new ESS allocated at bus #13 as well as the voltage for this bus. As can see at a particular period of time i.e., 12h00-13h00, the ESS operated in discharging mode for both cases i.e., the ESS with and without the primary droop control mode with a supervisory secondary control layer. As expected, the ESS operating in droop control mode with a supervisory secondary control layer can maintain the voltage refers to their nominal voltage setting V^{**}. Nonetheless, with ESS in PQ mode the voltage for the bus #13 in this case is below V^{**} of the DDG units. For the rest of period, the ESS for both cases were operated similarly.

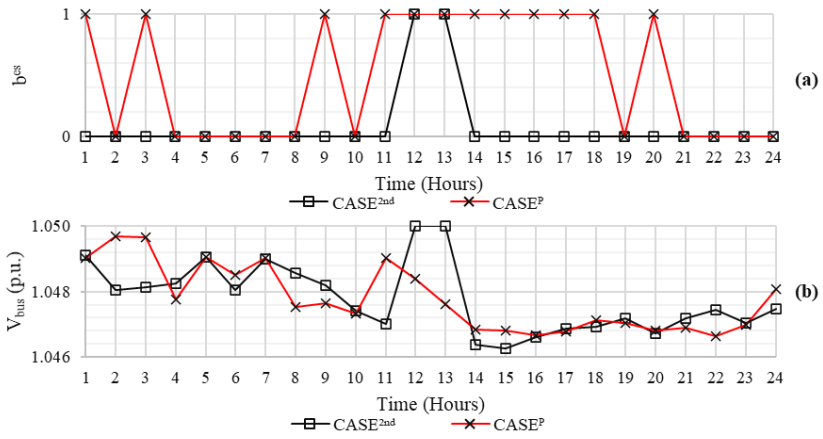

FIGURE 4. 15: Daily profile for (a) binary indicate charging/discharging state of ESS localized at bus #13 (b) voltage for the bus #13

Figure 4. 16 shows the active power profile for a particular period of ESS operating in discharging mode i.e., 12h00-13h00. When the ESS operates in PQ mode, the active power has been scheduled to inject its power into the network according to the optimal operation of the microgrid. Nonetheless, when the ESS operates in droop control mode with a supervisory secondary control layer, the ESS injects the specific amount of active power by $P_{13,A,t=12}^{dch} = 566.81$ kW and $P_{13,A,t=13}^{dch} = 559.96$ kW corresponding to the droop settings under $\delta_{A,t=12}^{MG} = 89.932°$ and $\delta_{A,t=13}^{MG} = 89.933°$, respectively.

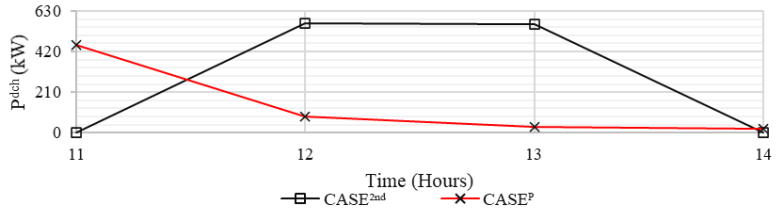

FIGURE 4. 16: Active discharged power of ESS localized on bus #13 for both case ESS with and without considering droop+2nd control

The overall optimization results have been summarized in Table 4. 4. The results show that the total cost is not dependent on the operating mode of the ESS. For the same reason, no load is curtailed in both cases. Nonetheless, the minimum voltage for $\mathrm{CASE}^{2\mathrm{nd}}$ is slightly higher than that in $\mathrm{CASE}^{\mathrm{P}}$ due to primary droop and the secondary control adopted. Finally, the maximum branch current and total energy loss were higher in $\mathrm{CASE}^{2\mathrm{nd}}$ compared to those obtained in $\mathrm{CASE}^{\mathrm{P}}$.

TABLE 4. 4: Optimization results for CASE^{2nd} and CASE^{P}

Indicators		CASE^{2nd}	CASE^{P}
Total C^{DDG}	($/24h)	5113.15	5113.15
Total C^{CURT}	($/24h)	0.00	0.00
Total cost	($/24h)	5188.24	5188.24
$\min\{V_{i,\Psi=A,t}\}$	(p.u.)	1.014	1.013
$\max\{V_{i,\Psi=A,t}\}$	(p.u.)	1.05	1.05
$\min\{\delta_{i,\Psi=A,t}\}$	(deg.)	88.000	88.113
$\max\{\delta_{i,\Psi=A,t}\}$	(deg.)	90.779	90.609
$\max\{I^{br}_{k,\Psi=A,t}\}$	(kA)	0.102	0.099
Total energy loss	(MWh)	0.912	0.896

4.5 Conclusion

An MINLP model for the optimal operation problem of unbalanced microgrid with hierarchical control structure was proposed. The model considers the microgrid philosophy of operation during GC and IS in a single comprehensive model. The energy storage system and the intermittent resources such as WTs and PVs were considered in the proposed model. Additionally, the proposed MINLP model was linearized and the MILP model of the problem was obtained which can be solved efficiently with commercial solvers. The obtained solutions can guarantee the optimal operation of the microgrid respecting to their philosophy of operation during both operation mode. Numerical simulation studies were conducted to prove the effectiveness of the proposed models. The error assessment was also conducted for validating the proposed model. The results showed that the proposed MILP model achieves the optimum results with significantly lower computational time compared to that in the MINLP. Such performance is crucially needed in the real-time and stochastic planning application for the microgrid.

Chapter 5 Resilience Oriented Microgrid Planning

Y. Vilaisarn, Y. R. Rodrigues, and M. Abdelaziz, “A Deep Learning based Multi-Objective Optimization for the Planning of Resilience Oriented Microgrids in Active Distribution System”. *Submitted in IEEE Access, Mars 2022.*

Résumé

Lorsqu'il est confronté à des phénomènes météorologiques violents, un système de distribution peut subir la perte ou la défaillance d'un ou plusieurs de ses composants, ce que l'on appelle les systèmes contingences à niveau N-K. Néanmoins, en tirant parti des sectionneurs électriques et de la disponibilité croissante des ressources énergétiques distribuées, un système de distribution peut être formé en micro-réseaux pour résister à de telles éventualités avec une interruption minimale de l'alimentation. Dans cette perspective, ce travail propose un nouveau cadre d'optimisation à deux niveaux pour la planification de micro-réseaux dans un système de distribution actif dans une perspective de résilience. Pour cela, tout d'abord, le niveau supérieur traite un problème d'optimisation multi-objectif pour allouer, de manière optimale les ressources d’énergies distribuées et les sectionneurs électriques dans le réseau de distribution en équilibrant les autres objectifs que sont le coût,la résilience et l'impact environnemental. Ensuite, le niveau interne traite du fonctionnement optimal des micro-réseaux qui peuvent être créés en exploitant les ressources énergies distribuées et les sectionneurs électrique d'isolement alloués dans le niveau supérieur. Ce cadre utilise des modèles d'apprentissage de réseaux de neurones profonds pour la prise en compte du comportement opérationnel des micro-réseaux, en surmontant les simplifications de modélisation visant à alléger la charge de calcul. En effet, cette charge de calcul peut compromettre l’étude des solutions de planification. Il faut prendre en compte le contrôle hiérarchique, les charges et les générations stochastiques, ainsi que la nature stochastique des pannes de ligne induites par la météo, qui sont des aspects particulièrement critiques dans le cadre d'une planification axée sur la résilience. Des études de cas de simulation sont développées pour démontrer l'efficacité de la méthode de planification proposée.

Abstract

When facing severe weather events, a distribution system may suffer from the loss or failure of one or more of its components, the so-called N-K contingencies. Nevertheless, taking advantage of the system’s isolate switches and the increasing availability of distributed energy resources (DERs), a distribution system may be clustered into microgrids able to withstand such contingencies with

minimal power interruption. In this perspective, this work proposes a novel bilevel optimization framework for planning microgrids in active distribution systems under a resilience-oriented perspective. For this, first, the outer level optimization features a multi-objective problem seeking to optimally allocate DERs and isolate switches in the distribution network while balancing the competing objectives of cost, resilience, and environmental impact. Next, the inner level handles the optimization problem pertaining to the optimal operation of the microgrids that can be created by harnessing local DERs and isolate switches allocated in the outer level. Further, given the proposed approach resilience-oriented focus, the developed framework employes deep learning models based on deep neural network (DNN) architectures trained using Bayesian Regularization Backpropagation (BRB) technique. This strategy allows for avoiding the modeling simplifications typically employed to alleviate the computational burden that can otherwise jeopardize planning solutions' feasibility. Thus, enabling the accurate consideration of microgrids' operational behavior, including hierarchal controls and the stochastic nature of loads, generation, and weather-induced line failures, especially critical aspects under resilience-oriented planning. Simulation case studies are developed to demonstrate the effectiveness of the developed planning framework.

5.1 Introduction

Regarding to the challenges discussed in the literature in chapter 1, in this chapter we propose a general framework for resilience oriented microgrid(s) planning that exploit deep learning to alleviate the computational burden associated with planning problem without sacrificing the model accuracy. The remainder of this chapter is organized as follows: First, basic outline for the proposed resilience oriented microgrid planning framework is presented in Section 5.2. Subsequently, the problem formulation for the outer and inner levels are descripted in Section 5.3. Then, the data preparation stage for the proposed planning approach is presented in Section 5.4. Next, a deep learning approach for a stochastic optimal operation level are discussed in Section 5.5. Later, Section 5.6 exhibits the detail for optimal microgrid planning approach NSGA-II based DNN models. Finally, section 5.7 and 5.8 present the results and concludes the paper, respectively.

5.2 Proposed Resilience Oriented Planning Framework

The availability of isolate switches (ISWs) along with the locations and capacities of the DERs, including DG units, renewable DG units and energy storage (ES) units, are salient for the successful creation of MG(s) in a distribution network. Additionally, the optimal operation of the MG’s resources should be considered to ensure the MG successful operation, minimize its operational costs and maximize its resilience. As such, the proposed resilience-oriented planning framework seeks to

identify the optimal allocation of DERs and ISWs in a distribution network considering the optimal operation of the MG(s) that will be created using these components. To this end, the analyzed problem is formulated as a stochastic bilevel optimization framework. First, an outer level featuring a metaheuristic multi-objective optimization is adopted for the optimal allocation of the DERs and ISWs seeking to balance the competing objectives of cost, resilience and environmental impact. Then, an inner level is proposed to handle the optimization problem pertaining to the optimal operation of the MG(s) that can be created by the DERs and ISWs allocated in the outer level. The problem of the MG's optimal operation is cast as a linear optimum power flow (LOPF) problem. In this work, the adopted LOPF model considers the operational behavior of the MG in both grid-connected (GC) and islanded (IS) modes of operation. Additionally, different scenarios are considered to account for the stochastic nature of the HILP events, as well as renewable DG units. In this sense, despite using a LOPF model, the detailed modeling of MGs and consideration of different stochastic scenarios in the inner level along with the metaheuristic nature of the outer level make solving the LOPF, for each of the stochastic scenarios for each individual in the metaheuristic optimization's population, using a numerical optimization solver computationally challenging. In other words, the combination of the need for numerous iterations to solve the LOPF of the inner level and the large populations from the metaheuristic presented in the outer level before reaching the final planning solution, make this problem computationally extremely demanding that it may be unsolvable with the traditional analytical methods. In this sense, in this work, a deep learning technique is adopted for deriving the information required from the LOPF solution for the stochastic scenarios under consideration. With this technique, DNN models are developed and trained to predict the solution delivered by the inner level that comprises the LOPF solution with the numerous stochastic scenarios, significantly reducing the computation burden, and thus eliminating the possible requirement for modelling simplication. This new perspective provides an effective strategy for solving MG planning framework, overcoming computation constraints that limit the consideration of detailed systems' modeling and scenarios, which are especially critical features for guaranteeing feasible solutions under a resilience-oriented outlook.

The full outline of the proposed resilience-oriented MG planning framework is shown in Figure 5. 1. The proposed planning framework comprises four cascading stages for delivering the final optimal allocation of the DERs and switches. 1) The first stage is concerned with data preparation. In this stage, the distribution system under consideration and its planning elements are identified along with the uncertainty scenarios describing the stochastic nature of the system and the planning elements. The target system for this work is a typical distribution system with the ability to disconnect from the

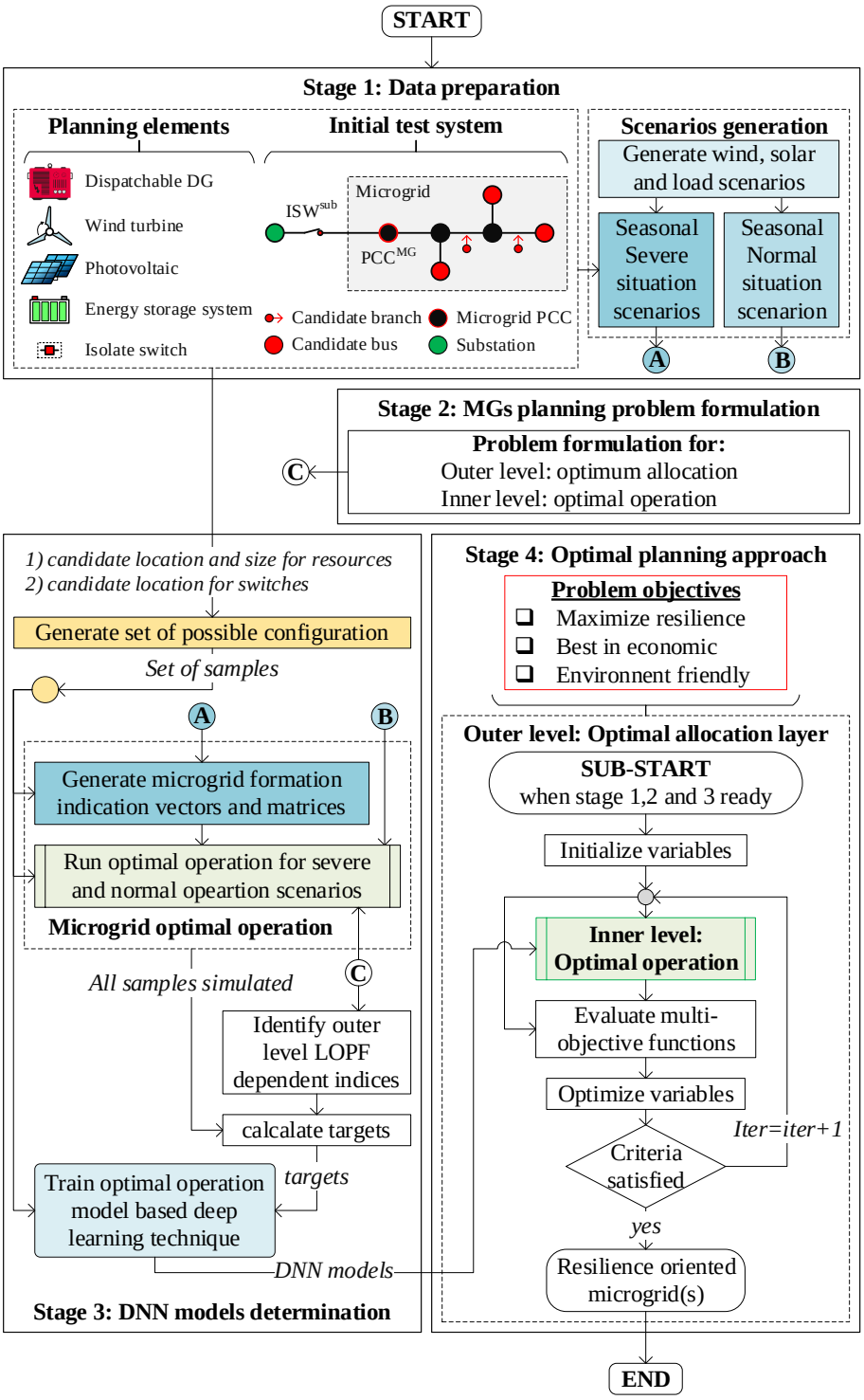

FIGURE 5. 1: Basic outline for the proposed Resilience Oriented Microgrids Planning framework

main grid via a main isolate switch, denotated by ISW^{sub}. The planning elements include dispatchable distributed generation (DDG), wind turbine (WT), photovoltaic (PV), energy storage system (ESS)

and isolate switch (ISW). Candidate buses and branches are specified as potential locations for the system's planning elements. Stochastic scenarios are considered for allowing for the uncertainty associated with the MG(s) creation, i.e., HILP, and operation (renewable generation and load). These uncertainty scenarios are seasonal, and include a set of scenarios representing the normal operation of the system and another set of scenarios representing the severe HILP events in which N-K contingencies occurred in the network within a certain time interval. 2) The second stage corresponds to the problem formulation of the proposed stochastic bilevel optimization framework. In this formulation, the outer level's objective functions are cost, resilience and environmental metrics (indices) that depend on the solution of LOPF for different stochastic scenarios in the inner level. 3) The third stage seeks to deliver the deep learning models that are used to determine the stochastic LOPF dependent indices required for the outer level. To this end, a set of samples DERs and switches allocation is developed considering randomly generated combinations of possible installation decisions for the candidate planning elements locations and capacities. Next, the stochastic LOPF is solved using a numerical optimization solver for each of the allocation samples under consideration for each of the stochastic scenarios. Based on the LOPF solutions obtained for these samples, the outer level cost, resilience and environmental indices are calculated. The calculated indices are considered as the target values of the allocation samples. The allocation samples and their corresponding target values are then employed for training the Deep Neural Network (DNN) models that map the planning elements installation decisions to the outer level's cost, resilience and environmental indices. Finally, in the fourth stage, the optimal planning approach is held. Using a population-based metaheuristic optimization exploiting the DNN models derived in the third stage, the optimal solution describing the optimal allocation of DERs and ISWs is determined respecting the optimal trade-off between the multi-objective functions, i.e., resilience, economic and environment impact. A flowchart outlining the proposed strategy four main stages is detail depicted in Figure 5. 1. Each of these four stages is individually addressed in the following sections.

5.3 Stage I: Data Preparation

In this section, the first stage responsible for data preparation is addressed, including the modeling of distribution system and planning elements, as well as generation uncertainty, normal operation and HILP event scenarios.

5.3.1 Distribution System and Planning Elements

The distribution system considered in this work is a typical distribution network with the ability to disconnect from the main grid via a main $\mathrm{ISW}^{\mathrm{sub}}$ located at the upstream interfacing substation.

Candidate buses and branches for the installation of DERs and isolation switches, respectively, are assumed to be selected arbitrarily by the Distribution System Operator (DSO). The planning elements include the DDGs, WTs, PVs, ESSs and ISWs. In grid connected mode, the DDGs are controlled to inject constant amounts of power prespecified by a higher level control layer typically seeking to realize an economic benefit [3]. On the other hand, in the islanding mode of operation the DDGs are controlled using $\mathrm{droop}/2^{\mathrm{nd}}$ control to follow the load variation and maintain the system voltage and frequency within adequate bounds, allowing for quick synchronization back with main grid when its ready. The WTs and PVs are intermittent resources and are as such operated in power control mode to allow for maximum power tracking. The ESSs are interfaced with a power electronic inverter and are controlled in a power control mode to inject/absorb power from the microgrid as needed. The ISWs are used to isolate faults in according to the considered N-K contingencies.

5.3.2 WT and PV Generation Model

The power generated by the WTs and PVs depend on the wind velocity and solar irradiance, respectively, and can be modeled using (5.1) and (5.2) similar to the work in [78].

$$P_{i,t,s,se}^{WT} = \begin{cases} 0, & v_{i,t,s,se}^{m} < v_i^{ci}, v_{i,t,s,se}^{m} \geq v_i^{co} \\ P_i^{WT,size} \frac{\left(v_{i,t,s,se}^{m} - v_i^{ci}\right)}{\left(v_i^{ra} - v_i^{ci}\right)}, & v_i^{ci} \leq v_{i,t,s,se}^{m} \leq v_i^{ra} \\ P_i^{WT,size}, & v_i^{ra} < v_{i,t,s,se}^{m} < v_i^{co} \end{cases}$$
$$,\forall i \in \Omega_{WT}^{can}, \forall t \in \Omega_T, \forall s \in \Omega_s' \cup \Omega_s'', \forall se \in \Omega_{se} \qquad (5.1)$$

$$P_{i,t,s,se}^{PV} = \begin{cases} P_i^{PV,size} \left(r_{i,t,s,se}^{m}\right)^2 / (R_i^{STD} - R_i^{C}), & r_{i,t,s,se}^{m} \leq R_i^{C} \\ P_i^{PV,size} \left(r_{i,t,s,se}^{m}\right)^2 / R_i^{STD}, & R^{C} < r_{i,t,s,se}^{m} < R_i^{STD} \\ P_i^{PV,size}, & r_{i,t,s,se}^{m} \geq R_i^{STD} \end{cases}$$
$$,\forall i \in \Omega_{PV}^{can}, \forall t \in \Omega_T, \forall s \in \Omega_s' \cup \Omega_s'', \forall se \in \Omega_{se} \qquad (5.2)$$

In this work, it is assumed that the WTs and PVs are operating with unity power factor. Thus, there is no reactive power injected by these units leading to (5.1) and (5.2) exclusively representing active power relations.

5.3.3 Load Model

The varying seasonal behavior of the loads is modeled using the annual peak load pattern [90]. In this sense, the load at bus $i \in \Omega_{BUS}$ at time $t \in \Omega_T$ can be calculated as the multiplication between the peak demand at this bus and the annual peak load factor at time $t \in \Omega_T$ for the season under

consideration. The active and reactive power demand for bus i at time t for scenarios s and season se can be calculated using (5.3) and (5.4).

$$P^{L}_{i,t,s,se} = \left(\frac{APL_{t,s,se}}{100}\right) \times P^{L,peak}_{i,t,s,se} \qquad ,\forall i \in \Omega_{BUS}, \forall t \in \Omega_T, \forall s \in \Omega'_s \cup \Omega''_s, \forall se \in \Omega_{se} \qquad (5.3)$$

$$Q^{L}_{i,t,s,se} = \left(\frac{APL_{t,s,se}}{100}\right) \times Q^{L,peak}_{i,t,s,se} \qquad ,\forall i \in \Omega_{BUS}, \forall t \in \Omega_T, \forall s \in \Omega'_s \cup \Omega''_s, \forall se \in \Omega_{se} \qquad (5.4)$$

5.3.4 Operation Scenarios

Given the resilience-based planning perspective of the proposed work, two sets of scenarios have been considered. First, scenarios representing normal system operations without contingencies are addressed. Second, scenarios representing severe HILP events, in which N-K contingencies occur during a certain time interval are tackled. These scenarios generation processes are described in the following subsections.

5.3.4.1 Normal Operation Scenarios

In the normal operation scenarios, the system is assumed operating in grid connected mode considering uncertainties associated with the renewable resources. For this, historical data sets comprising different 24-hours' time-series of wind speeds and solar irradiance are considered. Next, based on this data a fast forward reduction approach is employed [93], extracting N'_s scenarios per season representing the uncertainty associated with the renewable resources. This step seeks to avoid the higher computation burden, while keep a good approximation of the system. The wind speed and solar irradiance in a given scenario s can be expressed by (5.5) and (5.6), respectively.

$$\boldsymbol{v^{m}_{s,se}} = [v^{m}_{1,s,se}, v^{m}_{2,s,se}, \dots, v^{m}_{N_T,s,se}] \qquad ,\forall s \in \Omega'_s, \forall se \in \Omega_{se} \qquad (5.5)$$

$$\boldsymbol{r^{m}_{s,se}} = [r^{m}_{1,s,se}, r^{m}_{2,s,se}, \dots, r^{m}_{N_T,s,se}] \qquad ,\forall s \in \Omega'_s, \forall se \in \Omega_{se} \qquad (5.6)$$

5.3.4.2 Severe HILP Operation Scenarios

For scenarios representing the operation of the distribution system under severe HILP events, a similar approach to the work developed in [94] is employed. In this sense, by using the component availability matrix **AV**, the availability of the different system components (e.g., branch) at different time segments in the planning horizon is depicted. This matrix allows for the identification of the contingency level, as well as the fault location(s) at any instant in the planning horizons. This in turn enables the development of effective microgrid formation solutions that can meaningfully improve

distribution system resiliency. For considering the distribution system operation under severe HILP events, the following assumptions are made in this work:

- Severe wind events are considered as the main source of contingencies affecting the distribution network, similar to the work developed in [94].
- Only overhead lines are considered to be vulnerable to severe winds. Distribution substations and underground lines are able to withstand severe winds as depicted in [95].
- The distribution system buses are assumed to be geographically close enough that the trajectory of the wind passing through the distribution network cause the entire network to be exposed to the same weather conditions [96].

a) System Performance Analysis for HILP Scenarios Selection

Next, considering the aforementioned assumptions, when a severe wind event arises, the supply availability and the corresponding system performance progresses through multiple phases along Ω_T, leading to the typical progression curve for the system performance (SPF) during a severe event depicted in Figure 5. 2 [94], [56].

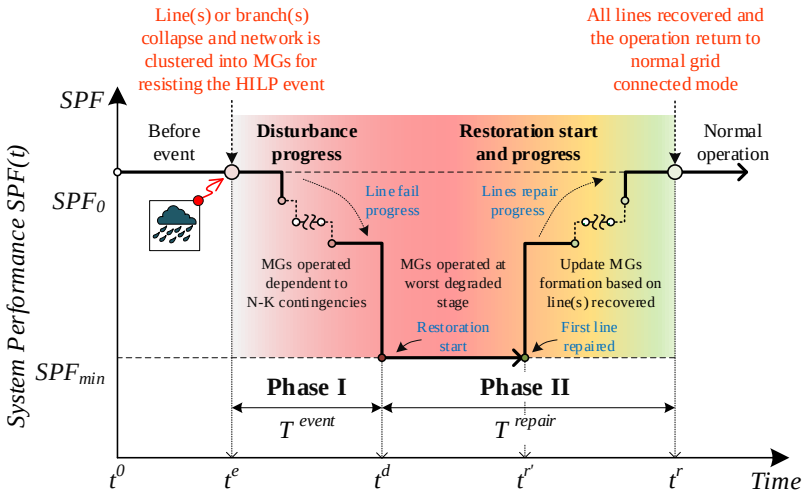

FIGURE 5. 2: Evolution of network's system performance during a severe event

In this perspective, the system performance can be represented as a function of the electricity supply level at time t, being divided into Phase I and II, where Phase I represents the disturbance progress period between the event start, t^e, and maximum system degradation state, t^d, i.e. $T^{event} = t^e - t^d$, and Phase II depicts the recovery period between the maximum degradation time until reparations conclusion, i.e., $T^{repair} = t^d - t^r$. Here it is important to note that there is typically a lead time in

Phase II between the moment where the event disturbance progression stops and the time where repairs' impact is effectively observed, i.e., $t^{r'}$. Detailed descriptions of Phase I and II leading to the developed weather-related algorithm for HILP scenarios selection and component availability matrix **AV** derivation are following presented.

b) Phase I: Disturbance Period

Assuming the event start and progression, during Phase I the affected system clusters into multiple MGs with topologies respecting local resources availability and isolate switches allocated in the network. The formation of MGs allows the system to improve its withstanding ability against the N-K contingencies cause by the severe wind and enhance the maintenance of the loads service. In this sense, given this work focus on resilience-based planning, the single most vulnerable wind scenario needs to be identified for each season in order to stress the system performance under worst-case condition, i.e., $\boldsymbol{v}_{se}^{worst}$. For this, based on works [97], [98] wind gusts can be calculated using (5.7), where the system most vulnerable scenario under a resilience perspective is given by the wind scenario within matrix $\mathbf{v}_{se}^{\mathbf{m}}$ containing the highest wind velocity.

$$\boldsymbol{v}_{se}^{gust} = k^{gust}\boldsymbol{v}_{se}^{worst} \qquad ,\forall se \in \Omega_{se} \tag{5.7}$$

Following, the failure probability of overhead lines for season se can be extracted by mapping poles and conductors' fragility curve for the calculated wind gust profile $\boldsymbol{v}_{se}^{gust}$. The fragility curve can be generated using the normal cumulative distribution function as generically illustrated in Figure 5. 3 for the distribution overhead line depicted in [95].

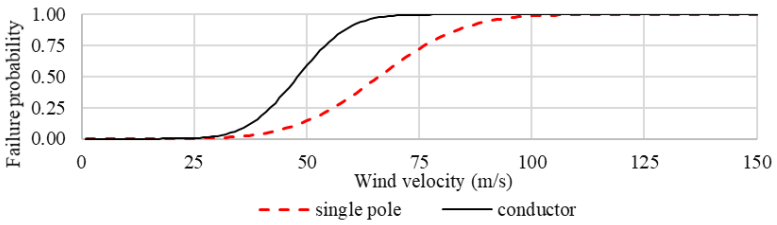

FIGURE 5. 3: Generic fragility curve for single pole and conductor against wind gust

Here, it is worth noting that a branch fails if a conductor, or any pole overhead line, connected between two adjacent nodes fails. In this sense, the total failure probability of the distribution overhead line should be calculated using (5.8)-(5.11).

$$\pi_{i,t,se}^{pole}\left(v_{t,se}^{gust}\right) = cdf^{nor}\left(v_{t,se}^{gust}, \mu_i^{pole}, \sigma_i^{pole}\right) \qquad ,\forall i \in \Omega_{LIN}, \forall t \in \Omega_T, \forall se \in \Omega_{se} \tag{5.8}$$

$$\pi_{i,t,se}^{cond}\left(v_{t,se}^{gust}\right) = cdf^{nor}(v_{t,se}^{gust}, \mu_i^{cond}, \sigma_i^{cond}) \quad ,\forall i \in \Omega_{LIN}, \forall t \in \Omega_T, \forall se \in \Omega_{se} \quad (5.9)$$

$$\pi_{i,t,se}^{poles}\left(v_{t,se}^{gust}\right) = 1 - \left[\left(1 - \pi_{i,t,se}^{pole}\left(v_{t,se}^{gust}\right)\right)^{N_i^{pole}}\right] \quad ,\forall i \in \Omega_{LIN}, \forall t \in \Omega_T, \forall se \in \Omega_{se} \quad (5.10)$$

$$\pi_{i,t,se}^{br}\left(v_{t,se}^{gust}\right) = \begin{pmatrix} \pi_{i,t,se}^{cond}\left(v_{t,se}^{gust}\right) \\ +\pi_{i,t,se}^{poles}\left(v_{t,se}^{gust}\right) \\ -\begin{pmatrix} \pi_{i,t,se}^{cond}\left(v_{t,se}^{gust}\right) \\ \times \pi_{i,t,se}^{poles}\left(v_{t,se}^{gust}\right) \end{pmatrix} \end{pmatrix} \quad ,\forall i \in \Omega_{LIN}, \forall t \in \Omega_T, \forall se \in \Omega_{se} \quad (5.11)$$

Eqs. (5.8) and (5.9) define the failure probability for a single pole and conductor during $v_{t,se}^{gust}$ based on the normal cumulative distribution function with parameter μ^{pole}, σ^{pole}, μ^{cond} and σ^{cond}. Eqs. (5.10) and (5.11) determine the general formulation for dealing with the failure probability of branch i according to the quantity of poles N_i^{pole} for the overhead line of branch i, assuming that the poles and conductor in the distribution system have same characteristic and age. For this, N_i^{pole} can be estimated based on the span length of the distribution overhead line [99]. For distribution systems, the span length is typically between 100 ft to 150 ft, significantly shorter when compared to those used for the transmission system [100].

The failure probability obtained for the branches is stored in matrix $\boldsymbol{\pi}_{se}$ as shown in (5.12). Next, similar to the work in [95], non-vulnerable branches are identified and disregarded by $\boldsymbol{\pi}_{se} = 0 | \boldsymbol{\pi}_{se}\left(\pi_{i,t,se}^{br} < \pi^{br,nvul}\right)$. Following, for enlarging the possibility space of N-K contingencies, N_s^{pre} scenarios of **AV** are generated and represented by $\mathbf{AV}_{s,se}^{\mathrm{I}}$ considering Phase I.

$$\boldsymbol{\pi}_{se}\left(\boldsymbol{v}_{se}^{gust}\right) = \begin{bmatrix} \pi_{i,t,se}^{br} & \cdots & \pi_{i,N_T,se}^{br} \\ \vdots & \ddots & \vdots \\ \pi_{n_{br},t,se}^{br} & \cdots & \pi_{n_{br},N_T,se}^{br} \end{bmatrix} \quad ,\forall se \in \Omega_{se} \quad (5.12)$$

$$\mathbf{AV}_{s,se}^{\mathrm{I}} = \begin{bmatrix} a_{i,t,s,se}^{br} & \cdots & a_{i,N_T,s,se}^{br} \\ \vdots & \ddots & \vdots \\ a_{n_{br},t,s,se}^{br} & \cdots & a_{n_{br},N_T,s,se}^{br} \end{bmatrix} \quad ,\forall i \in \Omega_{LIN}, \forall t \in \Omega_T, \forall s \in \Omega_s^{pre}, \forall se \in \Omega_{se} \quad (5.13)$$

where, $a_{i,t,s,se}^{br}$ is 0 if the i^{th} branch fails at time t for scenario s of season se, otherwise, $a_{i,t,s,se}^{br} = 1$. $a_{i,t,s,se}^{br}$ can be determined comparing the failure probability $\pi_{i,t,s,se}^{br}$ to the generated uniformed random binary number, as expressed by (5.14).

$$a_{i,t,s,se}^{br} = \begin{cases} a_{i,t-1,s,se}^{br} \times 1, \ \pi_{i,t,s,se}^{br} \leq r_{i,t,s} \\ a_{i,t-1,s,se}^{br} \times 0, \ \pi_{i,t,s,se}^{br} > r_{i,t,s} \end{cases}, \forall i \in \Omega_{LIN}, \forall t \in \Omega_T, \forall s \in \Omega_s^{pre}, \forall se \in \Omega_{se} \quad (5.14)$$

c) Phase II: Restoration Period

Once the system reaches the maximum degradation condition, Phase II begins repairing the system until all branches are fully recovered at t^r and the system is back to normal operation, i.e., grid connected. In this sense, considering the time to repair (TTR) overhead lines dependency to the wind velocity at the time of failure, i.e., $t = t_{i,s,se}^{br,fail}$ [94], while aware that due to safety reasons, there is no repair actions implemented until the end of the event at $t_{s,se}^{d}$ [94]. The weather-related restoration time expressed by (5.15) and (5.16) is employed for determining TTR, and $\varphi^{br}\left(v_{t,s,se}^{gust}\right)$ is determined using uniform distributed sampling $\varphi \sim U[h_1, h_2]$ as depicted in (5.17) [94],[101]. Once $\boldsymbol{TTR}_{s,se}^{\boldsymbol{br,fail}}$ and $t_{s,se}^{d}$ are determined, the recovered time for a single branch i can be determined by $t_{i,s,se}^{br,rep} = t_{s,se}^{d} + TTR_{i,s,se}^{br,fail}$. Thus, at $t_{i,s,se}^{br,rep}$, $a_{i,t,s,se}^{br}(t_{i,s,se}^{br,rep}) = a_{i,t,s,se}^{br,new} = 1$, which represents that branch i is recovered and turned back to the online state. Finally, the branch availability matrix considering Phase I and II $\mathbf{AV}_{s,se}^{\mathbf{I-II,orig}}$ can be obtained updating $\mathbf{AV}_{s,se}^{\mathbf{I}}$ with the new $a_{i,t,s,se}^{br,new}$ information as shown in (5.15)-(5.18).

$$\boldsymbol{TTR}_{s,se}^{\boldsymbol{br,fail}} = \left[TTR_{1,s,se}^{br,fail}, TTR_{2,s,se}^{br,fail}, \dots, TTR_{n_{br},s,se}^{br,fail}\right] \quad , \forall s \in \Omega_s', \forall se \in \Omega_{se} \quad (5.15)$$

$$TTR_{i,s,se}^{br,fail} = round\left(\begin{matrix}\varphi^{br}\left(v_{t=t_{i,s,se}^{br,fail0},s,se}^{gust}\right) \\ \times MTTR^{nw}\end{matrix}\right), \forall i \in \Omega_{LIN}^{fail}, \forall s \in \Omega_s^{pre}, \forall se \in \Omega_{se} \quad (5.16)$$

$$\varphi^{br}\left(v_{t,s,se}^{gust}\right) = \begin{cases} 1 \quad , \ if \ v_{t,s,se}^{gust} < v_{cri}^{low} \\ \varphi \sim U[h_1^{low}, h_2^{low}], \ if \ v_{cri}^{low} \leq v_{t,s,se}^{gust} \leq v_{cri}^{high} \\ \varphi \sim U[h_1^{high}, h_2^{high}], \ if \ v_{t,s,se}^{gust} > v_{cri}^{high} \end{cases}$$
$$, \forall i \in \Omega_{LIN}^{fail}, \forall s \in \Omega_s^{pre}, \forall se \in \Omega_{se} \quad (5.17)$$

$$\mathbf{AV}_{s,se}^{\mathbf{I-II,orig}} = \begin{bmatrix} a_{1,1,s,se}^{br}, a_{1,t=t_{i,s,se}^{br,rep},s,se}^{br,new}, \dots, a_{1,N_T,s,se}^{br,new} \\ a_{2,1,s,se}^{br}, a_{2,t=t_{i,s,se}^{br,rep},s,se}^{br,new}, \dots, a_{2,N_T,s,se}^{br,new} \\ \vdots \\ a_{n_{br},1,s,se}^{br}, a_{n_{br},t=t_{i,s,se}^{br,rep},s,se}^{br,new}, \dots, a_{n_{br},N_T,s,se}^{br,new} \end{bmatrix}, \forall s \in \Omega_s^{\prime\prime,orig}, \forall se \in \Omega_{se} \quad (5.18)$$

Next, the highest impact scenarios are determined for each season se until reaching the desired number of samples, i.e., $N-\left(K_{s,se}^{HI}\right)$ are chosen first, where $N-\left(K_{s,se}\right)$ denotes N-K contingencies for scenarios s,se, $K_{s,se}$ corresponds to the number of fault locations occurred in the network for scenarios s,se. In case the highest impact selected scenarios do not reach the expected number of samples, available space(s) are fulfilled by the scenarios $N-\left(K_{s,se}^{HI}-1\right)$, then $N-\left(K_{s,se}^{HI}-2\right)$ until the N-1 contingency.

$$\mathbf{AV}_{s,se}^{\mathbf{I-II}}=\mathbf{AV}_{s,se}^{\mathbf{I-II,orig}}\{N-(K)\} \qquad ,\forall s\in\Omega_s'',\forall se\in\Omega_{se} \tag{5.19}$$

The procedure for generating the **AV** matrix is illustrated in Figure 5. 4.

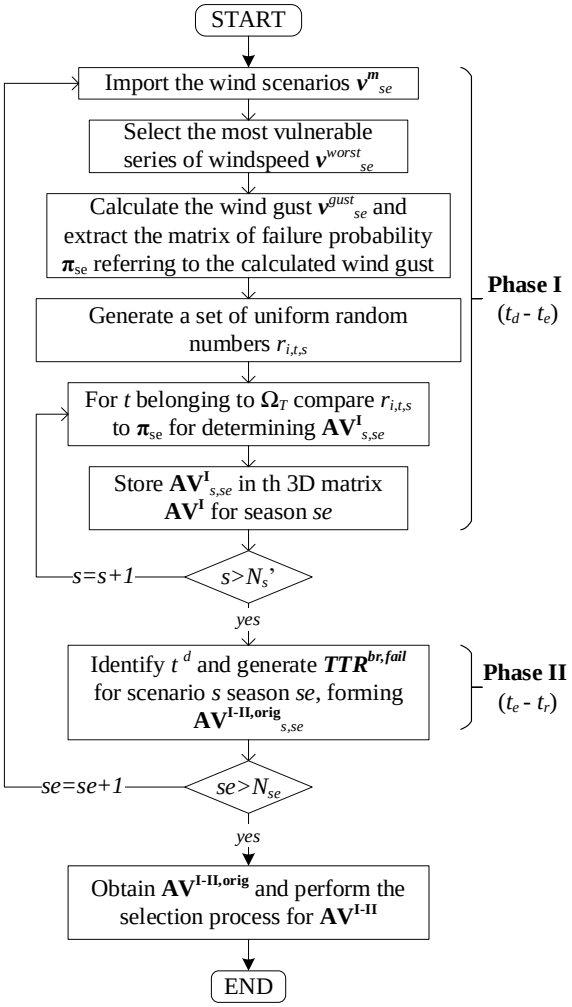

FIGURE 5. 4: Weather-related algorithm for generating branch availability matrix

5.4 Stage II: Planning Problem Formulation

In this section the problem formulation is detailed for both outer- and lower-levels, including respective discussions on objective functions, constraints, and decision variables.

5.4.1 Outer Level: Optimal Allocation Level

The outer level problem formulation is responsible for the allocation of the planning elements include the DDGs, WTs, PVs, ESSs and ISWs. For this, the following multi-objective problem formulations is developed.

5.4.1.1 Objective Function for Outer Level

The multi-objective function for the outer level considers three main perspectives, i.e., 1) resilience enhancement, 2) economic benefit, and 3) environmental impact mitigation. The proposed optimization problem is solved using a multi-objective optimization. This allows the solution to this problem to entail the best trade-off between these possibly conflicting objectives and enable to select the optimal design under each objective's consideration i.e., thought the pareto set. In this work, each objective detailed described in the following subsections.

a) Resilience Index

The resilience index is responsible for ensuring the system capacity to withstand HILP events. For this, the system's loss performance considering the duration of degradation and the importance of rapid recovery has been used [56]. The resilience index considering Phase I and II can be expressed using (5.20).

$$RESI = \frac{1}{t^r - t^e} \int_{t^e}^{t^r} \left[\frac{SPF_0(t) - SPF(t)}{SPF(t)} \right] dt \tag{5.20}$$

Then, by considering the set of scenarios s and season se according to Figure 5. 1, eq. (5.20) can be re-formulated into (5.21)-(5.22). This perspective allows for combining the multiple inner level season and scenarios information, i.e., $\forall s \in \Omega_s''$ and $\forall se \in \Omega_{se}$, in a way to determine a single value for the outer level resilience index.

$$RESI_{s,se} = \frac{1}{t^r_{s,se} - t^e_{s,se}} \int_{t^e_{s,se}}^{t^r_{s,se}} \left(\frac{\begin{pmatrix} \sum_{i \in \Omega_{BUS}} P^L_{i,t,s,se} \\ - \sum_{i \in \Omega_{BUS}} (1 - b^{curt}_{i,t,s,se}) P^L_{i,t,s,se} \end{pmatrix}}{\sum_{i \in \Omega_{BUS}} P^L_{i,t,s,se}} \right) dt \quad , \forall s \in \Omega_s'', \forall se \in \Omega_{se} \tag{5.21}$$

$$RESI^{OLEV} = \sum_{s\in\Omega_{se}} \frac{1}{N_s''} \sum_{s\in\Omega_s''} RESI_{s,se} \quad (5.22)$$

b) Economic Index

The second objective function relates to the economic benefit, i.e., capital cost, installation cost, and O&M cost for ISWs [91] and DERs [83], [85], [102]. Where, eq. (5.23) defines the total cost as the second objective function for the outer level. Eqs. (5.24)-(5.26) determine the capital and O&M cost for the DDG, while (5.27) normalizes the cost (5.24) and (5.26) for DDG units by considering the planning lifetime TL. Similarly, eqs. (5.28)-(5.33) summarize the capital and O&M cost for the allocated WTs and PVs. In term of the ESS, (5.34) and (5.35) determine the capital cost depending to ESS power and energy density, respectively. The annual O&M cost and the installation cost for the ESS can be calculated using (5.36) and (5.37), respectively. In (5.38) the normalized cost for ESS considering TL is expressed. Finally, the cost for ISWs can be determined using (5.39)-(5.41).

$$TC^{OLEV} = (C^{DDG} + C^{WT} + C^{PV} + C^{ESS} + C^{ISW}) \quad (5.23)$$

$$CPC^{DDG} = \sum_{\forall i\in\Omega_{DDG}^{can}} \left(P_i^{DDG,size} \sigma_{INV}^{DDG}\right) \quad (5.24)$$

$$OMC_{s,se}^{DDG} = S_{base} \begin{pmatrix} \sigma^{fuel}/\eta^{DDG} \\ +\sigma_{O\&M}^{DDG} \end{pmatrix} \sum_{\forall i\in\Omega_{DDG}} \sum_{\forall t\in\Omega_T} P_{i,t,s,se}^{DDG} \quad ,\forall s \in \Omega_s', \forall se \in \Omega_{se} \quad (5.25)$$

$$AOMC^{DDG} = \frac{365}{4} \sum_{\forall se\in\Omega_{se}} \sum_{\forall s\in\Omega_s'} \left(\pi_{s,se}^{wiso} OMC_{s,se}^{DDG}\right) \quad (5.26)$$

$$C^{DDG} = CPC^{DDG} + TL \times AOMC^{DDG} \quad (5.27)$$

$$CPC^{PV} = \sum_{\forall i\in\Omega_{PV}^{can}} \left(P_i^{PV,size} \sigma_{INV}^{PV}\right) \quad (5.28)$$

$$AOMC^{PV} = \sum_{\forall i\in\Omega_{PV}^{can}} \left(P_i^{PV,size} \sigma_{O\&M}^{PV}\right) \quad (5.29)$$

$$C^{PV} = CPC^{PV} + TL \times AOMC^{PV} \quad (5.30)$$

$$CPC^{WT} = \sum_{\forall i\in\Omega_{WT}^{can}} \left(P_i^{WT,size} \sigma_{INV}^{WT}\right) \quad (5.31)$$

$$AOMC^{WT} = \sum_{\forall i\in\Omega_{WT}^{can}} \left(P_i^{WT,size} \sigma_{O\&M}^{WT}\right) \quad (5.32)$$

$$C^{WT} = CPC^{WT} + TL \times AOMC^{WT} \quad (5.33)$$

$$CPC^{ESS,P} = \sum_{\forall i \in \Omega_{ESS}^{can}} \left(P_i^{ESS,size} \sigma_{INV}^{ESS,P} \right) \quad (5.34)$$

$$CPC^{ESS,E} = \sum_{\forall i \in \Omega_{ESS}^{can}} \left(E_i^{ESS,size} \sigma_{INV}^{ESS,E} \right) \quad (5.35)$$

$$AOMC^{ESS} = \sum_{\forall i \in \Omega_{ESS}^{can}} \left(P_i^{ESS,size} \sigma_{O\&M}^{ESS} \right) \quad (5.36)$$

$$INSC^{ESS} = \sum_{\forall i \in \Omega_{ESS}^{can}} \left(E_i^{ESS,size} \sigma_{INS}^{ESS} \right) \quad (5.37)$$

$$C^{ESS} = (CPC^{ESS,P} + TL \times AOMC^{ESS} + CPC^{ESS,E} + INSC^{ESS}) \quad (5.38)$$

$$CPC^{ISW} = \sum_{\forall i \in \Omega_{ISW}^{can}} (b_i^{ISW} \sigma_{INV}^{ISW}) \quad (5.39)$$

$$AOMC^{ISW} = 8760 \sum_{\forall i \in \Omega_{ISW}^{can}} (b_i^{ISW} \sigma_{O\&M}^{ISW}) \quad (5.40)$$

$$C^{ISW} = CPC^{ISW} + TL \times AOMC^{ISW} \quad (5.41)$$

c) Environmental Impact Index

The environment impact index aims to reduce the carbon footprint due to energy purchases from the main grid and energy generated by DDG [102], [103]. The annual carbon emission can be calculated using the expressions below. Eqs. (5.42) and (5.43) are the CO_2 emission quantity and their annualized kg/year from the DDGs generation. Eqs. (5.44) and (5.45) represent the CO_2 emission depending on the power imported from the main grid. Finally, (5.46) defines the total annualized Carbon emission as the third objective function for the outer level.

$$EMIS_{s,se}^{DDG} = K_{CO2}^{DDG} S_{base} \sum_{\forall i \in \Omega_{DDG}} \sum_{\forall t \in \Omega_T} P_{i,t,s,se}^{DDG} \quad ,\forall s \in \Omega_s', \forall se \in \Omega_{se} \quad (5.42)$$

$$AEMIS^{DDG} = \frac{365}{4} \sum_{\forall se \in \Omega_{se}} \sum_{\forall s \in \Omega_s'} \left(\pi_{s,se}^{wiso} EMIS_{s,se}^{DDG} \right) \quad (5.43)$$

$$EMIS_{s,se}^{GRID} = K_{CO2}^{GRID} S_{base} \sum_{\forall t \in \Omega_T} P_{t,s,se}^{GRID+} \quad ,\forall s \in \Omega_s', \forall se \in \Omega_{se} \quad (5.44)$$

$$AEMIS^{GRID} = \frac{365}{4} \sum_{\forall se \in \Omega_{se}} \sum_{\forall s \in \Omega_s'} \left(\pi_{s,se}^{wiso} EMIS_{s,se}^{GRID} \right) \quad (5.45)$$

$$AEMIS^{OLEV} = AEMIS^{DDG} + AEMIS^{GRID} \quad (5.46)$$

5.4.1.2 Constraints for Outer Level

Next, system's constraints and decision variables for optimizing the outer level are following depicted.

a) Discrete Size for DERs Constraints

The DERs size were discretized with a fixed step [103].

$$P_i^{DDG,size} = b_i^{DDG,size} P_{step}^{DDG} \quad ,\forall i \in \Omega_{DDG}^{can} \tag{5.47}$$

$$P_i^{WT,size} = b_i^{WT,size} P_{step}^{WT} \quad ,\forall i \in \Omega_{WT}^{can} \tag{5.48}$$

$$P_i^{PV,size} = b_i^{PV,size} P_{step}^{PV} \quad ,\forall i \in \Omega_{PV}^{can} \tag{5.49}$$

$$P_i^{ESS,size} = b_i^{ESP,size} P_{step}^{ESS} \quad ,\forall i \in \Omega_{ESS}^{can} \tag{5.50}$$

$$E_i^{ESS,size} = r_i^{ESS} \times P_i^{ESS,size} \quad ,\forall i \in \Omega_{ESS}^{can} \tag{5.51}$$

b) Maximum Bus Power Allowable Constraints

The DER(s) connected to an individual bus must respected the technical constraints defined by (5.52) [103]:

$$\sum_{\forall DER \in \{DDG,PV,WT,ESS\}} P_i^{DER,size} \leq P_i^{bus,max} \quad ,\forall i \in \Omega_{BUS} \tag{5.52}$$

c) Installation Discrete Binary Constraints

$$0 \leq b_i^{DDG,size} \leq P_i^{DDG,max} / P_{step}^{DDG} \quad ,\forall i \in \Omega_{DDG}^{can} \tag{5.53}$$

$$0 \leq b_i^{WT,size} \leq P_i^{WT,max} / P_{step}^{WT} \quad ,\forall i \in \Omega_{WT}^{can} \tag{5.54}$$

$$0 \leq b_i^{PV,size} \leq P_i^{PV,max} / P_{step}^{PV} \quad ,\forall i \in \Omega_{PV}^{can} \tag{5.55}$$

$$0 \leq b_i^{ESP,size} \leq P_i^{ESS,max} / P_{step}^{ESS} \quad ,\forall i \in \Omega_{ESS}^{can} \tag{5.56}$$

$$0 \leq b_i^{ISW} \leq 1 \quad ,\forall i \in \Omega_{ISW}^{can} \tag{5.57}$$

5.4.1.3 Decision Variables for Outer Level

The decision variables for optimizing the outer level are summarized in Table 5. 1. Here one should note that variables associated with each planning element are respectively set to zero for the case that the optimization decides to not place these elements on the candidate buses or branches. Otherwise, these variables are the integer numbers respecting to the upper bounds defined in (53)-(57), and the binary value '1' for b_i^{ISW}.

TABLE 5. 1: Decision Variables Type and Set Belonging for the Outer Level Problem

Variables $\boldsymbol{X^{OLEV}}$	type	Set $\forall i \in$
$b_i^{DDG,size}$	$\mathbb{Z}$	Ω_{DDG}^{can}
$b_i^{WT,size}$	$\mathbb{Z}$	Ω_{WT}^{can}
$b_i^{PV,size}$	$\mathbb{Z}$	Ω_{PV}^{can}
$b_i^{ESP,size}$	$\mathbb{Z}$	Ω_{ESS}^{can}
b_i^{ISW}	$\mathbb{Z}$	Ω_{ISW}^{can}

5.4.2 Inner Level: Optimal Power Flow for Microgrid

This level presents the problem to be solved using the proposed machine learning based technique. Still, first a pre-problem formulated as a MILP model similar to the work in [3] is developed. This inner level optimization solutions provide the samples solutions needed to train the proposed machine learning-based strategy using the upper-level solutions as inputs. For this, this problem models the ability of microgrids to operate in both grid-connected and IS mode, depending on the operation status of the main isolate switch (ISW^{sub}) as shown in Figure 5. 5. Details on the problem formulation and optimization strategy including objective function, constraints and decision variables are following depicted.

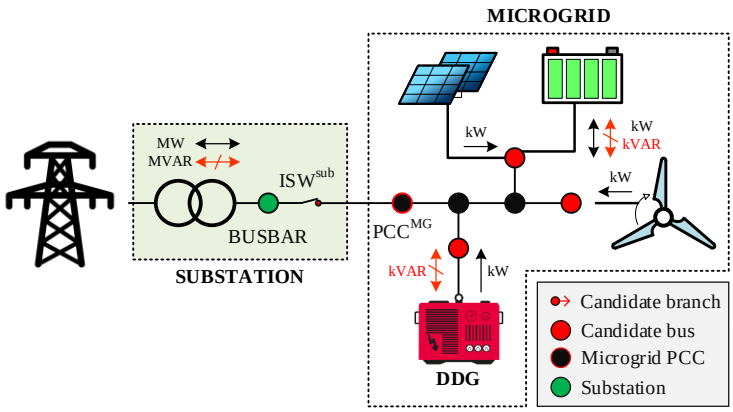

FIGURE 5. 5: Basic scheme of the single microgrid base ISW^{sub}

5.4.2.1 Objective Function and Constraints for Inner Level

The objective function formulated for the optimal operation in the inner level are expressed by (5.58)-(5.59). First, in (5.58) the objective function is obtained normalizing the four terms as a single total operation cost to be minimized. The first term in (5.58) represents the cost of power exchange between the microgrid and the main grid, which can be determined using (5.59). Then, the second term is given by (5.60), which refers to the fuel consumption cost for the DDG units in use at the MGs [104], [102]. As one may observe, (5.58), (5.59) and (5.60) are restricted to the grid-connected mode due to the association of the binary variable $b_{t,s,se}^{m}$, i.e., $b_{t,s,se}^{m}$ is the binary number that denotes the operation status for ISW$^{\text{sub}}$ along Ω_T, where $b_{t,s,se}^{m} = 1$ represents the microgrid operation in islanding mode, otherwise $b_{t,s,se}^{m} = 0$ denotes the system operation in grid-connected mode. In this sense, $b_{t,s,se}^{m}$ can be used as multiplication and integrated in the MILP model for allowing the objective function and constraints pertaining to the operation mode for microgrid. The third term given by (5.61) represents the cost for load curtailment, being restricted for islanded mode only [26]. The last term depicted in (5.62) represents the voltage violation index. This term seeks to improve the voltage quality of the microgrid during both operation modes. For this, the following assumptions are made: 1) during grid connected mode, the DDG units are operated in PQ$^{\text{mode}}$ [52], [54], 2) during IS mode the DDG units are operated under a secondary control layer with V^{**} identically set for all DDG units.

$$OF_{s,se}^{MILP} = \sum_{t\in\Omega_T}\left[C_{t,s,se}^{PCC}\left(1-b_{t,s,se}^{m}\right) + C_{t,s,se}^{DDG}\left(1-b_{t,s,se}^{m}\right) + C_{t,s,se}^{CURT}b_{t,s,se}^{m} + C_{t,s,se}^{VI}\right] \quad ,\forall s \in \Omega_s' \cup \Omega_s'', \forall se \in \Omega_{se} \qquad (5.58)$$

$$C_{t,s,se}^{PCC} = S_{base}\left(\sigma_{t,s,se}^{PCC}P_{i=1,t,s,se}^{PCC}\right)\Delta t \quad ,\forall t \in \Omega_T, \forall s \in \Omega_s' \cup \Omega_s'', \forall se \in \Omega_{se} \qquad (5.59)$$

$$C_{t,s,se}^{DDG} = S_{base}\left(\sum_{i\in\Omega_{DDG}} P_{i,t,s,se}^{DDG}\left(\sigma^{fuel}/\eta^{DDG} + \sigma_{O\&M}^{DDG}\right)\right)\Delta t \quad ,\forall t \in \Omega_T, \forall s \in \Omega_s' \cup \Omega_s'', \forall se \in \Omega_{se} \qquad (5.60)$$

$$C_{t,s,se}^{CURT} = S_{base}\left(\sigma^{curt}\sum_{i\in\Omega_{BUS}} b_{i,t,s,se}^{curt}w_i^{load}P_{i,t,s,se}^{L}\right)\Delta t \quad ,\forall t \in \Omega_T, \forall s \in \Omega_s' \cup \Omega_s'', \forall se \in \Omega_{se} \qquad (5.61)$$

$$C_{t,s,se}^{VI} = V_{base}\left(PC^{VI}\left[\sum_{i\in\Omega_{BUS}}\left(\left(1-b_{t,s,se}^{m}\right)V^{GC,spec} + b_{t,s,se}^{m}V_i^{**} - V_{i,t,s,se}\right)\right]\right)\Delta t \quad ,\forall t \in \Omega_T, \forall s \in \Omega_s' \cup \Omega_s'', \forall se \in \Omega_{se} \qquad (5.62)$$

Subject to:

$$V^{min} \le V_{i,t,s,se} \le V^{max} \quad ,\forall i \in \Omega_{BUS}, \forall t \in \Omega_T, \forall s \in \Omega_s' \cup \Omega_s'', \forall se \in \Omega_{se} \qquad (5.63)$$

$$0 \le b_{i,t,s,se}^{curt} \le b_{t,s,se}^{m} \qquad ,\forall i \in \Omega_{BUS}, \forall t \in \Omega_T, \forall s \in \Omega_s' \cup \Omega_s'', \forall se \in \Omega_{se} \qquad (5.64)$$

$$P_{i,t,s,se} = \begin{pmatrix} \sum_{j\in\Omega_{BUS}} G_{ij} V_{i,t,s,se} \\ -\sum_{j\in\Omega_{BUS}} B_{ij} \delta_{j,t,s,se} \end{pmatrix} = \begin{pmatrix} P_{i,t,s,se}^{PCC} + P_{i,t,s,se}^{DDG} \\ +P_{i,t,s,se}^{WT,use} + P_{i,t,s,se}^{PV,use} \\ +P_{i,t,s,se}^{dch} - \eta_i^{ESS} P_{i,t,s,se}^{ch} \\ -P_{i,t,s,se}^{L}\left(1 - b_{i,t,s,se}^{curt}\right) \end{pmatrix}$$
$$,\forall i \in \Omega_{BUS}, \forall t \in \Omega_T, \forall s \in \Omega_s' \cup \Omega_s'', \forall se \in \Omega_{se} \qquad (5.65)$$

$$Q_{i,t,s,se} = \begin{pmatrix} -\sum_{j\in\Omega_{BUS}} B_{ij} V_{i,t,s,se} \\ -\sum_{j\in\Omega_{BUS}} G_{ij} \delta_{j,t,s,se} \end{pmatrix} = \begin{pmatrix} +Q_{i,t,s,se}^{PCC} + Q_{i,t,s,se}^{DDG} \\ +Q_{i,t,s,se}^{ESS} \\ -Q_{i,t,s,se}^{L}\left(1 - b_{i,t,s,se}^{curt}\right) \end{pmatrix}$$
$$,\forall i \in \Omega_{BUS}, \forall t \in \Omega_T, \forall s \in \Omega_s' \cup \Omega_s'', \forall se \in \Omega_{se} \qquad (5.66)$$

$$P_{k,t,s,se}^{br} = \left(g_{i(k)j(k)}\left(V_{i,t,s,se} - V_{j,t,s,se}\right) + b_{i(k)j(k)}\left(\delta_{i,t,s,se} - \delta_{j,t,s,se}\right)\right)$$
$$,\forall k \in \Omega_{LIN}, \forall t \in \Omega_T, \forall s \in \Omega_s' \cup \Omega_s'', \forall se \in \Omega_{se} \qquad (5.67)$$

$$Q_{k,t,s,se}^{br} = \left(b_{i(k)j(k)}\left(V_{i,t,s,se} - V_{j,t,s,se}\right) + g_{i(k)j(k)}\left(\delta_{i,t,s,se} - \delta_{j,t,s,se}\right)\right)$$
$$,\forall k \in \Omega_{LIN}, \forall t \in \Omega_T, \forall s \in \Omega_s' \cup \Omega_s'', \forall se \in \Omega_{se} \qquad (5.68)$$

$$L_{k,t,s,se}^{br} = \begin{cases} \alpha_n^{1^{st}} P_{k,t,s,se}^{br} + \beta_n^{1^{st}} Q_{k,t,s,se}^{br} - \gamma^{1^{st}} I_k^{br,max} V_{i(k),t,s,se} \le 0 \\ -\alpha_n^{1^{st}} P_{k,t,s,se}^{br} + \beta_n^{1^{st}} Q_{k,t,s,se}^{br} - \gamma^{1^{st}} I_k^{br,max} V_{i(k),t,s,se} \le 0 \\ -\alpha_n^{4^{th}} P_{k,t,s,se}^{br} - \beta_n^{4^{th}} Q_{k,t,s,se}^{br} - \gamma^{4^{th}} I_k^{br,max} V_{i(k),t,s,se} \le 0 \\ \alpha_n^{4^{th}} P_{k,t,s,se}^{br} - \beta_n^{4^{th}} Q_{k,t,s,se}^{br} - \gamma^{4^{th}} I_k^{br,max} V_{i(k),t,s,se} \le 0 \end{cases}$$
$$,n = 1,2,\dots,n_{pw}, \forall t \in \Omega_T, \forall k \in \Omega_{LIN}, \forall i \in \Omega_{BUS}, \forall s \in \Omega_s' \cup \Omega_s'', \forall se \in \Omega_{se} \qquad (5.69)$$

$$P_{i,t,s,se}^{DDG} = \left(\left[-k^{i\omega}\left(\delta_{t,s,se}^{MG} - \pi/2\right)/m_i^p\right] b_{t,s,se}^{m} + \left(1 - b_{t,s,se}^{m}\right) P_{i,t,s,se}^{DDG}\right)$$
$$,\forall i \in \Omega_{DDG}, \forall t \in \Omega_T, \forall s \in \Omega_s' \cup \Omega_s'', \forall se \in \Omega_{se} \qquad (5.70)$$

$$Q_{i,t,s,se}^{DDG} = \left(\left[\left(V_i^* - V_{i,t,s,se} + u_{i,t,s,se}^{v}\right)/n_i^q\right] b_{t,s,se}^{m} + \left(1 - b_{t,s,se}^{m}\right) Q_{i,t,s,se}^{DDG}\right)$$
$$,\forall i \in \Omega_{DDG}, \forall t \in \Omega_T, \forall s \in \Omega_s' \cup \Omega_s'', \forall se \in \Omega_{se} \qquad (5.71)$$

$$V_{i,t,s,se} b_{t,s,se}^{m} = V_i^{**} b_{t,s,se}^{m} \qquad ,\forall i \in \Omega_{DDG}, \forall t \in \Omega_T, \forall s \in \Omega_s' \cup \Omega_s'', \forall se \in \Omega_{se} \qquad (5.72)$$

$$S_i^{DDG,max} = P_i^{DDG,size} \qquad ,\forall i \in \Omega_{DDG} \qquad (5.73)$$

$$m_i^p = \Delta\omega / S_i^{DDG,max} \qquad ,\forall i \in \Omega_{DDG} \tag{5.74}$$

$$n_i^q = \Delta V / 2\chi_i^{DDG,max} S_i^{DDG,max} \qquad ,\forall i \in \Omega_{DDG} \tag{5.75}$$

$$0 \le P_{i,t,s,se}^{DDG} \le S_i^{DDG,max} \qquad ,\forall i \in \Omega_{DDG}, \forall t \in \Omega_T, \forall s \in \Omega_s' \cup \Omega_s'', \forall se \in \Omega_{se} \tag{5.76}$$

$$\chi_i^{DDG,min} S_i^{DDG,max} \le Q_{i,t,s,se}^{DDG} \le \chi_i^{DDG,max} S_i^{DDG,max} \\ ,\forall i \in \Omega_{DDG}, \forall t \in \Omega_T, \forall s \in \Omega_s' \cup \Omega_s'', \forall se \in \Omega_{se} \tag{5.77}$$

$$-P_{i,t,s,se}^{DDG}\, tg\left(\cos^{-1} PF_i^{DDG,4th}\right) \le Q_{i,t,s,se}^{DDG} \le P_{i,t,s,se}^{DDG}\, tg\left(\cos^{-1} PF_i^{DDG,1st}\right) \\ ,\forall i \in \Omega_{DDG}, \forall t \in \Omega_T, \forall s \in \Omega_s' \cup \Omega_s'', \forall se \in \Omega_{se} \tag{5.78}$$

$$L_{i,t,s,se}^{DDG} = \begin{cases} \alpha_n^{1^{st}} P_{i,t,s,se}^{DDG} + \beta_n^{1^{st}} Q_{i,t,s,se}^{DDG} - \gamma^{1^{st}} S_i^{DDG,max} \le 0 \\ \alpha_n^{4^{th}} P_{i,t,s,se}^{DDG} - \beta_n^{4^{th}} Q_{i,t,s,se}^{DDG} - \gamma^{4^{th}} S_i^{DDG,max} \le 0 \end{cases} \\ ,n = 1,2,\dots,n_{pw}, \forall t \in \Omega_T, \forall i \in \Omega_{DDG}, \forall s \in \Omega_s' \cup \Omega_s'', \forall se \in \Omega_{se} \tag{5.79}$$

$$0 \le P_{i,t,s,se}^{WT,use} \le P_{i,t,s,se}^{WT} \qquad ,\forall i \in \Omega_{WT}, \forall t \in \Omega_T, \forall s \in \Omega_s' \cup \Omega_s'', \forall se \in \Omega_{se} \tag{5.80}$$

$$0 \le P_{i,t,s,se}^{PV,use} \le P_{i,t,s,se}^{PV} \qquad ,\forall i \in \Omega_{PV}, \forall t \in \Omega_T, \forall s \in \Omega_s' \cup \Omega_s'', \forall se \in \Omega_{se} \tag{5.81}$$

$$S_i^{ESS,max} = P_i^{ESS,size} \qquad ,\forall i \in \Omega_{ESS} \tag{5.82}$$

$$0 \le P_{i,t,s,se}^{dch} \le S_i^{ESS,max} b_{i,t,s,se}^{ESS} \qquad ,\forall i \in \Omega_{ES}, \forall t \in \Omega_T, \forall s \in \Omega_s' \cup \Omega_s'', \forall se \in \Omega_{se} \tag{5.83}$$

$$0 \le P_{i,t,s,se}^{ch} \le S_i^{ESS,max}\left(1 - b_{i,t,s,se}^{ESS}\right) \\ ,\forall i \in \Omega_{ES}, \forall t \in \Omega_T, \forall s \in \Omega_s' \cup \Omega_s'', \forall se \in \Omega_{se} \tag{5.84}$$

$$\chi_i^{ESS,min} S_i^{ESS,max} \le Q_{i,t,s,se}^{ESS} \le \chi_i^{ESS,max} S_i^{ESS,max} \\ ,\forall i \in \Omega_{ES}, \forall t \in \Omega_T, \forall s \in \Omega_s' \cup \Omega_s'', \forall se \in \Omega_{se} \tag{5.85}$$

$$L_{i,t,s,se}^{ESS} = \begin{cases} \alpha_n^{1^{st}}\left(P_{i,t,s,se}^{dch} - P_{i,t,s,se}^{ch}\right) + \beta_n^{1^{st}} Q_{i,t,s,se}^{ESS} - \gamma^{1^{st}} S_i^{ESS,max} \le 0 \\ -\alpha_n^{1^{st}}\left(P_{i,t,s,se}^{dch} - P_{i,t,s,se}^{ch}\right) + \beta_n^{1^{st}} Q_{i,t,s,se}^{ESS} - \gamma^{1^{st}} S_i^{ESS,max} \le 0 \\ -\alpha_n^{4^{th}}\left(P_{i,t,s,se}^{dch} - P_{i,t,s,se}^{ch}\right) - \beta_n^{4^{th}} Q_{i,t,s,se}^{ESS} - \gamma^{4^{th}} S_i^{ESS,max} \le 0 \\ \alpha_n^{4^{th}}\left(P_{i,t,s,se}^{dch} - P_{i,t,s,se}^{ch}\right) - \beta_n^{4^{th}} Q_{i,t,s,se}^{ESS} - \gamma^{4^{th}} S_i^{ESS,max} \le 0 \end{cases} \\ ,n = 1,2,\dots,n_{pw}, \forall t \in \Omega_T, \forall i \in \Omega_{ESS}, \forall s \in \Omega_s' \cup \Omega_s'', \forall se \in \Omega_{se} \tag{5.86}$$

$$E_{i,t,s,se}^{ESS} = \begin{cases} SOC_i^0 E_i^{ESS,size} + \left(\eta_i^{ESS} P_{i,t,s,se}^{ch} - P_{i,t,s,se}^{dch}\right)\Delta t, \ t = 1 \\ E_{i,t-1,s,se}^{ESS} + \left(\eta_i^{ESS} P_{i,t,s,se}^{ch} - P_{i,t,s,se}^{dch}\right)\Delta t, \ t \geq 2 \end{cases}$$
$$,\forall i \in \Omega_{ESS}, \forall t \in \Omega_T, \forall s \in \Omega_s' \cup \Omega_s'', \forall se \in \Omega_{se} \quad (5.87)$$

$$DoD_i^{max} E_i^{ESS,size} \leq E_{i,t,s,se}^{ESS} \leq E_i^{ESS,size}$$
$$,\forall i \in \Omega_{ESS}, \forall t \in \Omega_T, \forall s \in \Omega_s' \cup \Omega_s'', \forall se \in \Omega_{se} \quad (5.88)$$

$$E_{i,t=N_T,s,se}^{ESS} \geq SOC_i^0 E_i^{ESS,size} \quad ,\forall i \in \Omega_{ESS}, \forall s \in \Omega_s' \cup \Omega_s'', \forall se \in \Omega_{se} \quad (5.89)$$

$$-S_i^{TR,max}\left(1 - b_{t,s,se}^m\right) \leq P_{i,t,s,se}^{PCC} \leq S_i^{TR,max}\left(1 - b_{t,s,se}^m\right)$$
$$,\forall i \in \Omega_{PCC}, \forall t \in \Omega_T, \forall s \in \Omega_s' \cup \Omega_s'', \forall se \in \Omega_{se} \quad (5.90)$$

$$\chi_i{}^{TR,min} S_i^{TR,max}\left(1 - b_{t,s,se}^m\right) \leq Q_{i,t,s,se}^{PCC} \leq \chi_i{}^{TR,max} S_i^{TR,max}\left(1 - b_{t,s,se}^m\right)$$
$$,\forall i \in \Omega_{PCC}, \forall t \in \Omega_T, \forall s \in \Omega_s' \cup \Omega_s'', \forall se \in \Omega_{se} \quad (5.91)$$

$$L_{i,t,s,se}^{PCC} = \begin{cases} \alpha_n^{1^{st}} P_{i,t,s,se}^{PCC} + \beta_n^{1^{st}} Q_{i,t,s,se}^{PCC} - \gamma^{1^{st}} S_i^{TR,max} \leq 0 \\ -\alpha_n^{1^{st}} P_{i,t,s,se}^{PCC} + \beta_n^{1^{st}} Q_{i,t,s,se}^{PCC} - \gamma^{1^{st}} S_i^{TR,max} \leq 0 \\ -\alpha_n^{4^{th}} P_{i,t,s,se}^{PCC} - \beta_n^{4^{th}} Q_{i,t,s,se}^{PCC} - \gamma^{4^{th}} S_i^{TR,max} \leq 0 \\ \alpha_n^{4^{th}} P_{i,t,s,se}^{PCC} - \beta_n^{4^{th}} Q_{i,t,s,se}^{PCC} - \gamma^{4^{th}} S_i^{TR,max} \leq 0 \end{cases}$$
$$,n = 1,2,\dots,n_{pw}, \forall t \in \Omega_T, \forall i \in \Omega_{PCC},, \forall s \in \Omega_s' \cup \Omega_s'', \forall se \in \Omega_{se} \quad (5.92)$$

$$-P_{i,t,s,se}^{PCC}\, tg\left(\cos^{-1} PF_i^{TR,4th}\right) \leq Q_{i,t,s,se}^{PCC} \leq P_{i,t,s,se}^{PCC}\, tg\left(\cos^{-1} PF_i^{TR,1st}\right)$$
$$,\forall i \in \Omega_{PCC}, \forall t \in \Omega_T, \forall s \in \Omega_s' \cup \Omega_s'', \forall se \in \Omega_{se} \quad (5.93)$$

$$V_{i,t,s,se}\left(1 - b_{t,s,se}^m\right) = V^{GC,spec}\left(1 - b_{t,s,se}^m\right)$$
$$,\forall i \in \Omega_{PCC}, \forall t \in \Omega_T, \forall s \in \Omega_s' \cup \Omega_s'', \forall se \in \Omega_{se} \quad (5.94)$$

$$\delta_{i,t,s,se}\left(1 - b_{t,s,se}^m\right) = 0 \quad ,\forall i \in \Omega_{PCC}, \forall t \in \Omega_T, \forall s \in \Omega_s' \cup \Omega_s'', \forall se \in \Omega_{se} \quad (5.95)$$

The inequality (5.63) represents the general constrain that guarantees the voltage magnitude for difference individual buses within magnitude limits. Eq. (5.64) guarantees load curtailment during IS mode. The microgrid model is obtained using the power flow model given by (5.65)-(5.69). Constraints (5.65) and (5.66) are the linear version for the node-based power flow equation that refers to the power injected to the i^{th} bus of the microgrid [3]. It is worth noting here that, (5.65) and (5.66) have been generally formulated for all buses. Thus, the variables representing the power exchange and generation (i.e., by DDG, WT, PV, ESS) that are not relevant to the power flow equations written

for bus i can be disregarded by setting the upper bound for these variables to zeros. Next, eqs. (5.67) and (5.68) are the linear version defining the active and reactive power flowing along a branch k in the microgrid. Where, $i(k)$ and $j(k)$ denote buses i and j located at the upstream and downstream of branch k, respectively. Finally, (5.69) is the piecewise linearization of the quadratic constraint limiting the line ampacity.

The DDG units are modeled using the steady state model (5.70)-(5.79). Figure 5. 6 shows the steady state model employed for representing operation constraints for the DDG units with $\mathrm{droop}/2^{\mathrm{nd}}$. Details of the derivation of the DDG unit operation constraints can be found in [3]. Constraints (5.70) and (5.71) define the active and reactive power generated by the DDG units during IS or GC mode. These constraints are composed of two terms associated with the binary input $b^{m}_{t,s,se}$. The first term of these constraints refers to the operation of the DDG unit under $\mathrm{droop}/2^{\mathrm{nd}}$ control during IS mode. The second terms represent the operation of the DDG unit in PQ mode during grid connected mode. As one may observe, the activation of the terms in (5.70) and (5.71) are conditioned to the binary input $b^{m}_{t,s,se}$ status. Eq. (5.72) guarantees the voltage of the DDG bus restoration to the nominal secondary setting voltage in IS mode. Eq. (5.73) defines the apparent power equal to the DDG allocated unit rated size. In this work, loads are considering to be shared proportionally to the capacity of the DDG units [26],[54]. Thus, the active and reactive droop gain can be calculated via the capacity-based model as expressed in (5.74) and (5.75). Eqs. (5.76) and (5.77) establish minimum and maximum boundary limits to the active and reactive power.

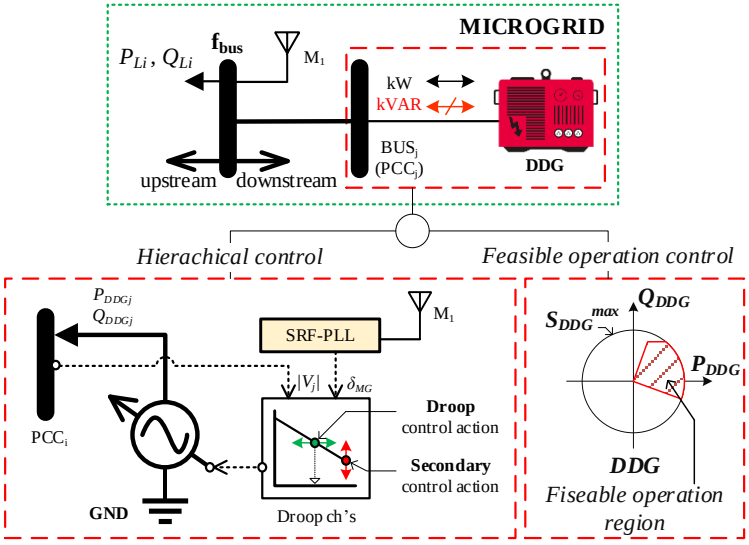

FIGURE 5. 6: Steady state model for DDG unit operate with $\mathrm{droop}/2^{\mathrm{nd}}$ in IS mode and their feasible operation region for both GC and IS mode

Constraint (5.78) guarantees that the relationship between the active and reactive power of a DDG unit is greater than the minimum set power factor. Finally (5.79) represents the set of piecewise linearization that ensures the operation of the DDG unit respecting its rated capacity $S_i^{DDG,max}$. Constraint (5.80) and (5.81) represent the power outputs of the WTs and PVs considering their actual MPPT power $P_{i,t,s,se}^{WT}$ and $P_{i,t,s,se}^{PV}$. ESS constraints are depicted in (5.82)-(5.89). For this, in this work, ESS unit are operated in PQ mode via its power electronic inverter interfaced (5.82). Nevertheless, with the power electronic interface the ESS can be operated with $\mathrm{droop}/2^{\mathrm{nd}}$ control similar to the work in [3]. Constraint (5.83)-(5.84) guarantee that the ESS units operation are restricted within the feasible operation region. In these constraints, the binary variable $b_{i,t,s,se}^{ESS}$ is introduced in (5.83) and (5.84) to avoid simultaneous charging and discharging states. Eq. (5.85) ensures that the reactive power delivered by the ESS units respect their maximum and minimum reactive power allowable setting. As the ESS unit is connected through an inverter, (5.86) defines the piecewise linearization representing the quadratic constrain for limiting the output to the maximum rated power denote by $S_i^{ESS,max}$. In (5.87) update SOC for the ESS are obtained for each time segment based on the charging/discharging energy flows, as well as considering the round-trip efficiency η_i^{ESS} [85], [84]. Constraint (5.88) guarantees that the energy stored in the ESS is restricted by its rated capacity and minimum energy storage setting. Finally (5.89) ensures that the energy stored in the ESS is available at the end of the planning horizons and ready for the next days.

Constraints for the power exchange between the microgrid and the main grid at the substation are given by (5.32)-(5.37). The constraints (5.90)-(5.93) guarantee the power exchange is restricted by transformers' feasible operation. First, (5.90) and (5.91) limit the active and reactive power exchange respecting to the transformer rated power. As well, the introduction of $b_{t,s,se}^{m}$ in (5.90) and (5.91) allows for deactivating these constraints during IS mode. Then, (5.92) is the piecewise linearization representing the quadratic constrain for limiting the active and reactive power exchange under the transformer rated capacity. The operation for transformer limits above the minimum power factor setting is given by (5.93). Finally (5.94) and (5.95) refer to the grid connected power flow conditions for voltage magnitude and phase angle at the $\mathrm{PCC}^{\mathrm{MG}}$ imposed by the main grid during grid connected mode.

The piecewise constraint coefficients for (5.69), (5.79), (5.86) and (5.92) can be calculated using (5.96)-(5.99). Details on the derivation of piecewise constrains coefficients for the quadratic constraints can be found in [3].

$$\alpha_n^{1^{st},4^{th}} = \cos\left(\varphi_n^{1^{st},4^{th}} + \left(n^{1^{st},4^{th}} - 1\right)\varphi_{sel}^{1^{st},4^{th}}/n_{pw}^{1^{st},4^{th}}\right) \quad ,n = 1,2,\dots,n_{pw} \tag{5.96}$$

$$\beta_n^{1^{st},4^{th}} = \sin\left(\varphi_n^{1^{st},4^{th}} + \left(n^{1^{st},4^{th}} - 1\right)\varphi_{sel}^{1^{st},4^{th}}/n_{pw}^{1^{st},4^{th}}\right) \quad ,n = 1,2,\dots,n_{pw} \tag{5.97}$$

$$\gamma^{1^{st},4^{th}} = \cos\left(\varphi_{sel}^{1^{st},4^{th}}/2n_{pw}^{1^{st},4^{th}}\right) \quad ,n = 1,2,\dots,n_{pw} \tag{5.98}$$

$$\varphi_0^{1^{st},4^{th}} = \varphi_{sel}^{1^{st},4^{th}}/2n_{pw}^{1^{st},4^{th}} \quad ,n = 1,2,\dots,n_{pw} \tag{5.99}$$

5.4.2.2 Decision variables for Inner Level

The decision variables for the MILP model seeking to optimize microgrids' operation are summarized in Table 5. 2.

TABLE 5. 2: Decision variables for MILP model for microgrid optimal operation

Variables		Set			
$\boldsymbol{X^{MILP}}$	Type	$\forall t \in$	$, \forall s \in$	$\forall se \in$	$\forall i,k \in$
$V_{i,t,s,se}$	$\mathbb{R}$	Ω_T	$\Omega_s' \cup \Omega_s''$	Ω_{se}	Ω_{BUS}
$\delta_{i,t,s,se}$	$\mathbb{R}$	Ω_T	$\Omega_s' \cup \Omega_s''$	Ω_{se}	Ω_{BUS}
$b_{i,t,s,se}^{curt}$	$\mathbb{Z}$	Ω_T	$\Omega_s' \cup \Omega_s''$	Ω_{se}	Ω_{BUS}
$P_{i,t,s,se}^{DDG}$	$\mathbb{R}$	Ω_T	$\Omega_s' \cup \Omega_s''$	Ω_{se}	Ω_{DDG}
$Q_{i,t,s,se}^{DDG}$	$\mathbb{R}$	Ω_T	$\Omega_s' \cup \Omega_s''$	Ω_{se}	Ω_{DDG}
$u_{i,t,s,se}^{v}$	$\mathbb{R}$	Ω_T	$\Omega_s' \cup \Omega_s''$	Ω_{se}	Ω_{DDG}
$P_{i,t,s,se}^{WT,use}$	$\mathbb{R}$	Ω_T	$\Omega_s' \cup \Omega_s''$	Ω_{se}	Ω_{WT}
$P_{i,t,s,se}^{PV,use}$	$\mathbb{R}$	Ω_T	$\Omega_s' \cup \Omega_s''$	Ω_{se}	Ω_{PV}
$P_{i,t,s,se}^{dch}$	$\mathbb{R}$	Ω_T	$\Omega_s' \cup \Omega_s''$	Ω_{se}	Ω_{ESS}
$P_{i,t,s,se}^{ch}$	$\mathbb{R}$	Ω_T	$\Omega_s' \cup \Omega_s''$	Ω_{se}	Ω_{ESS}
$Q_{i,t,s,se}^{ESS}$	$\mathbb{R}$	Ω_T	$\Omega_s' \cup \Omega_s''$	Ω_{se}	Ω_{ESS}
$E_{i,t,s,se}^{ESS}$	$\mathbb{R}$	Ω_T	$\Omega_s' \cup \Omega_s''$	Ω_{se}	Ω_{ESS}
$b_{i,t,s,se}^{ESS}$	$\mathbb{Z}$	Ω_T	$\Omega_s' \cup \Omega_s''$	Ω_{se}	Ω_{ESS}
$P_{i,t,s,se}^{PCC}$	$\mathbb{R}$	Ω_T	$\Omega_s' \cup \Omega_s''$	Ω_{se}	Ω_{PCC}
$Q_{i,t,s,se}^{PCC}$	$\mathbb{R}$	Ω_T	$\Omega_s' \cup \Omega_s''$	Ω_{se}	Ω_{PCC}
$P_{k,t,s,se}^{br}$	$\mathbb{R}$	Ω_T	$\Omega_s' \cup \Omega_s''$	Ω_{se}	Ω_{LIN}
$Q_{k,t,s,se}^{br}$	$\mathbb{R}$	Ω_T	$\Omega_s' \cup \Omega_s''$	Ω_{se}	Ω_{LIN}

5.5 Stage III: Optimal Operation based on Deep Neural Network (DNN) learning

The detailed modeling of the multiple components involved in microgrids for ensuring adequate operating conditions during grid-connected and isolated modes, make it unfeasible to solve this

problem using a MILP formulation due to the stochastic nature of the problem, and consequently, the implied high computational burden. In this sense, seeking to overcome these limitations while not reducing the modeling complexity in order to ensure feasible resilient solutions, a novel methodology using DNN technique is proposed. For this, effective training samples for the DNN models are necessary. These samples are composed of 1) the set of input samples for combinations of switch allocation and resources; and 2) the set of targets for the LOPF dependent indices used for determining the multi-objective functions of the outer level. To obtain this data, the LOPF model depicted in the Section 5.3 is used considering microgrid formation indicators-based N-K contingencies level. Here, given that the LOPF is simulated for set of sample inputs belonging to Ω_s, Ω_s'' and Ω_{se}, which are independent to each other, parallel computing can be employed as shown in Figure 5. 7. For this, any third-party solution based on well-knows multi-CPU cores or multi-GPU cores can be applied.

A general outline of this process based on the stochastic DL-LOPF^{AC} approach considering microgrids operation and control is presented in Figure 5. 7. Details for obtaining the set of input samples, as well as the targets provided by the LOPF model are described in the following section.

5.5.1 Set of Sample Inputs and Targets

The set of input samples is a combination of possible allocations for the DDGs, WTs, PVs, ESSs and ISWs, where $\mathbf{IN^{dnn}}$ denotes the matrix including a set of sample sp that can be expressed by (5.100)-(5.101).

$$\mathbf{IN^{dnn}} = \left[\boldsymbol{IN}_1^{\boldsymbol{dnn}}; \boldsymbol{IN}_2^{\boldsymbol{dnn}}; \dots; \boldsymbol{IN}_{sp}^{\boldsymbol{dnn}}\right] \qquad ,sp \in \Omega_{SAM} \tag{5.100}$$

$$\boldsymbol{IN}_{sp}^{\boldsymbol{dnn}} = \begin{bmatrix} round\left(\boldsymbol{r}_{a,sp}^{dnn}\right) \\ round\left(\boldsymbol{r}_{b,sp}^{dnn}.\frac{P^{DDG,max}}{P_{step}^{DDG}}\right)P_{step}^{DDG} \\ round\left(\boldsymbol{r}_{c,sp}^{dnn}.\frac{P^{WT,max}}{P_{step}^{WT}}\right)P_{step}^{WT} \\ round\left(\boldsymbol{r}_{d,sp}^{dnn}.\frac{P^{PV,max}}{P_{step}^{PV}}\right)P_{step}^{PV} \\ round\left(\boldsymbol{r}_{e,sp}^{dnn}.\frac{P^{ESS,max}}{P_{step}^{ES}}\right)P_{step}^{ESS} \end{bmatrix} \quad \begin{matrix} sp \in \Omega_{SAM} \\ a \in \Omega_{ISW}^{can} \\ b \in \Omega_{DDG}^{can} \\ , c \in \Omega_{WT}^{can} \\ d \in \Omega_{PV}^{can} \\ e \in \Omega_{ESS}^{can} \end{matrix} \tag{5.101}$$

The vector $\boldsymbol{IN}_{sp}^{\boldsymbol{dnn}}$ is dependent on the candidate location of the ISW and resources, where n_{feat} denotes the number of features for a single DNN training sample input, in this case $n_{feat} = n_{ddg} + n_{wt} + n_{pv} + n_{ess} + n_{isw}$, $\boldsymbol{r}_{sp}^{dnn}$ is a uniform random number between [0,1]. In this work, the uniform random is generated one time as a matrix with size $n_{feat} \times n_{sam}$ representing a whole Ω_{SAM} training

sample inputs before being classified into subset according to the candidate location of switch and resources as seen in (5.101). In this way, it guarantees that the generated random numbers cover all possible configuration in the space $n_{feat} \times n_{sam}$.

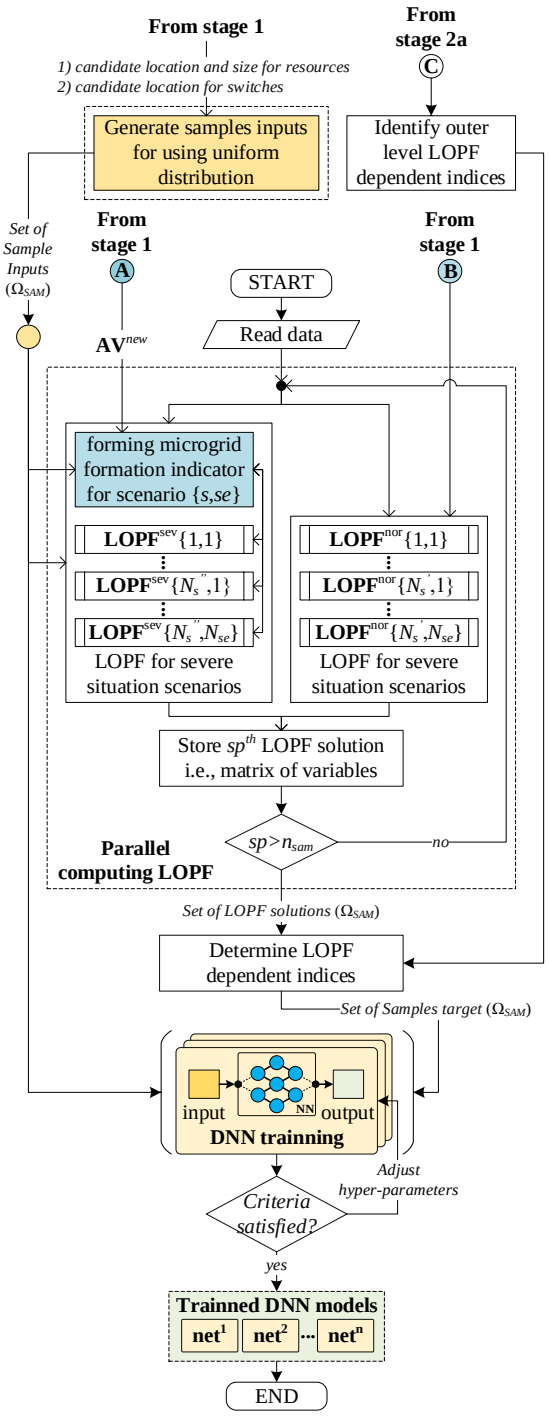

FIGURE 5. 7: Proposed optimal operation for hierarchical microgrids based on deep-learning technique

The set of targets are identified by outer level's indices dependent on the decision variables of the LOPF problem. In this case, from (5.21)-(5.46) the identified indices are $RESI^{OLEV}$, $AOMC^{DDG}$, $AEMIS^{DDG}$ and $AEMIS^{GRID}$, where $TG_{sp,n}$ denotes the DNN targets n corresponding to LOPF solution sample sp, the identification targets for training the DNN model can be given by (5.102)-(5.104).

$$TG_{sp,1} = RESI^{OLEV} \quad ,\forall sp \in \Omega_{SAM} \tag{5.102}$$

$$TG_{sp,2} = \begin{cases} \frac{AOMC^{DDG}}{\frac{365}{4} S_{base}\left(\frac{\sigma^{fuel}}{\eta^{DDG}} + \sigma^{DDG}_{O\&M}\right)} \\ or \\ \frac{AEMIS^{DDG}}{\frac{365}{4} S_{base} K^{DDG}_{CO2}} \end{cases} = \sum_{\forall se \in \Omega_{se}} \sum_{\forall s \in \Omega_s} \left(\pi^{wiso}_{s,se} \sum_{\forall i \in \Omega_{DDG}} \sum_{\forall t \in \Omega_T} P^{DDG}_{i,t,s,se}\right)$$

$$,\forall sp \in \Omega_{SAM} \tag{5.103}$$

$$TG_{sp,3} = \frac{AEMIS^{GRID}}{\frac{365}{4} S_{base} K^{GRID}_{CO2}} = \sum_{\forall se \in \Omega_{se}} \sum_{\forall s \in \Omega_s} \left(\pi^{wiso}_{s,se} \sum_{\forall i \in \Omega_{DDG}} \sum_{\forall t \in \Omega_T} P^{GRID+}_{t,s,se}\right)$$

$$,\forall sp \in \Omega_{SAM} \tag{5.104}$$

The first target (5.102), $RESI^{OLEV}$, is dependent to LOPF's decision variable $b^{curt}_{i,t,s,se}$. It is responsible for the training of DDN model for accounting $b^{curt}_{i,t,s,se}$ of the inner level. This allow the trained DNN model enable to predict the resilience index value which is corresponding to the first objective function as discussed in section 5.4. The second target (5.103) is related to $AOMC^{DDG}$ and $AEMIS^{DDG}$ indices dependent to the LOPF's decision variables $P^{DDG}_{i,t,s,se}$. It characterizes both indices shared by the same variable i.e., $P^{DDG}_{i,t,s,se}$ and leading to the possibility to predict only a single value for determining these two indices. As can see in (5.103), $TG_{sp,2}$ can be calculated via $AOMC^{DDG}$, or $AEMIS^{DDG}$, as those indices are dependent to the same $P^{DDG}_{i,t,s,se}$. In this case, the prediction results according to $TG_{sp,2}$ can be used for re-calculating $AOMC^{DDG}$ and $AEMIS^{DDG}$ respecting their corresponding multiplication constant requirement. These re-calculated provide the predicted results for $AOMC^{DDG}$ and $AEMIS^{DDG}$ which is necessary for determine the second/third objective function for the outer level (i.e., TC^{OLEV} and $AEMIS^{OLEV}$) accordingly. Finally (5.104) corresponding to $AEMIS^{GRID}$ which it dependent to $P^{GRID+}_{i,t,s,se}$, leading to the representation of the predicted value of the trained DNN model for the annualized CO_2 emission by the power imported from the main grid during GC mode, similar to (5.45) in section 5.4.

5.5.2 Microgrid Formation

The microgrid formation is the intermediate step within the stochastic optimal operation level. This step delivers the necessary indicators for optimal operation level representing the microgrids formation due to N-K contingencies level. These indicators are the matrices and vectors that represent the time-coupling topologies of test system during severe scenarios Ω_s''. The methodology for delivering the microgrid formation indicators respecting to the LOPF problem is detailed illustrated in Figure 5. 8.

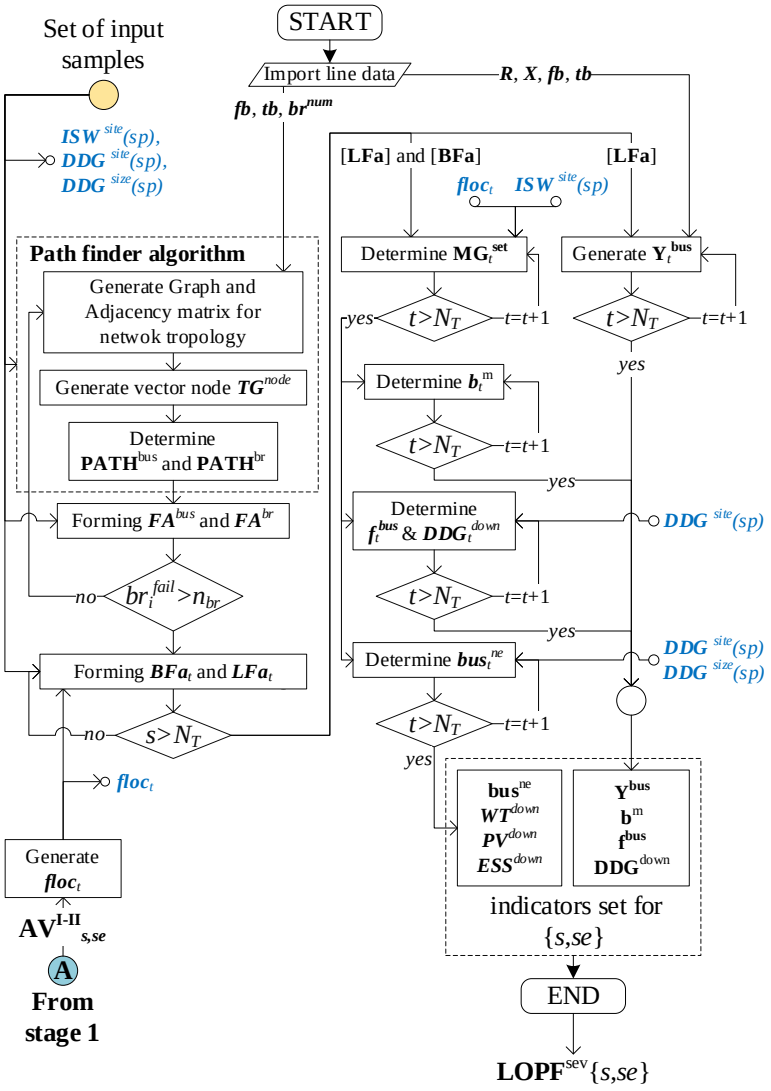

FIGURE 5. 8: Flowchart for generating the microgrid indicator matrices and vectors for time $t \in \Omega_T$ for scenarios s of season se

5.5.2.1 Fault Influence Path

First, the affected branch and bus path finder is proposed for searching the path(s) from the original fault location until the end branch (terminal edge) and end node (leaves node) respecting the graph representation of the network. This search algorithm is deployed in order to automatically search the path(s) whenever a single fault is located in the network. The respective step-by-step description of the algorithm solution is detailed in the following sections. On the other hand, more detail exemplifies the determination of the fault influence path can be found in Appendix C.

a) Step 1: Representation of the System Topology

Let the reference system topology be represented by the undirected graph $\mathbf{G^{bus}} = (\boldsymbol{ND^{bus}}, \boldsymbol{ED^{br}})$, where $\boldsymbol{ND^{bus}}$ are the set containing the vertices or nodes representing the buses in the reference system, while $\boldsymbol{ED^{br}}$ are the edge set representing the branch connected between two adjacent nodes in the test system. In this case, the adjacency matrix of $\mathbf{G^{bus}}$ is the $n_{bus} \times n_{bus}$ matrix denote by $\mathbf{M^{adj}} = [M_{ij}^{adj}]$ with M_{ij}^{adj} defined by (5.105) [105].

$$M_{ij}^{adj} = \begin{cases} 1, & \text{if } ND_i^{bus} ND_j^{bus} \in \boldsymbol{ED^{br}} \\ 0, & \text{otherwise} \end{cases} \tag{5.105}$$

As $\mathbf{G^{bus}}$ is an undirected graph, the adjacency matrix is the symmetrical square matrix with $M_{ij}^{adj} = M_{ji}^{adj}$. Here it is important to note that in case there is a reconfiguration in the reference system, $\mathbf{G^{bus}}$ and $\mathbf{M^{adj}}$ should be updated accordingly.

b) Step 2: Determination of the Target Nodes TG^{node}

Based on the graph $\mathbf{G^{bus}}$, the shortest path by Dijkstra's algorithm is adopted for determining the path(s), or road map(s), between the branch fail and the target node(s), where $fb\left(br^{fail}\right)$ denotes the start node for the shortest path, i.e. fault location, while the end of the shortest path are the target nodes including root node and leave nodes. More detail about the Dijkstra's algorithm can be found in [105],[106].

The target nodes can be identified using the adjacency matrix $\mathbf{M^{adj}}$, determining the row of $\mathbf{M^{adj}}$ with summation equal to one. In this sense, let i and j denote the row and column of $\mathbf{M^{adj}}$, $\sum_{j=1}^{n_{bus}} M_{i,j}^{adj} = 1$ indicates that node i is an end node with no connection elsewhere.

c) Step 3: Determination of the path(s)

Once the target nodes are identified, Dijkstra's algorithm is employed for determining the shortest path between the start node $fb\left(br^{fail}\right)$ and the target nodes TG_i^{node}. For this, considering the system topology information available in the $\mathbf{G^{bus}}$ matrix, where the weight of all branches are set to one, given that any connection between two nodes is established by a unique path for a radial distribution system.

The Dijkstra's algorithm solution ($DIJK$) identifying the shortest path between two nodes, respectively $fb\left(br^{fail}\right)$ and TG_i^{bus}, can be expressed by eq. (5.106).

$$\boldsymbol{path}_i^{\boldsymbol{bus}}\left(fb\left(br^{fail}\right), TG_i^{bus}\right) = DIJK\left(fb\left(br^{fail}\right), TG_i^{bus}\right) \quad ,\forall i \in \Omega_{TG}^{node} \qquad (5.106)$$

Next, the branch path denoted by $path_i^{br}$ vector can be obtained identifying the edges located within the solution path $fb\left(br^{fail}\right)$ to TG_i^{bus}. Following, vectors $path_i^{bus}$ and $path_i^{br}$ belonging to Ω_{TG}^{node} are stored in matrices $\mathbf{PATH^{bus}}$ and $\mathbf{PATH^{br}}$, respectively. These matrices are responsible for determining the fault influenced branch and bus matrices, being detailed elaborated in the following section.

5.5.2.2 Fault Influenced Branch and Bus Matrices

Following, once affected paths are determined, clearing procedures must be established to successfully isolate the fault and ensure the system resilience. In this sense, the representation of affected bus(es) and branch(es) by the respective fault(s) must be performed to enable planning algorithms solution. These representations are respectively held by matrices **LFa** and **BFa**, describing affected bus(es) and branch(es). In addition, the establishment of rules to ensure the adequate allocation of candidate isolated switches able to isolate the upstream and downstream of a branch fault is fundamental [107][108]. For this, the following rules are established:

- If the fault is found on the branch equipped with ISW, the fault stays in the middle of the branch and have been cleared by this ISW.

- If the fault is located on the branch without ISW, the fault in this case is cleared by the nearby ISWs located along the searching paths.

A detailed description of bus and branch affected matrices is presented in the following sections.

a) Branch Affected Matrix $(\boldsymbol{LFa})$

The branch, or line, affected matrix **LFa** is the binary matrix assembling all binary vectors $\boldsymbol{LFa}_t$ with t belong to Ω_T, where an online branch is represented by "1", i.e., non-affected branch, and affected branches by the fault(s) are represented by "0". For determining this matrix, first, the binary matrix denoted by $\mathbf{FA^{br}}$ is required. $\mathbf{FA^{br}}$ is the binary square matrix $n_{br} \times n_{br}$, in which its i^{th} single row describes the set of affected branches corresponding to the location of a single fault br_i^{fail} where $i \in \Omega_{LIN}$. Once matrix $\mathbf{FA^{br}}$ is obtained, a generic i^{th} fault located at a branch "a", i.e., $floc_{i,t} = a$, due to the severe event at time "t", allows for the determination of $\boldsymbol{LFa}_t$ by the row "a" of $\mathbf{FA^{br}}$. Moreover, $\mathbf{FA^{br}}$ is useful for manipulating the elements of $\boldsymbol{LFa_t}$ in case that multiple faults are featured in the test system (i.e., $floc_{i,t} \in \Omega_{floc}$). To this end. the location of the fault(s) can be identified by looking up on time segment t of $\mathbf{AV}_{s,se}^{\mathbf{I-II}}$.

If there is more than a single fault located in the system. Let, $\boldsymbol{floc}_t$ be a vector containing the faults locations, where its elements can be identified using $\mathbf{AV}_{s,se}^{\mathrm{I-II}}$. $\boldsymbol{LFa_t}$ at time t can be determined by looking up the multiple rows of $\mathbf{FA^{br}}$considering the correspondent element number of vectors $\boldsymbol{floc}_t$ as described in (5.107), where $\prod$ denotes the Hadamard multiplication.

$$\boldsymbol{LFa}_t = \prod_{i \in \Omega_{floc}} \left[\circ \, \mathbf{FA^{br}}(floc_i, :) \right] \tag{5.107}$$

Finally, **LFa** is obtained by repeating the same methodology for $\boldsymbol{LFa}_t$ for $t \in \Omega_T$. Here one must note that, if no fault(s) occur at time t, especially in the normal scenarios, i.e., Ω_s, the elements of $\boldsymbol{LFa}_t$ can be simply set by the vector constrained element of '1'. More detail elaborates the determination of $\boldsymbol{LFa}_t$ until **LFa** can be found in Appendix C.

b) Bus Affected Matrix $(\boldsymbol{BFa})$

Similar to the branches analysis, buses located within the fault zone bounded by the ISWs must be deactivated. In this sense, to represent this information, the binary matrix denote by **BFa** containing the bus(es) affected is required, where the **BFa** is an assembly of the binary vectors $\boldsymbol{BFa}_t$ where $t \in \Omega_T$, with term(s) equal to "1", corresponding to an online bus, and "0" for those affected by the fault(s) and deactivated.

Following the binary matrix denoted by $\mathbf{FA^{bus}}$ is required. $\mathbf{FA^{bus}}$ is a non-square matrix due to $n_{bus} = n_{br} + 1$, where the i^{th} single row of $\mathbf{FA^{bus}}$ describes the set of affected buses corresponding to the location of a single fault location br_i^{fail} given $i \in \Omega_{LIN}$. Once this matrix $\mathbf{FA^{bus}}$ obtained, the $\boldsymbol{BFa}_t$

can be determined by looking up to the row "a" of $\mathbf{FA^{bus}}$. Similar to $\mathbf{FA^{br}}$, $\mathbf{FA^{bus}}$ can be used for determining $\boldsymbol{BFa}_t$ in case the case there is a multi-fault in the network i.e., $floc_{i,t} \in \Omega_{floc}$.

For determining $\mathbf{FA^{bus}}$, first $\mathbf{PATH^{br}}$ and $\mathbf{PATH^{bus}}$ have been determined for $br_i^{fail} \in \Omega_{LIN}$. Then, $\boldsymbol{FA^{bus}}\{br_i^{fail}\}$ is obtained searching $\mathbf{PATH^{br}}\{br_i^{fail}\}$ and $\mathbf{PATH^{br}}\{br_i^{fail}\}$ using the proposed algorithm described in Table C. 1 in Appendix C.

For the case with multiple faults, a Hadamard multiplication $\prod$ is used according to $\mathbf{FA^{bus}}\{\boldsymbol{floc}_t\}$. Eq. (5.108) shows the formulation for determining $\boldsymbol{BFa}_t$ based on $\boldsymbol{floc}_t$.

$$\boldsymbol{BFa}_t = \prod_{i \in \Omega_{floc}} \left[\circ \, \mathbf{FA^{bus}}(floc_i, :) \right] \tag{5.108}$$

Similarly, $\boldsymbol{BFa}_t$ is repeatedly determined for $t \in \Omega_T$ and then stored in $\mathbf{BFa}$. For the case where there is no fault at time t, the methodology described above can be skipped and $\boldsymbol{BFa}_t$ can be simply set vector containing the element '1'. More detail elaborates the determination of $\boldsymbol{BFa}_t$ until $\mathbf{BFa}$ can be found in Appendix C

5.5.2.3 Microgrid Formation Set

The matrix $\mathbf{MG}_t^{\mathbf{set}}$ is used for indicating the set of possible microgrid formations once the fault is eliminated. In this sense, taking advantage of the Depth First Search (DFS) technique the matrix $\mathbf{MG}_t^{\mathbf{set}}$ for a generic $\boldsymbol{floc}_t$ and $\boldsymbol{ISW}^{site}$ is obtained employing the proposed algorithm described in Table C. 2 in Appendix C for all $t \in \Omega_T$. This is possible as the DFS technique allows the proposed algorithm able to track a set of microgrid(s) according to their roots noted by $root^{MG}$ which is corresponding to the location of the switch(es). More details about the DFS can be found in [109], [110]. The mathematically example detailed the $\mathbf{MG}_t^{\mathbf{set}}$ can be found in Appendix C.

5.5.2.4 Microgrid Formation Indicators

In this section, the time dependent microgrid formation indicators are determined. These indicators are the binary matrices and binary vectors representing the time-coupled microgrid tropology and operation especially during the N-K contingencies scenarios. The methodology applied for determining these indicators are described in the following subsection.

a) System Buses Operation Mode

The system buses operation mode are described by matrix $\mathbf{b^m}$**.** Matrix $\mathbf{b^m}$ assembles the binary vectors $\boldsymbol{b_t^m}$containing the binary elements responsible for indicating the operation mode, i.e., GC or IS, of each system bus; where, the element of $\boldsymbol{b_t^m}$ is "1" if the corresponding bus is located at microgrid area, otherwise "0" for those buses connected to the main grid. The formation of $\boldsymbol{b_t^m}$ can be expressed by (5.126). For the determine $\boldsymbol{b_t^m}$, the algorithm in Table C. 3 in Appendix C is adopted.

$$\boldsymbol{b_t^m} = [b_{1,t}^m, b_{2,t}^m, \dots, b_{n_{bus},t}^m] \tag{5.109}$$

b) Non-Energized System Buses

The microgrid can be operated in IS mode when there is at least a single DDG unit localized within the microgrid. In this sense, let a vector $\boldsymbol{MG_{m,t}^{set}}$ define the set of m^{th} microgrid found at time t, if there is no DDG unit installed in $\boldsymbol{MG_{m,t}^{set}}$, this $\boldsymbol{MG_{m,t}^{set}}$ can not operate in IS mode. For this reason, a binary vector $\boldsymbol{bus_t^{ne}}$ is adopt for indicating that the buses within the microgrid cannot be energized due to the lack of local DDG(s); where, the element of $\boldsymbol{bus_t^{ne}}$ is "1" when the corresponding bus is located in a with DDG(s), otherwise "0" for those buses located in microgrids lacking local DDG(s). The general formation for $\boldsymbol{bus_t^{ne}}$ is shown in (5.110). Then, the general algorithm for determiner $\boldsymbol{bus_t^{ne}}$ for an instance time $t \in \Omega_T$ is shown in Table C. 4 of Appendix C. See Appendix C for more detail exemplifies the formation of $\boldsymbol{bus_t^{ne}}$.

$$\boldsymbol{bus_t^{ne}} = [bus_{1,t}^{ne}, bus_{2,t}^{ne}, \dots, bus_{n_{bus},t}^{ne}] \tag{5.110}$$

c) Frequency-Controlled Buses and Deactivated DDGs

According to (5.70) there is a need to identify the location of buses with frequency control capability within the microgrid. Nonetheless, if more than a single microgrid is created, the frequency-controlled bus for each formed microgrid should be identified. For this, the vector $\boldsymbol{f_t^{bus}}$ is employed. Its elements indicate the location of frequency-controlled buses for each DDG. Still, there might be cases where a DDG is located within the fault area. In this case, the binary vector $\boldsymbol{DDG_t^{down}}$ is used, where elements corresponding to DDGs standing in fault areas are set to zero, otherwise set to "1". (5.111) and (5.112) shows the formation for $\boldsymbol{f_t^{bus}}$ and $\boldsymbol{DDG_t^{down}}$, respectively. The algorithm adopted for determining $\boldsymbol{f_t^{bus}}$ and $\boldsymbol{DDG_t^{down}}$ is show in Table C. 5 in Appendix C.

$$\boldsymbol{f_t^{bus}} = [f_{1,t}^{bus}, f_{2,t}^{bus}, \dots, f_{n_{ddg},t}^{bus}] \tag{5.111}$$

$$\boldsymbol{DDG}_t^{down} = [DDG_{1,t}^{down}, DDG_{2,t}^{down}, \dots, DDG_{n_{ddg},t}^{down}] \quad (5.112)$$

d) WT, PV and ESS Operation Status

WT, PV and ESS cannot maintain the microgrid operation in IS without DDG support. In this sense, WTs, PVs and ESSs that are located inside non-successful IS microgrid should be deactivated. For this, vectors indicating the WTs, PVs and ESSs deactivation status can be determined by simply mapping their location with $\boldsymbol{bus}_t^{ne}$ and can be as expressed by (5.113)-(5.115).

$$\boldsymbol{WT}_t^{down} = \boldsymbol{bus}_t^{ne}(\boldsymbol{WT}_{sp}^{site}) \quad (5.113)$$

$$\boldsymbol{PV}_t^{down} = \boldsymbol{bus}_t^{ne}(\boldsymbol{PV}_{sp}^{site}) \quad (5.114)$$

$$\boldsymbol{ESS}_t^{down} = \boldsymbol{bus}_t^{ne}(\boldsymbol{ESS}_{sp}^{site}) \quad (5.115)$$

e) Time-Coupled Y^{bus}

The initial system impedance is determined via the original system topology, i.e., $Z_{i,t,s,se} = Z_i^0$. Still, during severe event analysis the impedance of overhead line branches changes as the system topology adapts, i.e., opening the switch of an overhead line leads to an equivalent impedance $Z_{i,t,s,se} = \infty$. In this sense, the binary matrix **LFa** is used for updating $Z_{i,t,s,se}$ at an instance time t, where the element of **LFa** can be used as a multiplication for modifying the impedance $Z_{i,t,s,se}$ as expressed in (5.116).

$$Z_{i,t,s,se} = (1/LFa_{i,t,s,se})Z_i^0 \quad ,\forall i \in \Omega_{BUS}, \forall t \in \Omega_T, \forall s \in \Omega_s' \cup \Omega_s'', \forall se \in \Omega_{se} \quad (5.116)$$

The time-coupled $\mathbf{Y}_{s,se}^{\mathbf{bus}}$ can be expressed by (5.117) using the methodology found in [18]. Conductance matrix **G** and susceptance matrix **B** along the planning horizon Ω_T can be obtained using (5.118) and (5.119).

$$\mathbf{Y}_{s,se}^{\mathbf{bus}} = \left[\mathbf{Y}_{1,s,se}^{\mathbf{bus}}, \mathbf{Y}_{2,s,se}^{\mathbf{bus}}, \dots, \mathbf{Y}_{N_T,s,se}^{\mathbf{bus}}\right] \quad ,\forall s \in \Omega_s' \cup \Omega_s'', \forall se \in \Omega_{se} \quad (5.117)$$

$$\mathbf{G}_{s,se} = real\left(\mathbf{Y}_{s,se}^{\mathbf{bus}}\right) \quad (5.118)$$

$$\mathbf{B}_{s,se} = imag\left(\mathbf{Y}_{s,se}^{\mathbf{bus}}\right) \quad (5.119)$$

5.5.3 Integration of Microgrid Formation Indicators to Inner Level Optimization

In this section, the microgrid formation indicators are integrated in the LOPF problem allowing the capture of multi-microgrid topology and the status of available resources over the planning horizon Ω_T. For this, the LOPF formulation updated according to the multi-microgrid formation indicators are listed as follows:

a) Objective Function

With a new $\boldsymbol{b_t^m}$, the formulation (5.58) and (5.62) were replaced by (5.120) and (5.121) for introduce $b_{i,t,s,se}^m$:

$$OF_{s,se}^{MILP,MGs} = \sum_{t\in\Omega_T}\begin{bmatrix} C_{t,s,se}^{PCC}\left(1-b_{i=1,t,s,se}^m\right) \\ +C_{t,s,se}^{DDG}\left(1-b_{\forall i\in\Omega_{DDG},t,s,se}^m\right) \\ +C_{t,s,se}^{CURT}\, b_{\forall i\in\Omega_{BUS},t,s,se}^m \\ +C_{t,s,se}^{VI,MGs} \end{bmatrix} \quad ,\forall s\in\Omega_s'\cup\Omega_s'',\forall se\in\Omega_{se} \quad (5.120)$$

$$C_{t,s,se}^{VI,MGs} = V_{base}\left(PC^{VI}\left[\sum_{i\in\Omega_{BUS}} bus_{i,t,s,se}^{ne}\begin{pmatrix}\left(1-b_{i,t,s,se}^m\right)V^{GC,spec} \\ +b_{i,t,s,se}^m V_i^{**}-V_{i,t,s,se}\end{pmatrix}\right]\right)\Delta t$$
$$,\forall t\in\Omega_T,\forall s\in\Omega_s'\cup\Omega_s'',\forall se\in\Omega_{se} \quad (5.121)$$

b) Constraints

The update constraints considering the microgrids formulation indicators can be listed as follows:

$$\left(1-bus_{i,t,s,se}^{ne}\right)\le b_{i,t,s,se}^{curt}\le b_{i,t,s,se}^m$$
$$,\forall i\in\Omega_{BUS},\forall t\in\Omega_T,\forall s\in\Omega_s'\cup\Omega_s'',\forall se\in\Omega_{se} \quad (5.122)$$

$$P_{i,t,s,se} = \begin{pmatrix}\sum_{j\in\Omega_{BUS}} G_{ij,t,s,se}V_{i,t,s,se} \\ -\sum_{j\in\Omega_{BUS}} B_{ij,t,s,se}\delta_{j,t,s,se}\end{pmatrix} = \begin{pmatrix} P_{i,t,s,se}^{PCC}+P_{i,t,s,se}^{DDG} \\ +P_{i,t,s,se}^{WT}+P_{i,t,s,se}^{PV} \\ +P_{i,t,s,se}^{dch}-\eta_i^{ESS}P_{i,t,s,se}^{ch} \\ -P_{i,t,s,se}^{L}\left(1-b_{i,t,s,se}^{curt}\right)\end{pmatrix}$$
$$,\forall i\in\Omega_{BUS},\forall t\in\Omega_T,\forall s\in\Omega_s'\cup\Omega_s'',\forall se\in\Omega_{se} \quad (5.123)$$

$$Q_{i,t,s,se} = \begin{pmatrix}-\sum_{j\in\Omega_{BUS}} B_{ij,t,s,se}V_{i,t,s,se} \\ -\sum_{j\in\Omega_{BUS}} G_{ij,t,s,se}\delta_{j,t,s,se}\end{pmatrix} = \begin{pmatrix} +Q_{i,t,s,se}^{PCC}+Q_{i,t,s,se}^{DDG} \\ +Q_{i,t,s,se}^{ESS} \\ -Q_{i,t,s,se}^{L}\left(1-b_{i,t,s,se}^{curt}\right)\end{pmatrix}$$
$$,\forall i\in\Omega_{BUS},\forall t\in\Omega_T,\forall s\in\Omega_s'\cup\Omega_s'',\forall se\in\Omega_{se} \quad (5.124)$$

$$P_{k,t,s,se}^{br} = \begin{pmatrix} g_{i(k)j(k),t,s,se}\left(V_{i,t,s,se} - V_{j,t,s,se}\right) \\ +b_{i(k)j(k),t,s,se}\left(\delta_{i,t,s,se} - \delta_{j,t,s,se}\right) \end{pmatrix}$$

$$,\forall k \in \Omega_{LIN}, \forall t \in \Omega_T, \forall s \in \Omega_s' \cup \Omega_s'', \forall se \in \Omega_{se} \quad (5.125)$$

$$Q_{k,t,s,se}^{br} = \begin{pmatrix} b_{i(k)j(k),t,s,se}\left(V_{i,t,s,se} - V_{j,t,s,se}\right) \\ +g_{i(k)j(k),t,s,se}\left(\delta_{i,t,s,se} - \delta_{j,t,s,se}\right) \end{pmatrix}$$

$$,\forall k \in \Omega_{LIN}, \forall t \in \Omega_T, \forall s \in \Omega_s' \cup \Omega_s'', \forall se \in \Omega_{se} \quad (5.126)$$

$$P_{i,t,s,se}^{DDG} = \begin{pmatrix} \left[-k^{i\omega}\left(\delta_{f_{i,t}^{bus},t,s,se}^{MG} - \pi/2\right)/m_i^p\right] b_{i,t,s,se}^m \\ +\left(1 - b_{i,t,s,se}^m\right) P_{i,t,s,se}^{DDG} \end{pmatrix}$$

$$,\forall i \in \Omega_{DDG}, \forall t \in \Omega_T, \forall s \in \Omega_s' \cup \Omega_s'', \forall se \in \Omega_{se} \quad (5.127)$$

$$Q_{i,t,s,se}^{DDG} = \left[\left(V_i^* - V_{i,t,s,se} + u_{i,t,s,se}^v\right)/n_i^q\right] b_{i,t,s,se}^m + \left(1 - b_{i,t,s,se}^m\right) Q_{i,t,s,se}^{DDG}$$

$$,\forall i \in \Omega_{DDG}, \forall t \in \Omega_T, \forall s \in \Omega_s' \cup \Omega_s'', \forall se \in \Omega_{se} \quad (5.128)$$

$$V_{i,t,s,se} b_{i,t,s,se}^m = V_i^{**} b_{i,t,s,se}^m \quad ,\forall i \in \Omega_{DDG}, \forall t \in \Omega_T, \forall s \in \Omega_s' \cup \Omega_s'', \forall se \in \Omega_{se} \quad (5.129)$$

$$0 \le P_{i,t,s,se}^{DDG} \le S_i^{DDG,max} DDG_{i,t,s,se}^{down}$$

$$,\forall i \in \Omega_{DDG}, \forall t \in \Omega_T, \forall s \in \Omega_s' \cup \Omega_s'', \forall se \in \Omega_{se} \quad (5.130)$$

$$\chi_i^{DDG,min} S_i^{DDG,max} DDG_{i,t,s,se}^{down} \le Q_{i,t,s,se}^{DDG} \le \chi_i^{DDG,max} S_i^{DDG,max} DDG_{i,t,s,se}^{down}$$

$$,\forall i \in \Omega_{DDG}, \forall t \in \Omega_T, \forall s \in \Omega_s' \cup \Omega_s'', \forall se \in \Omega_{se} \quad (5.131)$$

$$0 \le P_{i,t,s,se}^{WT,use} \le P_{i,t,s,se}^{WT} WT_{i,t,s,se}^{down} \quad ,\forall i \in \Omega_{WT}, \forall t \in \Omega_T, \forall s \in \Omega_s' \cup \Omega_s'', \forall se \in \Omega_{se} \quad (5.132)$$

$$0 \le P_{i,t,s,se}^{PV,use} \le P_{i,t,s,se}^{PV} PV_{i,t,se}^{down} \quad ,\forall i \in \Omega_{PV}, \forall t \in \Omega_T, \forall s \in \Omega_s' \cup \Omega_s'', \forall se \in \Omega_{se} \quad (5.133)$$

$$0 \le P_{i,t,s,se}^{dch} \le S_i^{ESS,max} b_{i,t,s,se}^{ESS} ESS_{i,t,s,se}^{down}$$

$$,\forall i \in \Omega_{ESS}, \forall t \in \Omega_T, \forall s \in \Omega_s' \cup \Omega_s'', \forall se \in \Omega_{se} \quad (5.134)$$

$$0 \le P_{i,t,s,se}^{ch} \le S_i^{ESS,max} \left(1 - b_{i,t,s,se}^{ESS}\right) ESS_{i,t,s,se}^{down}$$

$$,\forall i \in \Omega_{ESS}, \forall t \in \Omega_T, \forall s \in \Omega_s' \cup \Omega_s'', \forall se \in \Omega_{se} \quad (5.135)$$

$$\chi_i^{ESS,min} S_i^{ESS,max} ESS_{i,t,s,se}^{down} \le Q_{i,t,s,se}^{ESS} \le \chi_i^{ESS,max} S_i^{ESS,max} ESS_{i,t,s,se}^{down}$$

$$,\forall i \in \Omega_{ESS}, \forall t \in \Omega_T, \forall s \in \Omega_s' \cup \Omega_s'', \forall se \in \Omega_{se} \quad (5.136)$$

$$-S_i^{TR,max}\left(1-b_{i,t,s,se}^m\right) \le P_{i,t,s,se}^{PCC} \le S_i^{TR,max}\left(1-b_{i,t,s,se}^m\right)$$
$$,\forall i \in \Omega_{PCC}, \forall t \in \Omega_T, \forall s \in \Omega_s' \cup \Omega_s'', \forall se \in \Omega_{se} \quad (5.137)$$

$$\chi_i^{TR,min} S_i^{TR,max}\left(1-b_{i,t,s,se}^m\right) \le Q_{i,t,s,se}^{PCC} \le \chi_i^{TR,max} S_i^{TR,max}\left(1-b_{i,t,s,se}^m\right)$$
$$,\forall i \in \Omega_{PCC}, \forall t \in \Omega_T, \forall s \in \Omega_s' \cup \Omega_s'', \forall se \in \Omega_{se} \quad (5.138)$$

$$V_{i,t,s,se}\left(1-b_{i,t,s,se}^m\right) = V^{GC,spec}\left(1-b_{i,t,s,se}^m\right)$$
$$,\forall i \in \Omega_{PCC}, \forall t \in \Omega_T, \forall s \in \Omega_s' \cup \Omega_s'', \forall se \in \Omega_{se} \quad (5.139)$$

$$\delta_{i,t,s,se}^{PCC}\left(1-b_{i,t,s,se}^m\right) = 0 \quad ,\forall i \in \Omega_{PCC}, \forall t \in \Omega_T, \forall s \in \Omega_s' \cup \Omega_s'', \forall se \in \Omega_{se} \quad (5.140)$$

First, (5.64) is replaced by (5.122) for allowing the load at the individual bus curtail during IS mode, while forcing $b_{i,t}^{curt} = 1$ for any bus i that corresponding to the bus non-energize $bus_{i,t,s,se}^{ne}$. Then, equations (5.123)-(5.126) are power flow constraints considering the microgrids topology using the time-coupled $\mathbf{Y}_{s,se}^{\mathbf{bus}}$. The updated constraints for the DDG units are expressed by (5.127)-(5.128). Comparing to (5.70)-(5.72), $b_{i,t,s,se}^m$ is introduced in (5.127)-(5.129), allowing the problem consideration individual DDG units operation, i.e., GC or IS mode. Moreover, for (5.127), $\delta_{f_{i,t}^{bus},t,s,se}^{MG}$ is dependent to frequency-controlled buses. Eqs. (5.77) and (5.78) are replaced by (5.130) and (5.131) for accounting the status of the DDG units i.e., online or failure. The inequalities (5.132)-(5.136) guarantee that WTs, PVs and ESSs are deactivated in case they are located inside a non-successful IS microgrids. Finally, eqs. (5.137)-(5.140) defined the updated power exchange constraints by introducing $b_{i,t}^m$.

c) MILP Model for LOPF Considering Microgrids Formation

According to the updated LOPF problem formulation the MILP model used for the deep-learning approach can be summarized as following:

$$\min_{\boldsymbol{X}^{MILP}} OF_{s,se}^{MILP,MGs} \quad (5.141)$$

Subject to:

- Voltage and load curtailment constraints: (5.63), (5.122)
- Power flow constraints: (5.123)-(5.126), (5.69)

- DDG operation constrains: (5.73)-(5.75), (5.78), (5.79), (5.127)-(5.131)
- WT and PV operation constrains: (5.133), (5.134)
- ESS operation constraints: (5.82), (5.86)-(5.89), (5.134)-(5.136)
- Power exchange constraints: (5.92), (5.93), (5.137)-(5.140)

5.5.4 Deep Neural Network (DNN) Model

At this stage, for each sample *sp*, the identified targets (5.102)-(5.104) can be calculated using the results obtained by the LOPF solution. Then, a set of sample inputs $\mathbf{IN^{dnn}}$ and the calculated targets (5.102)-(5.104) are used for training the DDN models, wherein 70% of the samples were arbitrarily selected for the training procedure and the remaining samples for the testing procedure. For simplicity, a single DNN model is trained for predicting the single identification target. In this work, each DDN model employed is formed as a multi-layer feedforward neural network with three levels, i.e., a single input layer, several hidden layers and a single output layer [111][112]. Figure 5. 9 shows the basic scheme for a multi-layer feed-forward neural network architecture.

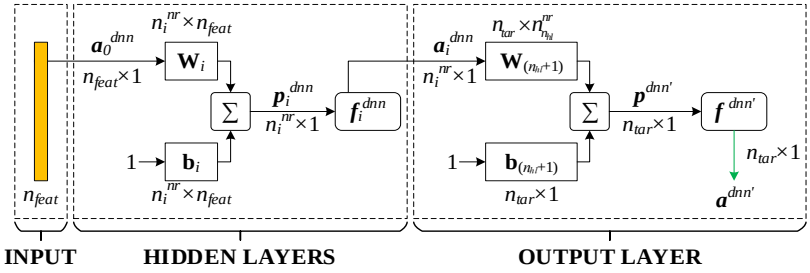

FIGURE 5. 9: General scheme of multi-layer feed-forward neural network architecture for predicting a single identified target

According $\mathbf{IN^{dnn}}$ and targets (5.102)-(5.104), a general DNN model architecture designed for a single sample can be expressed by (5.142)-(5.144).

$$\boldsymbol{a}_{0,sp}^{\boldsymbol{dnn}} = \boldsymbol{IN}_{sp}^{\boldsymbol{dnn}} \qquad ,sp \in \Omega_{SAM} \tag{5.142}$$

$$\boldsymbol{a}_{i,sp}^{\boldsymbol{dnn}} = f_i^{dnn}\left(\mathbf{W}_i \boldsymbol{a}_{i-1,sp}^{\boldsymbol{dnn}} + \mathbf{b}_i\right) \qquad ,i = 1,2,..,n_{hl}, sp \in \Omega_{SAM} \tag{5.143}$$

$$a_{sp}^{dnn'} = f^{dnn'}\left(\mathbf{W}_{n_{hl}+1} \boldsymbol{a}_{n_{hl},sp}^{\boldsymbol{dnn}} + \mathbf{b}_{n_{hl}+1}\right) \qquad ,sp \in \Omega_{SAM} \tag{5.144}$$

The input layer of the hidden layer receives the vector of input $\boldsymbol{a}_{0,sp}^{\boldsymbol{dnn}}$ expressed by (5.142). Then, each of layer in the hidden layer compute their neuron pre-activation $\boldsymbol{p}_{i,sp}^{\boldsymbol{dnn}}$ regarding to the weight matrix and biases, the activation function $f_i^{dnn}(.)$ employed to $\boldsymbol{p}_{i,sp}^{\boldsymbol{dnn}}$ for delivering the neuron activation for the next layer (5.143). At the end, the output layer computes a single prediction neuron activation, $n_{tar} = 1$, using the neuron activation $\boldsymbol{a}_{n_{hl},sp}^{\boldsymbol{dnn}}$ that is obtained by the last layer of the hidden layer (5.144). In this work, $f_i^{dnn}(.)$ is a sigmoid activation function for the hidden layer, while the output layer linear activation function denoted by $f^{dnn'}(.)$ is used. Finally, the DNN model has been trained via the Bayesian regularization backpropagation (BRB) algorithm [111]. This algorithm is a backpropagation-based approach focused on minimizing the mean squares sum of the network errors (MSE) during the DDN model training. Moreover, seeking to minimized and make the network response smoother, as well as likely reducing overfitting impact [111], [113]. The proposed algorithm also includes the network regularization based on the network sum of mean square weights (MSW).

As can be seen in Figure 5. 9, the prediction obtained by the trained DDN model should satisfy the criteria. In this work, the errors indicated in (5.145) have been used as a criteria calculated for every round of DNN training completion. Then, (5.144) and (5.145) are calculated for illustrating the performance of the model for different types of errors.

$$e_1^{dnn} = 100\% \times \max\left(\frac{\left|TG_{sp} - net^n(\boldsymbol{IN}_{sp}^{\boldsymbol{dnn}})\right|}{TG_{sp}}\right) \quad ,\forall sp \in \Omega_{SAM}^{test} \tag{5.145}$$

$$e_2^{dnn} = \text{mean}\left(\left|TG_{sp} - net^n(\boldsymbol{IN}_{sp}^{\boldsymbol{dnn}})\right|\right) \quad ,\forall sp \in \Omega_{SAM}^{test} \tag{5.144}$$

$$e_3^{dnn} = 100\% \times \frac{mean\left(\left|TG_{sp} - net^n(\boldsymbol{IN}_{sp}^{\boldsymbol{dnn}})\right|\right)}{mean(TG_{sp})} \quad ,\forall sp \in \Omega_{SAM}^{test} \tag{5.145}$$

Where, $net^n\left(\boldsymbol{IN}_{sp}^{\boldsymbol{dnn}}\right)$ is the prediction results for the input sample $\boldsymbol{IN}_{sp}^{\boldsymbol{dnn}}$ using DNN model corresponding to target n. First, e_1^{dnn} represents the relative error between the prediction and real value. In this case, we apply a maximum for delivering the worst error over the vector of relative error. Then, e_2^{dnn} and e_3^{dnn} represent the mean absolute and relative errors, presenting more generalized perspectives in comparison to e_1^{dnn}.

In this work, the hyper parameters are randomly selected for every round of DNN training, i.e., (a) activation function for hidden layers, (b) activation function for outer layer, (c) number of layers and corresponding neurons in the hidden layers. According to the BRB algorithm, the training round stops if the sum squared error and the sum squared weights are not improved over subsequent training

iterations (epochs) [111], [113]. Then, trained DNN models are validated though the testing set until satisfying criteria e_1^{dnn} threshold, guaranteeing that the worst relative error between the target and prediction is less than e_1^{dnn}. Finally, trained DNN models are used for predicting the targets and calculating the LOPF dependent indices $RESI^{OLEV}$, $AOMC^{DDG}$, $AEMIS^{DDG}$ and $AEMIS^{GRID}$ for the outer level. In this sense, let $net^n(\boldsymbol{X_{OLEV}})$ be a trained DDN network for target n depending on $\boldsymbol{X_{OLEV}}$, the LOPF dependent indices for the outer level calculated using the trained DNN model can be expressed by (5.146)-(5.152).

$$RESI^{OLEV,dl} = net^1(\boldsymbol{X_{OLEV}}) \quad ,\forall sp \in \Omega_{SAM} \tag{5.146}$$

$$TC^{OLEV,dl} = C^{DDG,dl} + C^{WT} + C^{PV} + C^{ESS} + C^{ISW} \tag{5.147}$$

$$C^{DDG,dl} = CPC^{DDG} + TL \times AOMC^{DDG,dl} \tag{5.148}$$

$$AOMC^{DDG,dl} = net^2(\boldsymbol{X_{OLEV}})\left(\frac{365}{4} S_{base}\left(\frac{\sigma^{fuel}}{\eta^{DDG}} + \sigma_{O\&M}^{DDG}\right)\right) \tag{5.149}$$

$$AEMIS^{OLEV,dl} = AEMIS^{DDG,dl} + AEMIS^{GRID,dl} \tag{5.150}$$

$$AEMIS^{DDG,dl} = net^2(\boldsymbol{X_{OLEV}})(\frac{365}{4} S_{base} K_{CO2}^{DDG}) \quad ,\forall sp \in \Omega_{SAM} \tag{5.151}$$

$$AEMIS^{GRID,dl} = net^3(\boldsymbol{X_{OLEV}})(\frac{365}{4} S_{base} K_{CO2}^{GRID}) \quad ,\forall sp \in \Omega_{SAM} \tag{5.152}$$

5.6 Stage IV: Solution for Optimum Planning

The proposed multi-objective optimization problem incorporating the DNN models for the resilience-oriented planning of microgrids can be summarized as follows:

$$\min_{\boldsymbol{X^{OLEV}}} \left(RESI^{OLEV,dl}, TC^{OLEV,dl}, AEMIS^{OLEV,dl}\right) \tag{5.153}$$

Subject to:

- DERs size constraint: (5.47)-(5.51)
- Maximum allowable bus power constraint: (5.52)
- ISWs and DERs installation constraints: (5.53)-(5.57)

The proposed problem has been solved using the population-based multi-objective optimization approach NSGA-II [114]. Figure 5. 10 shows the general outline of the proposed optimum planning NSGA-II based on DNN models.

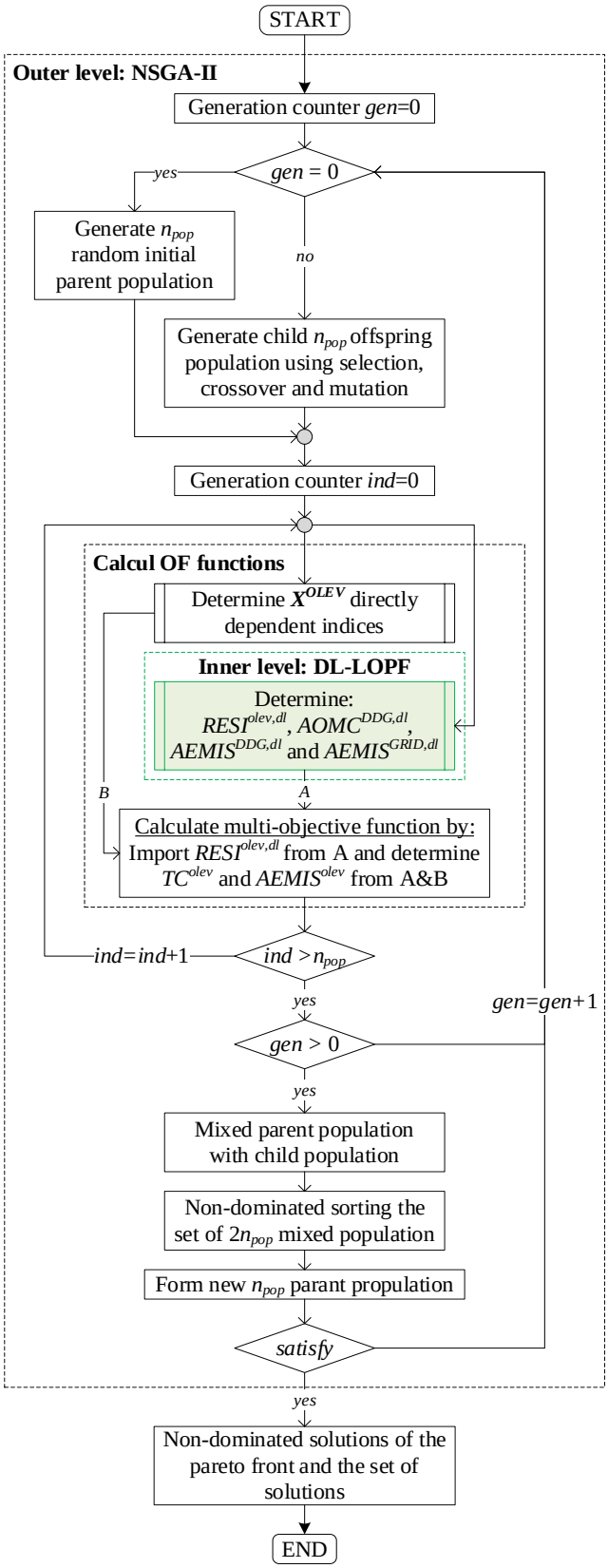

FIGURE 5. 10: Optimum planning approach

The NSGA-II is widely used for multi-objective optimization problems due to its computational efficient and faster convergence compared to the another techniques [114]. Moreover, the solution delivered by NSGA-II is closed to the true Pareto-optima frontier [114]. Additional details on NSGA-II and its implementation can be found in [114].

In the beginning, the first iteration at $gen = 0$ the NSGA-II starts generating an initial random parent population with n_{pop} individuals. In this work, a single individual includes the combination of the genes representing the allocation of the planning elements i.e., ISWs, DDGs, WTs, PVs and ESSs. Figure 5. 11 shows the structure of an individual or a chromosome. Then, considering each single individual, the multi-objective function can be determined from two directions A and B. For the following iteration $gen > 0$ the NSGA-II starts forming an n_{pop} child offspring population using the genetic operators, i.e., selection, crossover and mutation [114]. Similar to the parent population, the multi-objective functions are evaluated for n_{pop} child individuals, and a new parent population is determined.

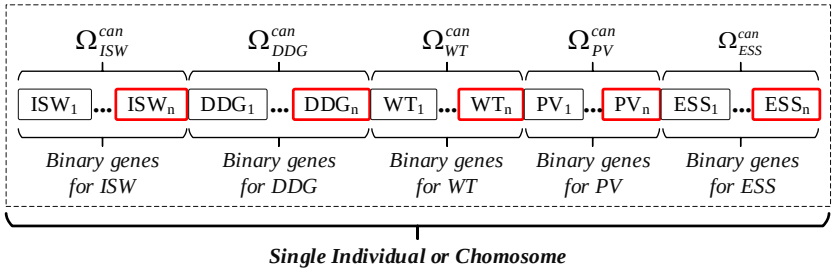

FIGURE 5. 11: Structure of chromosome for NSGA-II

First, the child population is combined with the parent population forming a mixed population with $2 \times n_{pop}$ individuals. Then, a new parent population is developed selecting n_{pop} individuals from the mixed population using the fast non-dominated sorting technique [114]. According to this technique, individual(s) classified in the lowest rank of the frontier are selected and moved up to the highest frontier until the quantity of selected individuals reach n_{pop}. If the last ranked individuals cause the quantity to exceed n_{pop}, the crowding distance is applied for selecting the remainder individuals. This process is repeated until satisfy the NSGA-II criteria.

5.7 Numerical Results

In order to validate the proposed method, the IEEE 33-bus test system is selected. This system is a typical distribution network with the ability to disconnected from the main grid via the main isolated switch, i.e., ISW^{sub}, installed at the upstream interfacing substation. Distribution lines infrastructure

are assumed as typical overhead power line, with loads weighing coefficient proportional to the annual peak load, Figure 5. 12, similar to the work found in [3].

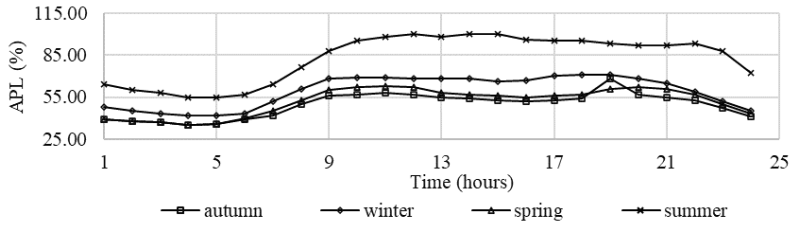

FIGURE 5. 12: Seasonal annual load pattern

The wind speed and irradiance data sets are obtained via the scenario generation procedure describe in Section 5.3 using fast forward reduction. For this, data series extracted from NREL [115] comprising the hourly profile for 10 years, respectively 2008-2017 for Victoria-BC, Canada, of wind speed in MPH (miles per hours) and for irradiance in w/m^2 are employed. Details pertaining to the obtained set of scenarios reduction are shown in Table G. 6 in the Appendix G. Based on the obtained data sets, the most vulnerable wind scenarios summarized in Table G. 7 are used for generating severe operation scenarios. For accounting the uncertainty of the N-K contingencies, N_s^{pre} is set sufficiently high, $N_s^{pre} = 10000$, allowing for the selection of 5 scenarios for each season se. This procedure steps are detailed depicted in Section 5.3, and the parameters related to the scenario generation are summarized in the Table G. 8. The daily market electricity price is extracted from NYISO [89], where corresponding days and years are shown in Table G. 6 and Table G. 7 in the Appendix G. The test system candidate buses and branches for the planning elements are shown in Figure 5. 13, with main characteristics summarized in Table G. 9 in the Appendix G [1].

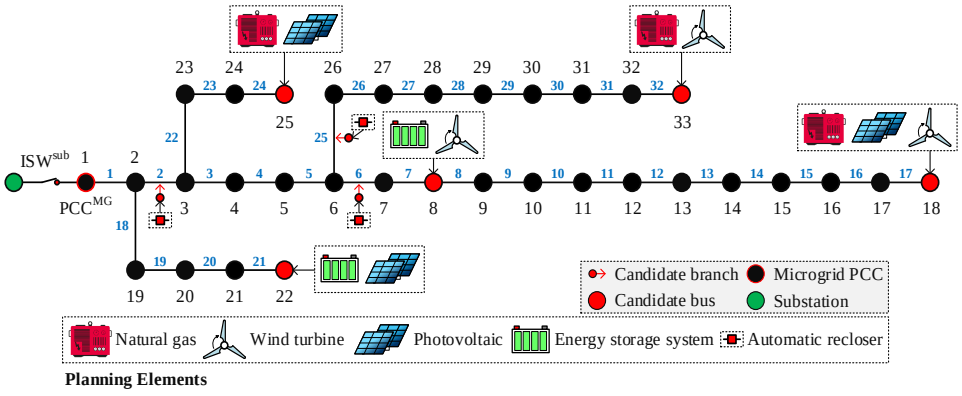

FIGURE 5. 13: 33-bus test system with candidate buses and branches

The proposed planning framework is developed in MATLAB environment, including the DNN models training procedure and the implementation of NSGA-II. It is worth noting that the NaS technology was selected for the ESSs due to its high number of lifecycles. In this work, the ESS capacity rating is proportional to their power rating, similarly to the work in [116]. In this case, the ratio between the rated capacity and rated power is set to 5 for all ESSs. This number was extracted from the optimal solution found in [83]. Additionally, the maximum DoD is arbitrary set to 70% to provide a balance between the battery lifecycle and its generation capability. The DDGs is the natural gas type which can be operated in PQ mode, during GC mode, and $\mathrm{droop}/2^{\mathrm{nd}}$, during IS mode. The general parameters used in this research are summarized in Table G. 10 in the Appendix G.

5.7.1 Deep Learning Solution Validation

In this section, the performance of the trained DDN models is evaluated. As discussed in Section 5.5, a single model is used for predicting the single target. The corresponding hyper-parameters for each DNN model architecture are summarized in the Table 5. 3.

TABLE 5. 3: Hyper-parameters setting for DNN models' architectures

Hyper-parameters	DNN Tanning Targets		
	$TG_{sp,1}$	$TG_{sp,2}$	$TG_{sp,3}$
No. of hidden layer	3	3	3
No. of neurons for hidden layer	25-130-25	25-80-25	25-60-25
Activation fcn. for hidden layer	log-sigmoid	log-sigmoid	log-sigmoid
Activation fcn. for output layer	linear	linear	linear
log-sigmoid: Logistic sigmoid activation function			

The number of samples are 40000 including 70% for the training set and 30% for testing set. Taking advantage of BRB algorithm, training is terminated if the sum squared error and the sum squared weights are not relatively improved over successive training iterations (epochs) [111], [113]. Additionally, an e_1^{dnn} threshold of 10% is considered for guaranteeing the accuracy of the DNN models. In this case, the Figure 5. 14, Figure 5. 15 and Figure 5. 16 illustrate the training/testing MSE and distributed error of the DNN model for predicting $TG_{sp,1}$, $TG_{sp,1}$ and $TG_{sp,1}$, respectively. To this end, the performance of the trained DNN models are summarized in Table 5. 4.

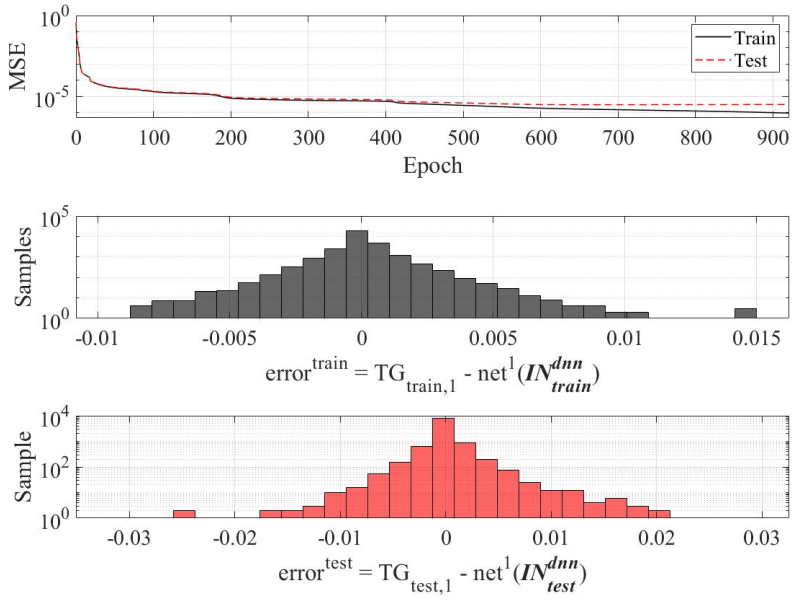

FIGURE 5. 14: MSE over epoch, distributed error of training set and test set of the first DNN model for predicting TG_1

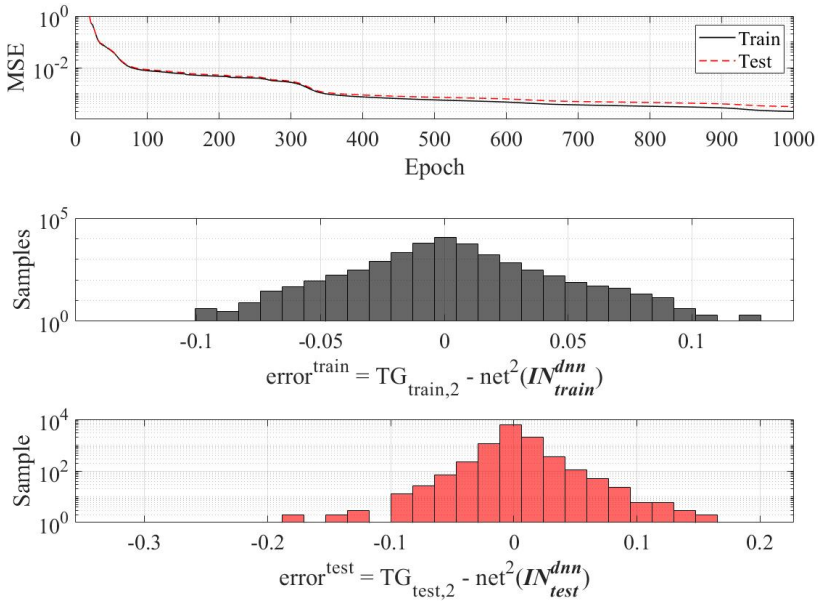

FIGURE 5. 15: MSE over epoch, distributed error of training set and test set of the first DNN model for predicting TG_2

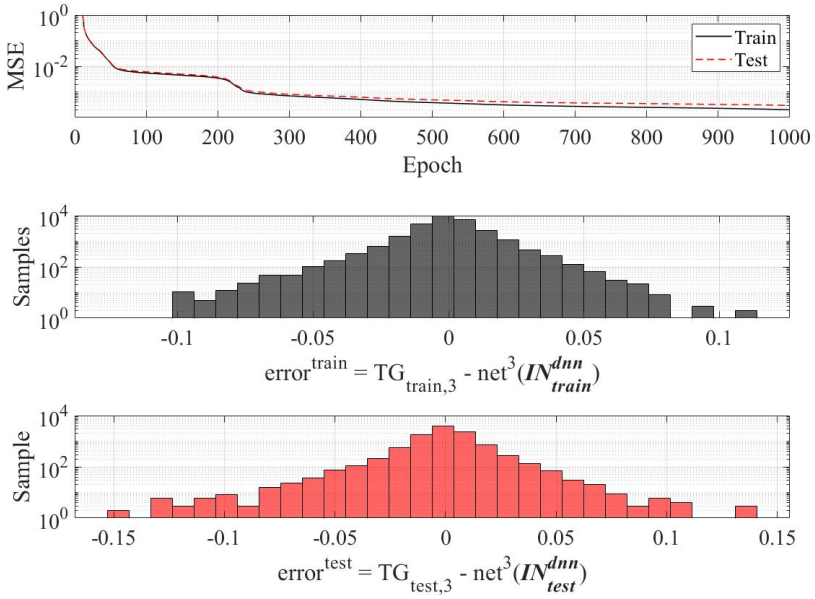

FIGURE 5. 16: MSE over epoch, distributed error of training set and test set of the first DNN model for predicting TG_3

Analyzing Table 5. 4, one can draw conclusions regarding the DDN models errors for the three targets of interest. First, the MSE, RMSE, and $max|y|$ for the training and testing procedures are found around 10^{-4} to 10^{-7}, 10^{-2} to 10^{-4}, and 10^{-1} to 10^{-2} ranges, for all targets. These results indicate the developed method significant ability to infer adequate optimal solutions, presenting errors significantly smaller than accepted deviations. Where respective variations in the errors range are due to the different units under consideration. In terms of the criteria, the e_1^{dnn} obtained for $TG_{sp,2}$, $TG_{sp,2}$ and $TG_{sp,3}$ are found less than the 10% threshold. The e_2^{dnn} is found at 7.75×10^{-4}, 1.06×10^{-2} kWh and 1.09×10^{-2} kWh for $TG_{sp,2}$, $TG_{sp,2}$ and $TG_{sp,3}$, respectively. Finally, e_3^{dnn} shows the ratio in percentage for e_2^{dnn} over the mean target, leading to an error of less than 1%.

TABLE 5. 4: Performance of trained DNN models

Indicators	Set	Training targets		
		$TG_{sp,1}$ -	$TG_{sp,2}$ (kWh)	$TG_{sp,3}$ (kWh)
MSE	Train	9.29×10^{-7}	2.03×10^{-4}	2.04×10^{-4}
	Test	3.13×10^{-6}	3.14×10^{-4}	3.00×10^{-4}
RMSE	Train	9.64×10^{-4}	1.43×10^{-2}	1.43×10^{-2}
	Test	1.77×10^{-3}	1.77×10^{-2}	1.73×10^{-2}
$max\|y\|$	Train	1.50×10^{-2}	1.36×10^{-1}	1.23×10^{-1}
	Test	3.15×10^{-2}	3.29×10^{-1}	1.52×10^{-1}
e_1^{dnn} (%)	-	7.96	1.97	0.09
e_2^{dnn} (kWh)	-	7.75×10^{-4}	1.06×10^{-2}	1.09×10^{-2}
e_3^{dnn} (%)	-	1.44×10^{-1}	2.80×10^{-2}	0.63×10^{-2}

5.7.2 NSGA-II Performance based DNN Model

In this section, the performance of the proposed NSGA-II based DNN model is evaluated. The NSGA-II is responsible for generating the multi-objective problem solution according to the pareto frontier. In this work, the maximum number of iterations and the population are set to 1000. The crossover and mutation probability are set to 0.8 and 0.01, respectively. These parameters were selected based on the guidelines available in [114], [117].

The solutions obtained including the $\mathbf{X_{OLEV}}$ and the multi-objective functions values are based DNN models' prediction. In order to validate these solutions, first the LOPF problem (5.141) is re-simulated for the obtained solution $\mathbf{X_{OLEV}}$. Then, the solution obtained by re-simulating the LOPF is used for calculating the real values of multi-objective functions. Then, R-square (R^2) and error indices (5.145)-(5.145) are calculated for evaluating the error between real objective functions and those obtained by (5.141).

Figure 5. 17 shows the comparison between the real multi-objective functions results and those obtained by (5.141).

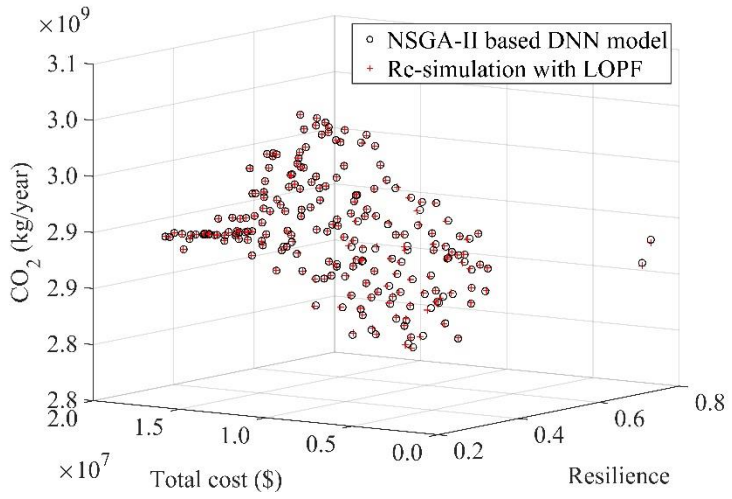

FIGURE 5. 17: Comparison multi-objective solutions obtained by proposed NSGA-II based DNN model and their corresponding real values

Then, Figure 5. 18, Figure 5. 19 and Figure 5. 20 illustrate the probability density as a histogram and the cumulative density of the set of errors $\boldsymbol{e_1^{OLEV^*}}$ for $\boldsymbol{RESI^{OLEV}}$, $\boldsymbol{TC^{OLEV}}$ and $\boldsymbol{AEMIS^{OLEV}}$, respectively. Where, $\boldsymbol{e_1^{OLEV^*}}$ denotes the set of relative errors, compared to the max/worst relative error with $e_1^{OLEV} = \max(\boldsymbol{e_1^{OLEV^*}})$.

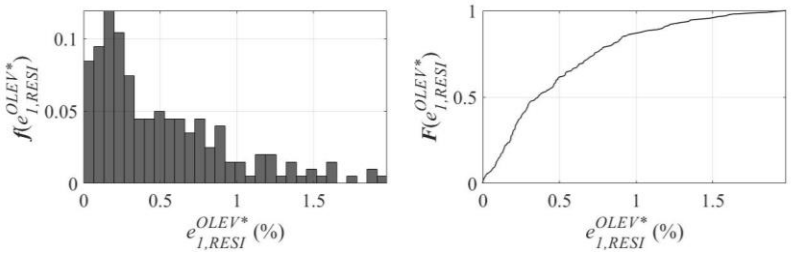

FIGURE 5. 18: Probability density as histogram and cumulative density curve of relative error $e_{1,RESI}^{OLEV^*}$ for $RESI^{OLEV}$

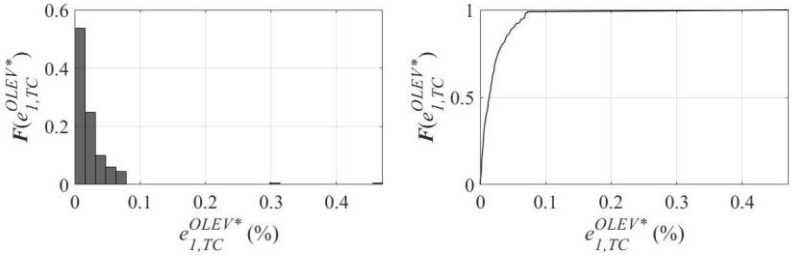

FIGURE 5. 19: Probability density as histogram and cumulative density curve of relative error $e_{1,TC}^{OLEV^*}$ for TC^{OLEV}

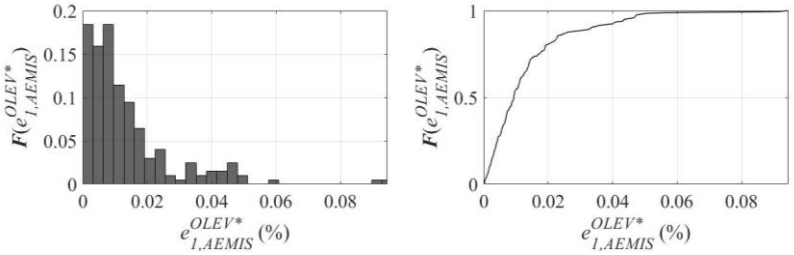

FIGURE 5. 20: Probability density as histogram and cumulative density curve of relative error $e_{1,AEMIS}^{OLEV^*}$ for $AEMIS^{OLEV}$

Finally, TABLE 5. 5: Performance of NSGA-IITable 5. 5 summarizes the R^2 and errors indices between both set of solutions. The R^2 obtained for the three objective functions are close to 1.00, e_1^{OLEV} for all objective functions are less than 2%, whereas e_2^{OLEV} and e_3^{OLEV} indicate absolute and relative errors of less than 1%.

TABLE 5. 5: Performance of NSGA-II

Indicators	**NSGA-II objective functions**		
	$RESI^{OLEV}$	TC^{OLEV}	$AEMIS^{OLEV}$
R^2	0.9993	1.000	0.9999
e_1^{OLEV}	1.98 (%)	4.71×10^{-1} (%)	9.45×10^{-2} (%)
e_2^{OLEV}	1.84×10^{-3}	1.57×10^{3} ($/year)	3.94×10^{5} (kg/year)
e_3^{OLEV}	5.27×10^{-1} (%)	1.69×10^{-2} (%)	1.36×10^{-2} (%)

5.7.3 Optimal Planning Solution

This section presents the optimal planning solution wherein the solution positioned in the pareto frontier respecting to the NSGA-II behavior. In this case, the solution can be classified into two group according to the 3D plan for multi-objective functions solutions shown in Figure 5. 21.

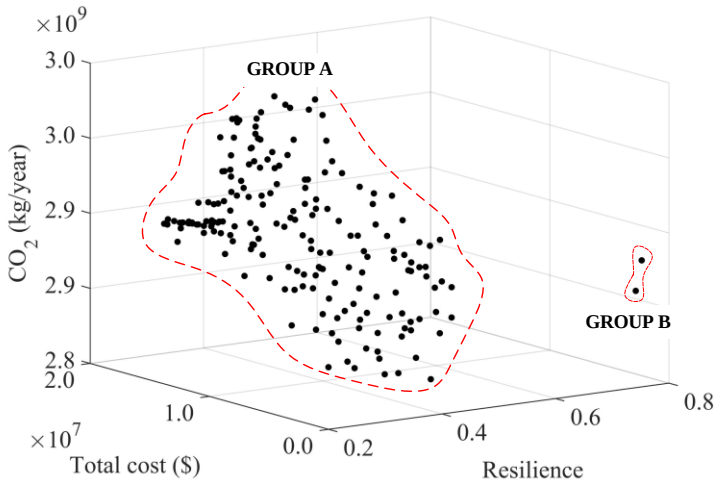

FIGURE 5. 21: Classification in Group A and Group B for the multi-objective function's solution obtained by NSGA-II based DNN model

Group A corresponds to the solution of $\boldsymbol{X^{OLEV}}$ where all three ISWs are installed on candidate branches of the test system. These solutions present variations due to the allocation of different DDGs size in the candidate buses and their deployment for maintaining the microgrid operation in islanded mode. Thus, affecting the evolution of the resilience index in the pareto frontier between ~0.2 and ~0.5. In contrast, Group B correspond to the solution $\boldsymbol{X^{OLEV}}$ where none of ISWs are allocated in the test system. Here, it is worth reminding that a resilience index close to zero represents a high performing network against severe event or any interruption requirement, i.e., load shedding. In this perspective, as expected the resilience indices value in Group B are significantly higher in comparison to Group A.

Detailed results are presented in Table 5. 6 showcasing the planning solution $\boldsymbol{X^{OLEV}}$ and multi-objective functions corresponding to: 1) the max/min value for each objective functions for Group A, and 2) the two solutions for Group B.

TABLE 5. 6: Planning solution corresponding the max/min in each objective function for group A and the planning solution for group B

Group	No.	Binary allocation size of DDGs, WTs, PVs and ESSs	$RESI^{OLEV}$	TC^{OLEV} ($/year)	$AEMIS^{OLEV}$ (kg/year)
A	1	1-4-1 /1-2-1/2-1-2/1-1	**0.512**	4.53×10^{6}	2.85×10^{9}
	2	10-16-14 /5-5-4/4-4-4/3-3	**0.275**	1.53×10^{7}	2.90×10^{9}
	3	3-30-30 /4-4-4/4-4-4/3-3	0.284	$\mathbf{1.78\times10^{7}}$	2.89×10^{9}
	4	1-4-1 /1-2-2/1-1-1/1-1	0.506	$\mathbf{4.24\times10^{6}}$	2.87×10^{9}
	5	8-16-15 /1-2-1/1-1-1/1-1	0.276	9.76×10^{6}	$\mathbf{3.02\times10^{9}}$
	6	1-4-2 /3-3-3/4-3-4/2-2	0.478	7.93×10^{6}	$\mathbf{2.79\times10^{9}}$
B	1	0-2-2 /0-0-0/0-1-1/0-0	0.773	1.53×10^{6}	2.86×10^{9}
	2	0-2-2 /0-0-0/0-0-0/0-0	0.774	1.03×10^{6}	2.88×10^{9}

First analyzing Group A, one can observe that cases A2, A3 and A5 show greater resilience in comparison to A1, A4 and A6. These results are due to the higher size of DDGs allocated, providing the microgrid with better management capacity for generation/load balancing and, consequently, avoiding additional curtailment. Nonetheless, increasing the size of DDGs consequently increases the TC^{OLEV} and $AEMIS^{OLEV}$ due to the additional cost associated. As can see in Table 5. 6, TC^{OLEV} and $AEMIS^{OLEV}$ for cases A2, A3 and A4 are greater than those in cases A1, A4 and A6. In this sense, the consideration of renewable resources as main sources leading to a cleaner energy system can significantly reduce $AEMIS^{OLEV}$. This perspective is clearly observed comparing cases A2 to A5, where $AEMIS^{OLEV}$ is significantly reduced for A2 in comparison to A1 due to its higher capacity of renewable resources. Still, $RESI^{OLEV}$ presents very similar values for both cases with TC^{OLEV} for A2 higher in comparison to A5 due to installation cost. On another perspective, Group B solutions feature significantly reduced resilience capacity, i.e., significantly higher $RESI^{OLEV}$ in comparison to Group A. However, given their trade-off between the three multi-objective functions, they are still placed on the pareto frontier, e.g., TC^{OLEV} for the cases in Group B are significantly lower in comparison to A1-A6.

5.7.4 Resilience Improvement

Next, in this section the obtained optimal planning solutions are stressed for a N-3 contingency scenario to illustrate the system performance in face of severe operating conditions. The N-3 contingency was selected corresponding to the spring season in which multiple faults are localized in the network, respectively on branches #12, #16 and #19. Following, the network performance represented by the energy supply level during the N-3 contingency is determined for the base case, case A1, case A2 and case B2. The corresponding wind gust profile and the binary state representing

the availability of branches #12, #16 and #19, according to the selected $\mathbf{AV^{I-II}}$, are presented in Figure 5. 22.

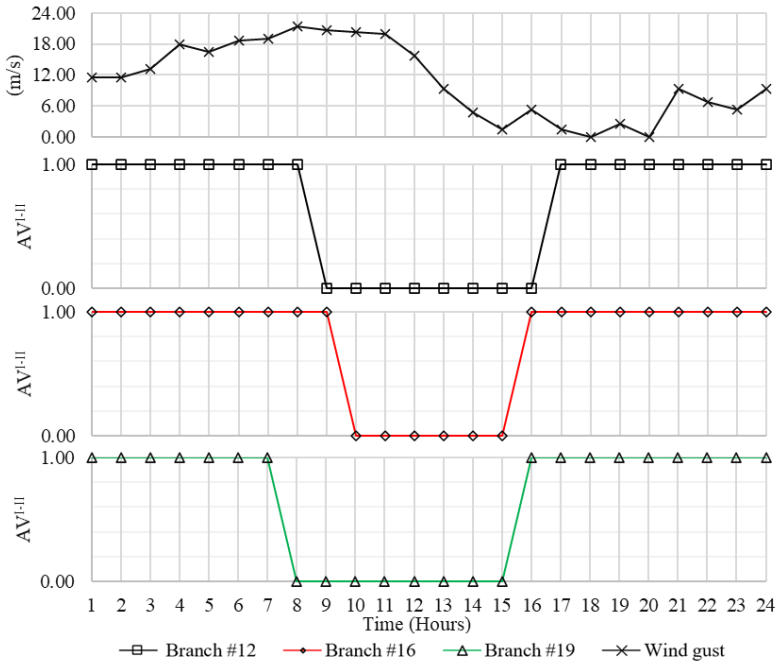

FIGURE 5. 22: Wind gust profile and the timeline of branch #12/#16/#19 availability corresponding to a selected scenario in spring

Whereas Table 5. 7 depicts the availability timeline for branches #12, #16 and #19 along the planning horizon.

TABLE 5. 7: Timeline of overhead line (branch) #12, #16 and #19 break down over the planning horizon of a selected scenario in spring

line no.	t^e	$t^{br,fail0}$	t^d	$TTR^{br,fail}$	$t^{br,rep}$	$t^{r'}$	t^r
	8:00	-	11:00	-	-	16:00	17:00
#12		9:00		6h	17:00		
#16	-	10:00	-	5h	16:00	-	-
#19		8:00		5h	16:00		

Based on this scenario, energy supply results are illustrated in Figure 5. 23 for the base case and optimal planning solutions identified in case A1, case A2 and case B2.

Analyzing Figure 5. 23, one can observe that the base case and case B2 are not able to resist to this severe event, leading to a direct drop of supply from 100% to 0% at t^e. As there is no ISWs placed

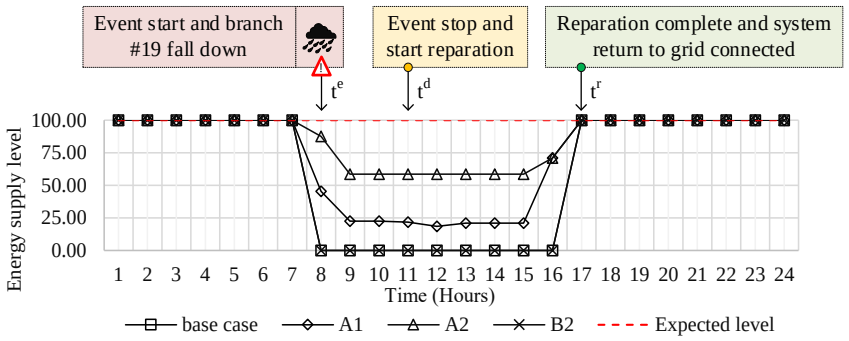

FIGURE 5. 23: Energy supply level and timeline event for representing system performance for base case, case A1, case A2 and case B2

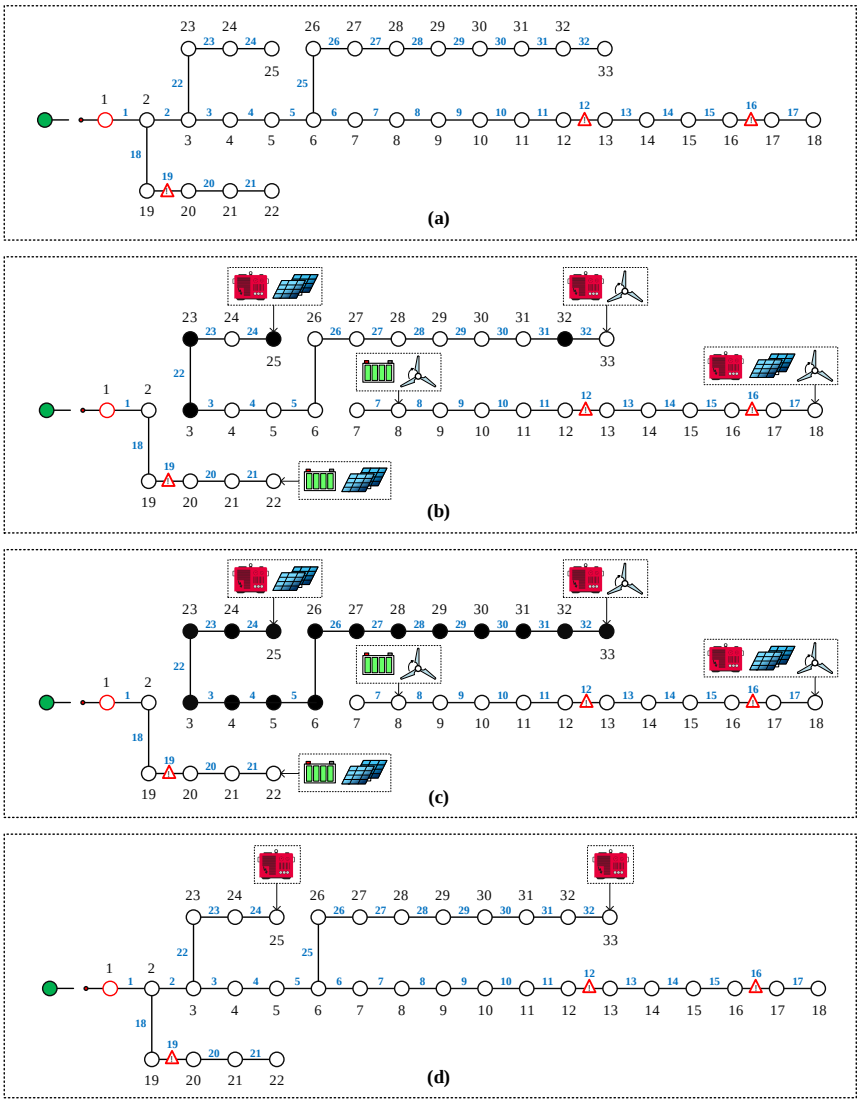

FIGURE 5. 24: Microgrid formations and bus's supply state at t^d for (a) Base case (b) Case A1 (c) Case A2 (d) Case B2

in the network, the microgrids could not be formed, while only ISW^{sub} found in the substation is open and take down a whole test system for clearing the faults in this N-3 contingencies. On the other hand, cases A1 and A2 allow for the formation of microgrids, maintaining the energy supply level according to the size of DDGs allocated. In this sense, due to the limited size of DDGs allocated in case A1, the energy supply level drops down to ~20% at t^d. In contrast, case A2 shows the best performance where the energy supply level drops down from 100% to 59% at t^d, where 41% of non-supplied loads correspond to buses located inside locations isolated by ISWs.

5.8 Conclusion

In this work, a novel resilience-oriented microgrid planning framework is proposed. The proposed framework develops a multi-objective optimization problem formulation incorporating stochastic DL-LOPF^{AC} models solved by NSGA-II based on DNN. The proposed DL-LOPF^{AC} framework provides planning solutions considering stochastic scenarios featuring renewable energy and load uncertainties, HILP events due to N-K contingencies caused by failures in overhead lines, while simultaneously solving for both GC and IS operation modes, including detailed modeling of control and operational requirements, such as droop/2nd during islanded. Next, in order to enable this comprehensive planning framework, NSGA-II based on DNN models is employed to overcome the computation burden and time execution limitations imposed by the stochastic nature of the resilience-oriented planning problem and consideration of the detailed systems' model. In this sense, by taking advantage of the proposed framework predicted solutions obtained by DL-LOPF^{AC} for the inner level present a computation efficient solutions that do not require numerous iterations as found in existing traditional analytical solution methodologies. Following, to verify the effectiveness of the proposed framework multiple numerical analyses are performed. First, the performance for the DL-LOPF^{AC} is evaluated by obtaining significantly reduced MSE/RMSE in relation to the expected error threshold. Moreover, the maximum relative error e_1^{dnn} is found significantly smaller than the threshold for the trained DNN models, demonstrating high accuracy for the DNN models' predicted results. Next, the proposed optimization level NSGA-II based DNN model is validated, demonstrating accuracy levels within accepted deviations, specifically the worst relative error e_1^{OLEV} found is less than 2% for all fitness functions. Finally, the overall planning solution is discussed, indicating the proposed approach ability to deliver optimal planning solutions capable of significantly improving the system resilience even when subjected to HILP events such as N-3 contingencies. Future directions of this work include the integration of electric vehicles into the optimization problems, as these new system elements can significantly impact the system operation, while introducing opportunities in the area of resilience-oriented planning.

Conclusion and Perspectives

6.1 Summary and Conclusions

The microgrid concept can offer significant benefits to the power distribution system through both its grid connected and islanded modes of operation. Given these potential benefits, the microgrid has been put forward as a key component of the future smart grid. This Ph.D. thesis has presented some analysis, operation and planning tools that address some of the challenges facing the existing microgrid power flow tools, optimization models and planning frameworks.

Chapter 2 and Chapter 3 have presented new power flow models needed for the steady state analysis of practical AC microgrid systems. First, Chapter 2 introduced a non-linear branch-based $\mathbf{Z_{bus}}$ algorithm for droop controlled islanded microgrids. This algorithm accounts for the distinct features of the islanded AC microgrid namely; (1) there is no slack bus available for imposing a reference voltage and frequency, (2) system frequency is not a constant and need to be one of the power flow variables, and (3) there is as least one DG unit that is being operated as a droop unit. The proposed algorithm is inversion free and is particularly well suited for sparse implementation. This allows the proposed algorithm to handle the power flow solution for islanded microgrids created in practical distribution systems and potentially comprising up to thousands of electrical nodes. The proposed power flow algorithm has been validated thought several case studies performed on standard balanced and unbalanced test systems. The numerical results demonstrate the effectiveness of the proposed algorithm in terms of the accuracy and computational efficiency. Then, Chapter 3 presented a node-based linear power flow (LPF) model for droop controlled islanded microgrid. Like the algorithm proposed in Chapter 2, this LPF model accounts for the special features of the AC islanded microgrid system. The node-based nature of the proposed LPF model allows for its integration in different planning and operation optimization models to account for the islanded microgrid power flow operation constraints. The effectiveness of the proposed LPF model has been validated thought different balanced and unbalanced case studies. The results demonstrated the accuracy of the proposed LPF model and ensures its suitability for the linear optimal power flow problem subsequently studied in this thesis.

In chapter 4, the necessary optimal power flow (OPF) models for the optimal operation of AC microgrids are studied. In this work, linear optimal power flow (LOPF) models for the optimal operation problem of both balanced and unbalanced AC microgrids with hierarchical control structure

were developed. To this end, the optimal operation problem has been first formulated as a MINLP model, then it was linearized and turned into a MILP model. The proposed MILP model accounts for the microgrid philosophy of operation during grid connected and islanded through a single comprehensive model. Several kinds of distributed generations (i.e., dispatchable and non-dispatchable) and energy storage resources were accounted for in the proposed model. Several numerical simulation studies were conducted to validate and prove the effectiveness of the proposed MILP model. The simulation result demonstrated the accuracy of the developed MILP model. Moreover, the results also reveals that the MILP model's computation time is significantly lower than that of its MINLP counterpart model. With such performance enhancement, the proposed LOPF model was subsequently adopted in the planning problem for accomplishing the main goal of this thesis.

In the last stage of the research, chapter 5 introduced the microgrid planning framework for resilience enhancement of the power distribution system when facing the N-K contingencies cause by HILP event. The proposed framework is based on a multi-objective optimization problem that is solved by NSGA-II. A deep-learning AC-LOPF (DL-LOPF^{AC}) model was developed to alleviate the computational burden associated with need to solve the LOPF for multiple candidate solutions and multiple stochastic scenarios during the evolution of the NSGA-II. In this work, the uncertainty of the renewable energy has been considered by considering different stochastic scenarios. In order to account the uncertainty of the N-K contingencies, a methodology for generating severe HILP operation scenarios depending on the weather has been adopted. The proposed stochastic DL-LOPF^{AC} accounted for the operation behavior of the microgrids including GC and IS modes of operation, while properly considering the microgrid's hierarchical control, by taking advantage of the proposed LOPF model developed in chapter 4 in the training of the deep learning model. To this end, the effectiveness of the proposed framework has been proved by numerical simulation results. First, the performance for the DL-LOPF^{AC} is evaluated and its accuracy is verified. Then, the proposed optimization level NSGA-II based DNN model is validated and the pareto optimal solution was derived.

This thesis is mainly conducted through a work presented in chapter 2 to 5 comprising the steady state analysis (i.e., power flow and optimal power flow carrier) and the planning methodology. The general contribution of this thesis can be summarized as follows:

- A branch-based inversion free $\mathbf{Z_{bus}}$ power flow algorithm for droop islanded microgrid is proposed. The proposed algorithm does not require bus renumbering, nor does it require a

DG to be allocated at the reference bus. Moreover, the proposed method is particularly well suited for sparse implementation and delivers an enhanced computational efficiency in delivering the power flow solution making it particularly useful for large scale microgrid systems comprising up to thousands of buses.

- Proposed a node based LPF model that accounts for the droop-controlled autonomous microgrid philosophy of operation as well as considering both balanced and unbalanced network characteristics.

- Proposed a time coupled MINLP and MILP OPF models for the optimum operation problem of balanced and unbalanced microgrid with hierarchical control structure. The proposed models consider the microgrid philosophy of operation during GC and IS. Moreover, the energy storage system and the renewable energy resources i.e., WTs and PVs have been accounted for.

- Proposed a general framework using meta-heuristic multi-objective optimization for planning resilience oriented microgrid(s) in active distribution systems considering economic, resilience and environmental points of views. The proposed framework employs novel deep learning models to speed up the determination of the economic, resilience and environmental metrics pertaining to the MG(s).

6.2 Perspective for the Future Work

This research has been carried out focusing on the steady-state analysis and the planning methodology. Future research directions include:

- Explore the new generic power flow and optimal power flow tool that consider multiple and integrated AC and DC grids.

- Explore other machine learning options and identify different methodologies for comparing and allowing the planning engineer to choose the appropriate machine learning approach for the case study under consideration.

- Several types of resources including generators and storages have been considered in the OPF and planning problems. On the other hand, electric vehicles are increasing in popularity and will have an impact on the system operation and planning. As such, integrating electric vehicles is of increasing importance especially in the resilience-oriented planning area.

- Explore the transmission level planning, while considering the microgrid at the distribution level; in the order to the develop the resilience enhancement strategy and planning accounting for both transmission and distribution systems.

- Test and validate the developed software package to develop an open source software package suitable for sharing on public repository such as GitHub.

- The studies are conducted using standard test systems. On the other hand, this research can be adapted and applied by considering the real practical in Laos country. This can lead to the possibility of exploring new benefit areas, new technologies and the performance enhancement of the national grid of Laos.

Bibliography

[1] Y. Vilaisarn and M. Abdelaziz, “An inversion-free sparse Z power flow algorithm for large-scale droop controlled islanded microgrids,” *Int. J. Electr. Power Energy Syst.*, vol. 121, no. August 2019, p. 106048, Oct. 2021, doi: 10.1016/j.ijepes.2020.106048.

[2] Y. Vilaisarn, M. Abdelaziz, and J. Cros, “Linear Three-Phase Power Flow Model for Autonomous Microgrid Systems,” *CIRED - Open Access Proc. J.*, vol. 2020, no. 1, pp. 50–53, 2021, doi: 10.1049/oap-cired.2021.0019.

[3] Y. Vilaisarn, M. Moradzadeh, M. Abdelaziz, and J. Cros, “An MILP formulation for the optimum operation of AC microgrids with hierarchical control,” *Int. J. Electr. Power Energy Syst.*, vol. 137, no. September 2021, p. 107674, May 2022, doi: 10.1016/j.ijepes.2021.107674.

[4] A. Hirsch, Y. Parag, and J. Guerrero, “Microgrids: A review of technologies, key drivers, and outstanding issues,” *Renewable and Sustainable Energy Reviews*, vol. 90, no. April. Elsevier Ltd, pp. 402–411, 2018, doi: 10.1016/j.rser.2018.03.040.

[5] C. Wang *et al.*, “Distributed Energy and Microgrids (DEM),” *Appl. Energy*, vol. 210, pp. 685–689, 2018, doi: 10.1016/j.apenergy.2017.11.059.

[6] R. Li, W. Wang, Z. Chen, J. Jiang, and W. Zhang, “A review of optimal planning active distribution system: Models, methods, and future researches,” *Energies*, vol. 10, no. 11. pp. 1–27, 2017, doi: 10.3390/en10111715.

[7] S. Parhizi, H. Lotfi, A. Khodaei, and S. Bahramirad, “State of the art in research on microgrids: A review,” *IEEE Access*, vol. 3, pp. 890–925, 2015, doi: 10.1109/ACCESS.2015.2443119.

[8] S. Lakshmi and S. Ganguly, “Transition of Power Distribution System Planning from Passive to Active Networks: A State-of-the-Art Review and a New Proposal,” in *Green Energy and Technology*, no. 9789811071874, 2018, pp. 87–117.

[9] C. A. C. D’ADAMO, S. JUPE, “Global Survey on Planning and Operation of Active Distribution Network-Update of CIGRE C6.11 Working Group Activities,” 2009.

[10] R. Hidalgo, C. Abbey, and G. Joós, “A review of active distribution networks enabling

technologies," in *IEEE PES General Meeting, PES 2010*, 2010, pp. 1–9, doi: 10.1109/PES.2010.5590051.

[11] D. T. Ton and M. A. Smith, "The U.S. Department of Energy's Microgrid Initiative," *Electr. J.*, vol. 25, no. 8, pp. 84–94, 2012, doi: 10.1016/j.tej.2012.09.013.

[12] R. H. Lasseter, "MicroGrids," in *2002 IEEE Power Engineering Society Winter Meeting. Conference Proceedings (Cat. No.02CH37309)*, 2002, vol. 1, pp. 305–308, doi: 10.1109/PESW.2002.985003.

[13] E. Bullich-Massagué, F. Díaz-González, M. Aragüés-Peñalba, F. Girbau-Llistuella, P. Olivella-Rosell, and A. Sumper, "Microgrid clustering architectures," *Appl. Energy*, vol. 212, no. August 2017, pp. 340–361, 2018, doi: 10.1016/j.apenergy.2017.12.048.

[14] D. E. Olivares *et al.*, "Trends in microgrid control," *IEEE Trans. Smart Grid*, vol. 5, no. 4, pp. 1905–1919, Jul. 2014, doi: 10.1109/TSG.2013.2295514.

[15] M. M. A. Abdelaziz, H. E. Farag, E. F. El-Saadany, and Y. A.-R. I. Mohamed, "A Novel and Generalized Three-Phase Power Flow Algorithm for Islanded Microgrids Using a Newton Trust Region Method," *IEEE Trans. Power Syst.*, vol. 28, no. 1, pp. 190–201, Feb. 2013, doi: 10.1109/TPWRS.2012.2195785.

[16] G. Agundis-Tinajero, J. Segundo-Ramírez, N. Visairo-Cruz, M. Savaghebi, J. M. Guerrero, and E. Barocio, "Power flow modeling of islanded AC microgrids with hierarchical control," *Int. J. Electr. Power Energy Syst.*, vol. 105, no. August 2018, pp. 28–36, Feb. 2019, doi: 10.1016/j.ijepes.2018.08.002.

[17] M. H. Moradi, V. B. Foroutan, and M. Abedini, "Power flow analysis in islanded Micro-Grids via modeling different operational modes of DGs: A review and a new approach," *Renew. Sustain. Energy Rev.*, vol. 69, no. August 2015, pp. 248–262, Mar. 2017, doi: 10.1016/j.rser.2016.11.156.

[18] J. D. Glover, M. S. Sarma, and T. J. Overbye, *Power System Analysis and Design*. 2012.

[19] Turan Gonen, *Modern Power System Analysis*. 2016.

[20] O. A. Afolabi, W. H. Ali, P. Cofie, J. Fuller, P. Obiomon, and E. S. Kolawole, "Analysis of the Load Flow Problem in Power System Planning Studies," *Energy Power Eng.*, vol. 07,

no. 10, pp. 509–523, 2015, doi: 10.4236/epe.2015.710048.

[21] S. Sunisith and K. Meena, “Backward / Forward Sweep Based Distribution Load Flow Method,” in *International Electrical Engineering Journal*, 2014, vol. 5, no. 9, pp. 1539–1544.

[22] P. J. Lagace, M. H. Vuong, and I. Kamwa, “Improving power flow convergence by Newton Raphson with a levenberg-marquardt method,” *IEEE Power Energy Soc. 2008 Gen. Meet. Convers. Deliv. Electr. Energy 21st Century, PES*, pp. 1–6, 2008, doi: 10.1109/PES.2008.4596138.

[23] G. Agundis-Tinajero *et al.*, “Extended-Optimal-Power-Flow-Based Hierarchical Control for Islanded AC Microgrids,” *IEEE Trans. Power Electron.*, vol. 34, no. 1, pp. 840–848, Jan. 2019, doi: 10.1109/TPEL.2018.2813980.

[24] H. Abdi, S. D. Beigvand, and M. La Scala, “A review of optimal power flow studies applied to smart grids and microgrids,” *Renew. Sustain. Energy Rev.*, vol. 71, no. December 2016, pp. 742–766, 2017, doi: 10.1016/j.rser.2016.12.102.

[25] A. Vaccaro and C. A. Cañizares, “A knowledge-based framework for power flow and optimal power flow analyses,” *IEEE Trans. Smart Grid*, vol. 9, no. 1, pp. 230–239, 2018, doi: 10.1109/TSG.2016.2549560.

[26] P. P. Vergara, J. C. Lopez, M. J. Rider, and L. C. P. Da Silva, “Optimal Operation of Unbalanced Three-Phase Islanded Droop-Based Microgrids,” *IEEE Trans. Smart Grid*, vol. 10, no. 1, pp. 928–940, 2019, doi: 10.1109/TSG.2017.2756021.

[27] S. A. Arefifar, Y. A.-R. I. Mohamed, and T. H. M. El-Fouly, “Supply-Adequacy-Based Optimal Construction of Microgrids in Smart Distribution Systems,” *IEEE Trans. Smart Grid*, vol. 3, no. 3, pp. 1491–1502, Sep. 2012, doi: 10.1109/TSG.2012.2198246.

[28] S. A. Arefifar, Y. A.-R. I. Mohamed, and T. H. M. EL-Fouly, “Optimum Microgrid Design for Enhancing Reliability and Supply-Security,” *IEEE Trans. Smart Grid*, vol. 4, no. 3, pp. 1567–1575, Sep. 2013, doi: 10.1109/TSG.2013.2259854.

[29] M. Ghasemi, A. Kazemi, A. Mazza, and E. Bompard, “A three-stage stochastic planning model for enhancing the resilience of distribution systems with microgrid formation

strategy," *IET Gener. Transm. Distrib.*, vol. 15, no. 13, pp. 1908–1921, 2021, doi: 10.1049/gtd2.12144.

[30] F. Hameed, M. Al Hosani, and H. H. Zeineldin, "A Modified Backward/Forward Sweep Load Flow Method for Islanded Radial Microgrids," *IEEE Trans. Smart Grid*, vol. 10, no. 1, pp. 910–918, Jan. 2019, doi: 10.1109/TSG.2017.2754551.

[31] F. Mumtaz, M. H. Syed, M. Al Hosani, and H. H. Zeineldin, "A Novel Approach to Solve Power Flow for Islanded Microgrids Using Modified Newton Raphson with Droop Control of DG," *IEEE Trans. Sustain. Energy*, vol. 7, no. 2, pp. 493–503, 2016, doi: 10.1109/TSTE.2015.2502482.

[32] A. Kumar, B. K. Jha, D. Singh, and R. K. Misra, "Current injection-based Newton–Raphson power-flow algorithm for droop-based islanded microgrids," *IET Gener. Transm. Distrib.*, vol. 13, no. 23, pp. 5271–5283, Dec. 2019, doi: 10.1049/iet-gtd.2019.0575.

[33] A. A. Nazari, R. Keypour, M. H. Beiranvand, and N. Amjady, "A decoupled extended power flow analysis based on Newton-Raphson method for islanded microgrids," *Int. J. Electr. Power Energy Syst.*, vol. 117, no. September 2019, p. 105705, 2020, doi: 10.1016/j.ijepes.2019.105705.

[34] A. Kumar, B. K. Jha, D. K. Dheer, R. K. Misra, and D. Singh, "A Nested-Iterative Newton-Raphson based Power Flow Formulation for Droop-based Islanded Microgrids," *Electr. Power Syst. Res.*, vol. 180, no. December 2019, p. 106131, 2020, doi: 10.1016/j.epsr.2019.106131.

[35] G. Diaz, J. Gomez-Aleixandre, and J. Coto, "Direct Backward/Forward Sweep Algorithm for Solving Load Power Flows in AC Droop-Regulated Microgrids," *IEEE Trans. Smart Grid*, vol. 7, no. 5, pp. 2208–2217, Sep. 2016, doi: 10.1109/TSG.2015.2478278.

[36] M. E. Nassar and M. M. A. Salama, "A novel branch-based power flow algorithm for islanded AC microgrids," *Electr. Power Syst. Res.*, vol. 146, pp. 51–62, May 2017, doi: 10.1016/j.epsr.2017.01.019.

[37] A. Kumar, B. K. Jha, D. K. Dheer, D. Singh, and R. K. Misra, "Nested backward/forward sweep algorithm for power flow analysis of droop regulated islanded microgrids," *IET Gener. Transm. Distrib.*, vol. 13, no. 14, pp. 3086–3095, 2019, doi: 10.1049/iet-

gtd.2019.0388.

[38] G. C. Kryonidis, E. O. Kontis, A. I. Chrysochos, K. O. Oureilidis, C. S. Demoulias, and G. K. Papagiannis, “Power Flow of Islanded AC Microgrids: Revisited,” *IEEE Trans. Smart Grid*, vol. 9, no. 4, pp. 3903–3905, 2018, doi: 10.1109/TSG.2018.2799480.

[39] T. Y. Hsieh, T. H. Chen, and N. C. Yang, “Matrix decompositions-based approach to Z-bus matrix building process for radial distribution systems,” *Int. J. Electr. Power Energy Syst.*, vol. 89, pp. 62–68, 2017, doi: 10.1016/j.ijepes.2017.01.004.

[40] N. C. Yang, “Three-phase power flow calculations using direct ZBUS method for large-scale unbalanced distribution networks,” *IET Gener. Transm. Distrib.*, vol. 10, no. 4, pp. 1048–1055, 2016, doi: 10.1049/iet-gtd.2015.0822.

[41] J. H. Teng, “A direct approach for distribution system load flow solutions,” *IEEE Trans. Power Deliv.*, vol. 18, no. 3, pp. 882–887, 2003, doi: 10.1109/TPWRD.2003.813818.

[42] P. Ling, C. Fang, L. Guo, X. Su, and S. Zheng, “A Novel Direct Load Flow Algorithm for Unbalanced Micro-grids Considering the Droop Characteristics of DG and Load,” *2018 Int. Conf. Power Syst. Technol. POWERCON 2018 - Proc.*, no. 201805280000069, pp. 2096–2101, 2019, doi: 10.1109/POWERCON.2018.8601869.

[43] X. Wang, M. Shahidehpour, C. Jiang, W. Tian, Z. Li, and Y. Yao, “Three-Phase Distribution Power Flow Calculation for Loop-Based Microgrids,” *IEEE Trans. Power Syst.*, vol. 33, no. 4, pp. 3955–3967, 2018, doi: 10.1109/TPWRS.2017.2788055.

[44] E. E. Pompodakis, G. C. Kryonidis, and M. C. Alexiadis, “A Comprehensive Load Flow Approach for Grid-Connected and Islanded AC Microgrids,” *IEEE Trans. Power Syst.*, vol. 35, no. 2, pp. 1143–1155, Mar. 2020, doi: 10.1109/TPWRS.2019.2945011.

[45] M. Abdelaziz, “GPU-OpenCL accelerated probabilistic power flow analysis using Monte-Carlo simulation,” *Electr. Power Syst. Res.*, vol. 147, pp. 70–72, Jun. 2017, doi: 10.1016/j.epsr.2017.02.022.

[46] Y. Wang, N. Zhang, H. Li, J. Yang, and C. Kang, “Linear three-phase power flow for unbalanced active distribution networks with PV nodes,” *CSEE J. Power Energy Syst.*, vol. 3, no. 3, pp. 321–324, 2017, doi: 10.17775/cseejpes.2017.00240.

[47] Z. Yang, K. Xie, J. Yu, H. Zhong, N. Zhang, and Q. X. Xia, “A General Formulation of Linear Power Flow Models: Basic Theory and Error Analysis,” *IEEE Trans. Power Syst.*, vol. 34, no. 2, pp. 1315–1324, 2019, doi: 10.1109/TPWRS.2018.2871182.

[48] M. M. A. Abdelaziz and H. E. Farag, “An Enhanced Supervisory Control for Islanded Microgrid Systems,” *IEEE Trans. Smart Grid*, vol. 7, no. 4, pp. 1941–1943, 2016, doi: 10.1109/TSG.2016.2553580.

[49] J. Rocabert, A. Luna, F. Blaabjerg, and P. Rodríguez, “Control of power converters in AC microgrids,” *IEEE Trans. Power Electron.*, vol. 27, no. 11, pp. 4734–4749, 2012, doi: 10.1109/TPEL.2012.2199334.

[50] D. Wu, F. Tang, T. Dragicevic, J. C. Vasquez, and J. M. Guerrero, “A Control Architecture to Coordinate Renewable Energy Sources and Energy Storage Systems in Islanded Microgrids,” *IEEE Trans. Smart Grid*, vol. 6, no. 3, pp. 1156–1166, 2015, doi: 10.1109/TSG.2014.2377018.

[51] X. Wu, X. Wang, and C. Qu, “A hierarchical framework for generation scheduling of microgrids,” *IEEE Trans. Power Deliv.*, vol. 29, no. 6, pp. 2448–2457, 2014, doi: 10.1109/TPWRD.2014.2360064.

[52] P. P. Vergara, J. C. López, L. C. P. da Silva, and M. J. Rider, “Security-constrained optimal energy management system for three-phase residential microgrids,” *Electr. Power Syst. Res.*, vol. 146, pp. 371–382, 2017, doi: 10.1016/j.epsr.2017.02.012.

[53] E. Riva Sanseverino, N. Nguyen Quang, M. L. Di Silvestre, J. M. Guerrero, and C. Li, “Optimal power flow in three-phase islanded microgrids with inverter interfaced units,” *Electr. Power Syst. Res.*, vol. 123, pp. 48–56, 2015, doi: 10.1016/j.epsr.2015.01.020.

[54] P. P. Vergara *et al.*, “A Generalized Model for the Optimal Operation of Microgrids in Grid-Connected and Islanded Droop-Based Mode,” *IEEE Trans. Smart Grid*, vol. 10, no. 5, pp. 5032–5045, 2018, doi: 10.1109/TSG.2018.2873411.

[55] F. H. Jufri, V. Widiputra, and J. Jung, “State-of-the-art review on power grid resilience to extreme weather events: Definitions, frameworks, quantitative assessment methodologies, and enhancement strategies,” *Appl. Energy*, vol. 239, no. February, pp. 1049–1065, 2019, doi: 10.1016/j.apenergy.2019.02.017.

[56] Z. Li, M. Shahidehpour, F. Aminifar, A. Alabdulwahab, and Y. Al-Turki, “Networked Microgrids for Enhancing the Power System Resilience,” *Proc. IEEE*, vol. 105, no. 7, pp. 1289–1310, 2017, doi: 10.1109/JPROC.2017.2685558.

[57] Y. Wang, A. O. Rousis, and G. Strbac, “On microgrids and resilience: A comprehensive review on modeling and operational strategies,” *Renew. Sustain. Energy Rev.*, vol. 134, no. November 2019, p. 110313, 2020, doi: 10.1016/j.rser.2020.110313.

[58] J. Kim and Y. Dvorkin, “Enhancing Distribution System Resilience with Mobile Energy Storage and Microgrids,” *IEEE Trans. Smart Grid*, vol. 10, no. 5, pp. 4996–5006, 2018, doi: 10.1109/TSG.2018.2872521.

[59] Y. Wang, A. Oulis-Rousis, and G. Strbac, “A three-level planning model for optimal sizing of networked microgrids considering a trade-off between resilience and cost,” *IEEE Trans. Power Syst.*, vol. 36, no. 6, pp. 5657–5669, 2021, doi: 10.1109/TPWRS.2021.3076128.

[60] J. Najafi, A. Peiravi, A. Anvari-Moghaddam, and J. M. Guerrero, “Resilience improvement planning of power-water distribution systems with multiple microgrids against hurricanes using clean strategies,” *J. Clean. Prod.*, vol. 223, pp. 109–126, 2019, doi: 10.1016/j.jclepro.2019.03.141.

[61] M. H. Amirioun, F. Aminifar, and H. Lesani, “Towards Proactive Scheduling of Microgrids Against Extreme Floods,” *IEEE Trans. Smart Grid*, vol. 9, no. 4, pp. 3900–3902, 2018, doi: 10.1109/TSG.2017.2762906.

[62] Q. Shi *et al.*, “Network reconfiguration and distributed energy resource scheduling for improved distribution system resilience,” *Int. J. Electr. Power Energy Syst.*, vol. 124, no. July 2020, p. 106355, 2021, doi: 10.1016/j.ijepes.2020.106355.

[63] J. Zhu, Y. Yuan, and W. Wang, “An exact microgrid formation model for load restoration in resilient distribution system,” *Int. J. Electr. Power Energy Syst.*, vol. 116, no. September 2019, p. 105568, 2020, doi: 10.1016/j.ijepes.2019.105568.

[64] X. Wu, Z. Wang, T. Ding, X. Wang, Z. Li, and F. Li, “Microgrid planning considering the resilience against contingencies,” *IET Gener. Transm. Distrib.*, vol. 13, no. 16, pp. 3534–3548, 2019, doi: 10.1049/iet-gtd.2018.6816.

[65] Y. Wang, A. O. Rousis, and G. Strbac, “Resilience-driven optimal sizing and pre-positioning of mobile energy storage systems in decentralized networked microgrids,” *Appl. Energy*, vol. 305, no. September 2021, p. 117921, 2022, doi: 10.1016/j.apenergy.2021.117921.

[66] X. Hu, H. Hu, S. Verma, and Z.-L. Zhang, “Physics-Guided Deep Neural Networks for Power Flow Analysis,” *IEEE Trans. Power Syst.*, vol. 36, no. 3, pp. 1–1, 2020, doi: 10.1109/TPWRS.2020.3029557.

[67] X. Pan, T. Zhao, M. Chen, and S. Zhang, “DeepOPF: A Deep Neural Network Approach for Security-Constrained DC Optimal Power Flow,” *IEEE Trans. Power Syst.*, vol. 36, no. 3, pp. 1–1, 2020, doi: 10.1109/TPWRS.2020.3026379.

[68] J. C. Bedoya, Y. Wang, and C. Liu, “Distribution System Resilience Under Asynchronous Information Using Deep Reinforcement Learning Juan,” *IEEE Trans. Power Syst.*, vol. 36, no. 5, pp. 4235–4245, 2021.

[69] M. Moradi-Sepahvand, T. Amraee, and S. Sadeghi Gougheri, “Deep Learning Based Hurricane Resilient Coplanning of Transmission Lines, Battery Energy Storages, and Wind Farms,” *IEEE Trans. Ind. Informatics*, vol. 18, no. 3, pp. 2120–2131, 2022, doi: 10.1109/TII.2021.3074397.

[70] M. Dabbaghjamanesh, A. Kavousi-Fard, and J. Zhang, “Stochastic Modeling and Integration of Plug-In Hybrid Electric Vehicles in Reconfigurable Microgrids with Deep Learning-Based Forecasting,” *IEEE Trans. Intell. Transp. Syst.*, vol. 22, no. 7, pp. 4394–4403, 2021, doi: 10.1109/TITS.2020.2973532.

[71] M. M. A. Abdelaziz, “OpenCL-Accelerated Probabilistic Power Flow for Active Distribution Networks,” *IEEE Trans. Sustain. Energy*, vol. 9, no. 3, pp. 1255–1264, Jul. 2018, doi: 10.1109/TSTE.2017.2781148.

[72] M. A. Allam, A. A. Hamad, M. Kazerani, and E. F. El-Saadany, “A novel dynamic power routing scheme to maximize loadability of islanded hybrid AC/DC microgrids under unbalanced AC loading,” *IEEE Trans. Smart Grid*, vol. 9, no. 6, pp. 5798–5809, 2018, doi: 10.1109/TSG.2017.2697360.

[73] “C. Ababei, REDS: REpository of Distribution Systems, 2012. [Online]. Available: http://www.dejazzer.com Accessed on: Aug. 11, 2016.” .

[74] G. K. V. Raju and P. R. Bijwe, “Efficient reconfiguration of balanced and unbalanced distribution systems for loss minimisation,” *Gener. Transm. Distrib. IET*, vol. 2, no. 1, pp. 7–12, doi: 10.1049/iet-gtd.

[75] M. M. A. Abdelaziz, H. E. Z. Farag, and E. F. El-Saadany, “Fuel-saving benefit analysis of islanded microgrid central controllers,” *Electr. Power Syst. Res.*, vol. 125, pp. 45–54, 2015, doi: 10.1016/j.epsr.2015.03.026.

[76] M. M. A. Abdelaziz, “Effect of Detailed Reactive Power Limit Modeling on Islanded Microgrid Power Flow Analysis,” *IEEE Trans. Power Syst.*, vol. 31, no. 2, pp. 1665–1666, 2016, doi: 10.1109/TPWRS.2015.2412690.

[77] H. E. Farag, M. M. A. Abdelaziz, and E. F. El-Saadany, “Incorporating voltage regulator and load models in unbalanced power flow studies of active distribution systems,” *IEEE Power Energy Soc. Gen. Meet.*, 2012, doi: 10.1109/PESGM.2012.6344972.

[78] M. Abdelaziz and M. Moradzadeh, “Monte-Carlo simulation based multi-objective optimum allocation of renewable distributed generation using OpenCL,” *Electr. Power Syst. Res.*, vol. 170, no. September 2018, pp. 81–91, May 2019, doi: 10.1016/j.epsr.2019.01.012.

[79] M. M. A. Abdelaziz, H. E. Farag, and E. F. El-Saadany, “Optimum Reconfiguration of Droop-Controlled Islanded Microgrids,” *IEEE Trans. Power Syst.*, vol. 31, no. 3, pp. 2144–2153, May 2016, doi: 10.1109/TPWRS.2015.2456154.

[80] J. M. Guerrero, M. Chandorkar, T. L. Lee, and P. C. Loh, “Advanced control architectures for intelligent microgridspart i: Decentralized and hierarchical control,” *IEEE Trans. Ind. Electron.*, vol. 60, no. 4, pp. 1254–1262, 2013, doi: 10.1109/TIE.2012.2194969.

[81] L. H. Macedo, S. Member, J. F. Franco, and M. J. Rider, “Optimal Operation of Distribution Networks Considering Energy Storage Devices,” *IEEE Trans. Smart Grid*, vol. 6, no. 6, pp. 1–12, 2015.

[82] S. M. Mohseni-Bonab, I. Kamwa, A. Moeini, and A. Rabiee, “Voltage Security Constrained Stochastic Programming Model for Day-Ahead BESS Schedule in Co-Optimization of T&D Systems,” *IEEE Trans. Sustain. Energy*, vol. 11, no. 1, pp. 391–404, 2020, doi: 10.1109/TSTE.2019.2892024.

[83] M. Moradzadeh and M. M. A. Abdelaziz, “A New MILP Formulation for Renewables and Energy Storage Integration in Fast Charging Stations,” *IEEE Trans. Transp. Electrif.*, vol. 6, no. 1, pp. 181–198, 2020, doi: 10.1109/TTE.2020.2974179.

[84] I. Alsaidan, A. Khodaei, and W. Gao, “A Comprehensive Battery Energy Storage Optimal Sizing Model for Microgrid Applications,” *IEEE Trans. Power Syst.*, vol. 33, no. 4, pp. 3968–3980, Jul. 2018, doi: 10.1109/TPWRS.2017.2769639.

[85] M. Moradzadeh and M. Abdelaziz, “A Stochastic Optimal Planning Model for Fully Green Stand-Alone PEV Charging Stations,” *IEEE Trans. Transp. Electrif.*, 2021, doi: 10.1109/TTE.2021.3069438.

[86] Z. Yang, H. Zhong, Q. Xia, A. Bose, and C. Kang, “Optimal power flow based on successive linear approximation of power flow equations,” *IET Gener. Transm. Distrib.*, vol. 10, no. 14, pp. 3654–3662, Nov. 2016, doi: 10.1049/iet-gtd.2016.0547.

[87] Z. Yang, A. Bose, H. Zhong, N. Zhang, Q. Xia, and C. Kang, “Optimal Reactive Power Dispatch With Accurately Modeled Discrete Control Devices: A Successive Linear Approximation Approach,” *IEEE Trans. Power Syst.*, vol. 32, no. 3, pp. 2435–2444, May 2017, doi: 10.1109/TPWRS.2016.2608178.

[88] Z. Yang, H. Zhong, A. Bose, T. Zheng, Q. Xia, and C. Kang, “A Linearized OPF Model with Reactive Power and Voltage Magnitude: A Pathway to Improve the MW-Only DC OPF,” *IEEE Trans. Power Syst.*, vol. 33, no. 2, pp. 1734–1745, 2018, doi: 10.1109/TPWRS.2017.2718551.

[89] “New York Independent System Operator. [Online]. Available: http://www.nyiso.com.” .

[90] M. Barani, J. Aghaei, M. A. Akbari, T. Niknam, H. Farahmand, and M. Korpas, “Optimal Partitioning of Smart Distribution Systems Into Supply-Sufficient Microgrids,” *IEEE Trans. Smart Grid*, vol. 10, no. 3, pp. 2523–2533, May 2019, doi: 10.1109/TSG.2018.2803215.

[91] F. S. Gazijahani and J. Salehi, “Robust Design of Microgrids with Reconfigurable Topology under Severe Uncertainty,” *IEEE Trans. Sustain. Energy*, vol. 9, no. 2, pp. 559–569, 2018, doi: 10.1109/TSTE.2017.2748882.

[92] F. Samadi Gazijahani and J. Salehi, “Optimal Bilevel Model for Stochastic Risk-Based

Planning of Microgrids Under Uncertainty," *IEEE Trans. Ind. Informatics*, vol. 14, no. 7, pp. 3054–3064, Jul. 2018, doi: 10.1109/TII.2017.2769656.

[93] A. J. Conejo, M. Carrion, and J. M. Morales, *Decision making under uncertainty in electricity markets*. IEEE, 2010.

[94] M. Bao, Y. Ding, M. Sang, D. Li, C. Shao, and J. Yan, "Modeling and evaluating nodal resilience of multi-energy systems under windstorms," *Appl. Energy*, vol. 270, no. January, p. 115136, 2020, doi: 10.1016/j.apenergy.2020.115136.

[95] M. H. Amirioun, F. Aminifar, and H. Lesani, "Resilience-Oriented Proactive Management of Microgrids Against Windstorms," *IEEE Trans. Power Syst.*, vol. 33, no. 4, pp. 4275–4284, 2018, doi: 10.1109/TPWRS.2017.2765600.

[96] M. H. Amirioun, F. Aminifar, H. Lesani, and M. Shahidehpour, "Metrics and quantitative framework for assessing microgrid resilience against windstorms," *Int. J. Electr. Power Energy Syst.*, vol. 104, no. January 2018, pp. 716–723, 2019, doi: 10.1016/j.ijepes.2018.07.025.

[97] J. W. Muhs and M. Parvania, "Stochastic Spatio-Temporal Hurricane Impact Analysis for Power Grid Resilience Studies," 2019, doi: 10.1109/ISGT.2019.8791647.

[98] Quanta Technology, "Cost-Benefit Analysis of the Deployment of Utility Infrastructure Upgrades and Storm Hardening Programs," *Satell. Commun.*, vol. 3021, pp. 1–108, 2009.

[99] Y. M. Darestani and A. Shafieezadeh, "Multi-dimensional wind fragility functions for wood utility poles," *Eng. Struct.*, vol. 183, no. August 2018, pp. 937–948, 2019, doi: 10.1016/j.engstruct.2019.01.048.

[100] T. A. Short, *Electric Power Distribution Equipment and Systems*. New York, 2006.

[101] S. Poudel, A. Dubey, and A. Bose, "Risk-based probabilistic quantification of power distribution system operational resilience," *IEEE Syst. J.*, vol. 14, no. 3, pp. 3506–3517, 2019.

[102] B. Mukhopadhyay and D. Das, "Optimal multi-objective expansion planning of a droop-regulated islanded microgrid," *Energy*, vol. 218, p. 119415, 2021, doi: 10.1016/j.energy.2020.119415.

[103] M. F. Shaaban and E. F. El-Saadany, “Accommodating high penetrations of pevs and renewable dg considering uncertainties in distribution systems,” *IEEE Trans. Power Syst.*, vol. 29, no. 1, pp. 259–270, 2014, doi: 10.1109/TPWRS.2013.2278847.

[104] A. Maulik and D. Das, “Optimal Operation of Droop-Controlled Islanded Microgrids,” *IEEE Trans. Sustain. Energy*, vol. 9, no. 3, pp. 1337–1348, Jul. 2018, doi: 10.1109/TSTE.2017.2783356.

[105] J. David, M. Van Nguyen, and N. Cohen, “Algorithmic Graph Theory,” 2012.

[106] R. Balakrishnan and K. Ranganathan, *A Textbook of Graph Theory*. New York, NY: Springer New York, 2012.

[107] H. E. Farag, M. M. A. Abdelaziz, and E. F. El-Saadany, “Voltage and reactive power impacts on successful operation of islanded microgrids,” *IEEE Trans. Power Syst.*, vol. 28, no. 2, pp. 1716–1727, 2013, doi: 10.1109/TPWRS.2012.2223491.

[108] M. M. A. Abdelaziz, H. E. Farag, and E. F. El-Saadany, “Optimum droop parameter settings of islanded microgrids with renewable energy resources,” *IEEE Trans. Sustain. Energy*, vol. 5, no. 2, pp. 434–445, 2014, doi: 10.1109/TSTE.2013.2293201.

[109] R. Tarjan, “Depth-First Search and Linear Graph Algorithms,” *SIAM J. Comput.*, vol. 1, no. 2, pp. 146–160, Jun. 1972, doi: 10.1137/0201010.

[110] C. S. Thomas H. Cormen, Charles E. Leiserson, Ronald L. Rivest, *Introduction to Algorithms, Third Edition*. 2009.

[111] H. and B. Hagan M. T., Demuth, *Neural Network Design (2nd Edition)*. Boston, 2014.

[112] S. Haykin, *Neural Networks and Learning*, vol. 1–3. Elsevier, 2008.

[113] M. H. Beale, M. T. Hagan, and H. B. Demuth, *Deep Learning Toolbox™ User’s Gude*. 2021.

[114] K. Deb, A. Pratap, S. Agarwal, and T. Meyarivan, “A fast and elitist multiobjective genetic algorithm: NSGA-II,” *IEEE Trans. Evol. Comput.*, vol. 6, no. 2, pp. 182–197, 2002, doi: 10.1109/4235.996017.

[115] “The National Renewable Energy Laboratory (NREL). [Onlne]. Available:

https://maps.nrel.gov/nsrdb-viewer.” .

[116] H. Haddadian and R. Noroozian, “Multi-microgrids approach for design and operation of future distribution networks based on novel technical indices,” *Appl. Energy*, vol. 185, pp. 650–663, 2017, doi: 10.1016/j.apenergy.2016.10.120.

[117] L. Wang, A. H. C. Ng, and K. Deb, *Multi-objective Evolutionary Optimisation for Product Design and Manufacturing*. London: Springer London, 2011.

[118] Dimitris Bertsimas, *Introduction to Linear Optimization*. 1997.

[119] “U.S. Energy Information Administration. [Online]. Available: https://www.eia.gov/dnav/ng/hist/n3035us3m.htm,” 2020. .

Appendix A: Element of square matrix

The elements of the square matrix (2.30) were derived by the partial derivative of the power flow equations (2.44) and (2.45) over V and δ.

$$P_{i,\Psi} = \left|\bar{V}_{i,\Psi}\right| \sum_{\substack{j=1 \\ j\neq i}}^{n_{bus}} \sum_{\beta\in\mathcal{F}} \begin{bmatrix} \left|\bar{V}_{i,\beta}\right| \left|Y_{ij}^{\Psi(\beta)}\right| \cos\left(\theta_{ij}^{\Psi\beta} + \delta_{i,\beta} - \delta_{i,\Psi}\right) \\ -\left|V_{j,\beta}\right| \left|Y_{ij}^{\Psi(\beta)}\right| \cos\left(\theta_{ij}^{\Psi\beta} + \delta_{j,\beta} - \delta_{i,\Psi}\right) \end{bmatrix} \quad ,\Psi \in \mathcal{F};\ \forall i \in \mathfrak{D} \qquad (2.44)$$

$$P_{i,\Psi} = \left|\bar{V}_{i,\Psi}\right| \sum_{\substack{j=1 \\ j\neq i}}^{n_{bus}} \sum_{\beta\in\mathcal{F}} \begin{bmatrix} \left|V_{j,\beta}\right| \left|Y_{ij}^{\Psi(\beta)}\right| \sin\left(\theta_{ij}^{\Psi\beta} + \delta_{j,\beta} - \delta_{i,\Psi}\right) \\ -\left|\bar{V}_{i,\beta}\right| \left|Y_{ij}^{\Psi(\beta)}\right| \sin\left(\theta_{ij}^{\Psi\beta} + \delta_{i,\beta} - \delta_{i,\Psi}\right) \end{bmatrix} \quad ,\Psi \in \mathcal{F};\ \forall i \in \mathfrak{D} \qquad (2.44)$$

In this work, the branch admittance was computed elements by elements thought the corresponding elements of $\mathbf{Z}^{\mathbf{br},3\Phi}$ expressed by (2.46). Hence, the formulation $\mathbf{Y}^{\mathbf{bus}}$ is unneeded. Then, (2.47) is the expression of branch admittance using in this work.

$$\mathbf{Z}^{\mathbf{br},3\Phi} = real\left(\mathbf{Z}^{\mathbf{br},3\Phi}\right) + imag\left(\mathbf{Z}^{\mathbf{br},3\Phi}\right)\frac{f^{3\Phi}}{f^{0}} \qquad (2.46)$$

$$\left|Y_{ij}^{\Psi\beta}\right| \angle\theta_{ij}^{\Psi\beta} = \frac{1}{\bar{Z}_{ij}^{br,\Psi\beta}} \qquad (2.47)$$

According to the active and reactive power injection delivered from the inner loop, the equation (2.48) to (2.55) illustrated the simplification partial derivative models of (2.44) and (2.45) depend on $P_i^{a,b,c}$ and $Q_i^{a,b,c}$:

$$\frac{\partial P_i^b}{\partial \delta_i^b} = -Q_i^b + \sum_{j=2}^{n_{bus}} \left|Y_{ij}^{bb}\right| \left|V_i^b\right| \left(\cos\theta_{ij}^{bb} - sin\theta_{ij}^{bb}\right) \qquad (2.48)$$

$$\frac{\partial P_i^c}{\partial \delta_i^c} = -Q_i^c + \sum_{j=2}^{n_{bus}} \left|Y_{ij}^{cc}\right| \left|V_i^c\right| \left(\cos\theta_{ij}^{cc} - sin\theta_{ij}^{cc}\right) \qquad (2.49)$$

$$\frac{\partial P_i^b}{\partial V_i^b} = \frac{P_i^b}{\left|V_i^b\right|} + \sum_{j=2}^{n_{bus}} \left|Y_{ij}^{bb}\right| \left|V_i^b\right| cos\theta_{ij}^{bb} \qquad (2.50)$$

$$\frac{\partial P_i^c}{\partial V_i^c} = \frac{P_i^c}{\left|V_i^c\right|} + \sum_{j=2}^{n_{bus}} \left|Y_{ij}^{cc}\right| \left|V_i^c\right| cos\theta_{ij}^{cc} \qquad (2.51)$$

$$\frac{\partial Q_i^b}{\partial \delta_i^b} = P_i^b + \sum_{j=2}^{n_{bus}} -\left|Y_{ij}^{bb}\right|\left|V_i^b\right|\left(\cos\theta_{ij}^{bb} + sin\theta_{ij}^{bb}\right) \quad (2.52)$$

$$\frac{\partial Q_i^c}{\partial \delta_i^c} = P_i^c + \sum_{j=2}^{n_{bus}} -\left|Y_{ij}^{cc}\right|\left|V_i^c\right|\left(\cos\theta_{ij}^{cc} + sin\theta_{ij}^{cc}\right) \quad (2.53)$$

$$\frac{\partial Q_i^b}{\partial V_i^b} = \frac{Q_i^b}{|V_i^b|} + \sum_{j=2}^{n_{bus}} -\left|Y_{ij}^{bb}\right|\left|V_i^b\right| sin\theta_{ij}^{bb} \quad (2.54)$$

$$\frac{\partial Q_i^c}{\partial V_i^c} = \frac{Q_i^c}{|V_i^c|} + \sum_{j=2}^{n_{bus}} -\left|Y_{ij}^{cc}\right|\left|V_i^c\right| sin\theta_{ij}^{cc} \quad (2.55)$$

Appendix B: Wind, PV and load models

In this work, the wind units (WTs) and photovoltaic units (PVs) are interfaced with the power electronic converter and able to track a MPPT power for the generation. As such, the WTs and PVs can be modeled as the sources of static injection power into the microgrid where their amount of power generated are respected to the capacity windspeed and irradiance, respectively. In this way the power generated via these resources can be calculated using the static model [78] and describe as following:

$$P_{i,t}^{WT,3\Phi} = \begin{cases} 0, & v_t^m < v^{ci}, v_t^m \geq v^{co} \\ S_i^{WT,max} PF_i^{WT} \left(v_t^m - v^{ci}\right)/(v^{ra} - v^{ci}), & v^{ci} \leq v_t^m \leq v^{ra} \\ S_i^{WT,max} \times PF_i^{WT}, & v^{ra} < v_t^m < v^{co} \end{cases} \quad ,\forall i \in \Omega_{WT}, \forall t \in N_T \quad (4.83)$$

then, the reactive power generated by the WTs can be calculated respecting to their specified setting power factor. The formulation used for this calculation are illustrated as following:

$$Q_{i,t}^{WT,3\Phi} = P_{i,t}^{WT,3\Phi}\, tg\left(\cos^{-1}\left(PF_i^{WT}\right)\right) \quad ,\forall i \in \Omega_{WT}, \forall t \in N_T \quad (4.84)$$

next, the PVs assumed controlled in the power factor unity mode in this work. As such, there is no reactive power participated via the PV units. The static model used for the PV units can be:

$$P_{i,t}^{PV,3\Phi} = \begin{cases} S_i^{PV,max} (r_t^m)^2/(R^{STD} - R^C), & r_t^m \leq R^C \\ S_i^{PV,max} (r_t^m)^2/R^{STD}, & R^C < r_t^m < R^{STD} \\ S_i^{PV,max}, & r_t^m \geq R^{STD} \end{cases} \quad ,\forall i \in \Omega_{PV}, \forall t \in N_T \quad (4.85)$$

In term of the demand, the load are modeled by considering the pattern percentage of the annual peak demands [90]. In this way, load at the time t can be calculated though the multiplication of their peak with the annual peak load factor along the planning horizon.

$$P_{i,\Psi,t}^{L} = (APL_t/100) \times P_{i,\Psi}^{L,peak} \quad ,\forall i \in \Omega_{BUS}, \Psi \in \mathcal{F}, \forall t \in N_T \quad (4.86)$$

$$Q_{i,\Psi,t}^{L} = (APL_t/100) \times Q_{i,\Psi}^{L,peak} \quad ,\forall i \in \Omega_{BUS}, \Psi \in \mathcal{F}, \forall t \in N_T \quad (4.87)$$

Appendix C: Algorithm & Example for MGs Formation

C.1 Algorithm for MGs Formation

TABLE C. 1: Algorithm for determining $FA^{bus}\{br_i^{fail}\}$

Algorithm: formation of $\boldsymbol{FA^{bus}}$
Initialize $\boldsymbol{FA^{bus}}(1{:}\,n_{bus}) = 1$
Generate $\mathbf{PATH^{br}}$ and $\mathbf{PATH^{bus}}$ using path finder for br_i^{fail}
for $pth = 1{:}\,n_{path}$
Set $\boldsymbol{FA^{bus}}(br_i^{fail}, [\boldsymbol{fb}(br_i^{fail}), \boldsymbol{tb}(br_i^{fail})] = 0$
for $br = 1{:}\,n_{path}$
if $\mathbf{PATH^{br}}(pth, br)$ corresponding to location of ISW
Denote $pis = \mathbf{PATH^{br}}(pth, br)$
Find a_{fb} is an element address of $\mathbf{PATH^{br}}(pth, br) = \boldsymbol{fb}(pis)$
Find a_{tb} is an element address of $\mathbf{PATH^{br}}(pth, br) = \boldsymbol{fb}(pis)$
$\mathbf{FA^{bus}}\left(br^{fail}, \mathbf{PATH^{bus}}(pth, 1{:}\,min(a_{fb}, a_{tb})\right) = 0$
Break for loop and go to next pth
elseif there is no ISW along path pth by $br = n_{path}$
Find index for the non-zero number $\boldsymbol{nz}$ from $\mathbf{PATH^{bus}}(pth, :)$
$\mathbf{FA^{bus}}\left(br^{fail}, \mathbf{PATH^{bus}}(pth, \boldsymbol{nz})\right) = 0$
Break for loop and go to next pth
end if of elseif
end for
end for

TABLE C. 2: Formation of matrix containing microgrid set

Algorithm: formation of $\mathbf{MG_t^{set}}$
Initialize the matrix $\mathbf{MG_t^{set}}(1{:}\,n_{bus}, 1{:}\,n_{bus}) = 0$
Determine $\boldsymbol{floc}_t = find\left(\mathbf{AV_{s,se}^{I-II}}(1{:}\,n_{bus}, t) = 0\right)$
if $\boldsymbol{floc}_t$ is empty
Set the matrix $\mathbf{MG_t^{set}}(1{:}\,n_{bus}, 1{:}\,n_{bus}) = 0$
else
Import $\boldsymbol{LFa}_t$ from **LFa**, then $\boldsymbol{BFa}_t$ from B**Fa**
Initialized the root of microgrid $root^{MG} = 0$
Set and initialize $\mathbf{MG^{set0}} = 0$
Initialize the status of the isolate switch by $st_n^{isw} = 0$
➔ Find st_n^{isw} of the set $\boldsymbol{ISW}^{site}$ for time *t*
for $n = 1{:}\,n_{isw}$
if $\boldsymbol{LFa}_t\left(\boldsymbol{ISW}_n^{site}\right) = 0$,
The $\boldsymbol{ISW}_n^{site}$ is open and set $st_n^{isw} = 0$
else

14: The $\boldsymbol{ISW_n^{site}}$ is still close and set $st_n^{isw} = 1$
15: **end if**
16: **end for**
17: Define $\boldsymbol{ISW^{open}} = \boldsymbol{ISW^{site}}\left(find\left(st_n^{isw} = 0\right)\right)$

➔ Determine the adjacent matrix for $\mathbf{MG}_t^{\mathbf{set}}$

18: Generate adjacency matrix $\mathbf{A}^{\mathbf{MG}}$ for the initial test system using (105)
19: **for** $n = 1{:}\, n_{isw}^{open}$
20: Set $\mathbf{A}^{\mathbf{MG}}\left(\boldsymbol{fb}\left(ISW_n^{open}\right), \boldsymbol{tb}\left(ISW_n^{open}\right)\right) = 0$
21: Set $\mathbf{A}^{\mathbf{MG}}\left(\boldsymbol{tb}\left(ISW_n^{open}\right), \boldsymbol{fb}\left(ISW_n^{open}\right)\right) = 0$
22: **end for**

➔ Determine the root of the microgrid(s) set

23: Determine $\boldsymbol{bus^{on}}$, by $\boldsymbol{bus^{on}} = find(\boldsymbol{BFa}_t = 1)$
24: **for** $m = 1{:}\, n_{isw}^{open}$
25: **if** ISW_m^{open} corresponding to the fault location
26: Set 1st root by $root^{MG}(m, 1) = fb(ISW_m^{open})$
27: Set 2nd root by $root^{MG}(m, 2) = tb(ISW_m^{open})$
28: **else**
29: Determine a single root node $root^{MG}(m, 1)$ equal to fb or tb of ISW_m^{open} corresponding to the online node
30: **end if**
31: **end for**
32: Do the intersection between $\mathbf{root}^{\mathbf{MG}}$ and $\boldsymbol{bus^{on}}$ for eliminating the overlap and selecting only the corresponding online node for forming vector $\boldsymbol{root^{MG}}$

➔ Forming $\mathbf{MG}_t^{\mathbf{set}}$ based on Depth First Search (DFS)

33: **for** $m = 1{:}\, n_{root}$
34: Do DFS on $\boldsymbol{A}^{\mathbf{MG}}$ for $root_m^{MG}$ then store resulting vector in $\boldsymbol{MG_m^{DFS}}$
35: Sort $\boldsymbol{MG_m^{DFS}}$
36: Update $\mathbf{MG}^{\mathbf{set0}}(m, 1{:}\, length\ of\ MG_m^{DFS}) = \boldsymbol{MG_m^{DFS}}$
37: **end for**
38: Check and eliminate the overlapping set of microgrid(s) in $\mathbf{MG}^{\mathbf{set0}}$
39: Store $\mathbf{MG}^{\mathbf{set0}}$ in $\mathbf{MG}_t^{\mathbf{set}}$
40: **end if**

TABLE C. 3: Algorithm for determining $\boldsymbol{b_t^m}$

Algorithm: formation of $\boldsymbol{b_t^m}$

1: Initialize $\boldsymbol{b_t^m}(1{:}\, n_{bus}) = 1$
2: **if** there is no fault(s) happening at time *t*
3: Set vector $\boldsymbol{b_t^m}(1{:}\, n_{bus})$ to *0*
4: **else**
5: Find the set microgrid in $\mathbf{MG}_t^{\mathbf{set}}$ that is adjacent to the main grid through bus 1
6: *Set* $\boldsymbol{b_t^m}$ to 0 for all buses corresponding to the set of microgrid that is adjacent to bus 1
7: **end if**

TABLE C. 4: Algorithm for forming $\boldsymbol{bus_t^{ne}}$

Algorithm: formation of $\boldsymbol{bus_t^{ne}}$
Initialize $\boldsymbol{bus_t^{ne}}(1{:}\,n_{bus}) = 1$
if there is no fault(s) happening at time *t*
All buses are energized by GC mode, set $\boldsymbol{bus_t^{ne}}(1{:}\,n_{bus}) = 1$
else
Define n_{MG} as the number of microgrid(s) from $\mathbf{MG_t^{set}}$
for $m = 1{:}\,n_{MG}$
if $\boldsymbol{MG_{m,t}^{set}}$ adjacent to the main grid
do nothing and jump to the next microgrid *m* of the for **loop**
elseif $\boldsymbol{MG_{m,t}^{set}}$ have a DDG unit installed by checking the element of $\boldsymbol{MG_{m,t}^{set}}$ with $\boldsymbol{DDG_{sp}^{site}}$ as well as confirm that $\boldsymbol{DDG_{sp}^{size}} \neq 0$
do nothing and jump to the next *m* of for **loop**
else
Define vector index $\boldsymbol{i^{ne}}$ that is equal to the non-zero element of $\boldsymbol{MG_{m,t}^{set}}$
Set $\boldsymbol{bus_t^{ne}}(\boldsymbol{i^{ne}}) = 0$
end if
end for

TABLE C. 5: Algorithm for determining $\boldsymbol{f_t^{bus}}$ and $\boldsymbol{DDG_t^{down}}$

Algorithm: formation of $\boldsymbol{f_t^{bus}}$ and $\boldsymbol{DDG_t^{down}}$
Initialize vector $\boldsymbol{f_t^{bus}}(1{:}\,n_{ddg}) = 1$ and vector $\boldsymbol{DDG_t^{down}}(1{:}\,n_{ddg}) = 1$
if there is no fault(s) happen at time t, it means MG operate in GC mode
Do nothing and let $\boldsymbol{f_t^{bus}}(1{:}\,n_{ddg})$ and $\boldsymbol{DDG_t^{down}}(1{:}\,n_{ddg})$ as initial value
else
for $n = 1{:}\,n_{ddg}$
Initialize $\boldsymbol{h^{ddg}}(1{:}\,n_{MG}) = 0$
for $m = 1{:}\,n_{MG}$
if there is an element of $\boldsymbol{MG_{m,t}^{set}}$ corresponding to $DDG_{n,sp}^{site}$
Set $h_m^{ddg} = 1$
else
Set $h_m^{ddg} = 0$
end if
end for
if $\sum \boldsymbol{h^{ddg}} = 0$ means $DDG_{n,sp}^{site}$ are not stay on any MG set in $\mathbf{MG_t^{set}}$
Set $f_{n,t}^{bus} = DDG_{n,sp}^{site}$ and $DDG_{n,t}^{down} = 0$
else
Set $f_{n,t}^{bus} = \boldsymbol{MG_{m,t}^{set}}(h^{ddg} = 1{,}1)$ and $DDG_{n,t}^{down} = 1$
end if
end for
end if

C.2 Mathematical example for MGs Formation

The reference 8-bus test system with a fault located at branch #2 and #4 respective paths that can be explored is described in Figure C. 1.

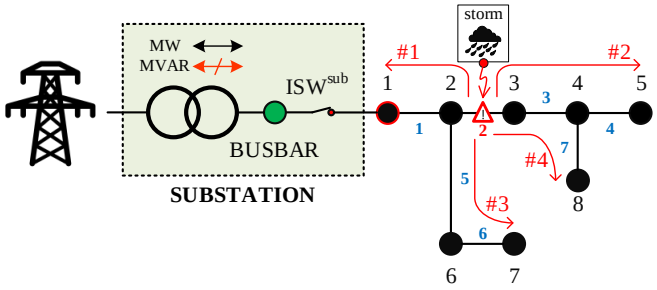

FIGURE C. 1: Path(s) search based on fault at branch #2

C.2.1 Fault influence path

a) Step 1: Representation of the System Topology

According to Figure C. 1, Figure C. 2 shows the undirected graph for the reference 8-bus system with nodes (vertices) and branches (edges). In this case, the adjacency matrix is determined using (5.105), and can be expressed for this reference system by (5.154).

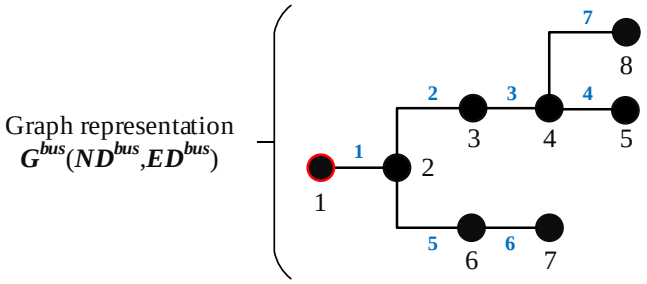

FIGURE C. 2: Undirected Graph Tree for 8-bus test system

$$\mathbf{M}^{\mathbf{adj}} = \begin{bmatrix} \boldsymbol{bus} & \# & 1 & 2 & 3 & 4 & 5 & 6 & 7 & 8 \\ \# & & - & - & - & - & - & - & - & - \\ 1 & | & 0 & 1 & 0 & 0 & 0 & 0 & 0 & 0 \\ 2 & | & 1 & 0 & 1 & 0 & 0 & 1 & 0 & 0 \\ 3 & | & 0 & 1 & 0 & 1 & 0 & 0 & 0 & 0 \\ 4 & | & 0 & 0 & 1 & 0 & 1 & 0 & 0 & 1 \\ 5 & | & 0 & 0 & 0 & 1 & 0 & 0 & 0 & 0 \\ 6 & | & 0 & 1 & 0 & 0 & 0 & 0 & 1 & 0 \\ 7 & | & 0 & 0 & 0 & 0 & 0 & 1 & 0 & 0 \\ 8 & | & 0 & 0 & 0 & 1 & 0 & 0 & 0 & 0 \end{bmatrix} \quad (5.154)$$

b) Step 2: Determination of the Target Nodes TG^{node}

This perspective is clearly described in (5.155) and Figure C. 3 for the reference 8-bus system to a fault $br^{fail} = 2$, where identified targets nodes are denoted by node #1 (root node), node #5 (leaf node), node #7 (leaf node) and node #8 (leaf node), e.g., for node #8, $\sum_{j=1}^{n_{bus}} M_{8,j}^{adj} = 1$.

$$\boldsymbol{TG}^{node} = find\left(\begin{bmatrix} \sum_{j=1}^{n_{bus}} M_{i,j}^{adj} \\ --- \\ \mathbf{1} \\ 3 \\ 2 \\ 3 \\ \mathbf{1} \\ 2 \\ \mathbf{1} \\ \mathbf{1} \end{bmatrix} = 1\right) = [\mathbf{1} \quad \mathbf{5} \quad \mathbf{7} \quad \mathbf{8}] \tag{5.155}$$

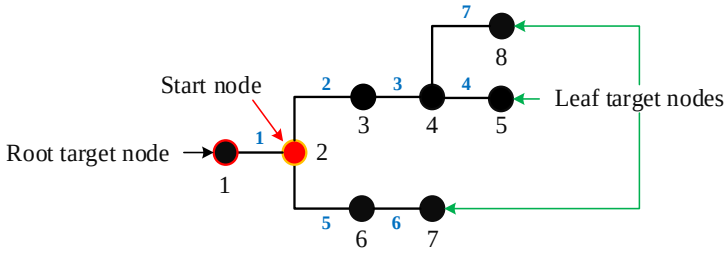

FIGURE C. 3: Start, Root and leaves nodes

c) Step 3: Determination of the Path(s)

The $\mathbf{PATH^{bus}}$ and $\mathbf{PATH^{br}}$ matrices for the reference 8-bus system with fault at branch #2 can be expressed by (5.156)-(5.157).

$$\mathbf{PATH^{bus}} = \begin{bmatrix} \boldsymbol{path^{bus}} & TG_i^{bus} & & fb(br^{fail}) & \rightarrow & \rightarrow & \rightarrow \\ \# & i = & & -- & -- & -- & -- \\ 1 & 1 & | & 2 & 1 & 0 & 0 \\ 2 & 5 & | & 2 & 3 & 4 & 5 \\ 3 & 7 & | & 2 & 6 & 7 & 0 \\ 4 & 8 & | & 2 & 3 & 4 & 8 \end{bmatrix} \tag{5.156}$$

$$\mathbf{PATH^{br}} = \begin{bmatrix} \boldsymbol{path^{br}} & & br^{fail} & \rightarrow & \rightarrow \\ \# & & -- & -- & -- \\ 1 & | & 2 & 1 & 0 \\ 2 & | & 2 & 3 & 4 \\ 3 & | & 2 & 5 & 6 \\ 4 & | & 2 & 3 & 7 \end{bmatrix} \tag{5.157}$$

C.2.2 Branch affected matrix (LFa)

a) Determination of FA^{br}

For determining $\mathbf{FA^{br}}$, as shown in Figure 5. 8 the $\mathbf{PATH^{br}}$ is determined for $br_i^{fail} \in \Omega_{LIN}$. Then, the row corresponding to br_i^{fail} for $\mathbf{FA^{br}}$ is obtained by searching $\mathbf{PATH^{br}}\{br_i^{fail}\}$. For example, Figure C. 4 shows the reference 8-bus system equipped with four isolate switches $\boldsymbol{ISW^{site}} = [1,4,5,7]$ for the fault br_2^{fail}.

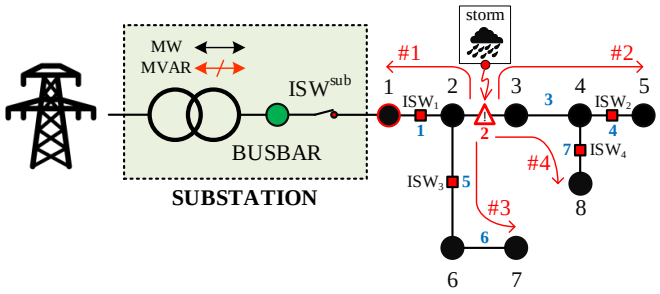

FIGURE C. 4: Simple 8-bus system with found ISWs and fault at branch #2

Then, for this case:

$$\mathbf{PATH^{br}}\left(br_2^{fail}\right) = \left[\begin{array}{cc|ccc} \boldsymbol{path^{br}} & & br^{fail} & \rightarrow & \rightarrow \\ \# & & - - & - - & - - \\ 1 & | & \mathbf{2} & \mathbf{1} & 0 \\ 2 & | & \mathbf{2} & \mathbf{3} & \mathbf{4} \\ 3 & | & \mathbf{2} & \mathbf{5} & 6 \\ 4 & | & \mathbf{2} & \mathbf{3} & \mathbf{7} \end{array}\right] \tag{5.158}$$

First, $\boldsymbol{FA^{br}}$ is initialized by $FA^{br} = [1\ 1\ 1\ 1\ 1\ 1\ 1]$. Next, all branches that have been affected by the fault br_2^{fail}, i.e., branch numbers highlighted in bold in (5.158), must have the fault cleared. In this sense, for paths #1, #2, #3 and #4 the fault has been cleared by the opening the ISWs localized at the branch #1, #4, #5 and #7; respectively. In contrast, the branch #6 has been protected by the ISW_3, thus not being highlighted. Finally, all elements of $\boldsymbol{FA^{br}}$ that correspond to affected branches, i.e., [1,2,3,4,5,7], are set to zero. The vector $\boldsymbol{FA^{br}}$ corresponding to br_2^{fail} and respecting to $\boldsymbol{ISW^{site}}$ can be expressed as follows:

$$\begin{array}{rcccccccc} br_i & : & 1 & 2 & 3 & 4 & 5 & 6 & 7 \\ \boldsymbol{FA_2^{br}}\left(br_2^{fail}\right) & = & [0 & 0 & 0 & 0 & 0 & 1 & 0] \end{array} \tag{5.159}$$

Applying the same methodology while respecting assumptions 1) and 2) discussed in the beginning of this section, the full matrix $\mathbf{FA^{br}}$ for the reference 8-bus test system can be formed as follows:

$$\mathbf{FA^{br}} = \begin{bmatrix} br_i & 1 & 2 & 3 & 4 & 5 & 6 & 7 \\ br_i^{fail} & - & - & - & - & - & - & - \\ 1 \mid & 0 & 1 & 1 & 1 & 1 & 1 & 1 \\ 2 \mid & 0 & 0 & 0 & 0 & 0 & 1 & 0 \\ 3 \mid & 0 & 0 & 0 & 0 & 0 & 1 & 0 \\ 4 \mid & 1 & 1 & 1 & 0 & 1 & 1 & 1 \\ 5 \mid & 1 & 1 & 1 & 1 & 0 & 1 & 1 \\ 6 \mid & 1 & 1 & 1 & 1 & 0 & 0 & 1 \\ 7 \mid & 1 & 1 & 1 & 1 & 1 & 1 & 0 \end{bmatrix} \tag{5.160}$$

a) Branch affected matrix (LFa) considering single fault location

The binary vector $\boldsymbol{LFa_t}$ can be obtained easily by searching a row of $\mathbf{FA^{br}}$ corresponding to the location of the fault(s), i.e., $floc_{i,t}$ for scenario *s* season se. For the case shown in Figure C. 4, there is only a single fault with $floc_t = 2$, in this case the vector $\boldsymbol{LFa_t}$ can be given as follows:

$$\boldsymbol{LFa_t} = \mathbf{FA^{br}}(floc_t, :) = [0\ 0\ 0\ 0\ 0\ 1\ 0] \tag{5.161}$$

a) Branch affected matrix (LFa) considering multiple fault location

To exemplify the case with multiple fault locations, assuming that faults simultaneously occur at branch #3 and #6 in the reference 8-bus system, i.e., $\boldsymbol{floc_t} = [3, 6]$. The vector $\boldsymbol{LFa_t}$ can be obtained using (5.162)-(5.164).

$$\boldsymbol{LFa}_t\{floc_{1,t} = 3\} = [0\ 0\ 0\ 0\ 0\ 1\ 0] \tag{5.162}$$

$$\boldsymbol{LFa}_t\{floc_{1,t} = 6\} = [1\ 1\ 1\ 1\ 0\ 0\ 1] \tag{5.163}$$

$$\boldsymbol{LFa}_t(\boldsymbol{floc_t}) = \begin{pmatrix} \boldsymbol{LFa}_t\{floc_{1,t} = 3\} \\ \circ\ \boldsymbol{LFa}_t\{floc_{1,t} = 6\} \end{pmatrix} = [0\ 0\ 0\ 0\ 0\ 0\ 0] \tag{5.164}$$

If there no fault(s) occur at time t, especially in the normal scenarios, i.e., Ω_s, $\boldsymbol{LFa_t} = [1\ 1\ 1\ 1\ 1\ 1\ 1]$.

C.2.4 Bus affected matrix (BFa)

a) Determination of FA^{bus}

Figure C. 5 shows the buses affected by the fault at branch #2.

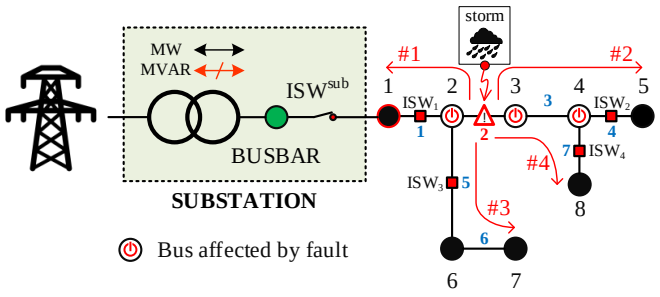

FIGURE C. 5: Buses affected by the original fault at branch #2

By using the algorithm in Table C. 1 for all $br_i^{fail} \in \Omega_{BR}$, the $\mathbf{FA^{bus}}$ obtained for the reference 8-bus system can be expressed as follows:

$$\mathbf{FA^{bus}} = \begin{bmatrix} br_i^{fail} \backslash bus_i & 1 & 2 & 3 & 4 & 5 & 6 & 7 & 8 \\ 1 & 1 & 1 & 1 & 1 & 1 & 1 & 1 & 1 \\ 2 & 1 & 0 & 0 & 0 & 1 & 1 & 1 & 1 \\ 3 & 1 & 0 & 0 & 0 & 1 & 1 & 1 & 1 \\ 4 & 1 & 1 & 1 & 1 & 1 & 1 & 1 & 1 \\ 5 & 1 & 1 & 1 & 1 & 1 & 1 & 1 & 1 \\ 6 & 1 & 1 & 1 & 1 & 1 & 0 & 0 & 1 \\ 7 & 1 & 1 & 1 & 1 & 1 & 1 & 1 & 1 \end{bmatrix} \quad (5.165)$$

As can be seen, comparing Figure C. 5, bus #2, #3 and #4 were deactivated by the fault br_2^{fail}. In this case, $\mathbf{FA^{bus}}(br_2^{fail},[2,3,4])$ is set to zero.

a) Bus affected matrix (BFa) considering single fault location

The $\boldsymbol{BFa}_t$ can be obtained by searching a row of $\mathbf{FA^{bus}}$ corresponding to the location of the fault(s), i.e., $floc_{i,t}$, for scenario *s* of season *se*. For the case shows in Figure C. 5, there is only a single fault $floc_t = 2$ and the vector $\boldsymbol{BFa}_t$ is obtained as follows:

$$\boldsymbol{LFa_t} = \mathbf{FA^{br}}(floc_t,:) = [1\ 0\ 0\ 0\ 1\ 1\ 1\ 1] \quad (5.166)$$

a) Bus affected matrix (BFa) considering multiple fault location

To exemplify the case with multiple fault location, the reference 8-bus system with faults at the branch #3 and #6 is assumed, i.e., $\boldsymbol{floc}_t = [3, 6]$. In this case, the vector $\boldsymbol{BFa}_t$ can be determined as:

$$\boldsymbol{BFa}_t\{floc_{1,t} = 3\} = [1\ 0\ 0\ 0\ 1\ 1\ 1\ 1] \quad (5.167)$$

$$\boldsymbol{BFa}_t\{floc_{1,t} = 6\} = [1\ 1\ 1\ 1\ 1\ 0\ 0\ 1] \tag{5.168}$$

$$\boldsymbol{BFa}_t(\boldsymbol{floc}_t) = \begin{pmatrix} \boldsymbol{BFa}_t\{floc_{1,t} = 3\} \\ \circ\ \boldsymbol{BFa}_t\{floc_{1,t} = 6\} \end{pmatrix} = [1\ 0\ 0\ 0\ 1\ 0\ 0\ 1] \tag{5.169}$$

For the case where there is no fault at time t, $\boldsymbol{BFa}_t$ can be simply set to $\boldsymbol{BFa}_t = [1\ 1\ 1\ 1\ 1\ 1\ 1\ 1]$.

C.2.5 Microgrid Formation set

Figure C. 6 describes the matrix $\mathbf{MG}_t^{\mathbf{set}}$ including all possible microgrid(s) formation options for the reference 8-bus system with fault located at branch #2.

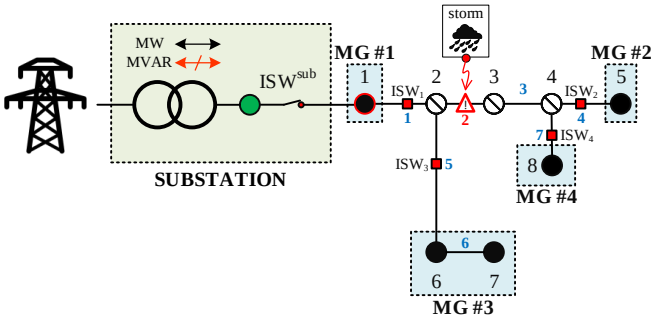

FIGURE C. 6: $\mathbf{MG}^{\mathbf{set}}$ formation

In this case, $\mathbf{MG}_t^{\mathbf{set}}$ can be expressed by (5.170):

$$\mathbf{MG}_t^{\mathbf{set}} = \begin{bmatrix} \boldsymbol{MG}\ \# & | & bus\ \# & bus\ \# \\ 1 & | & 1 & 0 \\ 2 & | & 5 & 0 \\ 3 & | & 6 & 7 \\ 4 & | & 8 & 0 \end{bmatrix} \tag{5.170}$$

C.2.6 Non-Energized system buses

Figure C. 7 exemplifies the microgrid formation for cases with and without local DDG installed capacity. In Figure C. 7(a), the bus #1 was protected by ISW #1 and stays connected to the main grid. According to ISW #2, #3 and #4, the MG #1, #2 and #3 can be formed, respectively. In term of resources, the DDG unit located at bus #4 corresponds to the area affected by the fault at branch #2. On the other hand, there are PV, WT and ESS located within the possibly formed microgrids #1, #2 and #3. Nevertheless, as the PV, WT and ESS could not operate with droop/2nd for maintaining the voltage and system frequency, these microgrids are considered as non-successful microgrids for

operation in IS mode. Thus, except for bus #1 all the element of $\boldsymbol{bus}_t^{ne}$ are set to zero. Similar to case (a), in Figure C. 7(b) three microgrids are formed. Among them, MG #3 could not operate in IS mode as there is no DDG located within this area. However, the DDGs in this case were placed in the MG #1 and #2, allowing these microgrids to operate in IS mode. In this case, bus #1 and the elements of $\boldsymbol{bus}_t^{ne}$ corresponding to buses located within microgrids with successful IS mode can be set to one (i.e., $\boldsymbol{bus}_t^{ne} = [1\ 0\ 0\ 0\ 1\ 1\ 1\ 0]$).

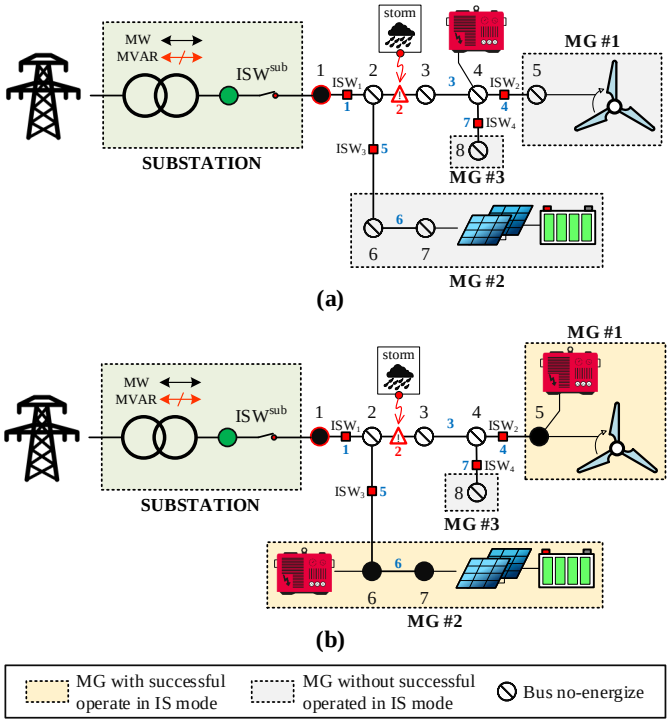

FIGURE C. 7: Microgrids formation and bus no-energize respecting to the location of DDGs

Appendix D: Feasible operating regions of DDGs

The operation range of the DDGs shown in Figure D. 1 has been derived with respect to the feasible operating regions of DDGs [19].

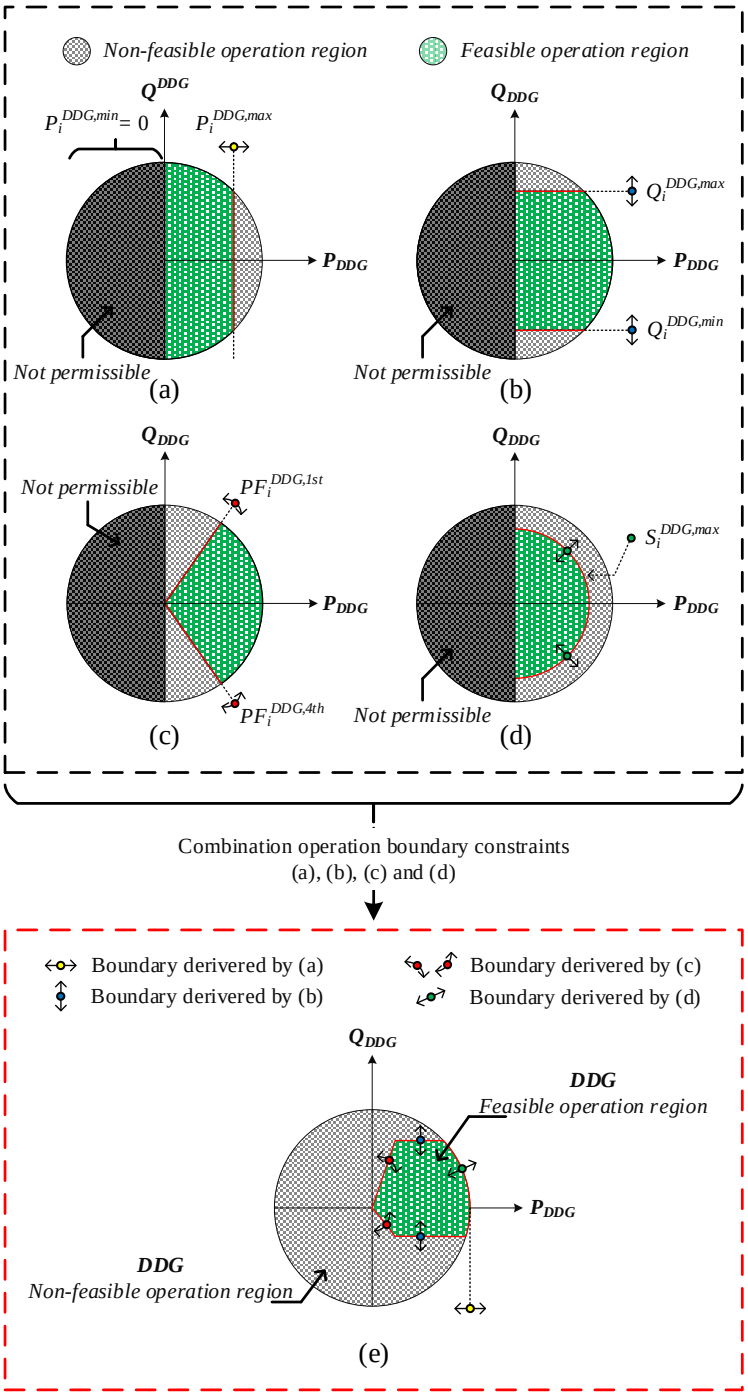

FIGURE D. 1: Derivation of DDG feasible operation region

In this work, it is assumed the DDGs are generating units and allowed to generate active power and to exchange reactive power using the interfaced power electronic devices. Figure D. 1 shows the procedure executed for extracting the DDGs' feasible operation region. Table D. 1 summarizes the relation between the constraints, Figure D. 1, and their relative parameters for determining the DDG's feasible operation region.

TABLE D. 1: Constraints and parameters related to the determination of DDG's feasible operation region

Constraint #	Fig. D.1	Parameters						
		$P_i^{DDG,min}$	$P_i^{DDG,max}$	$Q_i^{DDG,min}$	$Q_i^{DDG,max}$	$PF_i^{DDG,1st}$	$PF_i^{DDG,4th}$	$S_i^{DDG,max}$
(4.26)	(a)	0	$[0, \mathbb{R}]$	-	-	-	-	-
(4.27)	(b)	-	-	$[-\mathbb{R}, 0]$	$[0, \mathbb{R}]$	-	-	-
(4.28)	(c)	-	-	-	-	$[0, \mathbb{R}]$	$[0, \mathbb{R}]$	-
(4.29)	(d)	-	-	-	-	-	-	$[0, \mathbb{R}]$

The DDG i active power $P_i^{DDG,min}$ in (4.26) is set to as low as zero as the DDGs are supposed to be operating as a source of active power. As such, the left-hand side of the operating region is excluded as shown in Figure D. 1(a)-(d). The $P_i^{DDG,max}$ in (4.26), on the other hand, can be set according to the DDGs maximum allowable power generation to adjust the right-hand side operating region as illustrated by Figure D. 1(a). Nonetheless, $P_i^{DDG,max}$ is usually set to $S_i^{DDG,max}$ for allowing the DDGs to generate their active power proportional to their size. Figure D. 1(b) illustrates the impact of the reactive power limits, $Q_i^{DDG,min}$ and $Q_i^{DDG,max}$ given by (4.27), on the DDGs feasible operation region. They restrict the DDGs' reactive power generated to and received from the main grid, respectively. Hence, the DDGs feasible operating region is restricted. The power factor $PF_i^{DDG,1st}$ and $PF_i^{DDG,4th}$ in (4.28) limit the DDG's minimum generated active power proportional to its generated and received reactive power, respectively. As shown in Figure D. 1(c), $PF_i^{DDG,1st}$ and $PF_i^{DDG,4th}$ adjust the angle of the radius located in the first and fourth quadrant of the DDG's operating circle. Finally, Figure D. 1(d) demonstrates the impact of the quadratic power constraint (4.29). As can be seen, increasing $S_i^{DDG,max}$ expands the perimeter of the DDGs feasible operation circle. Finally, the feasible operation region for the DDGs can be determined by the constraints (4.26)-(4.29) as shown in Figure D. 1(e).

Appendix E: Linearization of absolute value operator

E.1 Linearization of Absolute Value Operator

In order to linearize the nonlinear expression $z = |y|$ in the problem with objective function Min $|y|$, where y is a continuous variable and the $|\,.\,|$ is the absolute value operator, the auxiliary constraints (4.89)-(4.90) are considered and the problem is reformulated as follows [118]:

$$\text{Min } z \tag{4.88}$$

$$y \leq z \tag{4.89}$$

$$-y \leq z \tag{4.90}$$

where, (4.88)-(4.89) perform the function of the absolute value operator for $y \geq 0$, while (4.88) and (4.90) do the same for $y \leq 0$.

E.2 Linearize the production between continuous and binary variables

Let $z = A \times b$ be the expression of the production between the continuous variable (A) and the binary variable (b), if A is bounded between zero and the big M i.e., A^{bigM}, then, a representing variable z can be introduced into the problem formulation subjected to (4.91)-(4.94) [83]:

$$\text{z} \leq A^{bigM} \times b \tag{4.91}$$

$$\text{z} \leq A \tag{4.92}$$

$$\text{z} \geq A - (1 - b)A^{bigM} \tag{4.93}$$

$$0 \leq \text{z} \leq A^{bigM} \tag{4.94}$$

Appendix F: Decision variables for OPF/LOPF problem

The decision variables of the model are formed by the combination of the groups of vectors of control and dependent variables which are illustrated in the table below. Here it is worth noting that the decision vector is the same for both IS and GC operation modes. However, the relevant decision variables, within the decision vector, are activated/disactivated by using the binary input parameter b_t^m in the proposed problem.

TABLE F. 1: Control and dependent variables of the MINLP and MILP model for minimizing their objective functions

Group	Variables			Type	Set	$X^{MILP,3\Phi}$	$X^{MINLP,3\Phi}$	Operation mode	
#					$\forall i,k \in$			IS	GC
1	$V_{i,\Psi,t}$	$,\Psi \in \mathcal{F}$	$,\forall t \in \Omega_T$	$\mathbb{R}$	Ω_{BUS}	✓	✓	✓	✓
2	$\delta_{i,\Psi,t}$	$,\Psi \in \mathcal{F}$	$,\forall t \in \Omega_T$	$\mathbb{R}$	Ω_{BUS}	✓	✓	✓	✓
3	$b_{i,t}^{curt}$		$,\forall t \in \Omega_T$	$\mathbb{Z}$	Ω_{BUS}	✓	✓	✓	-
4	$z_{i,t}^{curt}$		$,\forall t \in \Omega_T$	$\mathbb{Z}$	Ω_{BUS}	✓	-	✓	-
5	$P_{i,t}^{DDG,3\Phi}$		$,\forall t \in \Omega_T$	$\mathbb{R}$	Ω_{DDG}	✓	✓	✓	✓
6	$P_{i,\Psi,t}^{DDG}$	$,\Psi \in \mathcal{F}$	$,\forall t \in \Omega_T$	$\mathbb{R}$	Ω_{DDG}	✓	✓	✓	✓
7	$Q_{i,t}^{DDG,3\Phi}$		$,\forall t \in \Omega_T$	$\mathbb{R}$	Ω_{DDG}	✓	✓	✓	✓
8	$Q_{i,\Psi,t}^{DDG}$	$,\Psi \in \mathcal{F}$	$,\forall t \in \Omega_T$	$\mathbb{R}$	Ω_{DDG}	✓	✓	✓	✓
9	$u_{i,\Psi,t}^{v,int}$	$,\Psi \in \mathcal{F}$	$,\forall t \in \Omega_T$	$\mathbb{R}$	Ω_{DDG}	✓	✓	✓	-
10	$P_{i,t}^{dch,3\Phi}$		$,\forall t \in \Omega_T$	$\mathbb{R}$	Ω_{ESS}	✓	✓	✓	✓
11	$P_{i,t}^{ch,3\Phi}$		$,\forall t \in \Omega_T$	$\mathbb{R}$	Ω_{ESS}	✓	✓	✓	✓
12	$Q_{i,t}^{ESS,3\Phi}$		$,\forall t \in \Omega_T$	$\mathbb{R}$	Ω_{ESS}	✓	✓	✓	✓
13	$E_{i,t}^{ESS}$		$,\forall t \in \Omega_T$	$\mathbb{R}$	Ω_{ESS}	✓	✓	✓	✓
14	$b_{i,t}^{ESS}$		$,\forall t \in \Omega_T$	$\mathbb{Z}$	Ω_{ESS}	✓	✓	✓	✓
15	$P_{i,t}^{PCC,3\Phi}$		$,\forall t \in \Omega_T$	$\mathbb{R}$	Ω_{PCC}	✓	✓	-	✓
16	$P_{i,\Psi,t}^{PCC}$	$,\Psi \in \mathcal{F}$	$,\forall t \in \Omega_T$	$\mathbb{R}$	Ω_{PCC}	✓	✓	-	✓
17	$Q_{i,t}^{PCC,3\Phi}$		$,\forall t \in \Omega_T$	$\mathbb{R}$	Ω_{PCC}	✓	✓	-	✓
18	$Q_{i,\Psi,t}^{PCC}$	$,\Psi \in \mathcal{F}$	$,\forall t \in \Omega_T$	$\mathbb{R}$	Ω_{PCC}	✓	✓	-	✓
19	$P_{k,\Psi,t}^{br}$	$,\Psi \in \mathcal{F}$	$,\forall t \in \Omega_T$	$\mathbb{R}$	Ω_{LIN}	✓	✓	✓	✓
20	$Q_{k,\Psi,t}^{br}$	$,\Psi \in \mathcal{F}$	$,\forall t \in \Omega_T$	$\mathbb{R}$	Ω_{LIN}	✓	✓	✓	✓

Appendix G: Data information

G.1 Generator's information

TABLE G. 1: DGs locations and static droop coefficients

Test system	DG #	Bus #	m^p	n^q	f^*	V^*
			(p.u.)	(p.u.)	(p.u.)	(p.u.)
33-bus	1	1	0.05	0.05	1	1
Balanced	2	6	1.00	1.00	1	1
system	3	13	0.10	0.10	1	1
	4	25	1.00	1.00	1	1
	5	33	0.20	0.20	1	1
10476-bus	1	5	0.000042	0.00069	1	1.01
Balanced	2	18	0.000057	0.00095	1	1.01
system	3	120	0.000057	0.00095	1	1.01
	4	345	0.000063	0.00104	1	1.01
	5	598	0.000057	0.00095	1	1.01
	6	848	0.000052	0.00087	1	1.01
	7	5320	0.000078	0.00130	1	1.01
	8	6913	0.000096	0.00160	1	1.01
	9	8506	0.000089	0.00149	1	1.01
	10	9568	0.000069	0.00116	1	1.01
	11	8508	0.000078	0.00130	1	1.01
	12	5851	0.000066	0.00110	1	1.01
	13	6382	0.000114	0.00189	1	1.01
	14	6913	0.000057	0.00095	1	1.01
	15	7444	0.000057	0.00095	1	1.01
	16	7975	0.000052	0.00087	1	1.01
	17	9595	0.000066	0.00110	1	1.01
	18	9037	0.000069	0.00116	1	1.01
	19	9568	0.000078	0.00130	1	1.01
	20	10012	0.000052	0.00087	1	1.01
25-bus	1	13	0.005	0.05	1	1.01
Unbalanced	2	19	0.01	0.10	1	1.01
system	3	25	0.005	0.05	1	1.01

G.2 Data information exclusive for Chapter 4

TABLE G. 2: Daily information data input for the 33-bus and 25-bus test system

Time	σ_t^{PCC}	APL_t	w^t	r^t	Time	σ_t^{PCC}	APL_t	w^t	r^t
(h)	($/MWh)	(%)	(m/s)	(kW/m^2)	(h)	($/MWh)	(%)	(m/s)	(kW/m^2)
1:00	15.63	64.0	8.1	0	13:00	15.33	98.0	7.1	0.916
2:00	15.50	60.0	7.6	0	14:00	16.21	100.0	4.8	0.206
3:00	14.63	58.0	7.6	0	15:00	17.21	100.0	3.8	0.390
4:00	13.28	55.0	6.9	0	16:00	17.26	96.0	3.3	0.117
5:00	12.88	55.0	6.9	0	17:00	18.48	95.0	2.2	0.629
6:00	12.31	57.0	7.0	0.391	18:00	20.03	95.0	0.5	0.368
7:00	12.07	64.0	7.0	0.212	19:00	21.85	93.0	2.2	0
8:00	11.85	76.0	7.3	0.371	20:00	20.92	92.0	2.6	0
9:00	12.10	88.0	6.2	0.592	21:00	20.06	92.0	4.8	0
10:00	12.87	95.0	7.2	0.752	22:00	19.17	93.0	6.2	0
11:00	14.01	98.0	7.1	0.868	23:00	17.41	88.0	4.8	0
12:00	14.88	100.0	7.5	0.893	24:00	16.15	72.0	5.1	0

TABLE G. 3: Load weight and maximum duration of load curtailment 33-bus and 25-bus test system

33-bus (balanced)						25-bus (unbalanced)					
Bus	w_i^{load}	T_i^{curt} (h)	Bus	w_i^{load}	T_i^{curt} (h)	Bus	w_i^{load}	T_i^{curt} (h)	Bus	w_i^{load}	T_i^{curt} (h)
1	0	24	18	0.024	19	1	0.000	24	18	0.037	17
2	0.027	19	19	0.024	19	2	0.000	24	19	0.056	15
3	0.024	19	20	0.024	19	3	0.033	17	20	0.033	17
4	0.032	18	21	0.024	19	4	0.047	15	21	0.037	17
5	0.016	21	22	0.024	19	5	0.037	17	22	0.047	15
6	0.016	21	23	0.024	19	6	0.037	17	23	0.056	15
7	0.054	14	24	0.113	4	7	0.000	24	24	0.033	17
8	0.054	14	25	0.113	4	8	0.037	17	25	0.056	15
9	0.016	21	26	0.016	21	9	0.056	15			
10	0.016	21	27	0.016	21	10	0.033	17			
11	0.012	21	28	0.016	21	11	0.042	17			
12	0.016	21	29	0.032	18	12	0.047	15			
13	0.016	21	30	0.054	14	13	0.033	17			
14	0.032	18	31	0.04	16	14	0.047	15			
15	0.016	21	32	0.057	14	15	0.124	4			
16	0.016	21	33	0.016	21	16	0.037	17			
17	0.016	21				17	0.037	17			

TABLE G. 4: Characteristic of the DDG, WTs, PVs, ESS, transformer, and transmission line

	33-bus (balanced)							
	No.	**Bus**	S^{max}	CR_i^{DDG}	**Mode**	**PF**	E^{max}/E^{min}	I^{max}
			(kVA)	(cf/kWh)	(GC/IS)		(kWh)	(A/Ψ)
DDGs	1	2	1500	11.105	PQ/2nd	-	-	-
	2	9	900	7.806	PQ/2nd	-	-	-
	3	8	1700	11.165	PQ/2nd	-	-	-
	4	22	500	7.316	PQ/2nd	-	-	-
	5	25	2000	11.418	PQ/2nd	-	-	-
WTs	1	18	100	-	PQunity	1.00	-	-
	2	24	150	-	PQunity	1.00	-	-
	3	27	100	-	PQlag	0.95	-	-
	4	32	100	-	PQlag	0.95	-	-
PVs	1	24	100	-	PQunity	1.00	-	-
	2	29	200	-	PQunity	1.00	-	-
	3	31	200	-	PQunity	1.00	-	-
ESSs	1	21	350	-	PQ	-	550/160	-
	2	25	200	-	PQ	-	400/80	-
	3	33	200	-	PQ	-	400/80	-
TR	-	1	5300	-	-	-	-	-
Line	1-8	-	-	-	-	-	-	500
	9-32	-	-	-	-	-	-	200
	25-bus (unbalanced)							
	No.	**Bus**	S^{max}	CR_i^{DDG}	**Mode**	**PF**	E^{max}/E^{min}	I^{max}
			(kVA)	(cf/kW)	(GC/IS)		(kWh)	(A/Ψ)
DDGs	1	13	2000	11.148	PQ/2nd	-	-	-
	2	19	1400	11.105	PQ/2nd	-	-	-
	3	25	2500	11.165	PQ/2nd	-	-	-
WTs	1	12	100	-	PQunity	1.00	-	-
	2	22	200	-	PQlag	0.95	-	-
PVs	1	5	150	-	PQunity	1.00	-	-
	2	15	150	-	PQunity	1.00	-	-
ESSs	1	5	250	-	PQ	-	500/100	
	2	17	350	-	PQ	-	700/140	
TR	-	-	5000	-	-	-	-	-
Line	1-6	-	-	-	-	-	-	700
	7-24	-	-	-	-	-	-	350

TABLE G. 5: General parameter information

Parameter	Value
$P_i^{DDG,min}/P_i^{DDG,max}$	$0/S^{max}$
$Q_i^{DDG,min}/Q_i^{DDG,max}$	$-0.2S^{max}/+0.6S^{max}$
V^*/V^{**}	1.01/1.05
f_{bus}/ki^{ω}	2/4
$PF_i^{DDG,1st}/PF_i^{DDG,4th}$	0.4/0.4
σ^{fuel}	0.007 $/Mcf [119]
$Q_i^{ESS,min}/Q_i^{ESS,max}$	$-0.6S^{max}/+0.6S^{max}$
η_i^{ESS}	95 %
$PF_i^{TR,1st}/PF_i^{TR,4th}$	0.75/0.75

G.3 Data information exclusive for Chapter 5

TABLE G. 6: Set of scenarios and their probability obtained by fast forward selection and their corresponding calendar day/year for WT and PV

Season		Details
Fall	Scenario	{80, 352, 694, 717, 718}
	Day #	324, 322, 300, 323, 324
	Year	2008, 2011, 2015, 2015, 2015
	$\boldsymbol{\pi_{s,se}^{wiso}}$	{0.385, 0.024, 0.519, 0.048, 0.024}
Winter	Scenario	{291, 554, 586, 669, 854}
	Day #	352, 342, 374, 366, 369
	Year	2011, 2014, 2014, 2015, 2017
	$\boldsymbol{\pi_{s,se}^{wiso}}$	{0.042, 0.403, 0.120. 0.093. 0.341}
Spring	Scenario	{34, 103, 127, 563, 564}
	Day #	94, 71, 95, 76, 77
	Year	2008, 2009, 2009, 2014, 2014
	$\boldsymbol{\pi_{s,se}^{wiso}}$	{0.111, 0.021, 0.447, 0.405, 0.016}
Summer	Scenario	{152, 341, 342, 525, 619}
	Day #	212, 219, 220, 221, 224
	Year	2009, 2011, 2011, 2013, 2014
	$\boldsymbol{\pi_{s,se}^{wiso}}$	{0.523, 0.335, 0.014, 0.067, 0.061}

TABLE G. 7: The most vulnerable wind scenarios and their corresponding date

Season	Corresponding date			$\boldsymbol{max\ (v_{se}^{worst})}$	
	day	*month*	*year*	*m/s*	*(m/s)^{gust}*
Fall	19	November	2012	15.83	20.37
Winter	18	January	2011	16.11	20.74
Spring	12	Mars	2012	16.66	21.44
Summer	01	June	2010	15.55	20.01

TABLE G. 8: Parameter for generating scenario

Parameters	Unit	Set belong	Values				
N_s^{pre}	-	-	10000	$\mu_i^{pole}/\sigma_i^{pole}$	-	$\forall i \in \Omega_{LIN}$	65/15
N_s'/N_s''	-	-	5/5	$\mu_i^{cond}/\sigma_i^{cond}$	-	$\forall i \in \Omega_{LIN}$	47/9
v_i^{ci}	m/s	$\forall i \in \Omega_{WT}^{can}$	4	$\pi^{br,nvul}$	-	-	0.05
v_i^{co}	m/s	$\forall i \in \Omega_{WT}^{can}$	26	$v_{cri}^{low}/v_{cri}^{high}$	m/s	-	20/40
v_i^{ra}	m/s	$\forall i \in \Omega_{WT}^{can}$	16	$MTTR^{nw}$	h	-	2
R_i^C	kW/m^2	$\forall i \in \Omega_{PV}^{can}$	0.15	h_1^{low}/h_2^{low}	h	-	2/3
R_i^{STD}	kW/m^2	$\forall i \in \Omega_{PV}^{can}$	1	h_1^{high}/h_2^{high}	h	-	3/4
k^{gust}	-	-	1.287				

TABLE G. 9: Characteristic of the 33-bus test system

Line No.	**fb** #	**tb** #	**R** (ohm)	**X** (ohm)	L^{br} (m)	N_i^{pole}	$P_{tb}^{L,peak}$ (kW)	$Q_{tb}^{L,peak}$ (kVar)	w^{load}
1	1	2	0.092	0.047	100	4	100	60	0.027
2	2	3	0.492	0.251	500	14	90	40	0.024
3	3	4	0.365	0.186	350	10	120	80	0.032
4	4	5	0.380	0.194	350	10	60	30	0.016
5	5	6	0.817	0.706	800	21	60	20	0.016
6	6	7	0.187	0.618	200	6	200	100	0.054
7	7	8	0.710	0.235	700	19	200	100	0.054
8	8	9	1.028	0.739	1000	26	60	20	0.016
9	9	10	1.042	0.739	1000	26	60	20	0.016
10	10	11	0.196	0.065	200	6	45	30	0.012
11	11	12	0.374	0.124	350	10	60	35	0.016
12	12	13	1.465	1.153	1500	39	60	35	0.016
13	13	14	0.540	0.711	550	15	120	80	0.032
14	14	15	0.590	0.525	600	16	60	10	0.016
15	15	16	0.745	0.544	750	20	60	20	0.016
16	16	17	1.286	1.718	1300	34	60	20	0.016
17	17	18	0.731	0.573	700	19	90	40	0.024
18	2	19	0.164	0.156	150	5	90	40	0.024
19	19	20	1.501	1.353	1500	39	90	40	0.024
20	20	21	0.409	0.477	400	11	90	40	0.024
21	21	22	0.707	0.935	700	19	90	40	0.024
22	3	23	0.450	0.308	450	12	90	50	0.024
23	23	24	0.896	0.708	900	24	420	200	0.113
24	24	25	0.894	0.700	900	24	420	200	0.113
25	6	26	0.203	0.103	200	6	60	25	0.016
26	26	27	0.284	0.144	300	9	60	25	0.016
27	27	28	1.057	0.932	1000	26	60	20	0.016
28	28	29	0.802	0.699	800	21	120	70	0.032
29	29	30	0.506	0.258	500	14	200	600	0.054
30	30	31	0.972	0.961	950	25	150	70	0.040
31	31	32	0.310	0.361	300	9	210	100	0.057
32	32	33	0.340	0.529	350	10	60	40	0.016
						Total	3715	2300	

TABLE G. 10: General parameters

Elements	Parameters	Unit/detail	Values	Level problem	
				outer	inner
DDG	σ^{fuel}	\$/kWh	0.0205	✓	✓
	η_i^{DDG}	per unit	0.370	✓	✓
	σ_{INV}^{DDG}	\$/kW	1300	✓	✓
	$\sigma_{O\&M}^{DDG}$	\$/kWh	0.003	✓	✓
	K_{CO2}^{DDG}	kg/kWh	201.6	✓	-
	Mode	for GC/IS	PQ/2nd	-	✓
	$P_i^{DDG,max}$	MW	4.0	✓	-
	P_{step}^{DDG}	kW	100	✓	-
	V^*/V^{**}	p.u.	1.01/1.05	-	✓
	ki^{ω}	-	4	-	✓
	$PF_i^{DDG,1st}$	-	0.4	-	✓
	$PF_i^{DDG,4th}$	-	0.4	-	✓
	$\chi^{DDG,min}/\chi^{DDG,max}$	-	-0.2/0.6	-	✓
WT	σ_{INV}^{WT}	\$/kW	1686	✓	-
	$\sigma_{O\&M}^{WT}$	\$/kW/year	46	✓	-
	Mode	for GC/IS	PQunity	-	✓
	$P_i^{WT,max}$	MW	0.6	✓	-
	P_{step}^{WT}	kW	100	✓	-
PV	σ_{INV}^{PV}	\$/kW	2277	✓	-
	$\sigma_{O\&M}^{PV}$	\$/kW/year	21	✓	-
	Mode	for GC/IS	PQunity	-	✓
	$P_i^{PV,max}$	MW	0.3	✓	-
	P_{step}^{PV}	kW	100	✓	-
ES	$\sigma_{INV}^{ES,P}$	\$/kW	300	✓	-
	$\sigma_{O\&M}^{ES}$	\$/kW/year	80	✓	-
	$\sigma_{INV}^{ES,E}$	\$/kWh	350	✓	-
	σ_{INS}^{ES}	\$/kWh	8	✓	-
	Mode	for GC/IS	PQ	-	✓
	$P_i^{ES,max}$	MW	0.3	✓	-
	P_{step}^{ES}	kW	100	✓	-
	r^{ES}	-	5	✓	✓
	DoD^{max}	%	70	-	✓
	η_i^{ES}	%	95	-	✓
	SoC^0	%	50	-	✓
	$\chi^{ES,min}/\chi^{ES,max}$	-	-0.6/0.6	-	✓

TABLE G. 10: General parameters (continue)

Elements	Parameters	Unit/detail	Values	Level problem	
				outer	inner
TR	$S^{TR,max}$	kVA	5300	-	✓
	$\chi^{TR,min}/\chi^{TR,max}$	-	-0.6/0.6	-	✓
	$PF_i^{TR,1st}$	-	0.75	-	✓
	$PF_i^{TR,4th}$	-	0.75	-	✓
	V_{pcc}	p.u.	1.05	-	✓
Network	$P_i^{bus,max}$	kVA/ph	6.00[a],4.00[b]	✓	-
	$I_{k=1\to8}^{br,max}$	A/Ψ	500	-	✓
	$I_{k=9\to32}^{br,max}$	A/Ψ	350	-	✓
SSW	σ_{INV}^{SSW}	$/SSW	64.3	✓	-
	$\sigma_{O\&M}^{SSW}$	$/h	1.15	✓	-
General	N_T	h	24	-	✓
	TL	year	10	✓	-
	K_{CO2}^{GRID}	kg/kWh	143	✓	-
	σ^{curt}	$/kWh	3.4	-	✓
	PC^{VI}	$/kV	1.1	-	✓
	S_{base}	kVA	1000	✓	✓
	V_{base}	kV	12.66	-	✓
	$\varphi_{sel}^{1^{st},4^{th}}$	deg.	90	-	✓
	$n_{pw}^{1^{st},4^{th}}$	-	15	-	✓